Entanglement and Quantum Interactions with Macroscopic Gas Samples

Brian Julsgaard

Danish National Research Foundation
Center for Quantum Optics - QUANTOP
Department of Physics and Astronomy
University of Aarhus, Denmark

PhD thesis
October 2003

This thesis is submitted to the Faculty of Science at the University of Aarhus, Denmark, in order to fulfil the requirements for obtaining the PhD degree in Physics. The studies have been carried out under the supervision of Prof. Eugene Polzik in the Quantum Optics Laboratory at the Department of Physics and Astronomy, Aarhus University from August 1999 to January 2003, and at the Quantum Optics Laboratory, Niels Bohr Institute, Copenhagen University from February 2003 to October 2003.

Contents

List of Publications

[I] B. Julsgaard, A. Kozhekin, and E. S. Polzik, *Experimental long-lived entanglement of two macroscopic objects*, Nature **413**, 400 (2001).

[II] C. Schori, B. Julsgaard, J. L. Sørensen, and E. S. Polzik, *Recording Quantum Properties of Light in a Long-Lived Atomic Spin State: Towards Quantum Memory*, Phys. Rev. Lett. **89**, 057903 (2002).

[III] J. L. Sørensen, B. Julsgaard, C. Schori, J. Hald, and E. S. Polzik, *Quantum noise limited laser probing of atomic spin states*, Laser Physics **13**, 359 (2003).

[IV] E. S. Polzik, B. Julsgaard, J. Sherson, and J. L. Sørensen, *Entanglement and quantum teleportation with multi-atom ensembles*, Phil. Trans. Roy. Soc. A **361**, 1391 (2003).

[V] J. L. Sørensen, B. Julsgaard, C. Schori, and E. S. Polzik, *Quantum limits encountered in atomic spin measurements*, Spectrochim. Acta B **58**, 999 (2003).

[VI] E. S. Polzik, B. Julsgaard, C. Schori, and J. L. Sørensen, in *The Expanding Frontier of Atomic Physics*, Invited talks of the XVIII International Conference on Atomic Physics, eds. H. R. Sadeghpour, E. J. Heller, and D. Pritchard, World Scientific (2003).

[VII] B. Julsgaard, C. Schori, J. L. Sørensen, and E. S. Polzik, *Atomic Spins as a Storage Medium for Quantum Fluctuations of light*, Quantum Information and Computation **3**, Special issue, 518 (2003).

[VIII] B. Julsgaard, J. Sherson, J. L. Sørensen, and E. S. Polzik, *Characterizing the spin state of an atomic ensemble using the magneto-optical resonance method*, J. Opt. B: Quantum Semiclass. Opt. **6**, 5 (2004).

Preface

The work presented in this thesis is the result of a little more than four years of experimental work under supervision by Prof. Eugene Polzik. During these years I have experienced many different aspects of research which I have found very interesting. In addition to the physical insight gained by our research I learned laser physics, electronics, craftsmanship in the workshop, how to move entire laboratories to new locations, etc. I also had several opportunities to give oral presentations of our work at various international conferences.

In August 1999 I joined the Quantum Optics Laboratory at the Department of Physics and Astronomy at the University of Aarhus. At that time I had the pleasure to work with Jan Hald, Jens Lykke Sørensen, and Christian Schori who essentially taught me to adjust mirrors and tame crazy lasers. We co-operated on very interesting scientific work and we also relaxed together during numerous coffee breaks. During my time in Aarhus I also had the opportunity to work with Peter Møller Nielsen, Anton Verchovski, Wolfgang Tittel, Jens Kristian Mikkelsen, Daniel Oblak, and others.

Time went on, and Jacob Sherson joined my experiment in Aarhus. Since then we have had an excellent co-operation and obtained many interesting results. He also joined me in the relocation from the University of Aarhus to the Niels Bohr Institute at Copenhagen University. During that time I also had the pleasure to work with Carlos Alzar, Plamen Petrov, Jörg Helge Müller, and others.

From the theoretical side I worked with Alexander Kozhekin who came up with the idea that two oppositely oriented spins are interesting to study. I am also very grateful to Anders Sørensen and Klaus Mølmer who always took the time to give theoretical advice to an experimentalist. I also acknowledge interesting and useful discussions with Dmitri Kupriyanov. The technical and administrative staff at the University of Aarhus has always been very helpful, with special thanks to the workshop, to the electronics department, and to Grete Flarup.

I am very grateful to have experienced all this time together with my supervisor Eugene Polzik. We have had many enthusiastic discussions and Eugene has always been a safe guide in the entire process starting from an empty laser table to the final presentation of our research activities. Without Eugene's enthusiasm

and physical intuition we would never have reached our fruitful results.

Finally, I would like to thank my girlfriend Merete for being understanding during stressful times or late working hours. In particular I am grateful that she joined me in the relocation from Aarhus to Copenhagen.

October 2003, Brian Julsgaard.

CHAPTER 1

Outline of the Thesis

The subject of this thesis is mainly the generation of entangled states between macroscopic objects and the quantum mechanical understanding of the interaction between polarized laser light and atomic ground state spins. The work is primarily experimental but we also present theoretical calculations.

Different readers should read this thesis differently. Some chapters are meant as pedagogical introductions to the field, other chapters are very technical and may in some occasions be even clumsy! A general and hopefully understandable description of the work behind this thesis is of course the most important point. But we acknowledge the fact that younger students or co-workers following up on the work may find it useful to read about the detailed calculations and general considerations which have required a lot of effort for the author of this thesis.

Chaps. 2 and 3 give the general introduction to the field. In Chap. 2 the physical system of polarized laser light interacting with atomic ground state spins is introduced. Chap. 3 is a broader review of the field of quantum optics and puts our work into a general context. These chapters should be relevant for all readers. **Chap. 4** introduces many general aspects and techniques related to the experiments. This chapter is of course mainly for experimentalists but it also gives a general characterization of our physical system which is relevant for all readers. **Chap. 5** derives an effective Hamiltonian describing the light/matter interactions and **Chap. 6** states the equations of motion following this Hamiltonian. These two chapters are purely theoretical, the hard core experimentalist may read the main results in Secs. 6.2 and 6.3. In **Chap. 7** we start to consider experimental results and techniques in detail. This chapter is devoted to the magneto-optical resonance method for characterizing atomic ground state

spins. These purely classical results are very useful and extensively used for all other experiments of this thesis. **Chap. 8** describes theoretical and experimental investigation of the interaction between light and atoms at the quantum level. The results demonstrate that our theoretical understanding is correct to a high degree and that our physical systems are feasible for implementation of quantum information protocols. The purely theoretical **Chap. 9** and the purely experimental **Chap. 10** deal with the generation of entangled states between macroscopic cesium gas samples. The results presented in Sec. 10.1 demonstrate on demand creation of entangled states, this is the most important result of this thesis. Chaps. 7, 8, and 10 present experimental results of increasing importance and are relevant for most readers. Chap. 9 is not only for the theoretically interested reader, it also covers many practical considerations necessary for the understanding of the entanglement generation. **Chap. 11** gives an impression of possible future technological implementations of our research for quantum communication purposes. In **Chap. 12** we summarize the thesis work and give an outlook for the future.

The appendices are in general technical. **Apps. A and B** deal with the description of polarized light and atomic spins, respectively. **App. C** is more or less "text book material" on the quantum mechanical description of light/matter interactions. The emphasis is put on continuous description of light and matter. The reason for writing this down is the fact that the author (who is an experimentalist) found it difficult to find relevant references to text books and spent a huge amount of time on what may be really trivial for a theorist. It is the hope that other readers find this appendix useful. **App. D** singles out results of spherical tensor algebra directly applicable for the derivations in Chap. 5 and is only relevant for the theoretically interested reader. **App. E** reviews a few results of photo detection theory and connects these to our experiments (which deal with polarization states of light). The main problem here is time ordering of light creation and annihilation operators and turns out to be inelegant and clumsy. This appendix is reserved for readers who really want to understand every detail of the theoretical derivations in Chap. 8. **App. F** reviews the quadratic Zeeman effect and is included in this thesis for completeness, it is very useful for the understanding of magneto-optical resonance spectra presented in Chap. 7. **App. G** presents a few technical aspects of Langevin forces required for the theoretical modeling of decaying spins in Chap. 8.

CHAPTER 2

Atoms and Light as Interesting Quantum Systems

In this section we aim at explaining some general properties of atoms and light relevant for our experiments. Both atoms and light can be described in the language of quantum mechanics, but from our perspective this becomes interesting when we can couple the atomic and light degrees of freedom to each other in order to *exchange quantum information* between the two. Atoms are massive particles and therefore slow in the sense that we experimentally can keep them at a well controlled location for a long time. This means atoms are good for *storage* of quantum information. On the contrary, light is fast and is well suited for *transporting* quantum information between atomic systems or to various detection systems. In the following sections we describe in general terms how atoms and light experimentally can play these roles and we comment on the nature of the interaction between light and atoms.

2.1 The Atomic Ground State Spin

The experiments in this thesis are carried out using cesium atoms. One reason for this is the fact that lasers are available for relevant transitions, another is the fact that the definition of one second relies on the cesium atom. This atom was the preferred one when I joined the Quantum Optics Laboratory four years ago and motivating this choice is the availability of a tunable source of squeezed or entangled light at atomic transitions in cesium (we use this source in Chap. 8).

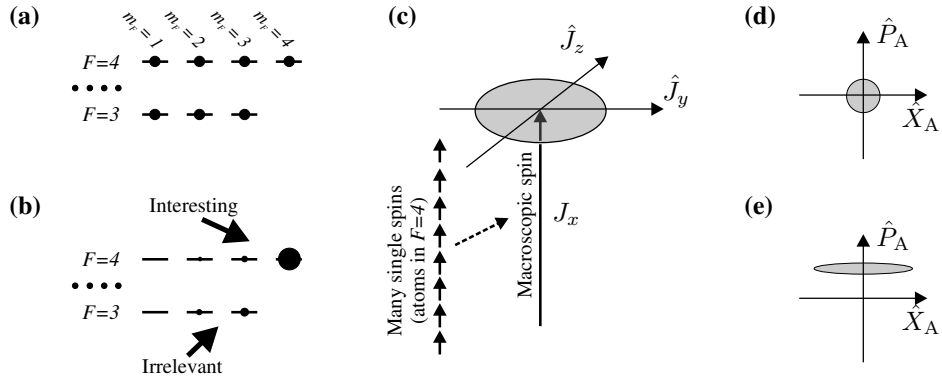

Figure 2.1: **(a)** The $6S_{1/2}$ ground state of cesium is split into two hyperfine states with $F = 3$ and $F = 4$. If atoms are left alone the spin state will populate all m_F-sublevels evenly as depicted by small circles. **(b)** In the experimental work in this thesis we are only interested in the atoms in the $F = 4$ state and it is possible to put (almost) all atoms into the outermost state with $m_F = 4$ (with the x-axis as direction of quantization). **(c)** The individual spins sum up to a macroscopic spin along the x-axis, the transverse spin components $\hat{J}_y$ and $\hat{J}_z$ have quantum uncertainties depicted by a gray disk, see Eq. (2.3). **(d)** The spin is often shown from above since only the transverse components have interesting quantum properties. The new variables $\hat{X}_\mathrm{A}$ and $\hat{P}_\mathrm{A}$ are defined in Eq. (2.4). It is in principle possible to create non-classical states, e.g. a squeezed stated as shown in **(e)**.

The ground states of cesium are characterized by the outermost electron which is in the $6S_{1/2}$ state, i.e. the orbital angular momentum $\mathbf{L}$ is zero. The electron spin $\mathbf{S}$ and thus the total electronic angular momentum $\mathbf{J}$ has quantum number $S = J = 1/2$. The nuclear spin $\mathbf{I}$ of cesium-133 has $I = 7/2$, and the coupling between the nucleus and the electron gives rise to the total angular momentum $\mathbf{F} = \mathbf{I} + \mathbf{J}$ with quantum numbers $F = 3$ and $F = 4$, see Fig. 2.1(a).

It is indeed the total angular momentum $\mathbf{F}$ which interests us in this thesis since F and the magnetic quantum numbers m_F define the energy levels of the ground states. Furthermore, we will often restrict ourselves to one hyperfine level, $F = 4$, which is possible experimentally since the hyperfine splitting $\nu_\mathrm{hfs} = 9.1926\mathrm{GHz}$ is large compared to typical resolutions of our laser systems. And now a bit of confusion, we choose to denote the total angular momentum of a *single atom* by $\mathbf{j}$ and for a collection of atoms (in the $F = 4$ state) we denote the *collective* total angular momentum by $\mathbf{J}$, i.e.

$$\mathbf{J} = \sum_{i=1}^{N} \mathbf{j}^{(i)}, \tag{2.1}$$

where N is the number of atoms in the $F = 4$ state and $\mathbf{j}^{(i)}$ is the total angular

momentum of the i'th atom. The reason for using $\mathbf{J}$ and not $\mathbf{F}$ is that J is generally more used in the literature for spins, and indeed, we wish to think about our spins more abstractly than just the properties of some atoms. Many results in this thesis should be applicable in a broader sense than to a collection of cesium atoms.

In our experiments the number of atoms N will be of the order 10^{12} and we will almost always aim at having all atoms polarized along one direction which we denote as the x-axis, see Fig. 2.1(b). With the x-axis as quantization axis we thus have $m_F = 4$ for all atoms to a high degree of accuracy, and the collective spin $\hat{J}_x$ will really be a macroscopic entity. With this experimental choice, we may treat the x-component of the collective spin as a classical c-number, i.e. we replace the operator $\hat{J}_x$ by the number J_x. The transverse spin components $\hat{J}_y$ and $\hat{J}_z$ maintain their quantum nature. They will typically have zero or a small mean value. The quantum fluctuations are governed by the commutation relation and the Heisenberg uncertainty relation (with $\hbar = 1$)

$$\left[\hat{J}_y, \hat{J}_z\right] = iJ_x \tag{2.2}$$

$$\Rightarrow \quad \mathrm{Var}(\hat{J}_y) \cdot \mathrm{Var}(\hat{J}_z) \geq \frac{J_x^2}{4}. \tag{2.3}$$

Pictorially, we add many small spins to a macroscopic spin, see Fig. 2.1(c), and the direction of this macroscopic spin has no precise meaning but can only be defined within the quantum uncertainty (depicted by the gray disk) stated quantitatively by Eq. (2.3). With 10^{12} atoms the angular quantum uncertainty of the collective spin direction is of the order 10^{-6}.

To connect our spin system to quantum mechanics more generally, we note that the classical J_x enable us to define new quantum variables $\hat{X}_\mathrm{A}$ and $\hat{P}_\mathrm{A}$ by

$$\hat{X}_\mathrm{A} = \frac{\hat{J}_y}{\sqrt{J_x}}, \quad \hat{P}_\mathrm{A} = \frac{\hat{J}_z}{\sqrt{J_x}}, \quad \Rightarrow \quad \left[\hat{X}_\mathrm{A}, \hat{P}_\mathrm{A}\right] = i, \tag{2.4}$$

where the subscript A refers to "atoms". The above is exactly on the form seen in many text books on introductory quantum mechanics. Even though we know that e.g. $\hat{J}_y$ has a discrete spectrum of eigenvalues, which must be inherited by $\hat{X}_\mathrm{A}$, we effectively have continuous quantum operators as ordinary position $\hat{x}$ and momentum $\hat{p}$ when N is large. For this reason we can depict the transverse spin variables $\hat{J}_y$ and $\hat{J}_z$ as seen from above as in Fig. 2.1(d,e). The disk or ellipse symbolizes the Heisenberg uncertainty relation as is often seen in the literature on e.g. description of the electromagnetic field. As we shall see in Chap. 11, protocols for quantum information processing can be very well described in the x, p-language with no specific reference to the cesium atom.

We finalize this section with a very important definition. If all atoms in the $F = 4$ state have $m_F = 4$ (or $m_F = -4$) the collective spin is said to be in the *coherent spin state* [1](CSS). In this state all atoms are independent of each other

[1]Coherent spin states are discussed more generally in [1]

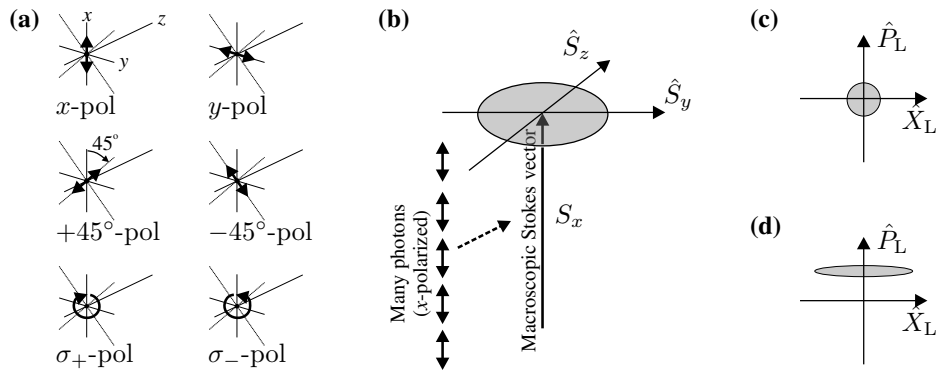

Figure 2.2: **(a)** Some different basis choices for the polarization of a photon. **(b)** For many x-polarized photons the Stokes vector has practically a classical S_x-component. The transverse components $\hat{S}_y$ and $\hat{S}_z$ must satisfy the Heisenberg uncertainty relation (2.8) symbolized by the gray disk. **(c)** We may restrict ourselves to a top view of (b) since only the transverse components $\hat{X}_\mathrm{L}$ and $\hat{P}_\mathrm{L}$ play a role concerning the quantum state. **(d)** Non-classical states of the Stokes vector are possible, here squeezing of one quadrature.

in the sense that the total wave function is the product function of each atom in $m_F = 4$. This state also fulfils the minimum uncertainty relation

$$\mathrm{Var}(\hat{J}_y) \cdot \mathrm{Var}(\hat{J}_z) = \frac{J_x^2}{4} \quad \text{(coherent spin state)} \tag{2.5}$$

and we will see in Chaps. 9 and 10 that this equality serves as a reference point for manifestly quantum states, i.e. states that have no classical analogue.

2.2 Polarization States of Light

All experiments in this thesis involve laser light interacting with atomic spin states, and it turns out that the polarization of the light is the relevant quantum variable to describe. Below we introduce the description of polarization states of light in general terms, for a more rigorous definition see App. A.

Now, consider a pulse of light, or a collection of photons, propagating in the z-direction. The polarization state is well described by the Stokes operators

$$\begin{aligned}
\hat{S}_x &= \frac{1}{2}\left(\hat{n}_\mathrm{ph}(x) - \hat{n}_\mathrm{ph}(y)\right), \\
\hat{S}_y &= \frac{1}{2}\left(\hat{n}_\mathrm{ph}(+45^\circ) - \hat{n}_\mathrm{ph}(-45^\circ)\right), \\
\hat{S}_z &= \frac{1}{2}\left(\hat{n}_\mathrm{ph}(\sigma_+) - \hat{n}_\mathrm{ph}(\sigma_-)\right),
\end{aligned} \tag{2.6}$$

where $\hat{n}_{\rm ph}(x)$ is the number of photons in the pulse with x-polarization, and so on (the different ways of describing polarization are depicted in Fig. 2.2(a)). The Stokes operators are dimensionless, they count photons. In other chapters we will also consider Stokes operators measuring photon fluxes.

We shall make our first approximation right away. We assume that almost all photons are linearly polarized along the x-direction (we could have chosen any direction). For a pulse containing many photons this means that we can treat $\hat{S}_x \to S_x$ as a c-number. Note, this is very similar to the approximation of a well polarized sample of spins in the previous section.

It can be shown that the Stokes vector satisfies angular commutation relations (see Eq. A.13), i.e.

$$\left[\hat{S}_y, \hat{S}_z\right] = iS_x \tag{2.7}$$

$$\Rightarrow \quad \mathrm{Var}(\hat{S}_y) \cdot \mathrm{Var}(\hat{S}_z) \geq \frac{S_x^2}{4} \quad \text{(pulse of light)}. \tag{2.8}$$

The operators $\hat{S}_y$ and $\hat{S}_z$ are our interesting quantum variables, they usually have zero mean value since a collection of x-polarized photons have polarization $\pm 45°$ or $\sigma_\pm$ with equal probability being one half. But we remark, that if the linear x-polarized light is rotated by an angle θ around the z-axis the balance between the $\pm 45°$-components is changed and $\hat{S}_y$ gets a non-zero mean value. In fact

$$\left\langle \hat{S}_y \right\rangle = 2S_x \cdot \theta \quad (\text{for } \theta \ll 1). \tag{2.9}$$

We see that $\hat{S}_y$ is a measure of the polarization rotation, and that the quantum fluctuations of $\hat{S}_y$ can be interpreted as quantum fluctuations in the direction of polarization. This kind of rotation will prove to be very important when we consider the interaction of polarized light with atomic spins.

The classical S_x component and the quantum uncertainty of the $\hat{S}_y$ and $\hat{S}_z$ can be depicted as in Fig. 2.2(b) (just like the case for atomic spins in Fig. 2.1(c)), the gray disk symbolizes the Heisenberg uncertainty relation (2.8). We may also see this disk from above as in Fig. 2.2(c,d), where we have defined the new quantum variables (subscript L refers to "light")

$$\hat{X}_{\rm L} = \frac{\hat{S}_y}{\sqrt{S_x}}, \quad \hat{P}_{\rm L} = \frac{\hat{S}_z}{\sqrt{S_x}}, \quad \Rightarrow \quad \left[\hat{X}_{\rm L}, \hat{P}_{\rm L}\right] = i. \tag{2.10}$$

We see, as in the case of atomic spins, the polarization quantum state of light is similar to the standard position/momentum operators. The mathematical equivalence of the spin and light operators motivate the search for possible implementations of quantum information protocols that exchange quantum states between light and atoms.

If we go into a little detail with the operators $\hat{X}_{\rm L}$ and $\hat{P}_{\rm L}$ it actually follows from Eq. (A.14) that

$$\hat{X}_{\rm L} = \frac{\hat{a}_y + \hat{a}_y^\dagger}{\sqrt{2}} \quad \text{and} \quad \hat{P}_{\rm L} = \frac{\hat{a}_y - \hat{a}_y^\dagger}{i\sqrt{2}}, \tag{2.11}$$

where $\hat{a}_y^\dagger$ and $\hat{a}_y$ are the creation and annihilation operators for photons with y-polarization. In our approximation with strong linear polarization along the x-axis the x-polarized part serves as a "reservoir" of photons controlling the strength of the pulse. It also serves as a phase reference for the y-polarized part which carries the interesting quantum fluctuations.

As a final remark of this section we consider an x-polarized pulse of light emerging from a laser. Then the y-polarized mode is in the vacuum state and we easily find

$$\mathrm{Var}(\hat{S}_y) \cdot \mathrm{Var}(\hat{S}_z) = \frac{S_x^2}{4} \quad \text{(light pulse, coherent state)}, \tag{2.12}$$

which is actually valid for the y-polarized mode being in any coherent state. As for atomic spins, this equality sets the benchmark point for non-classical states of the light polarization. If $\mathrm{Var}(\hat{S}_y) = \mathrm{Var}(\hat{S}_z) = S_x/2$ we say that the noise of $\hat{S}_y$ or $\hat{S}_z$ is at the so-called shot noise level.

2.3 Interaction Between Atomic Spins and Polarized Light

Let us now introduce the interaction of polarized light with the atomic spin state of a sample of atoms. A detailed calculation will be given in Chaps. 5 and 6. First, consider Fig. 2.3(a) which shows the level scheme of the $6S_{1/2}$ and $6P_{3/2}$ states of cesium. We tune a laser, which we call the probe laser, to the dipole transition between these two levels and we may choose a detuning Δ measured from the $F = 4 \rightarrow F' = 5$ transition with red detuning being positive.

The polarization state of this laser light may change in different ways if it interacts with an atomic sample. First of all, the absorption of one polarization component may be different than the absorption of another polarization component. This clearly changes the polarization state, but we will not consider this situation at all in this thesis. The absorption profile of the transition will look like the solid line graph in Fig. 2.3(b), in the wings it will fall off as $1/\Delta^2$. Going to a sufficiently far detuning we can make absorption effects negligible compared to dispersion effects, the latter fall off as $1/\Delta$. A typical dispersion profile (for a single $F \rightarrow F'$ transition) is shown with the dashed line graph in Fig. 2.3(b). Dispersion effects will change the polarization state of light if the index of refraction is different for two orthogonal polarization components, i.e. if the sample is birefringent.

Fig. 2.3(c) shows a pulse of light propagating in the z-direction through an atomic sample which is polarized along the x-direction. Classically, it is clear from simple symmetry reasoning that we may have $n_x \neq n_y$ (the sample has linear birefringence), while e.g. $n_{+45^\circ} = n_{-45^\circ}$ and $n_{\sigma_+} = n_{\sigma_-}$. Thus the x-direction is an optical axis and x- or y-polarized light will pass on without change, i.e. $\hat{S}_x$ will be unchanged by the interaction. If we let light with linear polarization along

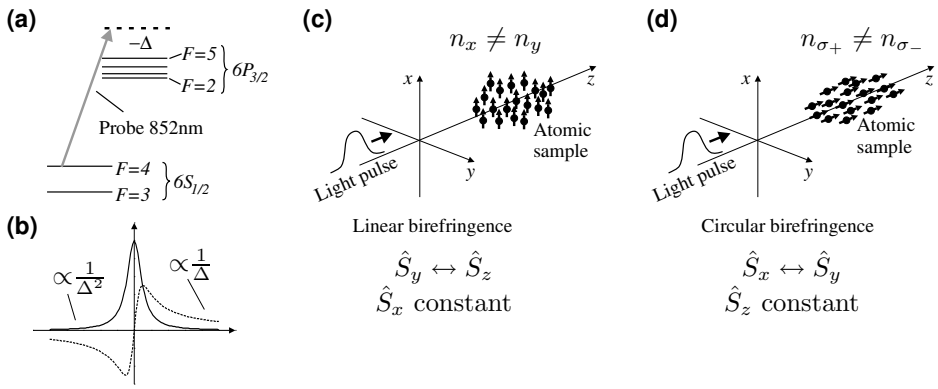

Figure 2.3: **(a)** The probe laser interacting with cesium atoms and the relevant level structure. The detuning Δ is defined relative to the $F = 4 \rightarrow F' = 5$-transition and is positive for red detuning. **(b)** The absorption (solid line) and refractive index (dashed line) in general for an optical transition. For sufficiently far detuning absorption effects are small since they fall off faster (as $1/\Delta^2$) than dispersion effects (fall off as $1/\Delta$). **(c)** A light pulse on an atomic sample which is aligned along the x-axis will change its polarization, the sample has linear birefringence with different indices of refraction $n_x \neq n_y$. A $\pm 45°$-polarized pulse will become elliptical and vice versa, i.e. $\hat{S}_y$ and $\hat{S}_z$ will change. With the x-axis as optical axis the $\hat{S}_x$ component is unchanged. **(d)** For spins oriented along the propagation direction, there is no preferred direction in the xy-plane, but the sample has circular birefringence with $n_{\sigma_+} \neq n_{\sigma_-}$. Linear polarization will rotate, i.e. $\hat{S}_x$ and $\hat{S}_y$ change, but the $\hat{S}_z$-component is unchanged.

the $+45°$-direction interact with the atoms, the light polarization has both an x- and y-part which are subject to different phase shifts. This will change the ellipticity of the light, or in other words $\hat{S}_y$ and $\hat{S}_z$ begin to mix up. A quantitative discussion of this effect is given in Sec. 6.4, see Eq. (6.16) and (6.17).

Another example is shown in Fig. 2.3(d), where the atoms now are oriented along the z-direction. Classically we have in this case $n_x = n_y = n_{+45°} = n_{-45°}$ since there is no preferred direction in the xy-plane. But spins pointing in one direction along the z-axis is, from a classical view point, the same as a charged particle rotating in one direction around the z-axis. This suggests that we may have $n_{\sigma_+} \neq n_{\sigma_-}$, the sample has circular birefringence. The different phase shift experienced by the σ_+- and σ_--part of the light will rotate the polarization around the z-axis, hence $\hat{S}_x$ and $\hat{S}_y$ begin to mix up. The number of σ_+- and σ_--photons cannot be changed by this phase shift, thus $\hat{S}_z$ is unchanged in the process. A quantitative discussion of circular birefringence is given in Sec. 6.2.

For our experiments the linear birefringence turns out to play a minor role compared to the circular birefringence. Linear birefringence is non-existing for

spin-1/2 particles[2], and if the detuning Δ is much greater than the excited states hyperfine splitting $\omega_{\mathrm{hfs,e}}$ the probe laser only experiences the spin-1/2 properties of the electron. We have approximately that linear birefringence is proportional to $\omega_{\mathrm{hfs,e}}/\Delta^2$. Circular birefringence is possible for a spin-1/2 particle and survives large detunings, i.e. is proportional to $1/\Delta$. Another way of understanding this is that the dispersive profile shown in Fig. 2.3(b) for each transition $F = 4 \rightarrow F' = 3, 4, 5$ will interfere destructively for the linear birefringence and constructively for circular birefringence. A quantitative measure of the above is partly expressed by the parameters defined in Eq. (5.16).

In the following we assume that linear birefringence is zero, and that light and atoms are polarized along the x-direction. We are now ready to give a qualitative derivation of the equations of interaction between polarized light and atomic spins. These equations are the basis of the work in this thesis.

First, when linearly polarized light passes the atomic spin in the z-direction, the circular birefringence caused by the spin component $\hat{J}_z$ will rotate the polarization of the light. Even though the mean value $\left\langle \hat{J}_z \right\rangle$ may be zero the quantum fluctuations of $\hat{J}_z$ cause polarization rotation. This is expressed quantitatively as

$$\hat{S}_y^{\mathrm{out}}(t) = \hat{S}_y^{\mathrm{in}}(t) + aS_x\hat{J}_z(t), \tag{6.11}$$

where "in" and "out" refers to the light before and after the interaction. The Stokes vector with strong x-component S_x is rotated by an angle $a\hat{J}_z$ around the z-axis where a is a constant describing the strength of the interaction. The above equation is calculated to first order with $a\hat{J}_z \ll 1$. This is also known as the Faraday effect. We know that circular birefringence does not affect $\hat{S}_z$ and we neglected linear birefringence, hence

$$\hat{S}_z^{\mathrm{out}}(t) = \hat{S}_z^{\mathrm{in}}(t). \tag{6.12}$$

The light leaving the atomic sample carries information about the spin component $\hat{J}_z$. We see that a measurement of $\hat{S}_y^{\mathrm{out}}$ will give information about $\hat{J}_z$, and if the interaction constant a is large so that the second term of (6.11) dominates the first we can get really detailed information about $\hat{J}_z$. The Heisenberg uncertainty relation (2.3) then requires the interaction also to affect $\hat{J}_y$. A calculation shows that the time evolution of $\hat{J}_y$ is

$$\frac{\partial}{\partial t}\hat{J}_y(t) = aJ_x\hat{S}_z(t). \tag{6.13}$$

The physical process involved is the Stark shift of the magnetic sublevels depending on the helicity of the light given by $\hat{S}_z$. The splitting caused by the light will, just like a constant magnetic field along the z-direction, cause rotation of the spin around the z-axis. The strong J_x component will then contribute in the

[2]Linear birefringence is caused by alignment terms, e.g. $\hat{\jmath}_x^2 - \hat{\jmath}_y^2$. For a spin-1/2 we have $\hat{\jmath}_x^2 = \hat{\jmath}_y^2 = 1/4$, hence no alignment.

y-direction, the angular rate of spin rotation being $a\hat{S}_z(t)$ where we normalized $\hat{S}_z(t)$ to measure photons per second. Finally, the $\hat{J}_z$ component is unaffected by the interaction,

$$\frac{\partial}{\partial t}\hat{J}_z(t) = 0. \tag{6.14}$$

This follows from the fact that $\hat{S}_z$ is constant and the conservation of angular momentum along the z-direction. Spin flips along z must be accompanied by changes of σ_+-photons into a σ_--photons or vice versa.

The strong components S_x and J_x are effectively unchanged by the interaction. In our experiments the typical rotation of light polarization or spin polarization amounts to approximately 10^{-6} radians, and we may clearly assume S_x and J_x to be constant.

The above equations are linear, they couple polarization states of light to the spin states of atoms. Note, that quantum properties of the spin state can be read out on light by (6.11) and that quantum properties of light can be fed into atoms by (6.13). We study the flow of quantum fluctuations of this kind in detail in Chap. 8.

Note also, that (6.11) enables us to measure $\hat{J}_z$ (if the first term is small), and at the same time (6.14) ensures that the state of $\hat{J}_z$ will not be destroyed in the measurement process. Thus, we are able to perform quantum non-demolition (QND) measurements of the atomic spin. This will prove very useful for generation of entangled states as we will describe in Chap. 9.

CHAPTER 3

Motivation - Quantum Information Processing and Communication

In this chapter we try to give the reader an overview of the field of quantum information processing and quantum communication. This is a part of physical science which has grown very rapidly since the beginning of the 1990'ies. The physics involved is very interesting in itself but technological advancement is also a motivation for studies in this field. We will briefly touch the areas of quantum cryptography, quantum computing, quantum communication, and precision measurements. We aim to describe for the reader where our work should be placed in this context.

3.1 Why Quantum State Engineering

In Chap. 2 we introduced our experimental systems, spin polarized atomic samples and polarization states of light. We explicitly concentrated on quantum variables and not classical mean values. There are some reasons for this being an interesting approach.

- Quantum states are rich in the sense that it takes many parameters to describe the quantum state. For our systems, which approximately are continuous like position $\hat{x}$ and momentum $\hat{p}$ of a particle, the quantum state is in principle described by a wave function ψ which for each x assigns a

complex number $\psi(x)$, a vast amount of complex numbers. We could also count e.g. individual spin-1/2 particles which each have a Hilbert space of dimension two. The joint quantum state of n spin-1/2 particles is described by 2^n complex numbers, an amount rapidly increasing with n. This richness is exploited in quantum computing protocols, as we will discuss in the next section.

- Quantum states cannot be cloned [2]. This means that there is some sort of *privacy* in quantum states. If I have a secret message encoded in a quantum state an eavesdropper will have to steal the entire quantum state in order to obtain this message, and accordingly I would loose the quantum state - a situation that I would recognize and act upon.

- The above point also presents a very big challenge. With only one copy of the quantum state we are very vulnerable to loss mechanisms. Information about the quantum state can "leak" into the surrounding environment and be inevitably lost. Excluding unwanted coupling to external degrees of freedom is thus a big challenge.

- The fact that we can reach a situation where quantum mechanics is essential to describe the evolution of physical systems and especially the need of quantum mechanics for the understanding of encoding and processing of messages is satisfactory in itself for a physicist and it may be a very crucial step for future technological achievements.

3.2 Technological Implementations

In the previous section we gave some rather abstract reasons for quantum states being interesting. In this section we concentrate a little more on what has actually been proposed or achieved.

- **Quantum cryptography** is an area of physics dealing with secret communication. The aim is often to distribute a key between two parties, Alice and Bob, and this key must be unknown to everyone else. Quantum cryptography exploits the fact that quantum states cannot be cloned [2]. For instance a single photon can bear information sent from Alice to Bob. An eavesdropper cannot steal this photon or perform measurements on it without being recognized. Quantum cryptography has been implemented using single photons or at least weak pulses which very seldom contain more than one photon [3]. Using single particles as information carriers is elegant and intuitive. But pulses containing many photons have also been demonstrated as an implementation for secret communication [4, 5, 6, 7, 8, 9]. If our physical systems should be implemented for cryptography it would possibly be along these lines.

- **Quantum computation** is a big motivation for exploiting and controlling quantum systems. The most famous proposals are Grover's search algorithm [10] and Shor's algorithm for prime factorizing integers [11]. Both algorithms will be much faster than any known algorithms on a classical computer. The theory of quantum computation utilizing *qubits* (quantum superpositions $|\psi\rangle = \alpha\,|0\rangle + \beta\,|1\rangle$ of two discrete states $|0\rangle$ and $|1\rangle$) and a few operations on qubits (e.g. the phase gate and the CNOT-gate) is well developed. With an appropriate combination of these basic building blocks any computation can in principle be performed [12]. Many small-scale experimental demonstrations of quantum computing have been performed. To mention a few, ion-traps have been proposed and used [13, 14, 15] and nuclear magnetic resonance (NMR) of molecules have been used to e.g. factor the integer $N = 15$ [16]. Scaling up of quantum algorithms to large systems have not yet been implemented, since it is a very difficult task. The process is very vulnerable to decoherence and must rely on quantum error correction. A review of quantum computing including error correction is given in [17].

  The above implementations all deal with discrete quantum systems. There are some proposals for quantum computation [18] and quantum error correction codes [19, 20] over continuous variables but the discrete implementations seem more promising. In [21] it has been shown how distinct coherent states can "discretize" continuous variables and thus simulate qubits. This proposal requires generation of superpositions of distinct coherent states (Schrödinger cat states) which is a difficult task. A proposal for generating such states in an ensemble of spin states like ours is given in [22]. Schrödinger cat states have been experimentally demonstrated for an electromagnetic field [23] and for the motional state of a trapped ion [24]

- **Quantum communication** is the transport of (unknown) quantum states from one place to another. This could be among e.g. two atomic samples or from an atomic sample to a beam of light (these process are in some cases called *teleportation*). Again, the no-cloning theorem [2] imposes some rules to follow. If a quantum state is to be sent from Alice to Bob, the initial state at Alice's place must be completely destroyed in order for Bob to recreate exactly the same state. Also, information about the state must not leak into the environment or be measured by any observer in the process. These facts require good isolation from external degrees of freedom and some cleverness in handling the quantum states. In Chap. 11 we will show that protocols actually exist for physical systems of our kind. In fact, continuous systems with many particles have an advantage over discrete systems in teleportation protocols. Quantum teleportation of quadratures of the electromagnetic field has been achieved [25]. Teleportation of discrete states of a photon has partly been performed [26, 27]. In these cases, however, a complete teleportation protocol that always works is difficult to implement [28, 29].

- **Quantum memory** is the process of storing and retrieving a quantum state from some long lived physical system. This could be achieved with the help from teleportation, e.g. the polarization state of a pulse of light could be teleported onto the spin state of an atomic sample. After some time (less than the atomic decoherence time) we could teleport the atomic spin state back to another pulse of light. Protocols along these lines are very relevant for us and will be discussed in Chap. 11. Another approach toward quantum memory is the use of electromagnetically induced transparency to map states of the electromagnetic field onto atomic variables [30]. This has been demonstrated experimentally for classical mean values [31, 32, 33] and is a promising candidate for a real quantum memory.

- **Entanglement generation** is a key ingredient for quantum teleportation protocols but also in itself it provides a very interesting study of quantum mechanics. Generation of entangled states of the electromagnetic field has been achieved in many cases, some examples can be found in [34, 35, 36, 37]. One of the really famous studies of such states was the first experimental violation of Bell's inequalities [38, 39] where the very basis of quantum mechanics was tested. We demonstrate the creation of an entangled state between two atomic samples in Chap. 10. See [40, 41] for other examples of entangled states between massive particles.

- **Precision measurements** is also a motivation for the study of quantum states. Spin squeezing can improve signal to noise ratios of certain measurements [42]. In fact in [43] it was shown that the best cesium frequency standards today are limited by the projection noise of spin states. Spin squeezing of atomic states have been demonstrated in [44, 45].

In short, there are many possible implementation of our research. Our particular physical systems with strong light pulses and macroscopic atomic samples is well suited for teleportation protocols, quantum memory protocols, entanglement generation, and precision measurements. There will probably be some applicability in the field of quantum cryptography. The field of quantum computation seems to be the hardest problem to address with our present knowledge.

3.3 Continuous Versus Discrete Systems

Our physical system with many photons and many atoms lead to continuous variables as introduced in Chap. 2. In this section we motivate the use of continuous systems for light/matter interactions and we draw attention to (dis)advantages of these kinds of systems.

A very important motivation for using many particles is the question of interaction strength. If light and atoms only induce weak changes to the quantum state of each other we would not be able to let quantum fluctuations flow from one system to the other with high efficiency. The interaction between light and

matter is (in the dipole approximation) basically governed by the Hamiltonian $\hat{H}_{\text{int}} = -\mathbf{d} \cdot \mathbf{E}$ where $\mathbf{d}$ is the dipole operator of the matter particle and $\mathbf{E}$ is the electromagnetic field. We need this Hamiltonian to be of sufficient magnitude which can be reached in a number of different ways.

- The electromagnetic field $\mathbf{E}$ can be made really big. One way to do this is to place a single particle inside a high finesse cavity which may enhance the interaction by many orders of magnitude [46].
- The dipole moment of a single particle can be made large by using Rydberg states of atoms. Examples are given in [47].
- Yet another possibility is our approach. Using many particles we will have a large joint dipole operator $\mathbf{D} = \sum \mathbf{d}_i$ and using a relatively strong field $\mathbf{E}$ we may approach a strong interaction regime. The figure of merit is here Eq. (6.11), we need the second term $aS_x\hat{J}_z$ to be of the order of the first term $\hat{S}_y^{\text{in}}$ to have strong coupling. With the quantum noise limited variances for spins (2.5) and polarization states of a light pulse (2.12) we conclude that $\text{Var}(aS_x\hat{J}_z) \geq \text{Var}(\hat{S}_y^{\text{in}})$ when $a^2 S_x J_x \geq 1$. The parameter a, which is given by Eq. (6.15), has for our setup typically a value such that the strong coupling condition is of the order $S_x J_x \geq 10^{25}$.

Of the three approaches above ours is by far the most simple from a technical perspective. We use free propagating light through a sample of atoms in the ground state. When technical challenges has been dealt with, the other two approaches reveal a more simple and elegant quantum system than ours. Especially, the internal atomic state is described by a low dimensional Hilbert space contrary to our practically infinite Hilbert space.

Another aspect of macroscopic continuous systems is robustness to decoherence. Some people often state mistakenly that a very big quantum system decoheres very fast simply because of the number of particles involved. This need not be the case. We deal with the collective properties of e.g. the spin state of an atomic ensemble with $\approx 10^{12}$ particles. The role of each atom is totally negligible, if one atom is lost the quantum state of the ensemble will be unchanged. If on the other hand 10% of the atoms are lost or subject to decoherence we will see the effect on the quantum state of the collective spin variable. The atoms cooperate in a fashion where each atom contributes very little but the huge number of particles together make a difference. So, we must screen our atoms in general from decoherence, but we need not care about a single atom alone.

If we should conclude this chapter with some general remarks about our approach with many particles and other approaches with small systems it would be: Large systems often have technical simplicity from an experimental point of view. They have a clear advantage in the fields of quantum communication but lack good ideas in the areas of quantum computation and error correction. Small systems are often very involved experimentally but that said the conceptual understanding is simple and elegant. These systems have an advantage for

purposes of quantum computation, quantum cryptography, and error correction. For quantum communication protocols they meet difficulties.

CHAPTER 4

Experimental Methods

In this chapter we discuss general aspects of our experiments. This includes details about lasers, glass cells with cesium atoms, magnetic fields and Larmor precession, spin life times, and optical pumping. We concentrate on properties of lasers and atomic samples common to many experiments and we discuss typical values of experimental parameters for the work presented in this thesis. More specific experimental details will be given in the different chapters connected to the experimental results.

During the past four years we have moved laboratories twice and made a major upgrade of the experimental setup. Some reasons for the upgrade are discussed in Sec. 10.2. The contents of the present chapter describe the newer setup since this will be more relevant to most readers. Important differences are mentioned in other chapters when appropriate.

4.1 Laser Systems

The level scheme of cesium is shown in Fig. 4.1 together with some transitions at which we apply laser beams. All our interesting physics mainly takes place in the $F = 4$ hyperfine multiplet, and we need lasers for state preparation and manipulations. The goal is to create high quality coherent spin states.

One laser called the *optical pump laser* is tuned to the $6S_{1/2}, F = 4 \rightarrow 6P_{1/2}, F = 4$ transition (894nm). Its main purpose is to pump atoms into the extreme $F = 4, m_F = 4$ ground state magnetic sub-level which is the starting point for many interesting experiments (see discussion in Sec. 2.1). Note, that

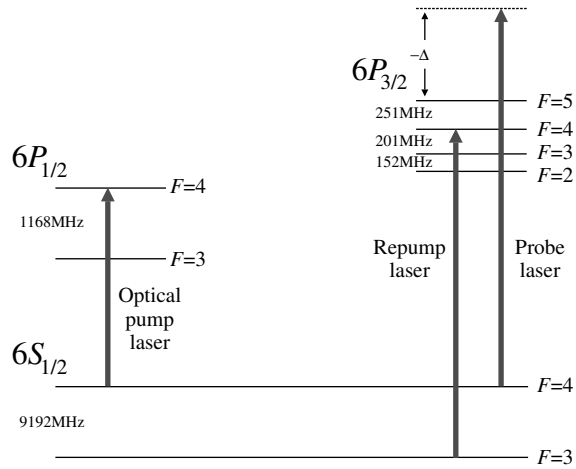

Figure 4.1: The level scheme of cesium and the lasers used in the experiment. The nuclear spin $I = 7/2$ creates hyperfine splitting with $F = 3, 4$ of the cesium ground state. All our experiments concentrate on atoms in the $F = 4$ hyperfine levels and to measure properties of these atoms the *probe laser* is coupled off-resonantly with detuning Δ to the $6S_{1/2}, F = 4 \rightarrow 6P_{3/2}$ transitions. The *repump laser* and the *optical pump laser* are tuned into resonance with the $6S_{1/2}, F = 3 \rightarrow 6P_{3/2}, F = 4$ and $6S_{1/2}, F = 4 \rightarrow 6P_{1/2}, F = 4$ transitions, respectively. These lasers redistribute atoms among the ground state levels by optical pumping, for more details see Sec. 4.5.

the $F = 4, m_F = 4$ state is a dark state if this laser has σ_+-polarization.

Another laser called the *repump laser* is tuned to the $6S_{1/2}, F = 3 \rightarrow 6P_{3/2}, F = 4$ transition (852nm). This laser is responsible for taking atoms out from the $F = 3$ ground state and into the $F = 4$ ground state. To some extent the strength of this laser controls the number of atoms in the for us relevant $F = 4$ sub-states.

The repump laser and the optical pump laser are both home built diode lasers, a picture is shown in Fig. 4.2. During the past four years a number of different laser designs have been used, the present one being the most successful. The diodes are anti-reflection coated and can be purchased from Eagleyard Photonics GmbH in Germany. The diodes work very well but we have had some problems with the life time. The laser cavity consists of the diode back side together with a diffraction grating with 1800 lines per mm in the Littrow configuration, see Fig. 4.2(a). This ensures tunability over a broad range of wavelengths. The light passes an optical isolator and a small fraction is split off for locking to the right transition by frequency modulated absorption spectroscopy [48, 49], see Fig. 4.2(b). The remaining beams are used in the experiment for optical pumping (see Sec. 4.5) creating macroscopic spin states with high degree of orientation. The lasers are running cw, at present we create pulses of light by acousto-optical

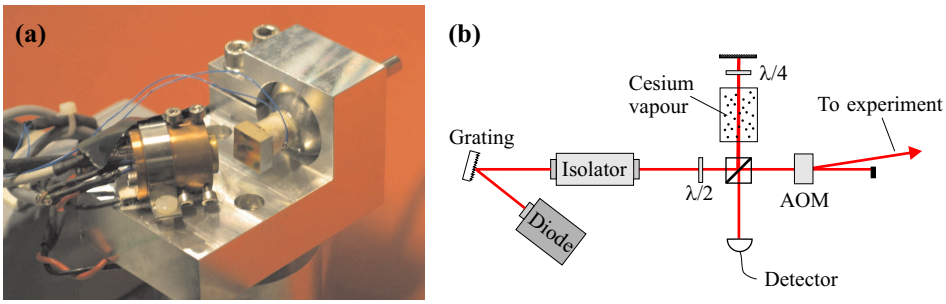

Figure 4.2: The diode lasers. **(a)** A picture of a laser diode hidden inside a copper block directing its beam to a diffraction grating (the small square). A piezo-element connects the grating to a steel ball which can be fixed by two screws seen at the top. This design is cumbersome to adjust but very stable when working. **(b)** The work principle of the laser. After the grating the light passes an isolator and a small fraction is reflected on a PBS for saturated FM absorption spectroscopy [48, 49]. The remaining beam is shaped into pulses by an AOM. When lasers are working well, more than 25mW of power is available for the experiments.

modulators (AOMs). Historically we have also been using a chopper for this purpose, but the AOMs are much more flexible in terms of timing the laser pulses.

A third laser called the *probe laser* is detuned by an amount Δ from the $6S_{1/2}, F = 4 \rightarrow 6P_{3/2}, F = 5$ transition (852nm). Different values of the detuning have been used around $\Delta \approx -1$GHz (negative for blue detuning). This detuning is much smaller than the ground state hyperfine splitting at $\approx$ 9GHz (so that light is sensitive to atoms in $F = 4$ only) and considerably larger than the hyperfine splitting of the upper state $6P_{3/2}$ (this reduces higher order effects which will be discussed further in Chap. 5). The probe laser beam is produced by a Microlase Ti:sapphire laser which can deliver typically around 1W of light at 852nm when being pumped by a Coherent Verdi V8 laser delivering 8W of light at 532nm (doubled Nd:YAG). The setup is shown in Fig. 4.3 where also the locking mechanism is pictured. The locking is similar to the case of diode lasers apart from the fact that the part split off is passing through a fiber coupled electro-optical modulator (EOM) which creates strong sidebands with frequencies up to more than 1GHz. In this fashion detunings up to more than 2GHz are available (we can use the second side band for locking also). The probe laser is also a cw laser, pulses were historically created by a chopper but now we use an EOM with a polarizing beam splitter (PBS). The Verdi laser has relaxation oscillations around 500kHz which are inherited in the spectrum of the probe laser. We are vulnerable to laser noise but we find that the noise spectrum is pretty quiet around 325kHz (it would also be quiet at high frequencies above 1MHz). In Sec. 4.3 we explain that our experiments are carried out in a way where the

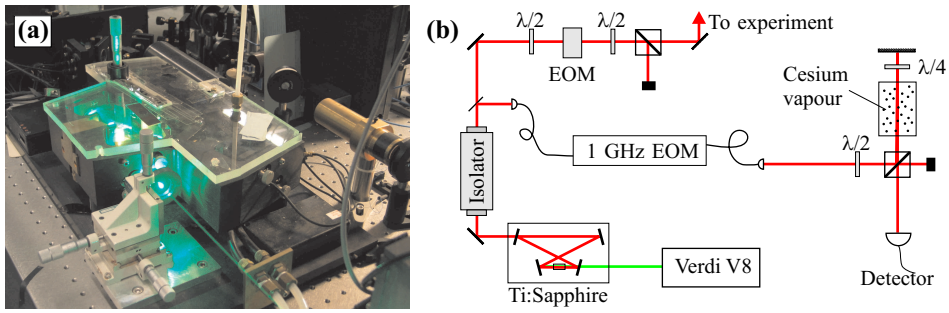

Figure 4.3: The probe laser. **(a)** A picture of the Ti:sapphire laser, the green 532nm pump beam is clearly visible. **(b)** The schematic view of the laser system, a Coherent Verdi V8 laser delivers 8W of pump power to the Ti:sapphire laser which typically delivers 1W of light power at 852nm. Part of this light is sent through an EOM to create strong sidebands at a chosen frequency of up to more than 1GHz. The sideband is used for FM absorption spectroscopy similarly to the diode lasers in Fig. 4.2. The main Ti:sapphire beam is shaped into pulses by an EOM and a PBS.

frequency components around 325kHz are important. The probe laser is used for quantum measurement of transverse components $\hat{J}_y$ and $\hat{J}_z$ of the atomic spin and for measuring the macroscopic size J_x of the spin states.

The AOMs and the EOM creating laser pulses can be programmed to produce pulses with soft edges (not step functions). This is important, a too steep pulse would have frequency components at 325kHz creating problems for the experiment. We also examined the possibility to use an AOM for the probe laser but found that this caused too much excess noise in the laser beam. AOMs are turned on and off by adjusting the power of an electric RF signal (in our case 125MHz). It is a non-trivial task to turn on and off such a signal, this is typically done by electronic mixers. We found that for the mixers we used there was a huge amount of noise added in the regime between on and off, hence a quiet soft pulse was impossible to create. For the case of an EOM the control is done by a high voltage at DC. It is easy to exclude 325kHz signals from a DC-signal, or rather our high voltage supply is not even able to work at frequencies around 325kHz.

4.2 Atomic Vapour Cells

Our atomic samples are very conveniently placed inside a paraffin coated glass cell, see Fig. 4.4. The glass cell consists of a volume not far from being a cube with six small cylindrical extension, the internal distance between two windows is 30mm and the volume inside the cell is roughly $18 \pm 1\text{cm}^3$. Taking the glass cell to be box-shaped this corresponds to an effective transverse area $A_{\text{eff}} \approx 6.0\text{cm}^2$.

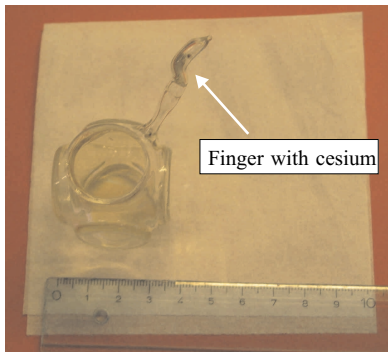

Figure 4.4: A picture of a paraffin coated vapour cell and a ruler showing the scale, the inside separation of two sides is 30mm. Note, that windows give the possibility to access the atoms with large laser beams from six directions. The finger contains solid droplets of cesium, the temperature of these decide the vapour pressure and hence density of atoms in the entire cell volume.

For the cell shown in the figure there are six windows which enable us to access the atoms by large laser beams from different directions. In addition, there is mounted a finger which contains droplets of solid cesium. The amount of cesium vapour in the cell volume is governed by the temperature of the solid cesium.

The cesium atoms are kept in the vicinity of room temperature which means that atoms are moving with velocity components of the order

$$\frac{1}{2}m_{\mathrm{Cs}}v^2_{\mathrm{rms,1dim}} = \frac{1}{2}k_{\mathrm{B}}T \quad \rightarrow \quad v^2_{\mathrm{rms,1dim}} \approx 137\mathrm{m/s}, \tag{4.1}$$

where k_{B} is Boltzmann's constant and m_{Cs} is the cesium atomic mass. With a cell dimension of 30 mm it takes of the order of 200μs between each time an atom collides with the cell wall. We discuss later (see Sec. 4.4) that the atomic spin life time is much longer than these time scales, the reason that atoms do not depolarize at the wall collision is the fact that a thin layer of paraffin has been placed on the inside of the glass walls. Our glass cells have all been produced by Michael Balabas, S. I. Vavilov State Optical Institute, St. Petersburg, Russia, for further information about the physics of paraffin coated cells we refer to [50, 51, 52].

Atoms moving at room temperature also cause Doppler broadening of the optical line by an amount (see e.g. [53])

$$\delta\nu_{\mathrm{D,HWHM}} = \frac{\nu_0}{c}\sqrt{\frac{2\ln 2k_{\mathrm{B}}T}{m_{\mathrm{Cs}}}} = 189\mathrm{MHz}, \tag{4.2}$$

where ν_0 is the optical frequency, c the speed of light, and we chose temperature $T = 300$K. In our experiments we are concerned with dispersive effects and not absorption. This also requires the probe laser beam to have a sufficiently far detuning $\Delta \gg 189$MHz.

The fact that atoms move around gives some advantages. First of all, the probe laser beam cannot fill the whole cell volume but the motion of atoms ensures that all atoms will pass the beam at some stage during each measurement. There will also be some averaging effects of atomic motion, some atoms will be closer to optical resonance than others, but at a later stage these atoms may be further from resonance. For sufficiently long measurement times all atoms will experience the same interaction conditions with the laser beam. And finally, possible inhomogeneities of magnetic fields cause different Larmor frequencies for different atoms, but some averaging reduces this effect (this is discussed more in Sec. 4.4).

4.3 The Rotating Frame and Magnetic Fields

All our experiments are carried out with atoms being placed in a constant homogeneous magnetic field $\mathbf{B}$ along a direction which we define as the x-axis in this thesis. This will split the magnetic sub-levels and cause spin precession around the direction of the magnetic field. In App. F we give a detailed discussion of the splitting of magnetic sub-levels, here we just state that we choose a magnetic field of magnitude ≈ 0.9Gauss which corresponds to precession frequency (Larmor frequency) of $\Omega = 325$kHz. There are several advantages and dis-advantages of this magnetic field.

Let us examine the implications of the static magnetic field on the equations of motion introduced in Sec. 2.3 and stated quantitatively in Eqs. (6.11-6.14). The magnetic field contribution to the Hamiltonian is $\hat{H} = \hbar\Omega\hat{J}_x$ where Ω is the Larmor frequency. This changes Eqs. (6.13) and (6.14) into $\partial\hat{J}_y(t)/\partial t = -\Omega\hat{J}_z(t) + aJ_x\hat{S}_z^{\text{in}}$ and $\partial\hat{J}_z(t)/\partial t = \Omega\hat{J}_y(t)$, while Eqs. (6.11) and (6.12) are unaffected. If we introduce rotating frame coordinates (marked with a prime)

$$\begin{aligned}\hat{J}'_y(t) &= +\hat{J}_y(t)\cos(\Omega t) + \hat{J}_z(t)\sin(\Omega t),\\ \hat{J}'_z(t) &= -\hat{J}_y(t)\sin(\Omega t) + \hat{J}_z(t)\cos(\Omega t),\end{aligned} \tag{4.3}$$

a little algebra shows that the equations of motion are turned into

$$\hat{S}_y^{\text{out}}(t) = \hat{S}_y^{\text{in}}(t) + aS_x\left(\hat{J}'_y(t)\sin(\Omega t) + \hat{J}'_z(t)\cos(\Omega t)\right), \tag{4.4}$$

$$\hat{S}_z^{\text{out}}(t) = \hat{S}_z^{\text{in}}(t), \tag{4.5}$$

$$\frac{\partial}{\partial t}\hat{J}'_y(t) = aJ_x\hat{S}_z^{\text{in}}(t)\cos(\Omega t), \tag{4.6}$$

$$\frac{\partial}{\partial t}\hat{J}'_z(t) = aJ_x\hat{S}_z^{\text{in}}(t)\sin(\Omega t). \tag{4.7}$$

Our first observation is the fact that the dynamics of the rotating spin component are encoded around the $\Omega = 325$kHz sideband of $\hat{S}_y^{\text{out}}$. Lasers are in general much more quiet at higher sideband frequencies compared to the carrier and since we are interested in quantum fluctuations of light and atoms interacting with each

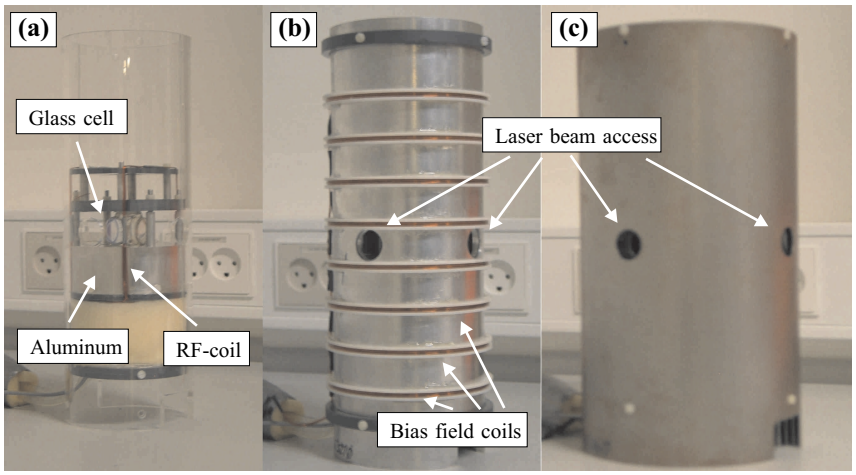

Figure 4.5: Pictures of the cell mounts and the magnetic field coils. **(a)** The glass cell is here placed in an aluminum block which can be heated or cooled by water. Close to the cell we see a set of coils which are used for creating a horizontally polarized RF-magnetic field. **(b)** The next layer consists of eight coils with different number of windings to create a homogeneous bias magnetic field along the vertical direction. **(c)** At the outside we place two layers of μ-metal and one layer of iron to protect the atoms from external magnetic fields.

other we cannot have our signals dominated by much stronger technical noise sources.

Having rotating spins also enable us to measure two orthogonal components $\hat{J}'_y$ and $\hat{J}'_z$ with one laser pulse as long as the measurement time T is much longer than the Larmor period Ω^{-1}. This fact will be clarified in Sec. 9.4 when we discuss entanglement generation. But the presence of the magnetic field will at the same time *force* us to measure both transverse spin components with the simultaneous pile up of noise according to (4.6) and (4.7). This is a strong limitation in some cases, see e.g. the discussion in Sec. 11.3. For a single spin sample the QND nature of the measurement has disappeared.

The energy splitting caused by the magnetic field ensures that all magnetic sub-levels are non-degenerate. This is important since the energy barrier prevents atoms from doing spin flips at a collision. This will be discussed further in Sec. 4.4 but we can now refer to Fig. 4.6 showing the spin life time T_1 versus the magnitude of the constant magnetic field $\mathbf{B}$.

The magnetic field homogeneity must be of sufficiently good quality. If this is not the case, different atoms following different paths in space will accumulate different phases and the joint spin state of atoms will decohere. This will be discussed in detail below in Sec. 4.4. The experimental setup for creating a high quality magnetic field with good stability is shown in Fig. 4.5. In part (a)

we see the glass cell mounted inside a plastic cylinder in a block of aluminum. The aluminum can be heated or cooled by water and hence controls the glass cell temperature[1]. A set of coils placed close to the cell enable us to create a horizontally polarized RF-magnetic field. The role of this is to modulate the spin state, see the discussion in Chap. 7. In Fig. 4.5(b) we see the coils creating the constant high quality magnetic field. Eight coils with equal spacing have different number of windings optimized for high homogeneity. Three independent current sources connected to these coils allow further optimization of the homogeneity. The current source driving these coils has a relative stability better than 10^{-5}. In Fig. 4.5(c) we show the outermost magnetic shielding consisting of two layers of μ-metal and one iron layer. The top and bottom are also shielded and we exclude laboratory fields from affecting the atoms. All together we create a magnetic field of sufficient quality, in next section we discuss quantitatively the requirements for the magnetic field.

4.4 Spin Life Times

The life time of our macroscopic spin states with a large spin component J_x along the x-axis and transverse spin components $\hat{J}_y$ and $\hat{J}_z$ is well described by two characteristic times T_1 and T_2 (which are well known concepts from the literature). T_1 is the decay time of the longitudinal spin J_x following the model $J_x(t) = J_x(0)e^{-t/T_1}$ and T_2 is the same for transverse components. We usually have $T_1 \approx$ 200-300ms which is much longer than $T_2 \leq$ 30ms. The decay mechanisms of J_x must overcome an energy barrier set by the splitting caused by the magnetic field. The transverse decay will also be affected by phase fluctuations and hence T_2 can be much faster than T_1. We often characterize the transverse life time by a line width or decoherence rate $\Gamma[\text{Hz}] = (\pi T_2[\text{s}])^{-1}$ and in this chapter we often discuss the rate Γ_{com} which is a decoherence rate common to all magnetic sub-levels. This rate is discussed more carefully in Chap. 7 where we also discuss in detail the methods for measuring both T_1 and T_2. In the following we discuss several experimental parameters that affect T_1 and T_2.

As mentioned above the static magnetic field $\mathbf{B}$ giving rise to the Larmor precession must be of a sufficient quality. In Fig. 4.6(a) we show the T_1 life time measured as a function of the magnitude of $\mathbf{B}$. We see that there is a threshold of the magnetic field strength of about 0.03Gauss above which we may obtain long spin life times T_1. Our working point is far above this point and we have usually T_1 values of some hundreds of milliseconds.

In Fig. 4.6(b) we see the transverse decoherence rate Γ as a function of an applied magnetic field gradient. We see that the rate increases quadratically with the gradient, we can understand this with help from a simple model discussed in [54]. First, divide the atomic sample into two parts, 1 and 2, along the

[1] At the time of writing we are working on replacing the aluminum by non-metallic components. Random currents in the aluminum have proved to create magnetic noise disturbing the experiments, see Sec. 10.3.

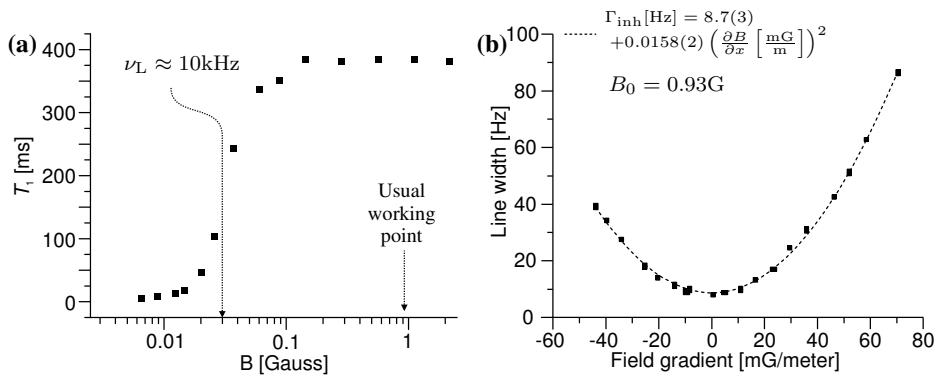

Figure 4.6: **(a)** T_1 versus magnetic field strength. We see that a too low field (below $\approx$ 0.03Gauss) prevents long spin life time. Our usual working point is around $B = 0.93$Gauss for which the spin life time yields some hundred milliseconds, here 380ms. **(b)** The magnetic field also needs a sufficient homogeneity to prevent dephasing of the spins. We plot the decoherence rate given by the line width Γ_{com} versus an applied magnetic field gradient and observe the increase of decoherence rate with increasing gradient. The measurement methods are explained in detail in Chap. 7.

bias magnetic field direction. If the sample length is L and the bias field $\mathbf{B}$ has strength B_0, the field strength in the two parts will be of order $B_0 \pm \partial B_x/\partial x \cdot L$ and the difference in Larmor frequency will be $(g_F\mu_B/\hbar)\partial B_x/\partial x \cdot L$ according to (F.4). We follow an atom during the time T it takes for it to decohere. If v is a typical speed of the atomic motion, the number of visits n_1 in part 1 or n_2 in part 2 will be of order Tv/L, since each visit has duration L/v. The difference $n_1 - n_2$ has mean zero and standard deviation of the order $\text{std}(n_1 - n_2) = \sqrt{Tv/L}$. Thus the uncertainty $\delta\phi$ in the accumulated phase during Larmor precession is

$$\delta\phi \approx \frac{g_F\mu_B}{\hbar}\frac{\partial B_x}{\partial x} L \cdot \frac{L}{v} \cdot \text{std}(n_1 - n_2) \approx 1$$
$$\Rightarrow \quad \Gamma_{\text{inh}} \approx \frac{1}{T} \approx \left(\frac{g_F\mu_B}{\hbar}\right)^2 \frac{L^3}{v}\left(\frac{\partial B_x}{\partial x}\right)^2. \tag{4.8}$$

In the first line we set $\delta\phi$ equal to unity since this is the situation after the time of decoherence T. We see that the broadening Γ_{inh} by inhomogeneities scales quadratically with the field gradient. If we take $g_F \approx 1/4$ (see eq. (F.5)), $L = 0.030$m, $v = \sqrt{k_B T/m_{\text{Cs}}} = 137$m/s at $T = 300$K, we get $g_F\mu_B/\hbar = 350$Hz/mG and expect the broadening to be $\Gamma_{\text{inh}} = 0.024\text{Hz} \cdot \text{m}^2/\text{mG}^2 \cdot (\partial B_x/\partial x)^2$.

The experimental investigation can be seen in Fig. 4.6(b) and we definitely confirm the scaling law predicted above. The numbers match within a factor of two which puts some confidence to our simple model but this is probably also partly luck since we were very crude in the model with respect to factors of 2 and π.

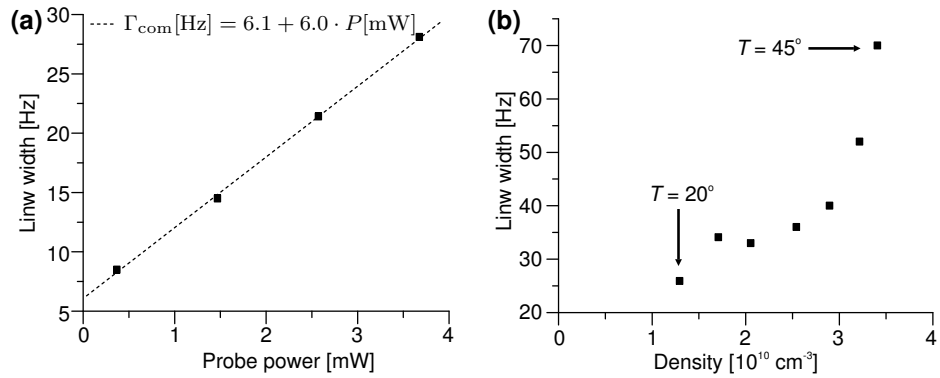

Figure 4.7: **(a)** The role of probe power broadening on spin decoherence rate $\Gamma_{\rm com}$. We observe the expected linear dependence from Eq. (4.9), the numbers are commented on in the text. Note, that we may also deduce the decoherence rate in the dark by this method, here we get $\Gamma_{\rm dark} = 6.1$Hz which corresponds to a spin coherence time $T_2 = 52$ms. **(b)** The spin decoherence rate versus atomic density. These data give a typical picture, the decoherence rate increases in a non-linear manner with increasing density. The density is controlled by raising the temperature of the vapour cell and measured by polarization rotation, see Eq. (6.9).

In Chap. 7 we will learn that having $\Gamma_{\rm inh} < \nu_{\rm QZ}$ is important, where $\nu_{\rm QZ}$ is the quadratic Zeeman splitting of some resonance spectra we utilize for spin state characterization (see the example in Fig. 7.2(b)). Comparing our experimental result with the splitting due to the quadratic Zeeman effect (F.7) we find for our particular setup that in order to have $\Gamma_{\rm inh} < \nu_{\rm QZ}$ we must have $1/B \cdot \partial B/\partial x \cdot L < 1.2 \cdot 10^{-3}$.

Another process leading to spin decoherence is the scattering of photons from the probe laser when atoms undergo real transitions. Even though the probe laser is detuned by ≈ 1GHz and the populations of excited state levels are very small they are not zero. The scattering rate $\Gamma_{\rm ph}$ can be estimated by the two-level atom result (see e.g. [55])

$$\Gamma_{\rm ph} = \frac{\gamma}{2}\frac{s}{1+s} \approx \frac{3I\lambda^3\gamma^2}{16\pi^2\hbar c\Delta^2}, \tag{4.9}$$

where $s = \frac{I/I_{\rm sat}}{1+(2\Delta/\gamma)^2}$ is the saturation parameter. I is the beam intensity with $I_{\rm sat} = 2\pi^2\hbar c\gamma/3\lambda^3$ being the saturation intensity. λ is the optical wave length, γ is the natural line width of the optical transition, and Δ is the detuning (assumed much greater than γ in the last step of the equation). If we insert typical experimental conditions $I = 1\text{mW/cm}^2$, $\Delta = 875$MHz, $\lambda = 852$nm, and $\gamma = 5.21$MHz we get $\Gamma_{\rm ph} = 132$Hz. This can be compared to experimental results shown in Fig. 4.7(a). First, however, we need to observe that the scattering rate de-

pends only weakly on beam size for a fixed power. This effect is caused by the atomic motion in and out of the beam. Even though the probe intensity can be strong, the atoms will only spend little time inside the beam if the size is small. The vapour cell geometry suggests an effective cross sectional area of the cell of $A_{\text{eff}} \approx 6\text{cm}^2$. Then the experimental observation $\Gamma_{\text{com}}[\text{Hz}] = 6.1 + 6.0 \cdot P[\text{mW}]$ corresponds to $\Gamma_{\text{ph}}[\text{Hz}] \approx 36 \cdot I[\text{mW/cm}^2]$. The experimental spin decoherence rate is here a factor of almost 4 smaller than the simple two-level atom estimate. We will not here try to do more correct quantitative estimates but just mention that the order of magnitude is correct.

The last decoherence mechanism we will comment on is the dependence on atomic density, see Fig. 4.7(b). These data are typical, the decoherence rate increases in a non-linear fashion with the atomic density. If the decoherence is caused by inter-atomic collisions we would expect the rate to increase quadratically with density, there is probably a quadratic contribution in the figure. But the situation is more complicated than this. The change in temperature may affect the properties of the paraffin, we have experimentally observed many strange kinds of dynamics without understanding them very well. Also, the temperatures are close to the cesium melting point at 28.4°C degrees which may also give rise to complicated effects. We do not wish to understand all these processes in detail as long as we can measure them. The main point is that at our working values of atomic density (up to 10^{11}cm^2) we have a reasonable decoherence rate but we cannot go much further up without sacrificing the coherence time.

4.5 Optical Pumping

A very crucial part of our experiments is optical pumping. In Sec. 2.1 we already mentioned the fact that we are interested in atoms in the hyperfine state $F = 4$ only and we commented on the importance of atoms being in the extreme $m_F = 4$ state (or close to this state) during the experiments. This is the so-called coherent spin state and we will see in Chap. 9 that the ability to create this state is crucial for entanglement generation.

We will not here comment in detail about the theory of optical pumping, it is a whole scientific field in itself and a review is given in [56]. The basic idea behind optical pumping is simple though and can bee seen in Fig. 4.8. The repump laser and optical pump laser which were described in Sec. 4.1 are applied to the atoms with circular polarization. After some time the extreme $F = 4, m_F = 4$ state is reached by many atoms. Depending on the strength of the repump laser a fraction of atoms will be in some of the $F = 3$ states and hence not contributing to the collective spin state measured by the probe laser. The ability to adjust the magnitude J_x of the spin state will prove to be important in Chaps. 8, 9, and 10.

A very important property of the atomic spins in the $F = 4$ states is the

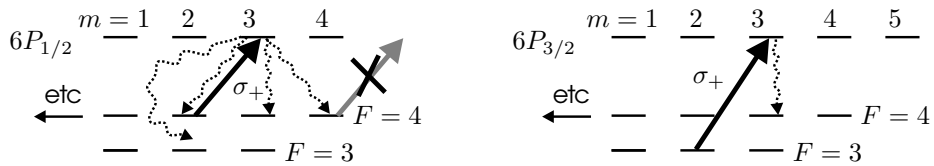

Figure 4.8: The principle of optical pumping, we wish to put all atoms into the $F = 4, m_F = 4$ magnetic sub-state. To this end we apply two σ_+-polarized lasers, the optical pump laser shown on the left part and the repump laser shown on the right part of the figure. The figure on the left shows an example where an atom is in the state $F = 4, m_F = 2$. The optical pump lifts this atom into the excited $F = 4, m_F = 3$ state from where it may decay into the ground states $F = 3$ or $F = 4$ with $m_F = 2, 3, 4$. The m_F value will never decrease in this process and will on average increase. If $m_F = 4$ is reached the atom is in a dark state and will not move further. The occasional decay to the $F = 3$ states is counteracted by the repump laser shown on the right. The number of atoms in the relevant $F = 4$ states can be adjusted by the power of the repump laser.

orientation defined by

$$p = \frac{1}{F} \sum_{-F}^{F} m \cdot \langle \hat{\sigma}_{m,m} \rangle \,, \tag{4.10}$$

where $F = 4$ in our case and $\hat{\sigma}_{m,m}$ is the density operator describing the population of atoms in the magnetic sub-states $|F = 4, m_F = m\rangle$. If all atoms are in $m = 4$ the orientation is equal to unity. For a completely unpolarized sample we have $p = 0$.

An experimental example of obtained orientations is shown in Fig. 4.9 where the orientation of a sample of cesium is studied while the power of the σ_+-polarized optical pumping laser is increased. The pump light is on resonance and contributes to the decoherence of the spin state with a rate Γ_{pump} (this will be carefully defined in Sec. 7.2). This rate is plotted on the abscissa in the figure and is a direct measure of how many optical pump photons each atom scatters on average per second. We see that a few photons per second are sufficient for obtaining a high degree of orientation, in this example 97%. This should be compared to a typical decay time T_1 of some hundreds of milliseconds, see Sec. 4.4. The repump laser is on at all times here and with its σ_+-polarization it helps creating an oriented sample. The repump laser alone can here be seen to generate a 82% oriented sample. The methods for measuring orientation is described in detail in Chap. 7.

We have obtained polarizations of up to more than 98% for higher densities. The optical pumping laser at the 894nm $D1$-line is essential to this achievement. We have tried to optically pump on the $D2$-line with somewhat lower orientation as a result (a little above $p = 0.9$). A possible explanation is that the re-scattered light on the $F = 4$, $m_F = 4 \rightarrow F = 5$, $m_F = 5$ transition from one atom

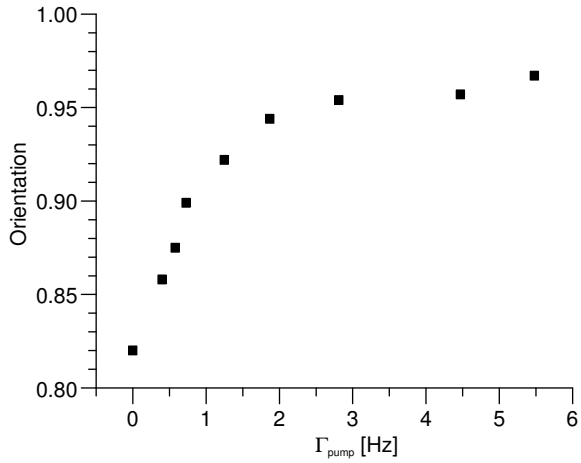

Figure 4.9: An example of orientation p measured for increasing power of the optical pump laser. On the abscissa we plot the power broadening Γ_{pump} caused by the optical pump laser which in turn is a measure of the strength of the pumping process. For zero optical pump power the orientation of 82% is created solely by the σ_+-polarized repump laser. Note, that a high degree of orientation (here $\approx 97\%$) is reached with a moderate amount of pumping. The atomic density is of the order 10^{10}cm^{-3}.

affects the state of other atoms. Indeed, according to [57], even with a dark state when using 894nm pumping light one would expect problems with densities higher than a critical density $\rho_{\text{C}} = (\sigma R)^{-1}$ because radiation will be trapped inside the sample. Here σ is the cross section for light absorption and R is the extent of the gas sample. Our atomic sample is Doppler broadened with the width $\delta\nu_{\text{D}} = 378\text{MHz}$. With a natural line width of the 894nm $D1$-transition of $\gamma = 4.6\text{MHz}$ and a sample extent of $R = 3\text{cm}$ we estimate the critical density ρ_{C} to be roughly $\rho_{\text{C}} \approx [\lambda^2/2\pi \cdot \gamma/\delta\nu_{\text{D}} \cdot R]^{-1} = 2 \cdot 10^{11}\text{cm}^{-3}$. This is only a little more than our typical values. However, the experiments tell us that the limitations are still small.

Optical pumping into the coherent spin state with all atoms in the state $|F = 4, m_F = 4\rangle$ can also be seen from another perspective. This state fulfils $\left\langle \hat{J}_y \right\rangle = \left\langle \hat{J}_z \right\rangle = 0$ and any deviation from this state is counteracted by optical pumping. In Chap. 8 we model the optical pumping by equations $\partial \hat{J}_y(t)/\partial t = -\Gamma \hat{J}_y(t) + \hat{\mathcal{F}}_y(t)$ and $\partial \hat{J}_z(t)/\partial t = -\Gamma \hat{J}_z(t) + \hat{\mathcal{F}}_z(t)$ where Γ describes the rate of optical pumping and the operators $\hat{\mathcal{F}}_{y,z}$ are Langevin forces ensuring correct quantum statistics. Optical pumping is in this sense a clean up of whatever state has been created by other processes. If e.g. two spin samples are in an entangled state the optical pumping will drive the spin state back to being two independent coherent spin states.

CHAPTER 5

The Effective Interaction Hamiltonian

In this section we will consider the real cesium atom with its hyperfine split ground and excited states. We couple these atoms off-resonantly to the $6S_{1/2} \rightarrow 6P_{3/2}$ dipole transition and we aim at the derivation of an effective Hamiltonian to describe the physics of this interaction at the quantum level. We neglect absorption effects and spontaneous emission which is justified if the detuning from the optical transition is large enough. We are left with dispersive effects which essentially arise from the shift of atomic energy levels in presence of light fields. This is known as the Stark effect. As we already briefly mentioned in Sec. 2.3, the interaction enables us to measure the spin state of atoms, and properties of the polarization state of light will at the same time be fed into the spin state of atoms.

This kind of interaction has been studied for some time now, for a historical review see [56] and references therein. The idea of using the interaction for QND measurements was given in [58, 59] and the calculations in the present chapter is closely related to these references. We will concentrate more on the continuous description of light and matter since this is convenient for describing the time dynamics that we actually measure. We also put attention to the fact that cesium is not a spin-1/2 system. This gives rise to higher order terms of the interaction. We end up with an effective Hamiltonian (5.18) which is a very convenient starting point for further calculations. The derivation is rather technical, we put many details in Apps. A-D.

5.1 Electric Dipole Interactions

We assume that the light interacting with the atoms has a cross sectional area $A \gg \lambda^2$ where λ is the wave length of the light. Then a one dimensional theory is sufficient and we only need to care about two polarization modes. With the propagation direction (z-axis) as quantization axis the electric field description (C.9) will be generalized to

$$E = \sqrt{\frac{\hbar\omega_0}{2\epsilon_0 A}} \left(\hat{a}_+(z,t)\mathbf{e}_{+1} + \hat{a}_+^\dagger(z,t)\mathbf{e}_{+1}^* + \hat{a}_-(z,t)\mathbf{e}_{-1} + \hat{a}_-^\dagger(z,t)\mathbf{e}_{-1}^* \right), \quad (5.1)$$

where the unit vectors $\mathbf{e}_{\pm 1}$ and field operators $\hat{a}_\pm(z,t)$ and $\hat{a}_\pm^\dagger(z,t)$ are discussed in Eqs.(A.6) and (A.7). The dipole operator $\mathbf{d} = -e\mathbf{r}$ of a single atom can conveniently be expressed in tensor components. We write the vector $\mathbf{r}$ as

$$\mathbf{r} = \mathbf{e}_{+1}^* r_{+1} + \mathbf{e}_0^* r_0 + \mathbf{e}_{-1}^* r_{-1}, \quad (5.2)$$

where the tensor components of $\mathbf{r}$ are given by

$$r_{+1} = -\frac{x+iy}{\sqrt{2}}, \quad r_0 = z, \quad r_{-1} = \frac{x-iy}{\sqrt{2}}. \quad (5.3)$$

With this definition the dipole operator can be expressed

$$\mathbf{d} = \sum_{F,m;F',m'} \left(d^-_{F,m;F',m'}\mathbf{e}_{+1}^* + d^0_{F,m;F',m'}\mathbf{e}_0^* + d^+_{F,m;F',m'}\mathbf{e}_{-1}^* \right) \hat{\sigma}_{F,m;F',m'} + \text{h.c.}, \quad (5.4)$$

where we let F and m sum over ground state levels while the primed letters F' and m' sum over excited states. The dipole moments are defined as

$$\begin{aligned} d^-_{F,m;F',m'} &= -e \langle F,m| r_{+1} |F',m'\rangle, \\ d^0_{F,m;F',m'} &= -e \langle F,m| r_0 |F',m'\rangle, \\ d^+_{F,m;F',m'} &= -e \langle F,m| r_{-1} |F',m'\rangle. \end{aligned} \quad (5.5)$$

The interaction Hamiltonian $\hat{H}_{\text{int}} = -\sum \mathbf{d}_j \cdot \mathbf{E}(\mathbf{R}_j)$ will contain the above dipole moments and the factor $\sqrt{\hbar\omega_0/2\epsilon_0 A}$. We absorb these into a single coupling constant $g^\pm_{F,m;F',m'} = \sqrt{\omega_0/2\hbar\epsilon_0 A} d^\pm_{F,m;F',m'}$ and the generalization of the Hamiltonian (C.15) will turn into (in the rotating wave approximation)

$$\begin{aligned} \hat{H}_{\text{int}} = \hbar \sum_{F,m;F',m'} \int_0^L \Big(&[g^+_{F,m;F',m'}\hat{a}_+(z,t) \\ &+ g^-_{F,m;F',m'}\hat{a}_-(z,t)]\hat{\sigma}_{F',m';F,m}(z,t) + \text{h.c.} \Big) \rho A dz. \end{aligned} \quad (5.6)$$

Here, the first term contains the annihilation operator $\hat{a}_+(z,t)$ for a photon at position z with polarization σ_+. This operator is accompanied by the density operator $\hat{\sigma}_{F',m';F,m}(z,t)$ which will take an atom from the ground state $|F,m\rangle$ into the

excited state $|F', m'\rangle$ thereby absorbing the photon at position z. The strength of this particular transition is governed by the coupling constant $g^{+}_{F,m;F',m'}$ which is non-zero only if $m' = m+1$, while $g^{-}_{F,m;F',m'}$ is non-zero for $m' = m-1$. These selection rules and the actual values of the coupling constants will be calculated carefully in App. D. The values will turn out to be real, and we have omitted the complex conjugation of these in (5.6).

We also need to state the atomic Hamiltonian to have all fundamental equations at hand. For the moment we assume that the energy levels of the ground states are degenerate (there is e.g. no static magnetic field present) and we specialize to one of the hyperfine ground states, i.e. $F = 4$. A possible non-degeneracy can be accounted for later. We get for the atomic Hamiltonian

$$\hat{H}_{\text{atom}} = \sum_{F'=3}^{5} \sum_{m'} \int_0^L \hbar(\omega_0 + \Delta_{F'}) \hat{\sigma}_{F',m';F',m'}(z,t) \rho A dz. \tag{5.7}$$

Here ω_0 is the laser frequency which is detuned $\Delta_{F'}$ from the upper state with total angular momentum F'. The density operator $\hat{\sigma}_{F',m';F',m'}(z,t)$ measures the probability for an atom at position z of being in the excited state $|F', m'\rangle$ and $\hbar(\omega_0 + \Delta_{F'})$ assigns the appropriate energy in this case.

5.2 The Off-resonant Limit

We will now change the interaction Hamiltonian (5.6) into an effective Hamiltonian which depends on the light amplitudes and the ground state spin operators. We can do this if we assume the optical laser field to be sufficiently far detuned from atomic resonance. In this case the population of the excited states is negligible and the coherences $\hat{\sigma}_{F,m;F',m'}$ between the ground states $|F, m\rangle$ and the excited states $|F', m'\rangle$ will follow the ground state and the light field adiabatically. We carefully work out the adiabatic elimination and solve for the coherence $\hat{\sigma}_{F,m-1;F',m}(z,t)$ in the following.

The time evolution of $\hat{\sigma}_{F,m-1;F',m}(z,t)$ is governed by the Heisenberg equation

$$\begin{aligned} \frac{\partial \hat{\sigma}_{F,m-1;F',m}(z,t)}{\partial t} &= \frac{1}{i\hbar} \left[\hat{\sigma}_{F,m-1;F',m}(z,t), \hat{H} \right] \\ &= -i(\omega_0 + \Delta_{F'}) \hat{\sigma}_{F,m-1;F',m}(z,t) \\ &\quad - i g^{+}_{F,m-1;F',m} \hat{a}_+(z,t) \hat{\sigma}_{F,m-1;F,m-1}(z,t) \\ &\quad - i g^{-}_{F,m+1;F',m} \hat{a}_-(z,t) \hat{\sigma}_{F,m-1;F,m+1}(z,t), \end{aligned} \tag{5.8}$$

where the commutation relation (C.17) has been used on the Hamiltonian (5.6) and two terms proportional to $\hat{\sigma}_{F',m;F',m}(z,t)$ and $\hat{\sigma}_{F',m-2;F',m}(z,t)$ have been neglected (no population in the excited states). The next step is to acknowledge that the light amplitudes $\hat{a}_+(z,t)$, $\hat{a}_-(z,t)$ and the coherence $\hat{\sigma}_{F,m-1;F',m}(z,t)$ are oscillating fast with frequencies ω_0 and $\omega_0 + \Delta_{F'}$ respectively. We go into the

rotating frame of the light field by introducing slowly varying operators

$$\hat{\sigma}_{F,m-1;F',m}(z,t) = \tilde{\sigma}_{F,m-1;F',m}(z,t)e^{-i\omega_0 t} \quad \text{and} \quad \hat{a}_{\pm}(z,t) = \tilde{a}_{\pm}(z,t)e^{-i\omega_0 t}, \tag{5.9}$$

i.e. a tilde marks the operator to be slow. Now the slow version of (5.8) becomes

$$\begin{aligned} \frac{\partial \tilde{\sigma}_{F,m-1;F',m}(z,t)}{\partial t} &= -i\Delta_{F'}\tilde{\sigma}_{F,m-1;F',m}(z,t) \\ &\quad - ig^{+}_{F,m-1;F',m}\tilde{a}_{+}(z,t)\hat{\sigma}_{F,m-1;F,m-1}(z,t) \\ &\quad - ig^{-}_{F,m+1;F',m}\tilde{a}_{-}(z,t)\hat{\sigma}_{F,m-1;F,m+1}(z,t). \end{aligned} \tag{5.10}$$

On the right hand side we now have a fast term oscillating at $\Delta_{F'} >> T^{-1}$ where T is a typical time scale for the variation of the last two terms. Then it is justified to put the time derivative equal to zero[1] and we get

$$\begin{aligned} \tilde{\sigma}_{F,m-1;F',m}(z,t) &= \frac{-1}{\Delta_{F'}}\Big[g^{+}_{F,m-1;F',m}\tilde{a}_{+}(z,t)\hat{\sigma}_{F,m-1;F,m-1}(z,t) \\ &\quad + g^{-}_{F,m+1;F',m}\tilde{a}_{-}(z,t)\hat{\sigma}_{F,m-1;F,m+1}(z,t)\Big], \\ \tilde{\sigma}_{F,m+1;F',m}(z,t) &= \frac{-1}{\Delta_{F'}}\Big[g^{-}_{F,m+1;F',m}\tilde{a}_{-}(z,t)\hat{\sigma}_{F,m+1;F,m+1}(z,t) \\ &\quad + g^{+}_{F,m-1;F',m}\tilde{a}_{+}(z,t)\hat{\sigma}_{F,m+1;F,m-1}(z,t)\Big], \end{aligned} \tag{5.11}$$

where we have also stated the result for the coherence $\tilde{\sigma}_{F,m+1;F',m}(z,t)$. The physical interpretation of the above equation is quite simple. In the first line we seek the coherence $\tilde{\sigma}_{F,m-1;F',m}$, i.e. we want to know to which extent our atomic state is in a superposition between the ground state $|F, m-1\rangle$ and the excited state $|F', m\rangle$. Such a superposition can be created in two ways.

In the first term on the right hand side, the population in the ground state $|F, m-1\rangle$ parametrized by the density operator $\hat{\sigma}_{F,m-1;F,m-1}$ is driven coherently toward the excited state $|F', m\rangle$ by the field $\hat{a}_{+}$ with strength $g^{+}_{F,m-1;F',m}$.

The second term describes another possibility, the atomic state could already be in a superposition between the ground states $|F, m-1\rangle$ and $|F, m+1\rangle$. This is parametrized by the density operator $\hat{\sigma}_{F,m-1;F,m+1}$. The fraction of the atomic wave function in the state $|F, m+1\rangle$ can then be driven into the excited state $|F', m\rangle$ by the field $\tilde{a}_{-}$ with strength $g^{-}_{F,m+1;F',m}$.

The solutions (5.11) can now be substituted into the interaction Hamilto-

[1] This is the adiabatic elimination, it can be shown to be equivalent to neglecting terms of magnitude $\Delta_{F'}T$ times smaller than the retained terms.

nian (5.6) to obtain an effective Hamiltonian;

$$\begin{aligned}\hat{H}^{\text{eff}}_{\text{int}} = \sum_m \int_0^L \Big\{ \Big[& c_+(\Delta,m)\hat{a}^\dagger_+(z,t)\hat{a}_+(z,t) \\ & + c_-(\Delta,m)\hat{a}^\dagger_-(z,t)\hat{a}_-(z,t)\Big]\,\hat{\sigma}_{F,m:F,m}(z,t) \\ & + b(\Delta,m)\Big[\hat{a}^\dagger_-(z,t)\hat{a}_+(z,t)\hat{\sigma}_{F,m+1;F,m-1}(z,t) \\ & + \hat{a}^\dagger_+(z,t)\hat{a}_-(z,t)\hat{\sigma}_{F,m-1;F,m+1}(z,t)\Big]\Big\}\,\rho A dz.\end{aligned} \tag{5.12}$$

This Hamiltonian only works on time scales long compared to $\Delta^{-1}_{F'}$ since this is the approximation in the adiabatic elimination. We have introduced a number of coefficients for brevity. The terms containing $c_\pm(\Delta,m)$ describe the Stark shift of the ground state $|F,m\rangle$ caused by the coupling to the excited state $|F',m\pm 1\rangle$. The coefficient is given by

$$c_\pm(\Delta,m) = -2\hbar \sum_{F'} \frac{(g^\pm_{F,m;F',m\pm1})^2}{\Delta_{F'}}. \tag{5.13}$$

The terms containing $b(\Delta,m)$ describe the possibility to change ground state from $|F,m-1\rangle$ to $|F,m+1\rangle$ through the excited state $|F',m\rangle$ by absorption of a σ_+ photon and emission of a σ_- photon (or vice versa). The coefficient is

$$b(\Delta,m) = -2\hbar \sum_{F'} \frac{(g^+_{F,m-1;F',m})\cdot(g^-_{F,m+1;F',m})}{\Delta_{F'}}. \tag{5.14}$$

The coefficients $(g^\pm_{F,m;F',m\pm1})^2$ and $(g^+_{F,m-1;F',m})\cdot(g^-_{F,m+1;F',m})$ are calculated in App. D, see Eqs. (D.12-D.14). Note, the denominator $\Delta_{F'}$ in the above two equations exclude us from applying the sum rules (D.15-D.17) and the entire description becomes a little more complicated. We notice however that we can group terms containing 1, m, m^2 from (D.12) and the square root from (D.14) such that (still for the special case of $F=4$)

$$\begin{aligned} c_\pm(m,\Delta) &= -\frac{\hbar c\gamma}{4A\Delta}\frac{\lambda^2}{2\pi}(a_0 \pm \frac{1}{2}a_1 m + a_2 m^2), \\ b(m,\Delta) &= -\frac{\hbar c\gamma}{4A\Delta}\frac{\lambda^2}{2\pi}a_2\sqrt{(4+m)(5+m)(4-m)(5-m)}, \end{aligned} \tag{5.15}$$

where the coefficients a_0, a_1, and a_2 are given by

$$\begin{aligned} a_0 &= \frac{1}{4}\left(\frac{1}{1-\Delta_{35}/\Delta} + \frac{7}{1-\Delta_{45}/\Delta} + 8\right) \to 4, \qquad (F=4) \\ a_1 &= \frac{1}{120}\left(-\frac{35}{1-\Delta_{35}/\Delta} - \frac{21}{1-\Delta_{45}/\Delta} + 176\right) \to 1, \\ a_2 &= \frac{1}{240}\left(\frac{5}{1-\Delta_{35}/\Delta} - \frac{21}{1-\Delta_{45}/\Delta} + 16\right) \to 0, \end{aligned} \tag{5.16}$$

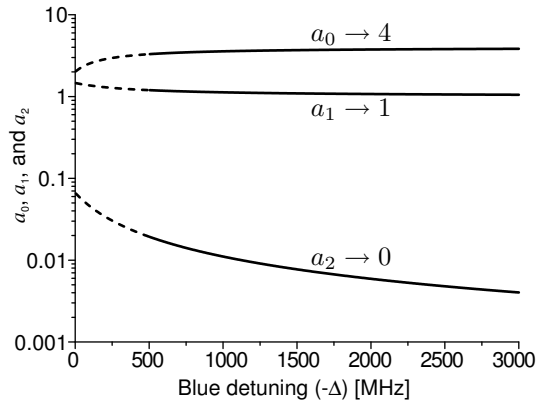

Figure 5.1: The parameters a_0, a_1, and a_2 defined in Eq. (5.16) for $F = 4$. These parametrize the strength of the 0th, 1st, and 2nd order terms in the Hamiltonian (5.18), respectively. On the vertical axis is the blue detuning ($-\Delta$), and the arrows indicate the limit for $-\Delta \to \infty$. We remind ourselves that the calculations are only valid for dispersive effects. Because of Doppler broadening we should be careful at low detunings.

where we have chosen to denote the detunings $\Delta_{F'}$ as $\Delta_{5'} = \Delta$, $\Delta_{4'} = \Delta - \Delta_{45}$, and $\Delta_{3'} = \Delta - \Delta_{35}$. Red detuning corresponds to positive values of Δ and the arrows indicate the limit $\Delta \to \pm\infty$. The values of a_0, a_1, and a_2 are depicted in Fig. 5.1. If we insert the expressions (5.15) into (5.12) we end up with

$$\begin{aligned}\hat{H}_{\text{int}}^{\text{eff}} = &-\frac{\hbar c\gamma}{4A\Delta}\frac{\lambda^2}{2\pi}\sum_m \int_0^L \Big(a_0 \left[\hat{a}_+^\dagger \hat{a}_+ + \hat{a}_-^\dagger \hat{a}_-\right] \hat{\sigma}_{m,m} \\ &+ \frac{a_1}{2}\left[\hat{a}_+^\dagger \hat{a}_+ - \hat{a}_-^\dagger \hat{a}_-\right] m\hat{\sigma}_{m,m} \\ &+ a_2 \left[\hat{a}_+^\dagger \hat{a}_+ + \hat{a}_-^\dagger \hat{a}_-\right] m^2 \hat{\sigma}_{m,m} \\ &+ a_2\sqrt{(4+m)(5+m)(4-m)(5-m)}\times \\ &\quad \left[\hat{a}_-^\dagger \hat{a}_+ \hat{\sigma}_{m+1,m-1} + \hat{a}_+^\dagger \hat{a}_- \hat{\sigma}_{m-1,m+1}\right]\Big)\, \rho A dz,\end{aligned} \tag{5.17}$$

where the (z, t) is left out for brevity. The density matrix operators and the light operators $\hat{a}_\pm$, $\hat{a}_\pm^\dagger$ are grouped in a nice way here, the light field operators can be written in terms of Stokes operators, see Eqs. (A.8-A.12), and the terms containing density operators can be expressed as spin operators with help from Eqs. (B.3) and (B.6-B.8). With these substitutions we may finally write the

effective Hamiltonian as

$$\begin{aligned}\hat{H}_{\text{int}}^{\text{eff}} = &- \frac{\hbar c\gamma}{4A\Delta}\frac{\lambda^2}{2\pi}\int_0^L \Big(a_0 \cdot \hat{\phi}(z,t) + a_1 \cdot \hat{S}_z(z,t)\hat{\jmath}_z(z,t) \\ &+ a_2\left[\hat{\phi}(z,t)\hat{\jmath}_z^2(z,t) - \hat{S}_-(z,t)\hat{\jmath}_+^2(z,t) - \hat{S}_+(z,t)\hat{\jmath}_-^2(z,t)\right]\Big)\rho A dz.\end{aligned} \tag{5.18}$$

Let us comment on the different terms. The first term containing a_0 will just give a Stark shift to all atoms independent on the internal state but proportional to the photon density $p\hat{h}i(z,t)$. The second term containing a_1 rotates the Stokes vector $\mathbf{S}$ and the spin vector $\mathbf{J}$ around the z-axis, known as Faraday rotation. The last terms proportional to a_2 are higher order couplings between the light and the atoms. All these terms conserve individually the z-projection of the total angular momentum of light and atoms, e.g. the $\hat{S}_-\hat{\jmath}_+^2$ term can change a σ_+ photon into a σ_- photon (changing the light angular momentum along z by $-2\hbar$ while the atoms receive $2\hbar$ mediated by the atomic raising operator j_+^2. The total angular momentum must have its z-projection invariant since the physical system is axially symmetric around the direction of light propagation (the z-axis). We remember that the parameters a_0, a_1, and a_2 depend on the detuning Δ and they are given in Eq. (5.16) for the case of $F = 4$. In general, the term proportional to a_1 is useful for us and the higher order terms proportional to a_2 create different problems. This will be discussed further in Chap. 6 where the calculations also will compare the magnitude of the a_1 and a_2 terms more quantitatively.

We could have performed all the steps in this section for $F = 3$ and ended up with the same result, only the a-parameters would be a little different, they are stated below for completeness.

$$\begin{aligned} a_0 &= \frac{1}{28}\left(\frac{25}{1+\Delta_{24}/\Delta} + \frac{63}{1+\Delta_{23}/\Delta} + 24\right) \to 4, \qquad (F=3) \\ a_1 &= \frac{1}{56}\left(-\frac{45}{1+\Delta_{24}/\Delta} + \frac{21}{1+\Delta_{23}/\Delta} + 80\right) \to 1, \\ a_2 &= \frac{1}{112}\left(\frac{5}{1+\Delta_{24}/\Delta} - \frac{21}{1+\Delta_{23}/\Delta} + 16\right) \to 0, \end{aligned} \tag{5.19}$$

where we just have chosen to denote the detunings $\Delta_{F'}$ as $\Delta_2 = \Delta$, $\Delta_3 = \Delta + \Delta_{23}$, and $\Delta_4 = \Delta + \Delta_{24}$. Note, red detuning still corresponds to positive Δ, and the limits for $\Delta \to \pm\infty$ are the same as in (5.16) for $F = 4$.

Concluding this chapter we remind ourselves of the approximations of the Hamiltonian (5.18). We assumed off-resonant interactions, i.e. there are no absorption effects in our description. This led us to the adiabatic elimination which is valid if optical beams are far from saturating the optical transition. We made no specific assumptions about the spin state of atoms or the polarization state of light, and therefore the Hamiltonian is in general a good starting point for many calculations involving what is essentially the Stark effect.

CHAPTER 6

Propagation Equations

In Chap. 5 we derived an effective Hamiltonian for the off-resonant interaction of polarized laser light with an atomic spin ensemble. In this chapter we will take these calculations one step further to derive actual equations of motion for our interesting spin state operators $\hat{J}_y$, $\hat{J}_z$ and Stokes operators $\hat{S}_y$, $\hat{S}_z$. We start out by deriving propagation equations in general and we will learn that these are in fact quite complicated. To couple collective spin operators to collective light operators we need to perform the approximation that the higher order terms proportional to a_2 of the Hamiltonian (5.18) can be neglected. Doing this we arrive at the most important equations of this chapter, Eqs. (6.11-6.15). We will then estimate the role of the higher order terms for our experimental purposes. Like the previous chapter, the derivations are somewhat technical. To understand the experiments of this thesis the results of Secs. 6.2 and 6.3 are important.

6.1 General Propagation Equations

We shall be concerned with the spin operators $\hat{\jmath}_x(z,t)$, $\hat{\jmath}_y(z,t)$, and $\hat{\jmath}_z(z,t)$ and the Stokes operators $\hat{S}_x(z,t)$, $\hat{S}_y(z,t)$, and $\hat{S}_z(z,t)$ where we continue the notation of Chap. 5. For the spin operators we state the Heisenberg equations (e.g. $\partial\hat{\jmath}_z(z,t)/\partial t = 1/i\hbar \cdot \left[\hat{\jmath}_z(z,t), \hat{H}\right]$) where we for a start take $\hat{H}$ to be the interaction Hamiltonian (5.18). Possible magnetic fields acting on the spin operators can be added later. With help from the commutation rules of App. B.3 and

Eq. (C.18) we get

$$\frac{\partial}{\partial t}\hat{\jmath}_x(z,t) = \frac{c\gamma}{4A\Delta}\frac{\lambda^2}{2\pi}\Big\{a_1\hat{S}_z\hat{\jmath}_y + a_2\Big(2\hat{S}_y[\hat{\jmath}_x\hat{\jmath}_z+\hat{\jmath}_z\hat{\jmath}_x] - (2\hat{S}_x-\hat{\phi})[\hat{\jmath}_z\hat{\jmath}_y+\hat{\jmath}_y\hat{\jmath}_z]\Big)\Big\}, \tag{6.1}$$

$$\frac{\partial}{\partial t}\hat{\jmath}_y(z,t) = \frac{c\gamma}{4A\Delta}\frac{\lambda^2}{2\pi}\Big\{-a_1\hat{S}_z\hat{\jmath}_x + a_2\Big(-(2\hat{S}_x+\hat{\phi})[\hat{\jmath}_x\hat{\jmath}_z+\hat{\jmath}_z\hat{\jmath}_x] - 2\hat{S}_y[\hat{\jmath}_z\hat{\jmath}_y+\hat{\jmath}_y\hat{\jmath}_z]\Big)\Big\}, \tag{6.2}$$

$$\frac{\partial}{\partial t}\hat{\jmath}_z(z,t) = \frac{c\gamma}{4A\Delta}\frac{\lambda^2}{2\pi}a_2\Big\{4\hat{S}_x[\hat{\jmath}_x\hat{\jmath}_y+\hat{\jmath}_y\hat{\jmath}_x] - 4\hat{S}_y[\hat{\jmath}_x^2-\hat{\jmath}_y^2]\Big\}, \tag{6.3}$$

where we for brevity have left out the (z,t)-notation on all operators on the right hand side. For the Stokes variables we can easily generalize Eq. (C.8) to be directly applicable to Stoke operators

$$\left(\frac{\partial}{\partial t}+c\frac{\partial}{\partial z}\right)\hat{S}(z,t) = \frac{1}{i\hbar}\left[\hat{S}(z,t),\hat{H}_{\text{int}}\right]. \tag{6.4}$$

Furthermore, we may in the following neglect effects of retardation, that is we assume the speed of light c is infinite. Since we in Chap. 5 already restricted ourselves to describing dynamics on a long time scale by deriving an effective Hamiltonian this does not impose strong restrictions. Neglecting retardation is mathematically equivalent to leave out the $\partial/\partial t$ term above. Then we get

$$\frac{\partial}{\partial z}\hat{S}_x(z,t) = \frac{\gamma\rho}{4\Delta}\frac{\lambda^2}{2\pi}\Big\{a_1\hat{S}_y\hat{\jmath}_z + a_2\cdot 2\hat{S}_z[\hat{\jmath}_x\hat{\jmath}_y+\hat{\jmath}_y\hat{\jmath}_x]\Big\}, \tag{6.5}$$

$$\frac{\partial}{\partial z}\hat{S}_y(z,t) = \frac{\gamma\rho}{4\Delta}\frac{\lambda^2}{2\pi}\Big\{-a_1\hat{S}_x\hat{\jmath}_z - a_2\cdot 2\hat{S}_z[\hat{\jmath}_x^2-\hat{\jmath}_y^2]\Big\}, \tag{6.6}$$

$$\frac{\partial}{\partial z}\hat{S}_z(z,t) = \frac{\gamma\rho}{4\Delta}\frac{\lambda^2}{2\pi}a_2\Big\{2\hat{S}_y[\hat{\jmath}_x^2-\hat{\jmath}_y^2] - 2\hat{S}_x[\hat{\jmath}_x\hat{\jmath}_y+\hat{\jmath}_y\hat{\jmath}_x]\Big\}, \tag{6.7}$$

where we again leave out the (z,t)-notation on the right hand side. Equations (6.1-6.3) and (6.5-6.7) are coupled to each other, and they are not even closed. On the right hand side we see spin operators like e.g. $\hat{\jmath}_x\hat{\jmath}_y+\hat{\jmath}_y\hat{\jmath}_x$ which again from Heisenberg's equations will get its own time evolution, and so on. From here we can go into many different directions depending on the actual physical system under consideration. For the rest of this chapter we specialize into different relevant cases, and we will also in these connections give some physical interpretations to the equations above.

6.2 Probing a Macroscopic Ensemble of Oriented Spins

A simple and useful tool for characterizing an ensemble of oriented atomic spins is the Faraday rotation of a linearly polarized laser beam propagating along

the direction of atomic spin orientation. We assume that a sample of spins are oriented along the direction of light propagation, i.e. the z-axis, and we will neglect quantum fluctuations for the moment. In this case the only spin operator with non-zero mean value in the equations of Sec. 6.1 is $\hat{j}_z$ in the propagation equations for $\hat{S}_x$ and $\hat{S}_y$. If a beam of light traverses a sample of atoms of length L we may show that the classical values of the Stokes operators evolve as

$$\begin{aligned} S_x^{\text{out}} &= S_x^{\text{in}} \cos(2\theta_{\text{F}}) - S_y^{\text{in}} \sin(2\theta_{\text{F}}), \\ S_y^{\text{out}} &= S_x^{\text{in}} \sin(2\theta_{\text{F}}) + S_y^{\text{in}} \cos(2\theta_{\text{F}}), \end{aligned} \tag{6.8}$$

where the angle θ_{F} is given by (in radians)

$$\theta_{\text{F}} = -\frac{a_1 \gamma \lambda^2 \rho L}{16\pi\Delta} \cdot \langle \hat{j}_z \rangle \,. \tag{6.9}$$

If a linearly polarized beam of light is rotated by the angle θ, the Stokes vector will be rotated 2θ. Thus, in the above, θ_{F} is the polarization rotation caused by the spin orientation along the direction of light propagation. The equations are valid for both $F = 3$ and $F = 4$ in the cesium ground state, where $a_1 \approx 1$ defined in Eq. (5.19) or (5.16) is depending on F. γ is the FWHM line width of the excited $6P_{3/2}$ state, λ is the optical wave length of the transition, ρ is the atomic density, and Δ is the optical detuning (red being positive), L is the sample length, and $\langle \hat{j}_z \rangle$ is the expectation value of the total angular momentum along the direction of light propagation of a single atom in the sample. We will see in Chap. 7 that this polarization rotation is a very useful tool for characterizing the spin state of an atomic ensemble.

6.3 Probing Transverse Spin Components

The most essential physical setting in this thesis is the situation of a macroscopic, oriented sample along the x-direction with an off-resonant probe propagating in the z-direction. In this case the probe measures a transverse spin component which is interesting to us at the level of quantum fluctuations, as mentioned in the introductory Chap. 2.

In this section we neglect the higher order effects of the atom/light interaction, i.e. we assume $a_2 = 0$ in the equations of Sec. 6.1. We have chosen the x-axis to coincide with the direction of spin orientation, and we shall also assume a linearly polarized probe along the x-direction (which actually is not strictly important, we could have chosen any direction). The interaction will practically be such that the state of light and the state of atoms do not deviate much from this situation, and we may describe the x-components of the spin $\mathbf{j}$ and the Stokes operator $\mathbf{S}$ by constant c-numbers, i.e. $\hat{S}_x \to S_x$ and $\hat{j}_x \to j_x$. Under these assumptions we have a zero on the right hand side of Eqs. (6.1, 6.3, 6.5, 6.7). Equations (6.2)

and (6.6) yield

$$\begin{aligned}\frac{\partial}{\partial t}\hat{\jmath}_y(z,t) &= -\frac{c\gamma}{4A\Delta}\frac{\lambda^2}{2\pi}\cdot a_1\hat{S}_z(z,t)j_x,\\ \frac{\partial}{\partial z}\hat{S}_y(z,t) &= -\frac{\gamma\rho}{4\Delta}\frac{\lambda^2}{2\pi}a_1 S_x\hat{\jmath}_z(z,t).\end{aligned} \tag{6.10}$$

Since we here have j_x and S_x constant in the whole sample of atoms we can easily integrate over z to get equations for the *collective* properties of the sample. We define the collective spin variable (with capital letter J) $\hat{J}_x = \int_0^L \hat{\jmath}_x(z,t)\rho A dz$ and so on for y, z-components. We also note that with $\partial\hat{S}_z(z,t)/\partial z = 0$ we may write $c\cdot\hat{S}_z(z,t) = \hat{S}_z^{\text{in}}(t)$ where the latter is the Stokes vector $\hat{S}_z$ at the beginning of the sample normalized to photons per second. Summarizing the above we get equations

$$\boxed{\begin{aligned}\hat{S}_y^{\text{out}}(t) &= \hat{S}_y^{\text{in}}(t) + aS_x\hat{J}_z(t), && (6.11)\\ \hat{S}_z^{\text{out}}(t) &= \hat{S}_z^{\text{in}}(t), && (6.12)\\ \frac{\partial}{\partial t}\hat{J}_y(t) &= aJ_x\hat{S}_z^{\text{in}}(t), && (6.13)\\ \frac{\partial}{\partial t}\hat{J}_z(t) &= 0, && (6.14)\\ a &= -\frac{\gamma}{4A\Delta}\frac{\lambda^2}{2\pi}a_1. && (6.15)\end{aligned}}$$

The Stokes operator S_x is classical, and $\hat{S}_y$, $\hat{S}_z$ are the quantum variables of the light polarization state normalized to photons per second. For atoms with J_x being classical we have quantum variables $\hat{J}_y$ and $\hat{J}_z$ normalized such that they describe the total spin of all atoms in the sample, i.e. J_x is of the order of the number of atoms in the sample. The interaction parameter a depends on the FWHM line width γ of the excited state $6P_{3/2}$, the optical wave length λ, the detuning Δ (red being positive), the beam cross section A, and the parameter $a_1 \approx 1$ defined in Eq. (5.19) or (5.16). Physically, a is the rotation angle of the macroscopic spin $\mathbf{J}$ around the z-axis per circularly polarized photon, or the rotation angle in Stokes vector space of $\mathbf{S}$ around the z-axis per unit of angular momentum along the z-axis. The above equations are the cornerstone for all experiments in this thesis. We remark that they arise from the first order terms proportional to a_1 in the equations of Sec. 6.1. The term $aS_x\hat{J}_z(t)$ in Eq. (6.11) enables us to read out properties of the spin state to the light. At the same time the term $aJ_x\hat{S}_z^{\text{in}}(t)$ of Eq. (6.13) feeds noise back to the spins. We often call the latter term for the *back action term*.

6.4 Inclusion of Higher Order Terms

Now, let us turn to the higher order terms proportional to a_2 of the equation in Sec. 6.1. For simplicity, we will assume that the atoms are oriented almost perfectly along the x-axis. This is in general the case for our experiments. We start out by an analysis of the classical mean values. In this case the only non-zero spin operators on the right hand side of the equations in Sec. 6.1 are $\langle \hat{\jmath}_x \rangle \approx \pm F$ and $\langle \hat{\jmath}_x^2 - \hat{\jmath}_y^2 \rangle \approx F(F - \frac{1}{2})$, see Eq. (B.15). The effect of the $\hat{\jmath}_x^2 - \hat{\jmath}_y^2$ terms can be understood by considering the propagation of a beam of light which is initially linearly polarized along $\mathbf{e}_{+45} = (\mathbf{e}_x + \mathbf{e}_y)/\sqrt{2}$. Then the most important terms of Eqs. (6.6) and (6.7) can be written

$$\begin{gathered} \frac{\partial}{\partial z}\hat{S}_y(z,t) = +k\hat{S}_z(z,t) \quad \text{and} \quad \frac{\partial}{\partial z}\hat{S}_z(z,t) = -k\hat{S}_y(z,t) \\ \text{with } k = -\frac{a_2\gamma\rho}{4\Delta}\frac{\lambda^2}{2\pi}F(2F-1), \end{gathered} \tag{6.16}$$

where Eq. (B.15) was used to evaluate $\hat{\jmath}_x^2 - \hat{\jmath}_y^2$. The solution of these equations is simply

$$\begin{aligned} \hat{S}_y(z,t) &= +\hat{S}_y(0,t)\cos(kz) + \hat{S}_z(0,t)\sin(kz), \\ \hat{S}_z(z,t) &= -\hat{S}_y(0,t)\sin(kz) + \hat{S}_z(0,t)\cos(kz). \end{aligned} \tag{6.17}$$

This is nothing more than the birefringence of the atomic sample which is oriented along the x-axis (with the x- and y-axes as major axes). The difference in phase shift experienced by x- and y-photons turns linear polarization into circular polarization and vice versa. This is a complication to the simple physical setup described in Sec. 2.3 where a strong linearly polarized beam of light passes through the atomic sample with constant $\hat{S}_z$-component and the $\hat{S}_y$-component only reading out the spin component $\hat{J}_z$. But there is more to this, the term $\hat{S}_y(\hat{\jmath}_x^2 - \hat{\jmath}_y^2)$ in Eq. (6.3) will change the mean value of $\hat{\jmath}_z$. This is just another way of stating, that if $\hat{S}_z$ is subject to changes these will also affect $\hat{\jmath}_z$ since the projection of the total angular momentum along z must be conserved. Also, in Eq. (6.17) if $\hat{S}_z$ in the propagation builds up a considerable non-zero mean value the terms proportional to $\hat{S}_z$ in Eqs. (6.1) and (6.2) will start rotating the macroscopic spin around the z-axis. This again affects $\hat{\jmath}_x^2 - \hat{\jmath}_y^2$ which started it all. We see the complicated structure of the interaction now and we really wish to minimize these effects. To characterize the strength of these effects the relevant parameter is kL where k is given in Eq. (6.16) and $L = 3.0$cm is the length of our atomic samples. For $F = 4$ we can conveniently relate kL to θ_{F} defined in Eq. (6.9) by

$$kL = \frac{7\pi}{90}\frac{a_2}{a_1}\theta_{\mathrm{F}}[\mathrm{deg}]. \tag{6.18}$$

For a typical detuning $\Delta = -1$GHz and a corresponding typical large value of $\theta_{\mathrm{F}} \approx 30$deg we get $kL \approx 7\%$ which we have to keep in mind. kL will decrease with

detuning and with atomic density, it is an atomic property and is independent on the power of the laser.

The term $\hat{\jmath}_x^2 - \hat{\jmath}_y^2$ describes *alignment* in the xy-basis. In the equations of Sec. 6.1 there are also spin terms $\hat{\jmath}_x\hat{\jmath}_y + \hat{\jmath}_y\hat{\jmath}_x$ which in a completely analogous way describe the alignment along the directions rotated by $\pm 45°$ in the xy-plane. These will have non-zero mean if we choose to orient atoms along either of the $\pm 45°$-directions instead of the x-direction.

To sum up so far, for mean values we understand all terms on the right hand side of Eqs. (6.5-6.7), terms including a_1 give rise to the Faraday effect caused by circular birefringence. The terms including a_2 are responsible for the linear birefringence.

But equations are also valid for fluctuations, quantum or classical. For our experiments we should keep in mind that with our constant bias magnetic field and the rotating frame, see Sec. 4.3, we should concentrate on frequency components around the Larmor frequency Ω for what regards $\hat{\jmath}_y$, $\hat{\jmath}_z$, $\hat{S}_y$, and $\hat{S}_z$. For instance, since $\hat{\jmath}_x^2 - \hat{\jmath}_y^2 \approx F(F - \frac{1}{2})$ primarily has a DC component, it is the AC components of $\hat{S}_y$ and $\hat{S}_z$ which couple to each other in Eqs. (6.6) and (6.7). Similarly, from the fact that Eq. (B.13) consists of first off-diagonal elements, we know that $\hat{\jmath}_x\hat{\jmath}_y + \hat{\jmath}_y\hat{\jmath}_x$ primarily has frequency components at Ω. Then it is the DC component of $\hat{S}_x$ and AC component of $\hat{S}_y$ that contribute to the time evolution of $\hat{\jmath}_z$ in Eq. (6.3).

Taking these considerations into account we conclude that DC terms of the time evolution of $\hat{\jmath}_x$ are small. Thus for a sample oriented along the x-direction we have a pretty stable system. What regards Eq. (6.2) the spin operator $\hat{\jmath}_y\hat{\jmath}_z + \hat{\jmath}_z\hat{\jmath}_y$ is small and has frequency components at 2Ω. This must couple to frequency components at Ω or 3Ω of $\hat{S}_y$ for the product to contribute at Ω in the time evolution of $\hat{\jmath}_y$. AC components of $\hat{S}_y$ are small independent of the direction of probe polarization, so we neglect the last term of Eq. (6.2).

Now, turn to the last term of Eq. (6.3). Since $\hat{\jmath}_x^2 - \hat{\jmath}_y^2$ is a DC term, the AC components of $\hat{S}_y$ at Ω will feed into $\hat{\jmath}_z$. This term can have a considerable magnitude, we wish to compare it to our favorite term which is the $a_1\hat{S}_z\hat{\jmath}_x$ back action term of Eq. (6.2). When we measure noise properties we have to square the fluctuations, and the correct comparison between the unwanted pile up in $\hat{\jmath}_z$ and the wanted back action noise (BAN) in $\hat{\jmath}_y$ is

$$\frac{\text{Bad pile up}}{\text{BAN}} = 4(2F-1)^2 \left(\frac{a_2}{a_1}\right)^2 \frac{\text{Noise}(\hat{S}_y)}{\text{Noise}(\hat{S}_z)}. \tag{6.19}$$

For our typical values of detuning we have $a_2/a_1 \approx 10^{-2}$ and the above tells us that (Bad pile up)/BAN $\approx 0.02 \cdot \text{Noise}(\hat{S}_y)/\text{Noise}(\hat{S}_z)$ for $F = 4$. If our laser beam is polarized along the x- or y-axis with a clean linear polarization, the noise of $\hat{S}_y$ and $\hat{S}_z$ at the frequency Ω will most likely both be limited by shot noise, i.e. by quantum noise (amplitude noise of the laser does not feed into $\hat{S}_y$ and $\hat{S}_z$ in the case of clean linear polarization). In this case the unwanted noise

only contributes $\approx 2\%$ of the total noise pile up. But if we choose arbitrary polarization directions in the xy-plane, the $\hat{S}_y$-component will have non-zero mean value, and the fluctuations at Ω will essentially be the amplitude noise of the laser at Ω. In this case, to keep the last term of Eq. (6.3) from piling up extra noise requires the laser *intensity* to be shot noise limited at Ω (which is a more difficult condition to meet than clean linear polarization). We thus have one motivation for choosing the laser to be polarized along the x- or y-direction and not in between.

Now, let us turn to the $\hat{\jmath}_x\hat{\jmath}_z + \hat{\jmath}_z\hat{\jmath}_x$ term of Eq. (6.2) and the $\hat{\jmath}_x\hat{\jmath}_y + \hat{\jmath}_y\hat{\jmath}_x$ term of Eq. (6.3). These spin operators have frequency components at Ω and we must then consider the DC components of $(2\hat{S}_x + \hat{\phi})$ and $4\hat{S}_x$, respectively. In the following we show, that the effect of these terms change the Larmor frequency Ω by a small amount, and we wish to calculate this for different directions of the linearly polarized laser.

To this end, assume that the laser has photon flux $\phi(t)$ and is polarized along $\mathbf{e}_1 = \cos(\alpha)\mathbf{e}_x + \sin(\alpha)\mathbf{e}_y$. Then we have mean values

$$\left\langle c(2\hat{S}_x(z,t) + \hat{\phi}(z,t))\right\rangle = (\cos(2\alpha)+1)\phi(t) \quad \text{and} \quad \left\langle 4c\hat{S}_x(z,t)\right\rangle = 2\cos(2\alpha)\phi(t). \tag{6.20}$$

Furthermore, since we assume a strong orientation along the x-axis we may relate the spin operators $\hat{\jmath}_x\hat{\jmath}_y + \hat{\jmath}_y\hat{\jmath}_x$ and $\hat{\jmath}_x\hat{\jmath}_z + \hat{\jmath}_z\hat{\jmath}_x$ to $\hat{\jmath}_y$ and $\hat{\jmath}_z$ by Eqs. (B.13) and (B.14). After some algebra we deduce that the time evolution of $\hat{\jmath}_y$ and $\hat{\jmath}_z$ become

$$\frac{\partial}{\partial t}\hat{\jmath}_y(z,t) = -\left(\Omega + \Omega_{\mathrm{S}}\frac{\cos(2\alpha)+1}{2}\right)\hat{\jmath}_z(z,t) + \ldots, \tag{6.21}$$

$$\frac{\partial}{\partial t}\hat{\jmath}_z(z,t) = +\left(\Omega + \Omega_{\mathrm{S}}\frac{2\cos(2\alpha)}{2}\right)\hat{\jmath}_y(z,t) + \ldots, \tag{6.22}$$

where the dots remind us that there are more terms in Eqs. (6.2) and (6.3) which we leave out for brevity. Above Ω is the magnetic field contribution and Ω_{S} is a Stark induced contribution normalized such that Ω_{S} is the extra contribution for $\alpha = 0$, i.e. for light polarization parallel to the spin orientation along the x-axis. We have Ω_{S} given by (in Hertz)

$$\Omega_{\mathrm{S}}[\mathrm{Hz}] = \frac{\gamma\lambda^2 a_2}{16\pi^2 A\Delta}\cdot\phi(t)\cdot 2(2F-1)\sigma^{j_x}. \tag{6.23}$$

Now, if $\alpha \neq 0$ the parentheses in Eqs. (6.21) and (6.22) are unequal, but for $\Omega \gg \Omega_{\mathrm{S}}$ we may easily show that the effective Larmor frequency becomes the average of the two parentheses. This amounts to

$$\Omega_{\mathrm{eff}}[\mathrm{Hz}] = \Omega[\mathrm{Hz}] + \frac{\gamma\lambda^2 a_2}{16\pi^2 A\Delta}\cdot\phi(t)\cdot(1+3\cos(2\alpha))\cdot\frac{(2F-1)\sigma^{j_x}}{2}, \tag{6.24}$$

where $\sigma^{j_x} = \pm 1$ for $\langle\hat{\jmath}_x\rangle = \pm F$. We see the Stark contribution to the Larmor frequency acts in opposite directions for oppositely oriented spin samples. Inserting typical values for the detuning $\Delta = 1\mathrm{GHz}$ and for the laser intensity of

1mW/cm^2 we obtain a shift in Larmor frequency of 160Hz for $\alpha = 0$. For two oppositely oriented spin samples the difference in Larmor frequency under these conditions is 320Hz. This can be a problem, but the shift is reduced to zero if $\alpha = 54.7°$. Thus we have a motivation for choosing polarization directions different from the x- or y-directions. But this opposes our desire to be polarized exactly along the x- or y-direction where pile up of laser noise is small according to Eq. (6.19). We shall study this Stark shift experimentally in Sec. 7.6 where we also present an alternative calculation of the change in Larmor frequency.

To conclude this section, we cannot easily solve analytically the equations of motion with the higher order terms proportional to a_2 included. The collective variables loose their meaning in this case. The most important effects include the mixing (6.17) of $\hat{S}_y$ and $\hat{S}_z$ by linear birefringence, the possible pile up of laser noise discussed around Eq. (6.19), and the shift in Larmor frequency discussed in Eq. (6.24). The $\hat{S}_y$, $\hat{S}_z$ mixing has strength parametrized by $kL \approx 7\%$ in the typical case. The laser noise pile up will probably be a few percent for x- or y-polarized probe beam. The effects of the Stark shifted Larmor frequency will be present for x- or y-polarization and absent for $\alpha = 54.7°$.

We also repeat the fact that Eqs. (6.1-6.3) and (6.5-6.7) are not closed, but for a well oriented sample with $\langle \hat{\jmath}_x \rangle \approx \pm F$ and with the approximations in Eqs. (B.12-B.14) we do have a closed set of linearly coupled equations. Even in this case an analytical solution will be very cumbersome. We shall not pursue any solution in this thesis.

CHAPTER 7

Atomic State Characterization

In this chapter we develop methods for the characterization of the atomic spin states that occur in different contexts in our experiments. We have several motivations for this; we would like to know the number of atoms in our sample (especially in order to check scalings of noise as we will discuss in Sec. 9.5), know the degree of orientation to tell whether we are in the coherent spin state or close to it, measure the decoherence time of the state for estimating the life time of interesting quantum states. We are able to address all the above questions. The contents of this chapter are published in [VIII].

We start out with some notation. We will consider a sample with N atoms in one hyperfine ground state F of cesium and describe the spin state with density operators $\hat{\sigma}_{ij}$ given by

$$\hat{\sigma}_{ij} = \frac{1}{N}\sum_{k=1}^{N}\hat{\sigma}_{ij}^{(k)} = \frac{1}{N}\sum_{k=1}^{N}|i\rangle_k \langle j|_k \,, \tag{7.1}$$

where $i, j = -F, -F+1, \ldots, F$, the sum is done over all individual atoms and $|j\rangle_k$ refer to the magnetic sub-level with $m_F = j$ of the k'th atom. With the x-axis as quantization axis we may express the total macroscopic angular momentum $\mathbf{J}$

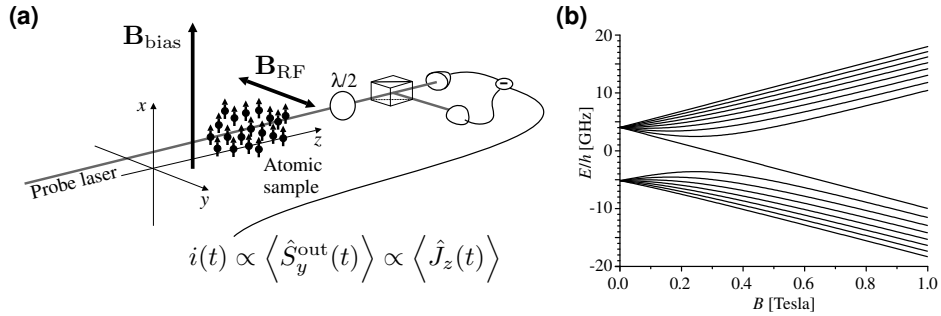

Figure 7.1: **(a)** The setup for magneto-optical resonance. A constant magnetic field $\mathbf{B}_{\text{bias}}$ is applied parallel to the atomic spin orientation along the x-axis. An RF-magnetic field is applied along the y-axis, and the $\hat{J}_z$ component of the spin is measured by a probe laser propagating along z. Magnetic resonance effects are read out optically by the probe in the photo current $i(t)$. **(b)** The energy levels of the magnetic sub-levels of the $F = 3$ and $F = 4$ ground states in cesium according to Eq. (F.2). We operate at $B_{\text{bias}} \approx 1$Gauss which is far into the lower linear regime where quadratic effects are small.

of the atoms in the hyperfine state F as

$$\hat{J}_x = N \sum_m m\hat{\sigma}_{m,m}, \tag{7.2a}$$

$$\hat{J}_y = N \sum_{m=-F}^{F-1} \frac{C(F,m)}{2} \left\{\hat{\sigma}_{m+1,m} + \hat{\sigma}_{m,m+1}\right\}, \tag{7.2b}$$

$$\hat{J}_z = N \sum_{m=-F}^{F-1} \frac{C(F,m)}{2i} \left\{\hat{\sigma}_{m+1,m} - \hat{\sigma}_{m,m+1}\right\}, \tag{7.2c}$$

where $C(F,m) = \sqrt{F(F+1) - m(m+1)}$, see Eqs. (B.9-B.11). In addition to the number of atoms N we see that the macroscopic spin $\hat{J}_x$ is described by the diagonal terms $\hat{\sigma}_{m,m}$ and the quantum variables $\hat{J}_y$ and $\hat{J}_z$ are described by the first off-diagonal terms $\hat{\sigma}_{m,m+1}$. We need to characterize each of the relevant density operators in detail in terms of magnitude and decoherence time.

7.1 The Magneto-Optical Resonance Method

We will use the so-called magneto-optical resonance to investigate the spin state of atoms, the basic setup is shown in Fig. 7.1(a). Atoms are placed in an external, constant magnetic field $\mathbf{B}_{\text{bias}}$ as discussed in Sec. 4.3. Applying another external radio frequency (RF) magnetic field we may induce transitions between the magnetic sub-levels if the RF is in resonance with the level splitting. More

exactly, as we will derive below, the RF-magnetic field couples to and drives the coherences $\hat{\sigma}_{m,m+1}$ and $\hat{\sigma}_{m+1,m}$. According to Eq. (7.2c) this will lead to a modulation of the spin component $\hat{J}_z$. This modulation can be read out optically by a probe laser, i.e. the photo current $i(t)$ of the detector setup of Fig. 7.1(a), which measures $\hat{S}_y$, will be proportional to the mean value $\left\langle \hat{J}_z \right\rangle$ according to Eq. (6.11).

The energy of the magnetic sub-levels of an atom in an external magnetic field $\mathbf{B}$ can be calculated and is given without approximation in Eq. (F.2). These levels are shown in Fig. 7.1(b). We see that for low magnetic fields the energy dependence on the magnetic field strength is linear with small corrections caused by the presence of the hyperfine splitting. In our experiments the magnetic field strength B_{bias} is around 1 Gauss which means that non-linear corrections are very small. We shall still include them to second order, which gives the Hamiltonian for a single atom with total angular momentum $\mathbf{j}$

$$\hat{H} = g_F \mu_{\text{B}} \mathbf{j} \cdot \mathbf{B} + O(B^2), \tag{7.3}$$

where μ_{B} is the Bohr magneton and the g_F-factor is defined in Eqs. (F.4) and (F.5). The bias magnetic field along the x-axis contributes $g_F \mu_{\text{B}} J_x B_{\text{bias}} + O(B_{\text{bias}}^2)$ to the Hamiltonian while the RF-magnetic field directed along the y-axis contributes $g_F \mu_{\text{B}} \hat{J}_y |B_{\text{RF}}| \cos(\omega t + \phi)$ where the RF-magnetic field is characterized by the amplitude $|B_{\text{RF}}|$, frequency ω, and phase ϕ. Retaining only the linear term is sufficient here. The Hamiltonian may now be written

$$\begin{aligned} \hat{H} = & \sum_{m=-F}^{F} \hbar \omega_m \cdot \hat{\sigma}_{mm} \\ & + \frac{g_F \mu_{\text{B}}}{4} \left(\hat{\jmath}_+ B_{\text{RF}} e^{-i\omega t} + \hat{\jmath}_- B_{\text{RF}}^* e^{i\omega t} \right), \end{aligned} \tag{7.4}$$

where $\hat{\jmath}_\pm = \hat{\jmath}_y \pm i \hat{\jmath}_z$ and $B_{\text{RF}} = |B_{\text{RF}}| e^{-i\phi}$ is the complex amplitude. The first term is the bias magnetic field contribution where we take the second order corrections into account by explicitly stating the energy levels $\hbar \omega_m$ of the m'th sub-level. The second order correction is calculated in Eq. (F.7) and will be discussed in more detail in the next section. The second term is the RF-magnetic field contribution in the rotating wave approximation. We may wish to write the Hamiltonian entirely in terms of the density operators $\hat{\sigma}_{ij}$:

$$\begin{aligned} \hat{H} = & \sum_{m=-F}^{F} \hbar \omega_m \cdot \hat{\sigma}_{mm} \\ & + \frac{g_F \mu_{\text{B}}}{4} \sum_{m=-F}^{F-1} \left(C(F,m) \hat{\sigma}_{m+1,m} B_{\text{RF}} e^{i\omega t} + \text{h.c.} \right) \end{aligned} \tag{7.5}$$

which follows directly from Eqs. (7.2b) and (7.2c). The equations of motion are

now determined by

$$\frac{\partial \hat{\sigma}_{ij}}{\partial t} = \frac{1}{i\hbar}\left[\hat{\sigma}_{ij}, \hat{H}\right] + \text{ decay terms}, \tag{7.6}$$

where the first term is the coherent evolution of the system, and the interaction with the environment will be put in by hand as decay terms.

We will now solve Eqs. (7.5) and (7.6), and to illuminate the method for solving these equations, we will pick out a single example and work it out thoroughly. The time derivative of e.g. $\hat{\sigma}_{12}$ is

$$\begin{aligned}\frac{\partial \hat{\sigma}_{12}}{\partial t} &= \frac{1}{i\hbar}\left[\hat{\sigma}_{12}, \hat{H}\right] - \Gamma/2 \cdot \hat{\sigma}_{12} \\ &= -i(\omega_2 - \omega_1)\hat{\sigma}_{12} - \Gamma/2 \cdot \hat{\sigma}_{12} \\ &\quad + \frac{i g_F \mu_{\mathrm{B}}}{4\hbar}\left\{C(F,1)[\hat{\sigma}_{22} - \hat{\sigma}_{11}]B_{\mathrm{RF}} e^{-i\omega t}\right. \\ &\quad \left. + [C(F,0)\hat{\sigma}_{02} - C(F,2)\hat{\sigma}_{13}]B^*_{\mathrm{RF}} e^{i\omega t}\right\},\end{aligned} \tag{7.7}$$

where we have just inserted the Hamiltonian (7.5) into (7.6) and added the decay term, $-\Gamma/2 \cdot \hat{\sigma}_{12}$. We will restrict ourselves to a description of spins in the case where $\hat{J}_y, \hat{J}_z \ll J_x$, i.e. the angle θ that the spins deviate from being oriented along the z-axis is much less than unity. From Eqs. (7.2a-7.2c) the order of magnitude can roughly be written as $O(\hat{\sigma}_{m+1,m}) \approx \theta \cdot O(\hat{\sigma}_{m,m})$, and following the same lines $O(\hat{\sigma}_{m+2,m}) \approx \theta^2 \cdot O(\hat{\sigma}_{m,m})$. It is then justified to neglect the coherences $\hat{\sigma}_{02}$ and $\hat{\sigma}_{13}$ in the above equation. For brevity we will define $\omega_{21} = \omega_2 - \omega_1$, which is the frequency corresponding to the transition from $m_F = 2$ to $m_F = 1$. This frequency is the Larmor frequency which typically has values around 325kHz. This is fast compared to the inverse time scale for dynamical evolution of the spin state which never exceeds 1kHz. Since the RF-magnetic field frequency ω will be in the vicinity of ω_{21} it will be convenient to define the slowly varying operators

$$\hat{\sigma}_{ij} = \tilde{\sigma}_{ij} e^{-i\omega t}. \tag{7.8}$$

Using this definition, Eq. (7.7) will turn into

$$\begin{aligned}\frac{\partial \tilde{\sigma}_{12}}{\partial t} &= (i[\omega - \omega_{21}] - \Gamma/2)\tilde{\sigma}_{12} \\ &\quad + \frac{i g_F \mu_{\mathrm{B}}}{4\hbar} C(F,1) B_{\mathrm{RF}}[\hat{\sigma}_{22} - \hat{\sigma}_{11}].\end{aligned} \tag{7.9}$$

The constant Γ will describe the decay of the *transverse* spin components. With the small angle assumption $\theta \ll 1$ the population difference $(\hat{\sigma}_{22} - \hat{\sigma}_{11})$ will not be affected by the RF-magnetic field. In addition, the typical life time of populations is $T_1 \approx 200 - 300$ms and we can safely assume $(\hat{\sigma}_{22} - \hat{\sigma}_{11})$ to be constant. Any decays of populations can even be compensated by external pumping processes. With an external pumping process we may let transients decay (takes time $1/\Gamma$)

and we are left with the steady state solution for the operator $\tilde{\sigma}_{12}$. By setting $\partial\tilde{\sigma}_{12}/\partial t = 0$ in the above equation we get

$$\hat{\sigma}_{12} = -\frac{i g_F \mu_{\mathrm{B}} B_{\mathrm{RF}} C(F,1) e^{-i\omega t}}{4\hbar \cdot (i[\omega - \omega_{21}] - \Gamma/2)} [\hat{\sigma}_{22} - \hat{\sigma}_{11}]. \tag{7.10}$$

This method applies to all density operators $\hat{\sigma}_{m,m+1}$, and substituting into Eqs. (7.2b) and (7.2c) we get

$$\hat{J}_y = \mathrm{Re}\left\{ \frac{i g_F \mu_{\mathrm{B}} B_{\mathrm{RF}} N}{4\hbar} \sum_{m=-F}^{F-1} \frac{[F(F+1) - m(m+1)] \cdot e^{i\omega t}}{i(\omega_{m+1,m} - \omega) - \Gamma_{m+1,m}/2} [\hat{\sigma}_{m+1,m+1} - \hat{\sigma}_{m,m}] \right\}, \tag{7.11a}$$

$$\hat{J}_z = \mathrm{Im}\left\{ \frac{i g_F \mu_{\mathrm{B}} B_{\mathrm{RF}} N}{4\hbar} \sum_{m=-F}^{F-1} \frac{[F(F+1) - m(m+1)] \cdot e^{i\omega t}}{i(\omega_{m+1,m} - \omega) - \Gamma_{m+1,m}/2} [\hat{\sigma}_{m+1,m+1} - \hat{\sigma}_{m,m}] \right\}. \tag{7.11b}$$

These equations can be interpreted as a number ($2F$) of two-level systems that all interact with the driving RF-magnetic field. Two adjacent magnetic sublevels m and $m+1$ act as one two-level atom with the usual Lorentzian response (resonance frequency $\omega_{m+1,m}$ and line width $\Gamma_{m+1,m}$ FWHM). Each two-level system does not respond with exactly the same weight which is reflected in the factor $F(F+1) - m(m+1)$. All the resonances add up coherently to give the overall response of the spin state to the RF-magnetic field. Note, that $\hat{J}_y$ and $\hat{J}_z$ oscillate at the driving frequency ω and not the "natural" frequencies $\omega_{m+1,m}$. This is the steady state behavior with damped transients. In Sec. 7.5 we will comment on non-steady state behavior of the spin system.

We conclude this section with some comments which are relevant for our particular experimental setup. We may write the photo current of the detector setup shown in Fig. 7.1(a) as $i(t) = \alpha \cdot \left\langle \hat{J}_z \right\rangle = \alpha \cdot \mathrm{Im}\{A(t)\}$ where α is a constant depending on experimental parameters, and $A(t)$ reflects the mean value of the curly bracket of Eq. (7.11b). We know from this equation that $A(t) \equiv A(\omega)e^{i\omega t}$ will posses only a single frequency component, namely the local oscillator frequency ω driving the transverse spins $\hat{J}_y$ and $\hat{J}_z$ away from zero. The amplitude of this frequency component is experimentally measured by inserting the photo current $i(t)$ into a lock-in amplifier and decomposing the signal into sine and cosine components:

$$\begin{aligned} i(t) &= \alpha \cdot \mathrm{Im}\{A(\omega)e^{i\omega t}\} \\ &= \alpha \cdot (\mathrm{Re}\{A(\omega)\}\sin(\omega t) + \mathrm{Im}\{A(\omega)\}\cos(\omega t)). \end{aligned} \tag{7.12}$$

We set the lock-amplifier to give the sum of the squared amplitudes of the sine and cosine components which in our case will be exactly $\alpha^2|A(\omega)|^2$. We shall call this signal our *magneto-optical resonance signal* at frequency ω (MORS(ω) in

short). Combining the above with Eq. (7.11b) and ignoring irrelevant constants we find

$$\mathrm{MORS}(\omega) = \mathrm{const} \cdot \left| N \sum_{m=-F}^{F-1} \frac{[F(F+1) - m(m+1)]}{i(\omega_{m+1,m} - \omega) - \Gamma_{m+1,m}/2} \langle \hat{\sigma}_{m+1,m+1} - \hat{\sigma}_{m,m} \rangle \right|^2 . \tag{7.13}$$

We see that the signal depends on the number of atoms N in the relevant hyperfine state F, the resonance frequencies $\omega_{m+1,m}$, the transverse spin decay rates $\Gamma_{m+1,m}$, and the populations $\hat{\sigma}_{m,m}$. All these parameters are of importance for us.

7.2 Spin State Modeling

In the previous section we derived how the spin $\mathbf{J}$ responds to an external RF-magnetic field, our motivation is to use this knowledge to characterize the spin state, i.e. we wish to deduce parameters like $\hat{\sigma}_{m,m}$, $\Gamma_{m+1,m}$ and so on. Now, for cesium in the e.g. $F = 4$ hyperfine ground state there are nine populations $\hat{\sigma}_{m,m}$ and eight line widths $\Gamma_{m+1,m}$ together with the resonance frequencies. To fit an experimentally measured spectrum (see e.g. Fig. 7.2(b)) to all these parameters will be very hard and in the following we will develop a model to significantly reduce the number of free parameters. We will just tailor a model and the justification for this model will be an experimental test.

Let us consider a case where we wish to orient all atomic spins along the x-direction, i.e. attempt to put many atoms into the $m = F$ sub-state. This can be done experimentally by illuminating the atoms with circularly polarized light, as was described in Sec. 4.5. It is then convenient to define the orientation p as an order of merit

$$p = \frac{1}{F} \sum_{-F}^{F} m \cdot \langle \hat{\sigma}_{m,m} \rangle = \frac{J_x}{NF}. \tag{7.14}$$

Note, that with this definition $p = 1$ if all atoms are in the extreme $m = F$ sub-level, and $p = 0$ for a completely unpolarized sample with $\hat{\sigma}_{m,m} = 1/(2F+1)$ for all m. We try to let the orientation p be the only parameter describing the relationship between the nine populations $\hat{\sigma}_{m,m}$. With the condition $\sum \hat{\sigma}_{m,m} = 1$ we have thus reduced eight free parameters to a single one.

Now, we describe ensembles of atoms and given p we will assume that the spin state maximizes the entropy $\hat{S} = -\mathrm{Tr}(\hat{\sigma} \ln \hat{\sigma})$. To find the individual $\hat{\sigma}_{m,m}$ we use the method of Lagrange multipliers. We must solve

$$\begin{aligned} &\frac{\partial}{\partial \langle \hat{\sigma}_{m,m} \rangle} \left(S - \alpha \sum \langle \hat{\sigma}_{m,m} \rangle - \beta \sum m \cdot \langle \hat{\sigma}_{m,m} \rangle \right) = 0 \\ &\qquad \Rightarrow \quad \langle \hat{\sigma}_{m,m} \rangle = e^{-1-\alpha} \cdot e^{-\beta \cdot m}. \end{aligned} \tag{7.15}$$

We now just need to adjust α and β in order that $\mathrm{Tr}(\hat{\sigma}) = 1$ and p is as desired. Doing this is more or less a computational problem and in principle not difficult. For the physical understanding we just need to remember that we can write $\langle \hat{\sigma}_{m,m} \rangle = \langle \hat{\sigma}_{F,F} \rangle \, \epsilon^{F-m}$ where $\epsilon = e^{\beta}$ is a parameter which is a function of p. This can go directly into Eq. (7.13).

For the eight line widths $\Gamma_{m+1,m}$ in the case of cesium we will make a model with two free parameters. First, a common line width Γ_{com} is assigned to all transitions independent of m. The physical cause for this type of decay could be magnetic field inhomogeneities, collisions, and loss mechanisms common to all atoms. In addition, if we wish to create a well oriented sample with m approaching F we will need to illuminate the atoms with resonant circularly polarized light. In our case this is the 894nm $6S_{1/2}, F = 4$ to $6P_{1/2}, F' = 4$ line. This light causes excitations from the atomic ground sub-level m with a rate $\gamma_m \propto |\langle 4, m, 1, 1 | 4, m+1 \rangle|^2 = (4-m)(5+m)/40$, where the second term is the square of Clebsch-Gordan coefficients. For a magnetic transition between ground sub-levels m and $m+1$ the resonant pumping light will contribute to the line broadening proportional to $\gamma_m + \gamma_{m+1}$. Thus we define the width Γ_{pump} caused by the optical pumping process such that

$$\Gamma_{m+1,m} = \Gamma_{\mathrm{com}} + \Gamma_{\mathrm{pump}} \frac{19 - 2m - m^2}{4}, \tag{7.16}$$

where the normalization is such that for the $m = 3 \rightarrow m = 4$ transition we have $\Gamma_{4,3} = \Gamma_{\mathrm{com}} + \Gamma_{\mathrm{pump}}$.

Finally, we must have the resonant frequencies as parameters in our model. We will write this as a central frequency ω_{center} and a splitting ω_{split} such that

$$\omega_{m+1,m} = \omega_{\mathrm{center}} + \omega_{\mathrm{split}} \left(m + \frac{1}{2} \right). \tag{7.17}$$

From the quadratic Zeeman effect we should have $\omega_{\mathrm{split}} = 2\pi \cdot \nu_{\mathrm{QZ}}$ (see Eq. (F.7)) but we keep it as a free parameter since in practice this splitting will also depend on the Stark shifts by the probe laser, see Sec. 7.6.

To sum up, a possible description of the ground spin state involves the total spin J_x and the orientation p together with the line widths Γ_{com} and Γ_{pump}, and the frequencies ω_{center} and ω_{split}. An equivalent but computationally easier way to represent J_x and p is to use the number of atoms $N_F = N \langle \hat{\sigma}_{F,F} \rangle$ of atoms in $m = F$ as one parameter and the parameter ϵ such that the population N_m can be expressed as $N_m = N \langle \hat{\sigma}_{m,m} \rangle = N_F \epsilon^{(F-m)}$.

7.3 Experimental Test of the Modeling

Let us make an experimental test of the magneto-optical resonance method and the models discussed in Sec. 7.2. To this end we setup our lasers as shown in Fig. 7.2(a). In the following all lasers run cw. The optical pump and repump

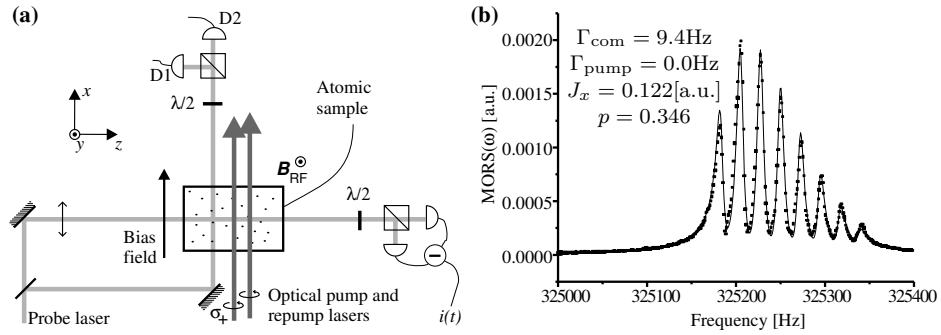

Figure 7.2: **(a)** The experimental setup for testing the magneto-optical resonance method and the spin state modeling. In addition to the situation discussed in Fig. 7.1(a) another linearly polarized laser (the DC-Faraday probe) is propagating parallel to the macroscopic spin polarization created by optical pump lasers along the x-axis. The MORS signal is recorded in the photo current $i(t)$ while the detectors D1 and D2 can tell about the polarization rotation $\theta_{\rm DC}$ of the DC-Faraday probe. **(b)** An experimental spectrum (dots) of magnetic transitions among the nine sub-levels of the $F = 4$ ground state in cesium. The solid line is a fit to Eq. (7.13) using the model described in Sec. 7.2. The many peaks tells us that atoms are distributed among all nine levels resulting in a low orientation $p = 0.346$. The line width 9.4Hz is a direct measure of the decay rate of spin coherence. According to Eq. (F.5) the corresponding $F = 3$ signal is approximately 1kHz away and does not interfere here.

lasers are tuned as described in Sec. 4.1 and their polarization can be adjusted at will. The probe laser is split into two parts, one measuring the transverse spin component $\hat{J}_z$ along the z-axis and the other one (called the DC-Faraday probe) measuring the longitudinal, macroscopic spin component J_x along the x-axis. The detuning of the probe laser is $\Delta = -1$GHz.

The rotation $\theta_{\rm DC}$ of the DC-Faraday probe is described by Eq. (6.9) and is directly proportional to the macroscopic spin (7.2a). The probe measuring $\hat{J}_z$ will lead to the MORS signal defined in Eq. (7.13). An example of a spectrum is shown in Fig. 7.2(b). In this case the optical pump laser is off and the repump laser has elliptical polarization which is relatively far from being circular. Here we see that there are eight peaks corresponding to the eight possible transitions between adjacent levels among the nine magnetic sub-levels in the $F = 4$ hyperfine state. The dots are experimental points and the solid line is a fit to the model (7.13) with J_x, p, $\Gamma_{\rm com}$, $\omega_{\rm center}$, and $\omega_{\rm split}$ as free parameters. $\Gamma_{\rm pump}$ is set to zero (since the optical pump laser is off). We see that the solid line matches the experimental points very well. Note, that $p = 0.346$ is the only parameter really describing the relative strength of the individual peaks, while the other parameters are common to all peaks. This gives strong support to the model described by Eq. (7.15) with $\langle\hat{\sigma}_{m,m}\rangle = \langle\hat{\sigma}_{F,F}\rangle\,\epsilon^{F-m}$. With $\omega = 2\pi\nu$ (experimentally we prefer Hertz and not

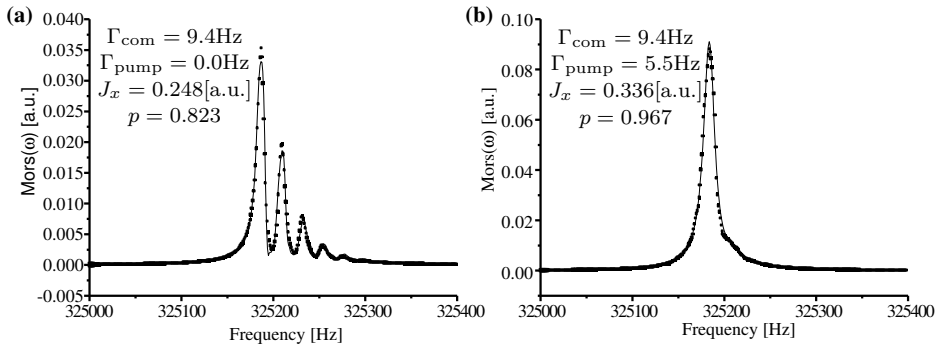

Figure 7.3: Two examples of experimental (dots) and fitted (solid line) traces. The left graph was obtained with pure σ-polarized repump laser and no optical pumping. On the right graph a small amount of optical pumping light is added giving rise to a non-zero $\Gamma_{\rm pump}$. One can, with a careful look, see that the lines now have different widths. Note also, that the height has grown by a factor of three compared to the graph on the left.

radians per second) the center frequency is $\nu_{\rm center} \approx 325250$Hz which predicts a quadratic Zeeman splitting of 23Hz according to Eq. (F.7). The observed splitting $\nu_{\rm split} = 22$Hz is very close, the small deviation is due to Stark shifts from the laser beams. For the line width we find $\Gamma_{\rm com} = 9.4$Hz (FWHM). This corresponds to a life time of the spin coherence of $T_2 = 34$ms, and we see that the experimental spectrum supports the model that all eight lines have the same width. Finally, the fit to the model (7.13) also gives a value of $J_x = 0.122$ which is in arbitrary units because we do not know the constant in front of Eq. (7.13).

Let us look at two other examples. First, with the settings as discussed above (and the optical pump laser still off) we adjust the polarization of the repump laser to be as circularly polarized as experimentally possible. This gives the spectrum shown in Fig. 7.3(a). Now the spectrum is much more asymmetric and the fit gives $p = 0.823$. This single parameter still seems to describe the shape with good accuracy. The third example we will show is seen in Fig. 7.3(b). Here the situation is as before but now with a weak optical pump present with pure circular polarization. We observe an additional broadening of the left most peak by $\Gamma_{\rm pump} = 5.5$Hz and we also note that the second peak seems much broader (should have an additional broadening by 15.1Hz according to Eq. (7.16)). Since the fit and the experimental points follow each other very well, we get support for the modeling of $\Gamma_{\rm pump}$. The orientation $p = 0.967$ shows that we are very close to having all atoms in $m_F = 4$ with only a moderate amount of optical pumping light.

In the three examples described above and more spectra of the same kind we get a fitted value for the macroscopic spin J_x. Now, with the DC-Faraday rotation signal $\theta_{\rm DC}$ giving an independent measure of J_x we may compare the

fitted J_x with θ_{DC} to get another consistency check of the model. This is shown in Fig. 7.4(a) where we plot the fitted J_x (in arbitrary units) as a function of θ_{DC}. The lowest points are taken with the repump laser only and varying repump polarization. The upper eight points are taken with purely circular optical pump of increasing intensity in addition to a purely circular repump laser. We see a very nice agreement between the fitted and the directly measured values giving strong support to both the derivations leading to Eq. (7.13) and the modeling of the spin state described in Sec. 7.2.

Let us conclude this section by noting that we developed a very simple model describing the spin state of atoms in the presence of optical pump and repump lasers. The parameter $\epsilon = e^{\beta}$ defined in the discussion around Eq. (7.15) is relying on "equilibrium physics" (the derivation includes maximizing the entropy). It is pure luck that this simple model is sufficient, our experience tell us that a long T_1 is required to observe this. We indeed have seen bad vapour cells for which this model does not hold, but this is no problem as long as we can choose a good vapour cell and test it. In the case of well oriented samples like Fig. 7.3(b) we can of course not say whether the model is good for the extreme magnetic sub-levels around $m_F = -4$ where the population must be exponentially small according to the model. But in this case the spin state is clearly defined by only a few magnetic sub-levels around $m_F = 4$ and everything is fine anyway. With these techniques as a starting point we may turn off the pumping lasers and we are left with a long lived and well characterized spin state for further experimental investigation.

7.4 Unresolved Lines

The spectra shown in the previous section have been more or less well resolved which enabled us to directly determine the orientation p. Now, how much information can we extract if the line widths are much broader than the quadratic Zeeman splitting ω_{split}? In this case it will be hard to observe asymmetry in the spectrum like e.g. Figs. 7.3.

First, assume that all atoms are subject to decoherence with the same rate described by $\Gamma_{\mathrm{com}} \gg \omega_{\mathrm{split}}$ and decay from pumping light is a small contribution. In this approximation we set $\Gamma_{\mathrm{pump}} = \omega_{\mathrm{split}} = 0$ and Eq. (7.13) reduces to

$$\mathrm{MORS}(\omega) = \mathrm{const} \cdot \left| 2N \frac{\sum m\hat{\sigma}_{m,m}}{i(\omega_0 - \omega) + \Gamma_{\mathrm{com}}} \right|^2 \propto |J_x|^2 \,, \tag{7.18}$$

where $\omega_0 = \omega_{m+1,m}$ for all m. We see that in this case the spectrum will be a single Lorentzian the size of which is only depending on J_x. In this case the independent measure from the DC-Faraday probe will only contribute exactly the same information and we will not be able to deduce the orientation p, e.g. we cannot tell the difference between having $N = 10^{12}$, $p = 1$ and $N = 2 \cdot 10^{12}$, $p = 0.5$.

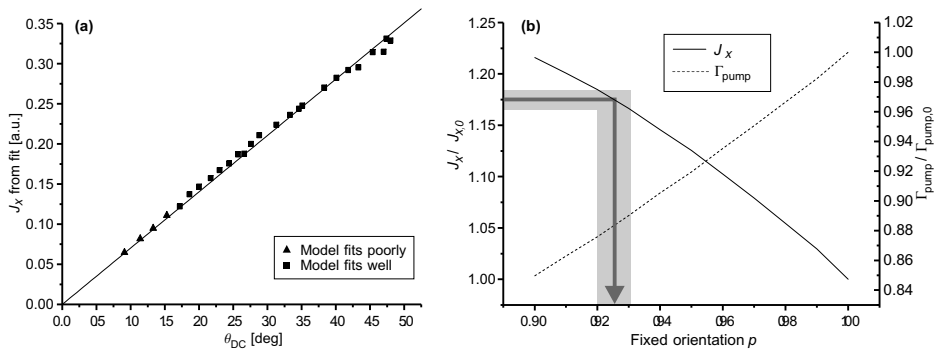

Figure 7.4: **(a)** Consistency check of the models. Fits to different spectra give an estimate of J_x. This can be compared directly to the independently measured DC-Faraday rotation signal θ_{DC} which is proportional to J_x. We indeed observe a straight line through the origin. Note, the model description $\langle \hat{\sigma}_{m,m} \rangle \propto \epsilon^m$ proved to be less accurate for the lowest four points, but by coincidence the points still fit well. **(b)** The interdependence of p, J_x and Γ_{pump} in the limit where Γ_{pump} dominates both the common width Γ_{com} and the quadratic Zeeman splitting ω_{split}. $J_{x,0}$ and $\Gamma_{\mathrm{opt},0}$ reflect the values at $p = 1$. If we can measure e.g. J_x independently with an accuracy of 2% the orientation can be defined within 1% in the example shown.

On the other hand, if Γ_{pump} dominates Γ_{com} and ω_{split} we will get a signal that depends on the internal atomic spin state. The reason for this is the fact that different resonance lines have different line widths according to Eq. (7.16). To examine this approximation we set $\Gamma_{\mathrm{com}} = \omega_{\mathrm{split}} = 0$ and try to fit the rest of the parameters to a spectrum which is a perfect Lorentzian. The correct fitting parameters of course have $p = 1$ and Γ_{pump} equal to the Lorentzian width but in practical life other sets of parameters will also fit the spectrum to an extent which one would find reasonable. We find that orientations in the range $p = 0.9$ to $p = 1$ all fit the perfect Lorentzian pretty well. We now fix p to a value in this range and make a fit of the Lorentzian. The resulting values of J_x and Γ_{opt} are shown in Fig. 7.4(b). We see that if we can estimate one of the parameters J_x or Γ_{opt} independently we should be able to calculate the orientation p. For instance, a measurement of J_x (by the DC-Faraday probe) to an accuracy of 2% will fix the orientation p to 1%. Keeping track of the optical pump power could lead to an estimate of Γ_{opt} and this could also help making bonds on p. One only needs to have one fix point, e.g. if one knows that we have $p = 1$ perfectly in one case, or if one can reduce Γ_{pump} to the point where the spectral lines become resolved and a calibration like Fig. 7.4(a) can be performed.

7.5 Pulsed Experiments

All previous derivations and measurements in this chapter have been carried out in cw settings, i.e. Eqs. (7.11a) and (7.11b) assume constant values of frequency ω and decay rates $\Gamma_{m+1,m}$. This is indeed valid if lasers are running cw and if we scan the frequency ω slowly enough. But some experiments must be carried out in a setting with pulsed lasers, e.g. one might wish to prepare the spin state in the maximally oriented state $F = 4$, $m_F = 4$ by illuminating atoms by a pulse of resonant, circularly polarized laser light, see e.g. the creation of entanglement in Chaps. 9 and 10. For the magneto-optical resonance method to be useful in such experiments it must be utilized in the correct experimental conditions which now means time varying decay rates $\Gamma_{m+1,m}$. In this section we outline the extensions into the pulsed regimes and discuss the applicability of the magneto-optical resonance method for characterization of spin states under these circumstances.

We assume for simplicity that atoms are pumped to the $F = 4$, $m_F = 4$ state to an extent that we only need to consider transitions between $m_F = 3$ and $m_F = 4$. The extension to all levels should be straightforward (but cumbersome). For these two levels we may write Eq. (7.9) as

$$\frac{\partial \tilde{\sigma}_{34}}{\partial t} = (i\Delta - \Gamma/2)\tilde{\sigma}_{34} + i\chi[\hat{\sigma}_{44} - \hat{\sigma}_{33}], \tag{7.19}$$

where $\Delta = \omega - \omega_{43}$ and $\chi = g_F \mu_B B_{RF} C(F,3)/4\hbar$. We assume as in Sec. 7.1 that the populations $\hat{\sigma}_{44}$ and $\hat{\sigma}_{33}$ can be treated as constants corresponding to small angle deviations from the x-axis. Then the solution of the above equation is straightforward

$$\begin{aligned}\tilde{\sigma}_{34}(t) = \tilde{\sigma}_{34}(0)e^{(i\Delta-\Gamma/2)t} \\ - \frac{i\chi}{i\Delta - \Gamma/2}[\hat{\sigma}_{44} - \hat{\sigma}_{33}]\left(1 - e^{(i\Delta-\Gamma/2)t}\right).\end{aligned} \tag{7.20}$$

This solution starts out with $\tilde{\sigma}_{34}(0)$ at $t = 0$ and makes a damped oscillation toward the steady state value $-i\chi[\hat{\sigma}_{44} - \hat{\sigma}_{33}]/(i\Delta - \Gamma/2)$. Note, this steady state value is exactly the result in (7.10), and it is reached in a time $\approx \Gamma^{-1}$. With the solution of $\tilde{\sigma}_{34}$ we can continue to find the actual spin, e.g. $\hat{J}_z$ given by (7.2c) and predict the results of a measurement.

Experimentally, we set up pumping lasers and a probe laser measuring the transverse spin state as in Fig. 7.1(a). The lasers are turned on and off with acousto- and electro-optical modulators. The decay rate in the absence of lasers is denoted Γ_{dark} which is typically small. When the probe laser is on an additional broadening of Γ_{probe} is present leading to a total decay rate of $\Gamma_{\text{probe}} + \Gamma_{\text{dark}}$. During the optical pumping pulse the atoms are typically subject to a high decay rate given in total by $\Gamma_{\text{pump}} + \Gamma_{\text{dark}}$. The probe laser is typically turned on shortly after the optical pumping has been turned off and is maintained for a time shorter than the decay time $(\Gamma_{\text{probe}} + \Gamma_{\text{dark}})^{-1}$. We are thus in the transient regime of

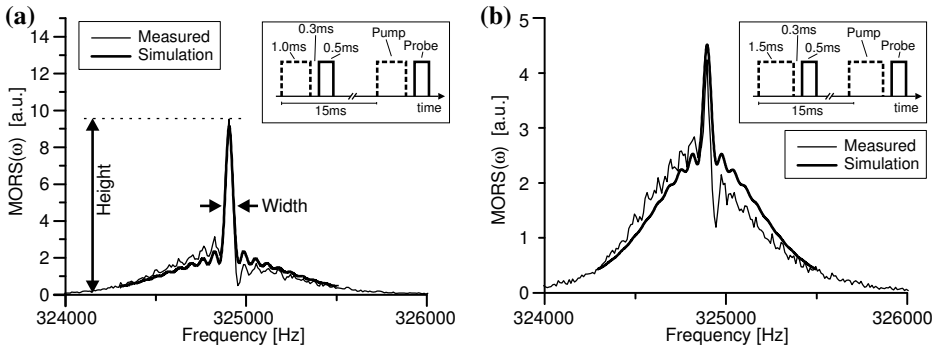

Figure 7.5: Examples of magneto-optical resonance signals in the pulsed regime. In a cw experiment we estimate $\Gamma_{\text{pump}} = 770$Hz, $\Gamma_{\text{dark}} = 18$Hz, and $\Gamma_{\text{probe}} = 2$Hz. The timing of pulses is shown in the two insets, the only difference between **(a)** and **(b)** is the pump duration being 1.0ms and 1.5ms, respectively. The thick solid line is a simulation as described in the text, the thin solid line is a measured spectrum. The only free parameter in the simulation is the height which is common for both figures (and for all data points in Fig. 7.6 below). We define the width and height of the traces as shown in part **(a)**, these will be discussed in Fig. 7.6.

Eq. (7.20) and given the frequency ω of the driving RF-magnetic field we cannot obtain a simple estimate of the amplitude of the response at that frequency as in (7.13). Instead we have time varying quadrature components of the measured photo current $i(t)$ and we simply integrate these over time in the presence of the probe laser. From the perspective of modeling we need to evolve $\tilde{\sigma}_{34}$ according to (7.20) with the relevant decay rates and integrate the result over the time of the probe laser pulse.

We perform the pulsed experiment and compare to simulations, experimental examples are shown in Fig 7.5. Given the laser powers we may from cw experiments deduce parameters like Γ_{pump}, Γ_{dark}, and Γ_{probe} for use in the simulations, and we choose the timing of pulses as shown in the insets of the figures. Only a common height to the simulated spectrum is a free parameter. From the figures we see that the model and the experimental data match to a high degree, only small details in the experimental spectra are not covered by the model. These details are partly noise and partly some asymmetry which arises from a possible non-perfect orientation and from the fact that the optical pump laser contributes a small Stark shift. The structure consists of a central peak which is dominant at short pump durations T_{pump}. We observe small sidebands with separation 67Hz $= T_{\text{pump}}^{-1}$ which increase in magnitude for longer pump durations. For very large T_{pump} we end up with a single, broad structure. As we show in Fig. 7.5(a) we define a height and width for the simulated and measured spectra. These are compared in Fig. 7.6, we see there is a very nice agreement for a longer range of

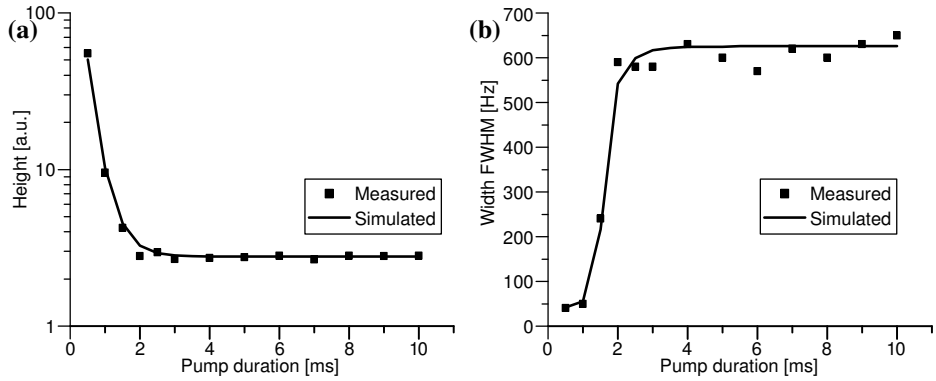

Figure 7.6: Comparison of heights and widths of the simulated and measured magneto-optical spectra, see Fig. 7.5. We have $\Gamma_{\text{pump}} \approx 770$Hz which corresponds to a characteristic time around a millisecond. We see that for $T_{\text{pump}} \geq 2$ms there is essentially no change in the height and width of the spectrum, the steady state value of Eq. (7.20) has been reached with the strong Γ_{pump}.

pump durations than the two shown in Fig. 7.5.

We do in general find good agreement with simulated and measured spectra. As another observation, we will state that with a good approximation the width of the pulsed spectrum grows proportionally with Γ_{pump} if we just to a reasonable extent have $\Gamma_{\text{dark}} + \Gamma_{\text{prob}} \ll \Gamma_{\text{pump}} \ll T_{\text{probe}}^{-1}$. In addition, we may show by dimensional arguments that (for fixed orientation) the area A of the spectrum is connected to the width Γ and to the macroscopic spin J_x by $A = \text{const} \cdot J_x^2/\Gamma$. In the experiment discussed in Sec. 10.1 this was partially used to estimate J_x.

7.6 Stark Shifts by the Probe

We conclude this chapter with a study of the influence of the Stark effect from the probe laser on the magneto-optical resonance lines. There are several motivations for this. Firstly, this is a direct experimental test of the higher order terms (proportional to a_2) in the interaction Hamiltonian (5.18), and secondly, we will get some understanding related to the fact that the laser beam does not cover all atoms at the same time. Finally, some experimental diagnostics can be applied from the Stark effect.

Let us calculate the Stark effect from the probe laser on the magnetic sublevels $|F, m\rangle$. We let the light be strong and linearly polarized along the vector

$$\mathbf{e}_1 = \mathbf{e}_x \cos\alpha + \mathbf{e}_y \sin\alpha, \tag{7.21}$$

i.e. α is the angle between the macroscopic spin direction (the x-axis) and the probe polarization direction. The Stark effect on magnetic sub-levels is in our

case much weaker than the splitting caused by the constant magnetic field and can be calculated in non-degenerate perturbation theory from the interaction Hamiltonian (5.18). The a_0 term is common to all levels, the a_1 term is zero on average since $\left\langle \hat{S}_z \right\rangle = 0$, and we are left with the higher order components proportional to a_2. For the linearly polarized probe we may show that

$$\left\langle \hat{S}_+(t) \right\rangle = \frac{\phi(t)}{2} e^{2i\alpha} \quad \text{and} \quad \left\langle \hat{S}_-(t) \right\rangle = \frac{\phi(t)}{2} e^{-2i\alpha}, \tag{7.22}$$

where $\phi(t)$ is the photon flux and Stokes operators are normalized to photons per second. Then the higher order terms of the interaction Hamiltonian for a single atom can then be written

$$\hat{H}_{\text{int}}^{\text{eff}} = -\frac{\hbar\gamma}{4A\Delta}\frac{\lambda^2}{2\pi} a_2 \cdot \phi(t) \cdot \left(\hat{\jmath}_z^2 - [\hat{\jmath}_x^2 - \hat{\jmath}_y^2]\cos(2\alpha) - [\hat{\jmath}_x\hat{\jmath}_y + \hat{\jmath}_y\hat{\jmath}_x]\sin(2\alpha)\right). \tag{7.23}$$

Now, in the basis quantized along the x-axis we may easily derive

$$\begin{aligned} \langle m| \hat{\jmath}_x^2 |m\rangle &= m^2, \\ \langle m| \hat{\jmath}_y^2 |m\rangle &= \frac{F(F+1) - m^2}{2}, \\ \langle m| \hat{\jmath}_z^2 |m\rangle &= \frac{F(F+1) - m^2}{2}, \\ \langle m| \hat{\jmath}_x\hat{\jmath}_y + \hat{\jmath}_y\hat{\jmath}_x |m\rangle &= 0. \end{aligned} \tag{7.24}$$

We can now calculate in perturbation theory the contribution of the Stark shift to the energy levels from the above Hamiltonian.

$$E_m^{\text{Stark}} = \frac{\hbar\gamma}{4A\Delta}\frac{\lambda^2}{2\pi} a_2 \cdot \phi(t) \cdot \left[\frac{1+3\cos(2\alpha)}{2} \cdot m^2 - \frac{1+\cos(2\alpha)}{2} F(F+1)\right]. \tag{7.25}$$

Comparing to the quadratic Zeeman effect of App. F we easily derive that the Stark effect causes an additional splitting between two resonance *lines* of the magneto-optical resonance signal of

$$\begin{aligned} \nu_{\text{Stark}}[\text{Hz}] &= -\frac{\gamma\lambda^2 a_2}{16\pi^2 A\Delta} \cdot \phi(t) \cdot [1 + 3\cos(2\alpha)] \\ &= 1.03 \cdot 10^6 \text{Hz} \frac{P[\text{mW}] \cdot a_2(\Delta) \cdot [1 + 3\cos(2\alpha)]}{A[\text{cm}^2] \cdot \Delta_{\text{blue}}[\text{MHz}]}, \end{aligned} \tag{7.26}$$

where we inserted $\gamma = 5.21$MHz and $\lambda = 852$nm, and we related the flux $\phi(t)$ to the probe power P. a_2 was defined in Eq. (5.16). We remark that we have here presented an alternative calculation of Eq. (6.24). The additional factor $(2F-1)\sigma^{j_x}/2$ arises from the fact that in Eq. (6.24) we calculated the shift of the outermost resonance lines $m = F \leftrightarrow m = F-1$ or $m = -F \leftrightarrow m = -F+1$.

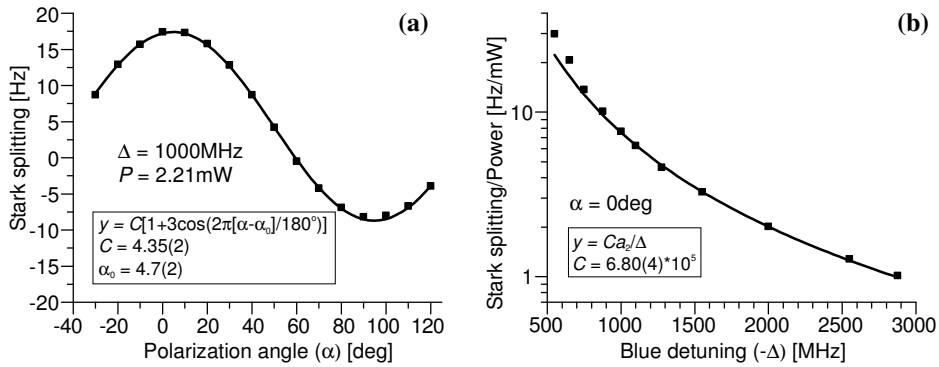

Figure 7.7: **(a)** The Stark splitting ν_{Stark} versus polarization direction α. The dots are experimental and the solid line a fit. We confirm the $1 + 3\cos(2\alpha)$ dependence predicted by Eq. (7.26). The fitted constant C can be compared quantitatively with the theory, see the text for details. **(b)** The Stark splitting per milliwatt of probe power ν_{Stark}/P versus blue detuning $(-\Delta)$. Again there is agreement with theory, we confirm the dependence on a_2/Δ. The small deviation at low detuning can be explained by Doppler broadening.

The Stark splitting can be measured with high precision by magneto-optical resonance signals like the example shown in Fig. 7.2(b). From the experimentally measured splitting we subtract the quadratic Zeeman contribution (F.7) $\nu_{\text{QZ}} = 23.0\text{Hz}$ to obtain the Stark contribution ν_{Stark}.

We set up an experiment to measure MORS for different values of the angle α, the probe power P, the detuning Δ, and the beam cross section A. First of all, we find that the Stark splitting is independent on the beam cross section A. The reason for this is the fact that atoms are moving in and out of the laser beam. For a constant power P all atoms see the same average number of photons independent on A. We also confirm experimentally that the splitting is proportional to the power P.

Next, we examine the dependence on the angle α. The results is shown in Fig. 7.7(a). We make a fit to Eq. (7.26) with an overall constant C and an offset angle α_0 as only free parameters. We find an offset $\alpha_0 = 4.7\text{deg}$ which we take as a mis-calibration of the polarization direction α. The experimental uncertainty in α is about one degree. We also find that the dependence on $(1 + 3\cos(2\alpha))$ is confirmed, and the constant C matches the prediction (7.26) if we take $A = 5.8\text{cm}^2$. This is very close to the effective transverse area of our vapour cell $A_{\text{eff}} \approx 6.0\text{cm}^2$ which we mentioned in Sec. 4.2.

We also examine the dependence of the Stark splitting on the blue detuning $(-\Delta)$. To obtain a higher precision we take several points with different probe powers P. We plot the measured splitting versus probe power and make a linear fit to the data. This results in a slope ν_{Stark}/P which is plotted in Fig. 7.7(b). This is fitted to the model $y = Ca_2/\Delta_{\text{blue}}$ and we see that the data and the solid

line fit match very well. A small disagreement for low detuning is probably a result of the Doppler broadening. We find agreement with Eq. (7.26) if we take $A = 6.1\text{cm}^2$. Again there is good agreement with an effective area of 6.0cm^2.

We conclude that our predictions match very well with experiments, both qualitatively and quantitatively. Thus we have confidence that the Hamiltonian (5.18) is correct. We also learn that the atomic motion can be modeled by an effective transverse area $A_{\text{eff}} = 6.0\text{cm}^2$ of the vapour cell (at least for classical mean values). Finally, we saw that the measurements could indicate a mis-calibration of the polarization angle α. Also, by comparing the Stark splitting for two atomic samples we have the possibility to measure the light loss in the propagation between the samples (we cannot place power meters inside the vapour cells).

CHAPTER 8

Recording Quantum Fluctuations of Light in Atoms

In this chapter we examine the interaction between atomic spins and the polarization state of light at the quantum level. Our motivation for this is two fold. First of all, we would like some evidence that the theory described in Chaps. 5 and 6 leads to correct predictions for experimental results. In the present chapter we take the basic equations of interaction (6.11-6.14) as our starting point. With these at hand, we develop an understanding of the dynamical evolution of the quantum spin state in the presence of a laser beam in a non-classical polarization state. We will find convincing agreement between theory and experiment. Secondly, the experimental results demonstrate that our atomic spin states indeed are sensitive to the quantum fluctuations of a light beam. This is one necessary step toward the realization of a full scale quantum memory for light based on back action of quantum measurements. We discuss this more carefully in Secs. 8.5 and 11.3.

Other approaches toward a quantum memory for light exist. With the aid of electromagnetically induced transparency, the amplitudes of an electric field can be mapped onto coherences of atomic ground state spins [30]. This has been demonstrated experimentally in [31, 32, 33] for classical mean values of amplitudes and phase. Theoretically this should also work for quantum fluctuations.

The contents of the present chapter are published in [II,VII]. The work of the present chapter also sheds light on the ultimate sensitivity of spin measurements. This is discussed in [III,V].

A schematic view of the experiment is shown in Fig. 8.1. An atomic sample

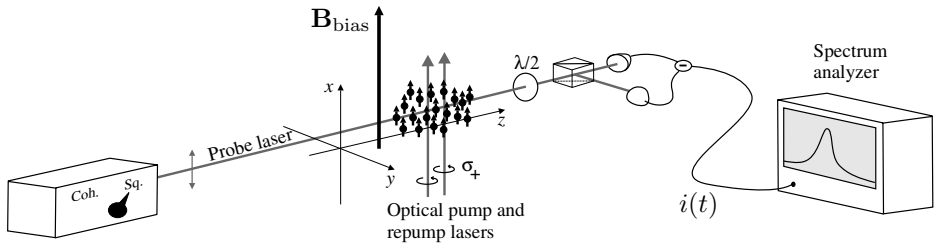

Figure 8.1: Schematic view of the experimental setup. A probe laser is sent through a sample of oriented atoms. The optical and repump laser maintain the spin orientation. A detection system measures the fluctuations of the light leaving the atomic sample. A constant magnetic field $\mathbf{B}_{\text{bias}}$ moves atomic fluctuations to the Larmor frequency Ω.

is placed in a constant magnetic field $\mathbf{B}_{\text{bias}}$ and the atomic spins are oriented parallel to this magnetic field along the x-axis. The spins will rotate with Larmor frequency $\Omega = g_{\text{F}}\mu_{\text{B}}B_{\text{bias}}/\hbar$ (see App. F). The spin orientation is maintained by the optical pump and repump lasers which are running cw. The optical pump and repump power can be adjusted, especially the resonant optical pump laser will cause decay of the spin state with a rate Γ depending on laser power. The probe laser emerges from a source that will be described in Sec. 8.2. The quantum polarization state of the probe laser can be coherent or squeezed. The probe laser passes the atoms and exchanges quantum fluctuations with these. The outgoing laser beam is measured by a detection system, and the photo current $i(t) \propto \left\langle \hat{S}_y^{\text{out}}(t) \right\rangle$ (see Eq. (E.1)) is fed into a spectrum analyzer. Our goal is to predict the spectrum of $i(t)$ and connect this to the quantum variables of the atomic spins and the polarization state of the probe laser.

8.1 Theoretical Approach

We write up Eqs. (6.11-6.14) with the addition of the Larmor rotation and the spin decoherence. This reads

$$\hat{S}_y^{\text{out}}(t) = \hat{S}_y^{\text{in}}(t) + aS_x\hat{J}_z(t), \tag{8.1}$$

$$\hat{S}_z^{\text{out}}(t) = \hat{S}_z^{\text{in}}(t), \tag{8.2}$$

$$\frac{\partial}{\partial t}\hat{J}_y(t) = -\Omega\hat{J}_z(t) - \Gamma\hat{J}_y(t) + \hat{\mathcal{F}}_y(t) + aJ_x\hat{S}_z(t), \tag{8.3}$$

$$\frac{\partial}{\partial t}\hat{J}_z(t) = \Omega\hat{J}_y(t) - \Gamma\hat{J}_z(t) + \hat{\mathcal{F}}_z(t). \tag{8.4}$$

The magnetic field adds the term $\hbar\Omega\hat{J}_x$ to the Hamiltonian which leads to the first terms of Eqs. (8.3) and (8.4). The decoherence of the spin variables is put in

by hand with a decay rate Γ. This decay term must be accompanied by Langevin forces $\hat{\mathcal{F}}_y$ and $\hat{\mathcal{F}}_z$ to preserve the correct quantum statistics. The properties of these Langevin forces are calculated in App. G.

The above equations are conveniently solved in Fourier space. In addition, with the knowledge of the correlation function $\left\langle \hat{S}_y^{\text{out}}(\omega)\hat{S}_y^{\text{out}}(-\omega')\right\rangle$ we may directly deduce the spectrum of fluctuations of the photo current defined by $\Phi(\omega) = 1/\sqrt{2\pi}\int \langle i(t)i(t+\tau)\rangle\, e^{i\omega\tau}d\tau$. We will find mathematically

$$\phi(\omega)\cdot\delta(\omega-\omega') \propto \left\langle \hat{S}_y^{\text{out}}(\omega)\hat{S}_y^{\text{out}}(-\omega')\right\rangle + \left\langle \hat{S}_y^{\text{out}}(-\omega)\hat{S}_y^{\text{out}}(\omega')\right\rangle. \tag{8.5}$$

This is essentially the Wiener-Khintchine theorem [86], for more details see App. E. We define the Fourier transform by $\hat{S}_y^{\text{out}}(\omega) = \frac{1}{\sqrt{2\pi}}\int \hat{S}_y^{\text{out}}(t)e^{i\omega t}dt$ and with some algebra the above equations turn into

$$\hat{S}_y^{\text{out}}(\omega) = \hat{S}_y^{\text{in}}(\omega) + aS_x\hat{J}_z(\omega), \tag{8.6}$$

$$\hat{S}_z^{\text{out}}(\omega) = \hat{S}_z^{\text{in}}(\omega), \tag{8.7}$$

$$\hat{J}_y(\omega) = \frac{(\Gamma - i\omega)\hat{\mathcal{F}}_y(\omega) - \Omega\hat{\mathcal{F}}_z(\omega) + (\Gamma - i\omega)aJ_x\hat{S}_z^{\text{in}}(\omega)}{(\Omega-\omega)(\Omega+\omega) - 2i\Gamma\omega + \Gamma^2}, \tag{8.8}$$

$$\hat{J}_z(\omega) = \frac{\Omega\hat{\mathcal{F}}_y(\omega) + (\Gamma - i\omega)\hat{\mathcal{F}}_z(\omega) + \Omega aJ_x\hat{S}_z^{\text{in}}(\omega)}{(\Omega-\omega)(\Omega+\omega) - 2i\Gamma\omega + \Gamma^2}. \tag{8.9}$$

Inserting (8.9) into (8.6) gives the Fourier components of the outgoing $\hat{S}_y$ operator. We need to calculate the correlation function $\left\langle \hat{S}_y^{\text{out}}(\omega)\hat{S}_y^{\text{out}}(-\omega')\right\rangle$ and to this end we need the correlation functions of the Langevin forces $\hat{\mathcal{F}}_y$, $\hat{\mathcal{F}}_z$, and the Stokes operators $\hat{S}_y^{\text{in}}$, $\hat{S}_z^{\text{in}}$. The Stokes operators are discussed in App. E, the Fourier transform of Eqs. (E.10) and (E.11) yields

$$\begin{aligned}\left\langle \hat{S}_y^{\text{in}}(\omega)\hat{S}_y^{\text{in}}(-\omega')\right\rangle &= \epsilon_y\frac{S_x}{2}\delta(\omega-\omega'),\\ \left\langle \hat{S}_z^{\text{in}}(\omega)\hat{S}_z^{\text{in}}(-\omega')\right\rangle &= \epsilon_z\frac{S_x}{2}\delta(\omega-\omega'),\end{aligned} \tag{8.10}$$

where we have introduced the squeezing parameters ϵ_y and ϵ_z such that $\epsilon_y = \epsilon_z = 1$ for the input light in the coherent state (classical laser light) and $\epsilon_y < 1$ or $\epsilon_z > 1$ for light with squeezed $\hat{S}_y$-component or vice versa. The Heisenberg uncertainty relation requires $\epsilon_y\cdot\epsilon_z \geq 1$. The ϵ-parameters measure the noise level of the Stokes components relative to the level with coherent state light. Physically, the delta function $\delta(\omega-\omega')$ times the constant $S_x/2$ gives the light noise a white power spectrum which grows proportionally to the flux of photons.

The Langevin forces are derived in App. G, Fourier transforming Eq. (G.6) yields

$$\left\langle \hat{\mathcal{F}}_y(\omega)\hat{\mathcal{F}}_y(-\omega')\right\rangle = \left\langle \hat{\mathcal{F}}_z(\omega)\hat{\mathcal{F}}_z(-\omega')\right\rangle = \Gamma|J_x|\delta(\omega-\omega'), \tag{8.11}$$

where Γ is the spin decay rate introduced in Eqs. (8.3) and (8.4), and $|J_x|$ is the magnitude of the macroscopic spin state along x. There are also non-zero cross correlations like $\left\langle \hat{\mathcal{F}}_y \hat{\mathcal{F}}_z \right\rangle$ which are all delta-correlated as the direct terms.

Now, from Eqs. (8.6) and (8.9) we note that (apart from c-numbers) $\hat{S}_y^{\text{out}}(\omega)$ only depends on the quantum variables $\hat{S}_y^{\text{in}}(\omega)$, $\hat{S}_z^{\text{in}}(\omega)$, $\hat{\mathcal{F}}_y(\omega)$, and $\hat{\mathcal{F}}_z(\omega)$. Since all these have correlation function proportional to $\delta(\omega - \omega')$ it follows that this is the case for $\hat{S}_y^{\text{out}}(\omega)$. From Eq. (8.5) and some lengthy but simple algebra we derive the spectrum $\Phi(\omega)$ of the photo current $i(t)$. Leaving out irrelevant front factors we get

$$\Phi(\omega) = \frac{S_x}{2}\epsilon_y + \frac{\frac{1}{4}a^2 S_x^2}{(\Omega - \omega)^2 + \Gamma^2}\left\{\frac{a^2 J_x^2 S_x \epsilon_z}{2} + 2\Gamma|J_x|\right\} + \text{neg. freq.} \tag{8.12}$$

We have made the narrow band approximation $\Gamma \ll \Omega$ and $|\Omega - \omega| \ll \Omega$ which clarifies the resonant structure of the power spectrum around Ω with width Γ. There is also a similar negative frequency component around $-\Omega$. The cross correlations of the Langevin forces and Stokes operators do not contribute here, this is a result of the special form of Eq. (8.5) which again is a result of time-ordered light field operators (see App. E).

The spectrum (8.12) is very intuitive. The first term is the noise of the incoming light, it has a white spectrum and is proportional to the photon flux. For $\epsilon_y = 1$ we are at the *shot noise level* (SNL). The second term has a Lorentzian profile centered at the Larmor frequency Ω with line width Γ (HWHM). This corresponds to the slow time dynamics of the spin state evolution being of order Γ^{-1}. The first term inside the curly brackets is called back action noise, it is a result of the quantum fluctuations of light being stored in the spin state. The last terms in the curly brackets is the projection noise of the spin state.

To find a convenient way to compare theoretical predictions with measurement we integrate the power spectrum over frequencies. We define the *back action noise area* and the *projection noise area* by

$$\text{BANA}_{\epsilon_z} = \frac{\pi a^4 J_x^2 \epsilon_z}{\Gamma}\left(\frac{S_x}{2}\right)^3, \qquad \text{PNA} = 2\pi a^2 |J_x| \left(\frac{S_x}{2}\right)^2, \tag{8.13}$$

i.e. the integral over the first and second narrow band term in the curly brackets in (8.12). We note that the BANA scales with the photon flux to the third power, with J_x^2, and inversely with Γ. The PNA scales linearly with the spin size J_x, this is the usual finger print of quantum noise imposed by the Heisenberg uncertainty principle. Note also the quadratic scaling with photon flux and the independence of the width Γ, projection noise cannot be washed away by decay processes. The shot noise level SNL $= S_x/2$ connects the BANA_1 (with coherent state light, $\epsilon_y = \epsilon_z = 1$) and the PNA in the following way

$$\text{PNA} = 2\sqrt{\pi\Gamma(\text{BANA}_1) \times (\text{SNL})}. \tag{8.14}$$

We may denote the area of additional noise contributions to the atomic noise as *technical noise area* TNA. Technical noise (from e.g. lasers or radio stations)

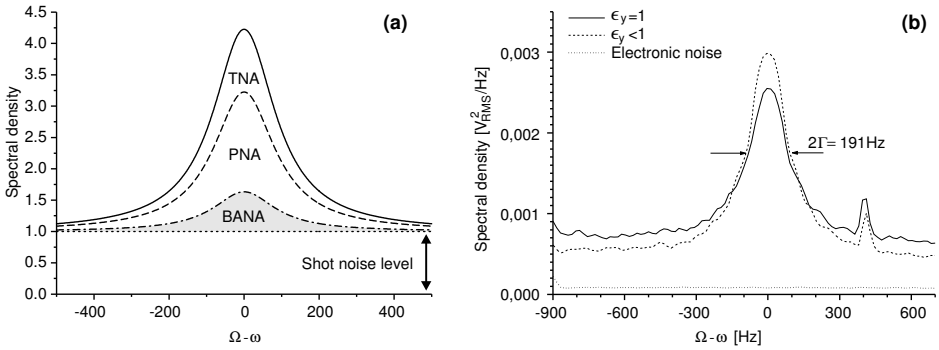

Figure 8.2: **(a)** A pictorial description of different noise contributions. The shot noise of light has a white spectrum and is represented by the flat dotted line. The narrow band contribution is divided in to three terms, the back action noise, the projection noise, and the technical noise (see text for more details). The back action contribution (shaded with gray scale) can be considered as the "memory part" of the atoms. **(b)** An example of a measured spectrum. The solid line is obtained with the input light in a vacuum state ($\epsilon_y = \epsilon_z = 1$). When the input mode is in a squeezed state (dashed line) the Lorentzian part from atoms increases while the wings decrease. The peak on the right is technical noise. In the experiment $\Omega = 325$kHz.

can scale in different ways, but an important fact is that external sources will be common to all atoms in the sample. As a consequence the TNA will scale as J_x^2.

The different kinds of noise are illustrated in Fig. 8.2(a). On top of the flat shot noise level (SNL) are the narrow band contributions PNA, BANA, and TNA. These three contributions add up to one joint Lorentzian structure, in Fig. 8.2(b) we show two experimental spectra of this kind. The solid line is taken with coherent state probe ($\epsilon_y = \epsilon_z = 1$). The dashed line differs from the solid line solely by a changed quantum state of the input light, we have squeezed $\hat{S}_y$ such that $\epsilon_y < 1$ and $\epsilon_z > 1$. We note the reduction in the base line according to the first term in Eq. (8.12), and we see that the Lorentzian peak has become larger caused by the extra noise in the anti-squeezed component $\hat{S}_z$, see Eq. (8.13) for BANA. We wish to single out the individual contributions PNA, BANA, and TNA from experimental measurements. To this end we may fit the narrow structures of Fig. 8.2(b) by a Lorentzian shaped function obtaining the total narrow band noise area. In the case of coherent probe (solid line in Fig. 8.2(b)) we denote the area A_{COH} and in the case of a squeezed probe (dashed line in Fig. 8.2(b)) we get the area A_{SQ}. We must have

$$A_{\mathrm{COH}} \equiv \mathrm{BANA}_1 + \mathrm{PNA} + \mathrm{TNA}, \qquad A_{\mathrm{SQ}} \equiv \mathrm{BANA}_1 \cdot \epsilon_z + \mathrm{PNA} + \mathrm{TNA}, \quad (8.15)$$

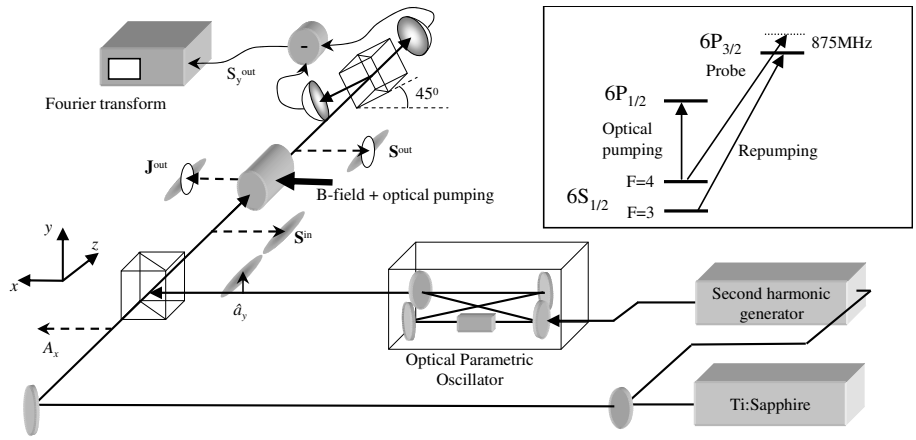

Figure 8.3: The experimental setup. A Ti:sapphire laser is frequency doubled in a second harmonic generator and down-converted in an optical parametric oscillator to give the quantum field $\hat{a}_y$. This field is mixed with a strong field A_x derived from the same Ti-sapphire laser to obtain non-classical polarization states of $\hat{S}_y$ and $\hat{S}_z$, see Eq. (A.14). This light is sent through an atomic cesium ensemble. The light polarization and the atomic spin state exchange quantum fluctuations, and the resulting laser beam is measured at a polarization state analyzer. The different lasers used in the experiment are depicted in the inset.

and we can solve this to obtain the experimental values

$$\mathrm{BANA}_1 = \frac{A_{\mathrm{SQ}} - A_{\mathrm{COH}}}{\epsilon_z - 1}, \qquad \mathrm{PNA} + \mathrm{TNA} = \frac{\epsilon_z A_{\mathrm{COH}} - A_{\mathrm{SQ}}}{\epsilon_z - 1}. \tag{8.16}$$

The shot noise level (SNL) and the squeezing parameters ϵ_y, ϵ_z are easy to access by measuring noise of light without atoms. The PNA can be estimated from Eq. (8.14) and we have thus separated all different noise contributions.

8.2 Experimental Setup

The experimental setup for the study of quantum fluctuation exchange between atoms and light is shown in Fig. 8.3. The light incident on atoms described by quantum variables $\hat{S}_y^{\mathrm{in}}$ and $\hat{S}_z^{\mathrm{in}}$ is engineered by overlapping a strong x-polarized beam of light with amplitude $\hat{a}_x(t) \approx A_x$ and a quantum field linearly polarized along the y-axis with amplitude $\hat{a}_y(t)$ on a polarizing beam splitter. The latter is generated by frequency doubling a ti:sapphire laser and subsequent down-conversion in an optical parametric oscillator (OPO) below threshold. This process is not a part of my thesis work, we refer to [37, 60] for details. The important fact is that the OPO generates squeezed vacuum which is characterized by noise

reduction (below the standard quantum limit of classical light) in either of the quadrature amplitudes $\hat{x}(t) = (\hat{a}_y(t) + \hat{a}_y^\dagger(t))/\sqrt{2}$ or $\hat{p}(t) = (\hat{a}_y(t) - \hat{a}_y^\dagger(t))/i\sqrt{2}$ while the other gets more noisy. This corresponds exactly to the case introduced in Chap. 2 around Eqs. (2.10) and (2.11), we stress that the quantum fluctuations of the polarization state of light is entirely given by the quantum state of the y-polarized mode emerging from the OPO.

The ti:sapphire laser is blue detuned by $\Delta = -875$MHz from the D2 line and the strong x-polarized beam has power up to 5mW limited by saturation of our S_y detectors. The noise level in the squeezed vacuum is -4.5dB in the quiet quadrature and 8.0dB in the noisy quadrature both relative to the classical noise level. However due to propagation losses, non perfect detection, finite beam overlap and weakly birefringent optics after the PBS only about -3.0dB squeezing and 7.0dB excess noise is left at the detection. For squeezing of $\hat{S}_y$ this corresponds to $\epsilon_y = 0.5$ and $\epsilon_z = 5.0$. The bandwidth of squeezing is 8.0MHz HWHM and consequently we can consider our polarization squeezed probe broadband relative to the atomic spin noise resonance which has a width of no more than 1kHz FWHM (this was assumed in App. E leading to the theoretical Eqs. (8.10)).

The laser beam now passes through the atomic cesium sample which has macroscopic angular momentum J_x created by the repump and optical pump lasers, see Sec. 4.1. Both lasers are circularly polarized with the same helicity. By adjusting the relative power of the lasers we are able to control the number of atoms in the $F = 4$ ground state. The decay rate Γ is almost only set by the optical pumping laser which is resonant with atoms in $F = 4$. The degree of spin polarization (better than 95%) and the number of atoms is measured by the magneto-optical resonance method described in Chap. 7.

The output Stokes parameter $\hat{S}_y$ is measured by a polarizing beam splitter. The power spectrum of the photo current $i(t)$ is recorded in a frequency window varying from 1.6kHz to 3.2kHz around Ω. The resulting spectrum is a narrow Lorentzian centered at $\Omega = 325$kHz with a width Γ in the range of 100Hz to 1kHz FWHM.

8.3 Experimental Investigation of the Model

Now, let us investigate our theoretical model in detail. First of all, the shape of the experimental traces in Fig. 8.2(b) resembles the theoretical prediction (8.12), there is a Lorentzian structure on top of a flat noise level. The flat back ground level is observed to rise or fall with respect to the shot noise level when $\hat{S}_y$ is anti-squeezed or squeezed, respectively. We also observe an increase of the Lorentzian peak when $\hat{S}_y$ is squeezed and $\hat{S}_z$ is anti-squeezed, see Fig. 8.2(b). The opposite example with squeezed $\hat{S}_z$ has only led to a very marginal decrease of the Lorentzian peak size. First of all, the effect is ten times less pronounced ($\epsilon_z = 0.5$ instead of $\epsilon_z = 5.0$). Just as important is technical difficulties with phase locking the strong x-polarized beam and the y-polarized quantum field

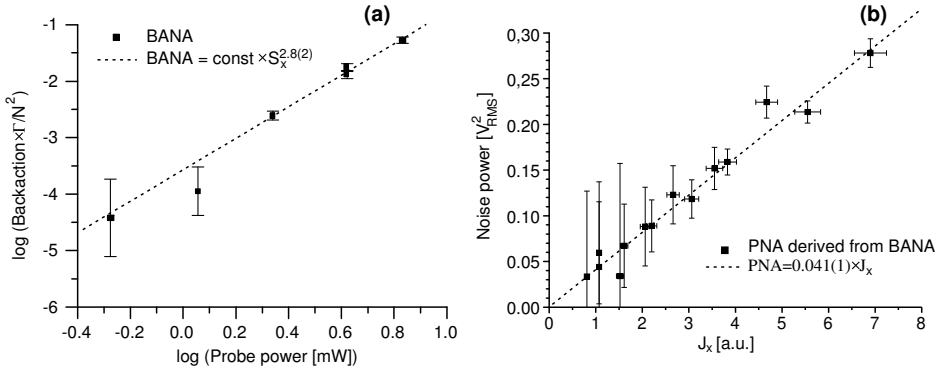

Figure 8.4: The back action noise area BANA as a function of probe power on log-log scale **(a)**. The probe power is proportional to S_x. Varying the probe power will cause slight changes to the number of atoms N and the line width Γ. This is taken care of by plotting BANA$\cdot\Gamma/N^2$ on the ordinate axis. We see the data is consistent with BANA$\propto S_x^3$. **(b)** The projection noise area derived from (8.14). The data is, in fact, compiled from two series with different Γ's, giving strong quantitative support of the model.

in the case of $\hat{S}_y$-anti-squeezing. With the qualitative confirmation of the spectrum (8.12), we now turn to a more quantitative comparison between theoretical predictions (8.13, 8.14) with experimental results. First, we try to vary the probe power (i.e. to vary S_x). This will have a slight influence on the number of atoms, i.e. on J_x, and some influence on Γ due to power broadening. From (8.13) we expect BANA $\cdot\,\Gamma/N^2$ to be proportional to S_x^3. This is indeed confirmed experimentally, see Fig. 8.4(a). We also wish to confirm that BANA scales with J_x^2 and that the predicted projection noise area PNA scales linearly with J_x, given by Eqs. (8.13). Note, these two scaling relations are equivalent since we predict the PNA from the BANA and the shot noise level. The experimental results are shown in Fig. 8.4(b). We again confirm the predicted scaling, and in addition, the constant of proportionality is consistent for different values of Γ.

Finally, let us examine the BANA as a function of Γ. The line width Γ is controlled by increasing the power of the optical pump laser. Doing this only affects the macroscopic spin weakly, and we can directly examine the scaling. This is done in Fig. 8.5(a), where we clearly see the correct scaling with Γ^{-1}. We may also consider the noise not originating from the back action effect. This *residual noise area* (abbreviated RSN) given by the projection noise plus the technical noise (PNA + TNA, see Eq. (8.16)) is plotted together with the predicted PNA in Fig. 8.5(b). We see that the RSN decreases with increasing Γ and seems to approach the PNA. The physical interpretation is simple. The technical noise picked up from some unknown source can be reduced by increasing the power of the optical pump laser. This will exactly destroy the spin state created by technical noise and push the spin toward the coherent spin state. The coherent

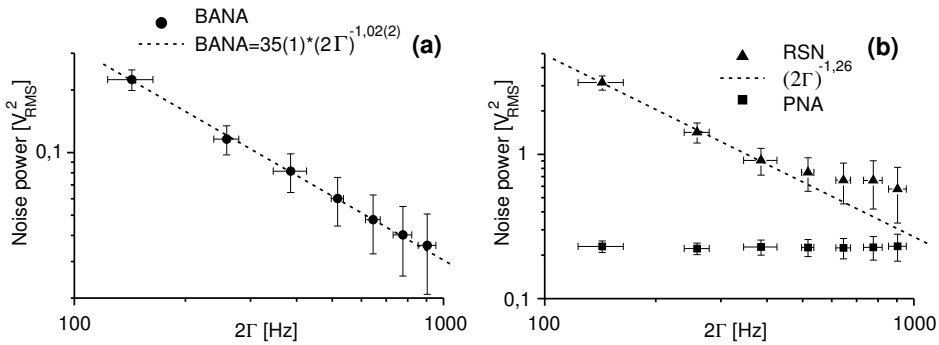

Figure 8.5: **(a)** The measured back action noise area (BANA) for the vacuum light input as a function of decay rate Γ on a log-log scale. **(b)** The measured residual spin noise (RSN) and the inferred projection noise area (PNA) calculated from (8.13).

spin state has an inherent quantum noise (the PNA) which can by no means be reduced. Thus we see in Fig. 8.5(b) that the PNA is independent on Γ, and that the residual noise will not decrease below the PNA.

In Fig. 8.5(a) we also see, that the back action noise BANA can indeed be reduced in the same way as technical noise. Back action noise is a pile up of quantum noise from the probe laser and the optical pump will clear up this again. The stronger the optical pump, the lesser piling up of back action noise (and technical noise).

A comment should be added to Fig. 8.5(b). Theoretically, the RSN should really converge to the PNA in the limit of large Γ if our understanding is correct. Experimentally, we could not go further than $\Gamma = 1$kHz, but even so one may still suspect that the RSN is converging to a slightly higher value. There could be several reasons for this, e.g. non-perfect orientation of the spin, higher order effects discussed in Sec. 6.4, effects of beam geometry, etc. We do not have experimental data suggesting which of these effects (if any) play an important role here so we will not dig further into that. But this does not change the overall impression of the results. There is a very good agreement between the theoretical predictions and the experimental data, and we have a good understanding of the various noise sources. All together the Faraday effect has been studied in detail and found to agree with the theory on the level of quantum fluctuations.

8.4 Broadband Atomic Noise

For completeness, in this section we will briefly discuss some broad band noise which has been observed in addition to the narrow band structure given by Eq. (8.12). Consider Fig. 8.6(a) which shows a noise spectrum similar to the one in Fig. 8.2(b). Here we see the recorded signal in presence of atoms and in the

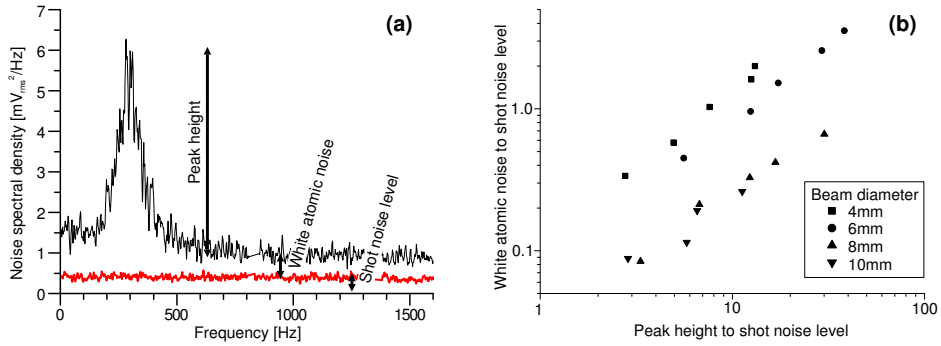

Figure 8.6: **(a)** An example of the recorded spectrum with atoms (upper trace) and without atoms (lower trace). We see that in the case with atoms we have some *white atomic noise* on top of the *shot noise level*. The frequency is relative to the demodulation frequency at 325kHz. **(b)** Plotted is the white atomic noise level as a function of the *peak height* of the narrow structure (see part (a) of the figure), note the log-log scale. The noise levels are normalized to shot noise. The probe power and beam size are varied in this experiment. See text for details.

absence of atoms. The important fact is that the flat background is higher than the shot noise level in presence of atoms, i.e. the atoms contribute some broad band noise which we denote *white atomic noise* (white since it seems to be quite broad band).

In Fig. 8.6(b) this white atomic noise is plotted versus the *peak height* of the narrow band atomic noise (both normalized to the shot noise level) where we for different beam sizes vary the probe power. The beam size is controlled by clipping a large beam with an iris. The fact that Fig. 8.6(b) reveals a linear dependence (slope close to unity on log-log scale) just tells that when the narrow atomic noise increases the white noise part increases in the same way, the increase is here caused by variations in the probe power. We have not extensively studied the white noise dependence on various parameters but we do have indications that it scales linearly with number of atoms and quadratically with the probe power. What is also clearly seen from the figure is the fact that the white noise seems to contribute more for a smaller beam size. The reason for plotting the white noise as a function of the peak height (a property of the narrow noise) is that we exclude the growth of the white noise to be caused by a simple overall growth in noise. We explicitly see that the fraction of white noise increases with decreasing probe diameter.

To understand the white atomic noise we need to carry out more experiments, it could be interesting to know the bandwidth of this noise but bandwidth limitations of detectors and electronics exclude us from doing this in an easy fashion. But we certainly have sufficient information to start speculating on the reason for the white noise. One should remember that broad band noise corresponds

to fast decoherence times, if the white noise contribution is relatively large there are relatively many atoms which live for a very short time or which are only measured for a very short time. Since the white noise contribution is largest for small beam sizes we propose that it is caused by atoms which have spent little time inside the volume illuminated by probe light. If an atom traverses a beam of 5mm diameter with a typical speed of 137m/s (see Sec. 4.2) the time duration will be of order 37μs corresponding to a typical frequency bandwidth of order 27kHz which is broad band with our typical frequency scales. The narrow peak would then be caused by atoms which have had several opportunities to enter and leave the region illuminated by the probe laser. We stress that this explanation would gain more confidence with more experiments. In the experiments reported in previous sections a Gaussian beam with waist 5.1mm was used. The white atomic noise was observable but all results were concentrating solely on the narrow part of the atomic noise.

8.5 Discussion of the Results

Let us summarize and discuss the results of this chapter. We started out in Sec. 8.1 with the basic equations of interaction (6.11-6.14) and developed a model to describe the particular experimental setup of a polarized laser beam interacting with a sample of polarized spins. The theoretical predictions were demonstrated experimentally and we conclude that we understand the light/matter interaction in detail, this includes the exchange of quantum fluctuations between light and matter.

The fact that the y-polarized mode could be illuminated with squeezed vacuum demonstrated the sensitivity of the spin state to a quantum field of light. The atoms responded to this light in a way which was not much weaker than e.g. uninteresting technical noise sources, the clear difference between the two Lorentzians in Fig. 8.2(b) is solely due to the quantum statistics of the y-polarized mode emerging from the squeezing source (the OPO). In fact, for our specific values of the gain of the OPO the y-polarized field contains about one photon per second per Hz of the bandwidth [60]. The atoms measured in Fig. 8.2(b) are only sensitive to frequency components of light in a width $\Gamma = 200$Hz. Thus the difference between the solid an dashed line in this case is the absence/presence of about 200 photons/sec. The atoms have a characteristic memory time of the order Γ^{-1} which means that on the time scale of the spin life time the atoms have been influenced by roughly one photon. This definitely underlines the quantum sensitivity of the interaction. We note that the measuring and averaging time necessary to create the two Lorentzians in Fig. 8.2(b) is much more than one spin life time but the difference of atomic state is the presence of a single photon per spin decoherence time.

If we direct the discussion toward the outlook for a future implementation of quantum memory we need to understand what interesting properties of the quantum field can be stored. First of all, for a real quantum memory we need to

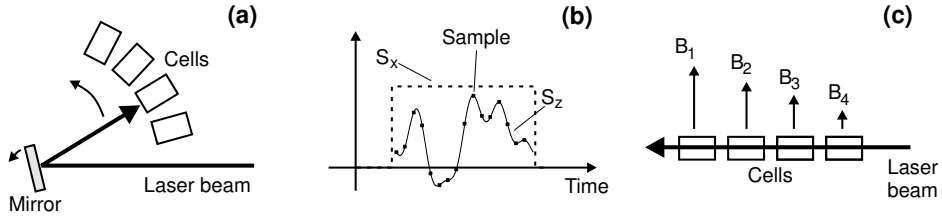

Figure 8.7: **(a)** A possible scenario for storing details about a light pulse. A rotating mirror will direct a laser beam to different storage cells thereby recording different time bins of the pulse. This is further illustrated in **(b)**, the interaction is on when S_x is high (symbolized by the dashed line). The evolution of $\hat{S}_z$ is then sampled at different times. **(c)** The same in Fourier space, different frequency components are recorded in each cell since the magnetic field varies.

store the properties of non-commuting variables. For instance, for a pulse of light with polarization state described by the variables $\hat{S}_y$ and $\hat{S}_z$ it is desirable to map $\hat{S}_y \to \hat{J}_y$ and $\hat{S}_z \to \hat{J}_z$. This is not what we demonstrate in the present chapter. We show how the $\hat{S}_z$-component of light piles up in the atomic spin state. Starting out with the light field in a squeezed state should lead to atomic spins ending up in a squeezed state in order to call the exchange of quantum fluctuations a complete quantum map. A protocol for performing the full quantum map will be discussed in Chap. 11.

In addition to the above discussion we also note, that the atoms are only sensitive to fluctuations around the Larmor frequency Ω in the bandwidth Γ. For storage of the state of light in atoms it is desirable to have a long memory time and accordingly a small Γ. Hence we can only store a single frequency component of a light pulse in a single atomic sample, or in other words, if the Larmor frequency is zero we only store the average value of $\hat{S}_z$ over the light pulse. To store more detailed time dynamics of a light pulse we could imagine a setup as depicted in Fig. 8.7(a). Chopping a long pulse into smaller pieces and storing each piece in a separate atomic sample accomplishes some time resolution. In a classical picture as in Fig. 8.7(b) this corresponds to sampling the value of $\hat{S}_z$ at different times. But this must be equivalent to sampling different frequency components of light, we could choose to shine the light through several atomic samples each with its own Larmor frequency as depicted in Fig. 8.7(c). This would be sampling in frequency space. If atoms were stationary a magnetic field gradient would accomplish the same. A possible implementation for this could also be a inhomogeneously broadened rare-earth doped solid [33].

In short, the experiments described in this chapter is a first step in the direction of implementation of a real quantum memory. In Chap. 11 we describe the remaining steps to reach this goal.

CHAPTER 9

Entanglement, Theoretical Approach

This chapter is devoted to theoretical questions and definitions in connection to entanglement generation between samples of cesium gases. We consider two systems 1 and 2 as shown in Fig. 9.1 where two macroscopic spins are oriented oppositely along the x-direction with $\left\langle \hat{J}_{x1} \right\rangle = J_x = -\left\langle \hat{J}_{x2} \right\rangle$. This setting opens up the possibility to generate an entangled state similar to the EPR-example in [61] as we will see in the following sections. The trick is to perform a suitable measurement which will "collapse" the state of the atomic spins into an entangled state, see [62]. This is a different approach than other experimental demonstrations of entanglement between massive particles [40, 41].

In this chapter we define what we mean by entanglement and we describe how to understand the process of entanglement generation by a measurement. The latter follows quite naive models which are motivated by the fact that the polarization state of light and the atomic spin state can be described collectively in the $\hat{X}, \hat{P}$-representation as we discussed in Chap. 2. We also discuss general experimental aspects like the rotating frame, losses for light propagation, non-perfect detectors, and methods for proving the generation of entangled states. Actual detailed description of experiments and data analysis is given in Chap. 10.

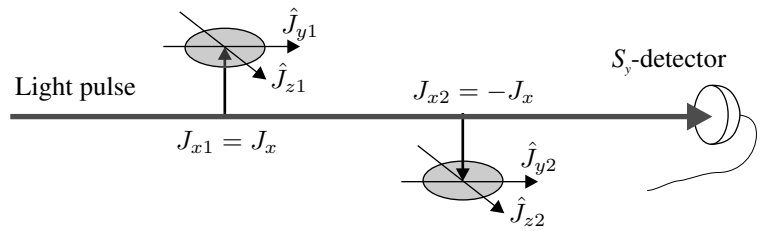

Figure 9.1: The schematic setup of two spin states for entanglement generation. Two spins are prepared in coherent spin states with opposite directions and the same magnitude J_x. This setup opens up the possibility to perform joint quantum non-demolition (QND) measurements on the two states [62].

9.1 Definition of Entanglement

Let us characterize entangled states between samples of macroscopic ensembles of cesium gases that we use in our experiments. To this end let us start with the usual definition of entanglement. We consider two systems 1 and 2 which are described by a joint wave function ψ. If this wave function cannot be written as a product $\psi = \psi_1(x_1) \cdot \psi_2(x_2)$ where $\psi_{1,2}$ are wave functions of the individual systems 1 and 2 depending on parameters $x_{1,2}$ of two systems, then the state of the two systems is entangled. A well known entangled state is the singlet state of two spin-1/2 particles $|\psi\rangle = \frac{1}{\sqrt{2}}(|\uparrow\downarrow\rangle - |\downarrow\uparrow\rangle)$. It is easy to see that this state cannot be expressed as a product wave function.

Now, the above is a pure state definition, for mixed states described by density operators there is a similar definition. Consider again two systems 1 and 2 and let the joint density operator be given by ρ. If ρ_{i1} and ρ_{i2} are sets of density operators describing the individual systems 1 and 2, and if ρ cannot be decomposed into a sum of products of these, i.e.

$$\rho \neq \sum_i p_i \rho_{1i} \otimes \rho_{2i} \quad \Leftrightarrow \quad \text{State is entangled,} \tag{9.1}$$

where the p_i's are positive, then the system is in an entangled state. The above definitions are intuitive, they tell that individual stories ψ_1 and ψ_2 or for mixed states ρ_{1i} and ρ_{2i} are not enough to characterize the entire system described by ψ or ρ, something extra is needed. But while being intuitive the definitions are not necessarily easy to apply for an experimentalist in the laboratory. However, from this definition Refs. [63, 64] have derived the following result:

For two continuous variable systems 1 and 2 a sufficient condition for having entanglement is satisfaction of the inequality

$$\mathrm{Var}\left(\hat{X}_1 + \hat{X}_2\right) + \mathrm{Var}\left(\hat{P}_1 - \hat{P}_2\right) < 2, \tag{9.2}$$

where $\hat{X}_1$, $\hat{P}_1$ and $\hat{X}_2$, $\hat{P}_2$, are continuous variables describing the two sub-systems

satisfying the commutation relations $\left[\hat{X}_j, \hat{P}_j\right] = i$ for $j = 1, 2$. If we consider Gaussian states this is also a necessary condition. This entanglement criterion is easy to apply for an experimentalist, variances of measured variables are easily estimated by statistical means.

Now, in Chap. 2 we described how our spin systems could be regarded as continuous variables described by operators $\hat{X}$ and $\hat{P}$. For our system of oppositely oriented spins the above inequality turns into

$$\mathrm{Var}\left(\hat{J}_{y1} + \hat{J}_{y2}\right) + \mathrm{Var}\left(\hat{J}_{z1} + \hat{J}_{z2}\right) < 2J_x \quad \Leftrightarrow \quad \text{State is entangled.} \tag{9.3}$$

This entanglement criterion is intuitive. If we assume the two systems to be independent of each other, how low can the left hand side of the inequality then be? The answer lies in Eq. (2.5). For minimum uncertain states (coherent spin states) we have $\mathrm{Var}(\hat{J}_{y1}) = \mathrm{Var}(\hat{J}_{y2}) = \mathrm{Var}(\hat{J}_{z1}) = \mathrm{Var}(\hat{J}_{z2}) = J_x/2$. For independent states we have $\mathrm{Var}(\hat{J}_{y1} + \hat{J}_{y2}) = \mathrm{Var}(\hat{J}_{y1}) + \mathrm{Var}(\hat{J}_{y2})$ and similar for the z-components. Taking all this together we see that equality of the above criterion is the best we can obtain classically.

We should also here make a reference to [65] which raises some intriguing questions about the validity of the use of Eq. (9.2) for spin systems. However, it is agreed that the criterion (9.3) is valid.

9.2 Entanglement Generation

Let us now discuss the methods we apply in order to generate entanglement. First of all, consider the commutator

$$\left\langle \left[\hat{J}_{y1} + \hat{J}_{y2}, \hat{J}_{z1} + \hat{J}_{z2}\right] \right\rangle = i \left\langle \hat{J}_{x1} + \hat{J}_{x2} \right\rangle = i(J_x - J_x) = 0. \tag{9.4}$$

The fact that this commutator has zero mean for two oppositely oriented spins ensures the existence of entangled states, the variances $\mathrm{Var}(\hat{J}_{y1} + \hat{J}_{y2})$ and $\mathrm{Var}(\hat{J}_{z1} + \hat{J}_{z2})$ can simultaneously be arbitrarily small and break the inequality of the entanglement criterion (9.3).

We will generate the entangled state by a quantum non-demolition (QND) measurement of the two operators $\hat{J}_{y1} + \hat{J}_{y2}$ and $\hat{J}_{z1} + \hat{J}_{z2}$ as discussed in [62]. To describe this process we will for simplicity start out with two oppositely oriented spins $\mathbf{J}_1$ and $\mathbf{J}_2$ in *zero* magnetic field, we comment on the rotating frame with a non-zero magnetic field below. Placing the spins as depicted in Fig. 9.1 and applying a probe laser beam through both samples, the equations of interaction

(6.11-6.14) will turn into

$$\hat{S}_y^{\text{out}}(t) = \hat{S}_y^{\text{in}}(t) + aS_x(\hat{J}_{z1}(t) + \hat{J}_{z2}(t)), \tag{9.5}$$

$$\hat{S}_z^{\text{out}}(t) = \hat{S}_z^{\text{in}}(t), \tag{9.6}$$

$$\frac{\partial \hat{J}_{y1}(t) + \partial \hat{J}_{y2}(t)}{\partial t} = aJ_{x1}\hat{S}_z^{\text{in}}(t) + aJ_{x2}\hat{S}_z^{\text{in}}(t) = 0, \tag{9.7}$$

$$\frac{\partial \hat{J}_{z1}(t) + \hat{J}_{z2}(t)}{\partial t} = 0, \tag{9.8}$$

where the Stokes operators here are normalized to photons per second. We see that a measurement of $\hat{S}_y^{\text{out}}$ will provide information about $\hat{J}_{z1} + \hat{J}_{z2}$, and if the second term of Eq. (9.5) is large compared to the first one we will make effective measurements of the spins. At the same time, the vanishing time derivatives (9.7) and (9.8) ensures the measurement to be non-destructive. For the time derivative of $\hat{J}_{y1} + \hat{J}_{y2}$ to be zero, it is important that the spins are opposite with same magnitude J_x and the absence of light losses between the samples is also required here. If losses are present the $\hat{S}_z$-component seen by the two spin samples will be different, see Sec. 9.6.

We will let the probe laser be on for a time duration T while measuring the $\hat{S}_y$-component of the light. We measure the photo current $i(t)$ and for the rest of this chapter we assume that it is (in appropriate units) equal to $\hat{S}_y^{\text{out}}$. This corresponds to a perfect detector efficiency, see detection theory in App. E and Eq. (E.1). We will write $i(t) \doteq \hat{S}_y^{\text{out}}$ where the dot symbolizes that a measurement is performed. Defining the integrated value of the outcome as $A = \int_0^T i(t)dt$, we find that A is a the outcome of a measurement of the operator

$$A \doteq \int_0^T \hat{S}_y^{\text{out}}(t)dt = \int_0^T \hat{S}_y^{\text{in}}(t)dt + aS_xT(\hat{J}_{z1}(0) + \hat{J}_{z2}(0)). \tag{9.9}$$

After this process we may apply another laser beam along the y-direction, or alternatively rotate the two spins by 90 degrees with help from a magnetic field and apply the same laser once again. Then a non-destructive measurement of $\hat{J}_{y1} + \hat{J}_{y2}$ is performed and the z-components are unaffected.

Now, we will quantify the magnitude of the second term versus first term in Eq. (9.9). If we calculate the variance we obtain

$$\begin{aligned}
\text{Var}\left(\int_0^T \hat{S}_y^{\text{out}}(t)dt\right) &= \int_0^T \int_0^T \left\langle \hat{S}_y^{\text{in}}(t)\hat{S}_y^{\text{in}}(t')\right\rangle dtdt' \\
&\quad + a^2(S_xT)^2\text{Var}\left(\hat{J}_{z1}(0) + \hat{J}_{z2}(0)\right) \\
&= \frac{S_xT}{2} + a^2(S_xT)^2J_x = \frac{S_xT}{2}\left(1 + 2a^2S_xTJ_x\right) \\
&\equiv \frac{S_xT}{2}\left(1 + 2\kappa^2\right),
\end{aligned} \tag{9.10}$$

where we used the fact that $\left\langle \hat{S}_y^{\rm in}(t)\hat{S}_y^{\rm in}(t')\right\rangle = S_x/2\cdot\delta(t-t')$, see Eq. (E.10). We defined $\kappa^2 = a^2 S_x T J_x$ as a figure of merit for the spin contribution compared to the light noise contribution. Above we assumed the spins to be prepared in the coherent spin state with variances equal to $J_x/2$, see Eq. (2.5). For efficient entanglement generation we need to have κ^2 large compared to unity. We see that we gain by increasing the magnitude of the spins J_x, by increasing the total photon number $n_{\rm ph} = S_x T/2$, or by adjusting the interaction parameter a given by Eq. (6.15).

It is here appropriate to connect the concept of entanglement between spin states to the concept of spin squeezing. If we in the above considerations only had one spin sample (sample 1 for instance) the measurement of $\hat{S}_y^{\rm out}$ for a laser beam propagating along the z-direction would obtain information about $\hat{J}_{z1}$, and the variance of $\int_0^T \hat{S}_y^{\rm out}(t)dt$ would have been $S_x T/2\cdot(1+\kappa^2)$. At the same time the effect of the probe laser on the $\hat{J}_{y1}$-component would be governed by $\partial\hat{J}_{y1}(t)/\partial t = aJ_x\hat{S}_z^{\rm in}(t)$ which leads to

$$\begin{aligned}
\hat{J}_{y1}(T) &= \hat{J}_{y1}(0) + aJ_x\int_0^T \hat{S}_z^{\rm in}(t)dt \quad \Rightarrow \\
{\rm Var}\left(\hat{J}_{y1}(T)\right) &= {\rm Var}\left(\hat{J}_{y1}(0)\right) + a^2J_x^2\int_0^T dt\int_0^T dt'\left\langle Sz^{\rm in}(t)\hat{S}_z^{\rm in}(t')\right\rangle \\
&= \frac{J_x}{2} + \frac{a^2J_x^2S_xT}{2} = \frac{J_x}{2}(1+\kappa^2),
\end{aligned} \tag{9.11}$$

where the initial spin state is assumed to be the coherent spin state with variance $J_x/2$. We see that when we for higher κ^2 obtain better information about the $\hat{J}_{z1}$-component of the spin we pile up more noise in the $\hat{J}_{y1}$-component which is required in order not to violate Heisenberg's uncertainty principle (2.3). This uncertainty relation is a consequence of the non-commuting property $\left[\hat{J}_{y1},\hat{J}_{z1}\right] = iJ_x$. Now, for our two samples we have commutators

$$\left[\hat{J}_{y1}+\hat{J}_{y2},\hat{J}_{z1}-\hat{J}_{z2}\right] = 2iJ_x \quad \text{and} \quad \left[\hat{J}_{z1}+\hat{J}_{z2},\hat{J}_{y1}-\hat{J}_{y2}\right] = 2iJ_x, \tag{9.12}$$

while all the other combinations vanish, i.e.

$$\begin{aligned}
\left[\hat{J}_{y1}+\hat{J}_{y2},\hat{J}_{y1}-\hat{J}_{y2}\right] &= \left[\hat{J}_{z1}+\hat{J}_{z2},\hat{J}_{z1}-\hat{J}_{z2}\right] = \\
\left[\hat{J}_{y1}+\hat{J}_{y2},\hat{J}_{z1}+\hat{J}_{z2}\right] &= \left[\hat{J}_{y1}-\hat{J}_{y2},\hat{J}_{z1}-\hat{J}_{z2}\right] = 0.
\end{aligned} \tag{9.13}$$

This motivates the interpretation of entanglement to be squeezing of two independent modes $\hat{J}_{y1}+\hat{J}_{y2}$ and $\hat{J}_{z1}+\hat{J}_{z2}$ at the expense of anti-squeezing the conjugate variables $\hat{J}_{z1}-\hat{J}_{z2}$ and $\hat{J}_{y1}-\hat{J}_{y2}$, respectively (such representation has been discussed in [66]). We have the two corresponding Heisenberg uncertainty

relations

$$\begin{aligned} \mathrm{Var}\left(\hat{J}_{y1}+\hat{J}_{y2}\right)\mathrm{Var}\left(\hat{J}_{z1}-\hat{J}_{z2}\right) &\geq J_x^2 \quad \text{and} \\ \mathrm{Var}\left(\hat{J}_{z1}+\hat{J}_{z2}\right)\mathrm{Var}\left(\hat{J}_{y1}-\hat{J}_{y2}\right) &\geq J_x^2. \end{aligned} \tag{9.14}$$

In the case of two spin samples a calculation similar to Eq. (9.11) will show how much noise is piled up in the anti-squeezed variables $\hat{J}_{y1}-\hat{J}_{y2}$ and $\hat{J}_{z1}-\hat{J}_{z2}$,

$$\mathrm{Var}\left(\hat{J}_{y1}(T)-\hat{J}_{y2}(T)\right)=\mathrm{Var}\left(\hat{J}_{z1}(T)-\hat{J}_{z2}(T)\right)=J_x(1+2\kappa^2). \tag{9.15}$$

All equations in this section are coherent evolution of the spin states. But we also perform measurements which change the spin states in a non-coherent way and hopefully create the entangled states. In next section we try to model this measurement and the corresponding spin state evolution. The above considerations will play an important role in the understanding of the results.

9.3 Wave Function Modeling

The fact that the collective properties of light and atoms can be described by position and momentum like operators (see Chap. 2) motivates a simple model where the entire spin state is described by a wave function $\psi(x)$ like it is well known for a single particle in elementary quantum mechanics. For simplicity we will in the following describe a single spin ensemble and the effect of a measurement as we already discussed around Eq. (9.11). As in Eqs. (2.10) and (2.4) we define

$$\hat{X}_{\mathrm{L}}=\frac{\int_0^T \hat{S}_y(t)dt}{\sqrt{S_xT}} \quad \text{and} \quad \hat{P}_{\mathrm{L}}=\frac{\int_0^T \hat{S}_z(t)dt}{\sqrt{S_xT}} \tag{9.16}$$

for light pulses (indexed by L) of duration T and for the atomic spin state (indexed by A) we define

$$\hat{X}_{\mathrm{A}}=\frac{\hat{J}_y}{\sqrt{J_x}} \quad \text{and} \quad \hat{P}_{\mathrm{A}}=\frac{\hat{J}_z}{\sqrt{J_x}}. \tag{9.17}$$

These definitions fulfil $\left[\hat{X},\hat{P}\right]=i$. We now assume the state of light and atoms to be described by a Gaussian wave function on the form

$$\psi(x)=N\exp\left(-\frac{(x-x_0)^2}{4\sigma_x^2}+ip_0x\right), \tag{9.18}$$

where N is a suitable normalization constant. A Gaussian distribution is motivated by the fact that our physical system is composed of a huge number of particles each having their own statistical properties. The central limit theorem ensures that the collective properties will be Gaussian if the individual particles are not too far from being independent of each other. The above state fulfils

$\left\langle \hat{X} \right\rangle = x_0$, $\left\langle \hat{P} \right\rangle = p_0$, $\mathrm{Var}(\hat{X}) = \sigma_x^2$, and $\mathrm{Var}(\hat{P}) = \sigma_p^2 = 1/(4\sigma_x^2)$. We always have $\mathrm{Var}(\hat{X})\mathrm{Var}(\hat{P}) = 1/4$, i.e. we are in the minimum uncertainty state. For the coherent state of light or atoms we have $\sigma_x^2 = \sigma_p^2 = 1/2$. The operators are described by the usual substitution $\hat{X} \to x$ and $\hat{P} \to -i\partial/\partial x$. We may change from x to p representation by a Fourier transform

$$\begin{aligned} \psi(x) &= \frac{1}{\sqrt{2\pi}} \int e^{ipx} \psi(p) dp, \\ \psi(p) &= \frac{1}{\sqrt{2\pi}} \int e^{-ipx} \psi(x) dp, \end{aligned} \tag{9.19}$$

which for Eq. (9.18) would turn into

$$\psi(p) = N \exp\left(-\frac{(p-p_0)^2}{4\sigma_p^2} - ix_0 p \right). \tag{9.20}$$

Now, prepare the atomic sample to be in the coherent spin state described by $\psi(p_\mathrm{A}) = N\exp(-p_\mathrm{A}^2/2)$ and the light also in the coherent state described by $\psi(p_\mathrm{L}) = N\exp(-p_\mathrm{L}^2/2)$. Now, when light and atoms interact, the evolution is governed by the Hamiltonian (this is essentially Eq. (5.18) with neglected higher order terms)

$$\begin{aligned} \hat{H} = \hbar a \hat{S}_z(t) \hat{J}_z(t) \quad &\Rightarrow \\ \exp\left(-\frac{i}{\hbar} \int_0^T \hat{H} dt \right) &= \exp\left(-ia \int_0^T \hat{S}_z(t) \hat{J}_z(t) dt \right) \\ = \exp\left(-ia\sqrt{S_x T J_x} \hat{P}_\mathrm{L} \hat{P}_\mathrm{A} \right) &= \exp\left(-i\kappa \hat{P}_\mathrm{L} \hat{P}_\mathrm{A} \right), \end{aligned} \tag{9.21}$$

where we used the fact that $\hat{J}_z(t)$ is constant and κ is as defined in the previous section. With the joint state of atoms and light given by $\psi(p_\mathrm{L}, p_\mathrm{A}) = \exp(-[p_\mathrm{L}^2 + p_\mathrm{A}^2]/2)$ we calculate the evolution to be

$$\psi(p_\mathrm{L}, p_\mathrm{A}) \to \exp\left(-i \int_0^T \hat{H} dt \right) \psi(p_\mathrm{L}, p_\mathrm{A}) = N \exp\left(-\frac{[p_\mathrm{L}^2 + p_\mathrm{A}^2]}{2} - i\kappa p_\mathrm{L} p_\mathrm{A} \right). \tag{9.22}$$

If we Fourier transform this into the x-basis of light corresponding to $\hat{S}_y$ we obtain (compare Eqs. (9.18) and (9.20) to see this)

$$\psi(x_\mathrm{L}, p_\mathrm{A}) = N \exp\left(-\frac{[x_\mathrm{L} - \kappa p_\mathrm{A}]^2}{2} - \frac{p_\mathrm{A}^2}{2} \right). \tag{9.23}$$

So far we described coherent evolution of the state under the influence of the interaction Hamiltonian. Now we perform a measurement of $\hat{X}_L$ which we model by letting $x_\mathrm{L}^\mathrm{meas} \doteq \hat{X}_\mathrm{L}$, i.e. we assume the light part of the state to collapse to a

definite measured number. The remaining atomic state is then described by the above equation with the variable x_{L} replaced by the constant $x_{\mathrm{L}}^{\mathrm{meas}}$,

$$\psi(p_{\mathrm{A}}) \to N \exp\left(-\frac{[p_{\mathrm{A}} - \frac{\kappa}{1+\kappa^2} x_{\mathrm{L}}^{\mathrm{meas}}]^2}{4 \cdot \frac{1}{2(1+\kappa^2)}}\right). \tag{9.24}$$

This state reveals the statistics $\left\langle \hat{P}_{\mathrm{A}} \right\rangle = \frac{\kappa}{1+\kappa^2} x_{\mathrm{L}}^{\mathrm{meas}}$ and $\mathrm{Var}(\hat{P}_{\mathrm{A}}) = \frac{1}{2(1+\kappa^2)}$. We also have $\left\langle \hat{X}_{\mathrm{A}} \right\rangle = 0$ and $\mathrm{Var}(\hat{X}_{\mathrm{A}}) = \frac{1+\kappa^2}{2}$. Let us convert this back to the spin variables $\hat{J}_y$ and $\hat{J}_z$. We get

$$\mathrm{Var}\left(\hat{J}_y\right) = \frac{J_x}{2} \cdot (1+\kappa^2) \quad \text{and} \quad \mathrm{Var}\left(\hat{J}_z\right) = \frac{J_x}{2} \cdot \frac{1}{1+\kappa^2}. \tag{9.25}$$

For the $\hat{J}_y$-component we obtain exactly the variance given by Eq. (9.11). The back action noise from the light $\hat{S}_z$-component supplies the extra noise added to $\hat{J}_y$. The Heisenberg uncertainty then allows the variance of the $\hat{J}_z$-component to be reduced up to a factor $1+\kappa^2$. In our simple pure state model we stay in the minimum uncertainty state and obtain exactly the reduction of $\mathrm{Var}(\hat{J}_z)$ by the factor $(1+\kappa^2)$.

For the mean values of the spin components it is convenient to use the units of the detected signal, i.e. since we measure $\int i(t)dt \doteq \int \hat{S}_y^{\mathrm{out}}(t)dt = \int \hat{S}_y dt + aS_xT\hat{J}_z$ we multiply the spins by aS_xT and calculate

$$aS_xT\left\langle \hat{J}_y \right\rangle = 0 \quad \text{and} \quad aS_xT\left\langle \hat{J}_z \right\rangle = \frac{\kappa^2}{1+\kappa^2}\int_0^T i(t)dt. \tag{9.26}$$

We remember from the previous section that κ^2 is the ratio of atomic noise to light noise in a measurement with one spin sample. The correction factor $\kappa^2/(1+\kappa^2)$ is then intuitively understandable. This factor is the ratio of atomic noise to the total noise and it is the atomic portion that bears the spin state information. In the limit $\kappa^2 \to 0$ we obtain no information about the spin state, and there is no back action. Then the best bet for the mean value is the initial coherent spin state value of zero. On the other hand, if $\kappa^2 \gg 1$ the light noise is negligible and the correction factor should be unity.

Now, we may apply the above considerations to the case of two spin samples. If we measure $\hat{J}_{z1} + \hat{J}_{z2}$ by integrating the equation $\hat{S}_y^{\mathrm{out}}(t) = \hat{S}_y^{\mathrm{in}}(t) + aS_x(\hat{J}_{z1} + \hat{J}_{z2})$ we know from Eq. (9.10) that the ratio of atomic to light noise is $2\kappa^2$. Integrating the measured $\hat{S}_y^{\mathrm{out}}(t)$ we find that the mean value of the state after the measurement is

$$aS_x\left\langle \hat{J}_{z1} + \hat{J}_{z2} \right\rangle = \frac{2\kappa^2}{1+2\kappa^2}\int_0^T i(t)dt. \tag{9.27}$$

From Eq. (9.15) we remember that the pile up of noise in the conjugate variable $\hat{J}_{y1} - \hat{J}_{y2}$ is $J_x(1+2\kappa^2)$. With the preservation of the minimum uncertainty

relation in our simple model we find the variance of the created state to be

$$\mathrm{Var}\left(\hat{J}_{z1}+\hat{J}_{z2}\right)=\frac{J_x}{1+2\kappa^2} \tag{9.28}$$

which is the coherent spin state variance reduced by a factor $1+2\kappa^2$. The same considerations apply for the y-components of the spins. We have checked that the above results for two spin samples (in zero magnetic field) match the result of a wave function analysis with Gaussian wave packets.

Our models are quite simple and rely on the assumption that the collection of spins or photons can be described by a wave function depending on the *collective* variables. To get more insight into the microscopic picture of the measurement process we refer to [67] in the case of measurements on a single spin ensemble and to [68] for the opposite spin setup with entanglement generation.

9.4 Rotating Frame and Entanglement

As we already discussed in Sec. 4.3 we place the atomic samples in magnetic fields. The spin precession forces us to consider the above calculations in the rotating frame and we introduce the rotating frame coordinates $\hat{J}'_{y1}$, $\hat{J}'_{z1}$, $\hat{J}'_{y2}$, and $\hat{J}'_{z2}$ in analogy with Eq. (4.3). After a little algebra Eqs. (9.5-9.8) can be written

$$\begin{aligned}\hat{S}_y^{\mathrm{out}}(t)&=\hat{S}_y^{\mathrm{in}}(t)\\&\quad+aS_x\left(\cos(\Omega t)[\hat{J}'_{z1}(t)+\hat{J}'_{z2}(t)]+\sin(\Omega t)[\hat{J}'_{y1}(t)+\hat{J}'_{y2}(t)]\right),\end{aligned} \tag{9.29}$$

$$\hat{S}_z^{\mathrm{out}}(t)=\hat{S}_z^{\mathrm{in}}(t), \tag{9.30}$$

$$\frac{\partial[\hat{J}'_{y1}(t)+\hat{J}'_{y2}(t)]}{\partial t}=\frac{\partial[\hat{J}'_{z1}(t)+\hat{J}'_{z2}(t)]}{\partial t}=0. \tag{9.31}$$

We see that the rotating spin coordinates are constants of motion (regarding the coherent evolution) and that these can be measured simultaneously by measuring $\hat{S}_y^{\mathrm{out}}$. The sine and cosine components can be separated electronically from the measured photo current $i(t)$ if the time of measurement T fulfils $\Omega T\gg 1$. If we define

$$A=\int_0^T i(t)\sin(\Omega t)dt \quad\text{and}\quad B=\int_0^T i(t)\cos(\Omega t)dt, \tag{9.32}$$

we get for $\Omega T\gg 1$

$$\begin{aligned}A&\doteq\int_0^T\hat{S}_y^{\mathrm{in}}(t)\sin(\Omega t)dt+\frac{aS_xT}{2}\left[\hat{J}'_{y1}(0)+\hat{J}'_{y2}(0)\right],\\B&\doteq\int_0^T\hat{S}_y^{\mathrm{in}}(t)\cos(\Omega t)dt+\frac{aS_xT}{2}\left[\hat{J}'_{z1}(0)+\hat{J}'_{z2}(0)\right].\end{aligned} \tag{9.33}$$

These operators are measured by multiplying the photo current by $\cos(\Omega t)$ and $\sin(\Omega t)$ respectively and integrating over time T. The ratio of measured atomic noise to light noise can be evaluated and we find that A and B are outcomes of stochastic variables with variances

$$\mathrm{Var}\,(A) = \mathrm{Var}\,(B) = \frac{S_x T}{4}(1+\kappa^2), \tag{9.34}$$

where $\kappa^2 = a^2 S_x T J_x$ is as defined in previous sections and we assumed the spin state at $t = 0$ to be the coherent spin state. Compared to the previous section the atomic to light noise ratio is κ^2 and not $2\kappa^2$. The reason is the fact that during the time T we now spent time measuring both y- and z-components of the spins and not just a single component.

We may also consider the conjugate variables $\hat{J}'_{y1}(t) - \hat{J}'_{y2}(t)$ and $\hat{J}'_{z1}(t) - \hat{J}'_{z2}(t)$ as we did in previous section. The evolution of these can be shown to be

$$\frac{\partial[\hat{J}'_{y1}(t) - \hat{J}'_{y2}(t)]}{\partial t} = 2aJ_x\hat{S}_z^{\mathrm{in}}\cos(\Omega t), \tag{9.35}$$

$$\frac{\partial[\hat{J}'_{z1}(t) - \hat{J}'_{z2}(t)]}{\partial t} = -2aJ_x\hat{S}_z^{\mathrm{in}}\sin(\Omega t), \tag{9.36}$$

and we can integrate this from $t = 0$ to $t = T$ to evaluate the amount of noise piled up in these variables. The result turns out to be

$$\mathrm{Var}\left(\hat{J}'_{y1}(t) - \hat{J}'_{y2}(t)\right) = \mathrm{Var}\left(\hat{J}'_{z1}(t) - \hat{J}'_{z2}(t)\right) = J_x(1+\kappa^2). \tag{9.37}$$

Now we may compare the results of this section to the previous one and extrapolate the reasoning with minimum uncertainty states to the rotating frame. After having performed the measurement our best estimate for the mean values and variances are

$$\begin{aligned}
\frac{aS_xT}{2}\left\langle \hat{J}'_{y1}(T) + \hat{J}'_{y2}(T)\right\rangle &= \frac{\kappa^2}{1+\kappa^2}\int_0^T i(t)\sin(\Omega t)dt,\\
\frac{aS_xT}{2}\left\langle \hat{J}'_{z1}(T) + \hat{J}'_{z2}(T)\right\rangle &= \frac{\kappa^2}{1+\kappa^2}\int_0^T i(t)\cos(\Omega t)dt,\\
\mathrm{Var}\left(\hat{J}'_{y1}(T) + \hat{J}'_{y2}(T)\right) &= \mathrm{Var}\left(\hat{J}'_{y1}(T) + \hat{J}'_{y2}(T)\right) = \frac{J_x}{1+\kappa^2}.
\end{aligned} \tag{9.38}$$

Again, let us comment on the results. If $\kappa^2 \to \infty$ we simply have zero variance of $\hat{J}'_{y1} + \hat{J}'_{y2}$ and $\hat{J}'_{z1} + \hat{J}'_{z2}$ while $\int_0^T i(t)\sin(\Omega t)dt = aS_xT/2 \cdot [\hat{J}'_{y1} + \hat{J}'_{y2}]$ holds (and similarly for $\hat{J}'_{z1} + \hat{J}'_{z2}$). This is just a perfect measurement of the spin components and is consistent with the total neglect of the term $\hat{S}_y^{\mathrm{in}}(t)$ in Eq. (9.29). On the other hand, if $\kappa^2 \to 0$ the measurement is effectively non-existing and the spin state is unaltered. Hence we must have variances equal to the initial coherent state variance J_x and the mean value should be zero independent on the measured photo current $i(t)$, the latter is just light noise bearing no information about the spin state.

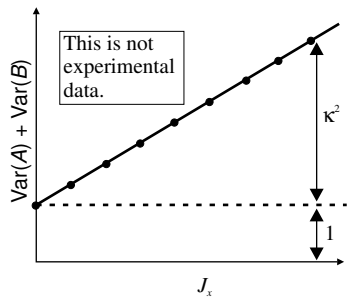

Figure 9.2: The theoretically expected noise in a measurement of transverse spin components $\hat{J}_{y1}+\hat{J}_{y2}$ and $\hat{J}_{z1}+\hat{J}_{z2}$ if the spins are prepared in oppositely oriented coherent spin states, see Eq. (9.39). There is a constant noise contribution from light (dashed line) and the atomic contribution will grow linearly with the spin magnitude J_x following the solid line.

9.5 Entanglement Estimation

As experimentalists we wish to create an entangled state between two cesium gas samples, in this section we describe some strategies for proving that an entangled state has been created. To this end we must keep in mind the entanglement criterion (9.3) and be able to use it. One of the most important tasks is to calibrate this inequality in the sense that we must know which values of the variances correspond to equality. To this end remember that if the two samples 1 and 2 are independent of each other then $\mathrm{Var}(\hat{J}_{y1}+\hat{J}_{y2}) = \mathrm{Var}(\hat{J}_{y1})+\mathrm{Var}(\hat{J}_{y2})$ and $\mathrm{Var}(\hat{J}_{z1}+\hat{J}_{z2}) = \mathrm{Var}(\hat{J}_{z1})+\mathrm{Var}(\hat{J}_{z2})$. Furthermore, for coherent spin states the spins will be in the minimum uncertainty state where these individual variances amount to $J_x/2$, see Eq. (2.5). We conclude that for two oppositely oriented coherent spin states we have the equality $\mathrm{Var}(\hat{J}_{y1}+\hat{J}_{y2})+\mathrm{Var}(\hat{J}_{z1}+\hat{J}_{z2}) = 2J_x$. If we for a given magnitude J_x can create coherent spin states and measure these variances we have calibrated the inequality.

Experimentally we will be in the rotating frame and we will create the coherent spin states by optical pumping processes, see Sec. 4.5. Then we will measure the values A and B as in Eq. (9.33) and we will do this several times. By statistical means we can then estimate the mean and variance of A and B and study the statistics as a function of the spin magnitude J_x.

For $J_x = 0$ we only see the light noise (and maybe some electronics noise from the detectors). It is easy to judge whether this light noise is limited by quantum noise (also called shot noise) by varying the photon number n_{ph} of the laser pulse, the noise variance should grow linearly with n_{ph}, see Eq. (2.12). We will very often normalize our units of noise to the shot noise of light since the light noise is easy to measure.

Now, we would start to increase J_x to non-zero values and measure the noise variances once again. If the additional atomic noise is limited by quantum pro-

jection noise, the atomic contribution should increase proportionally with J_x, see Eq. (2.5). This fact is also reflected by the equality of the criterion (9.3). In Fig. 9.2 we show what a plot of the measured variances $\mathrm{Var}(A) + \mathrm{Var}(B)$ versus J_x should look like in the case of the atomic noise being characterized by the quantum projection noise of the coherent spin states. The solid line would then be a fit to the measured points and serve as calibration for the entanglement criterion (9.3). The dashed line symbolizes the shot noise of light. Note from Eq. (9.33), that the sum $\mathrm{Var}(A) + \mathrm{Var}(B)$ actually measures the variances $\mathrm{Var}(\hat{J}'_{y1} + \hat{J}'_{y2}) + \mathrm{Var}(\hat{J}'_{z1} + \hat{J}'_{z2}) +$ light noise, i.e.

$$\begin{aligned}\mathrm{Var}(A) + \mathrm{Var}(B) &= \frac{S_x T}{2} + \left(\frac{a S_x T}{2}\right)^2 \left(\mathrm{Var}\left(\hat{J}'_{y1} + \hat{J}'_{y2}\right) + \mathrm{Var}\left(\hat{J}'_{z1} + \hat{J}'_{z2}\right)\right) \\ &= \frac{S_x T}{2}\left(1 + \kappa^2 \frac{\mathrm{Var}\left(\hat{J}'_{y1} + \hat{J}'_{y2}\right) + \mathrm{Var}\left(\hat{J}'_{z1} + \hat{J}'_{z2}\right)}{2J_x}\right)\end{aligned} \tag{9.39}$$

such that the contribution above the dashed line is exactly the left hand side of (9.3). To connect this calibration to the considerations in the previous section we note that the atomic contribution is equal to κ^2 in the units where shot noise of light has unity variance.

We will now turn our attention toward the evidence of entanglement generation. The possibly entangled state is created by the first measurement of A and B which we denote by A_1 and B_1 (indices 1 for first pulse). We need to perform a second measurement A_2 and B_2 in order to characterize the state created by the first one.

Let us discuss what could be observed if the pure state model of Sec. 9.3 holds exactly. In this case the first pulse measurement A_1 and B_1 both have zero mean and variance $1 + \kappa^2$ (which we already showed in Fig. 9.2). The second measurement variables A_2 and B_2 will theoretically fulfil

$$\begin{gathered}\langle A_2 \rangle = \frac{\kappa^2 A_1}{1+\kappa^2} \quad \text{and} \quad \langle B_2 \rangle = \frac{\kappa^2 B_1}{1+\kappa^2}, \\ \mathrm{Var}\left(A_2 - \frac{\kappa^2 A_1}{1+\kappa^2}\right) = \mathrm{Var}\left(B_2 - \frac{\kappa^2 B_1}{1+\kappa^2}\right) = 1 + \frac{\kappa^2}{1+\kappa^2} = \frac{1+2\kappa^2}{1+\kappa^2}.\end{gathered} \tag{9.40}$$

For the variances of A_2 (or B_2) minus the mean value the term 1 is the light noise contribution of the second pulse and the term $\kappa^2/(1+\kappa^2)$ is the variance of the created entangled state. If by measurements and statistical calculations we could confirm these results we would have proved experimentally that the entangled state was created. Let us also here discuss the expected variance of the second measurement alone. We would obtain

$$\mathrm{Var}(A_2) = \mathrm{Var}(B_2) = 1 + \frac{\kappa^2}{1+\kappa^2} + (1+\kappa^2)\left(\frac{\kappa^2}{1+\kappa^2}\right)^2 = 1 + \kappa^2. \tag{9.41}$$

The term 1 is the shot noise of the second pulse, the term $\kappa^2/(1+\kappa^2)$ is the variance of the created entangled state, and the last term arises from the fact that the mean value of e.g. A_2 is random, A_1 has variance $1+\kappa^2$ and the correction factor $\kappa^2/(1+\kappa^2)$ must be squared. The result is $1+\kappa^2$ which is the same as the variance of the first pulse. This fact reflects the QND nature of the measurement. If we perform a measurement and if a "secret" observer had already performed the same measurement on the spins without telling us the outcome we would not be able to notice.

Now, the pure state model and its implications discussed above need not hold. The model could simply be wrong, or several physical effects could change the picture. For instance if decoherence is strong between the first and second measurement pulse entanglement could be hard to observe. In order to apply the above considerations in a more realistic setting we assume more generally that the first measurement (A_1, B_1) creates a state with mean value $(\alpha A_1, \alpha B_1)$ and variance $\mathrm{Var}(\hat{J}_{y1} + \hat{J}_{y2}) + \mathrm{Var}(\hat{J}_{z1} + \hat{J}_{z2}) = 2J_x \cdot \sigma^2$. In this case we can estimate α and σ^2 by performing a large number N of measurements each giving results $(A_1[i], B_1[i], A_2[i], B_2[i])$, where i is indexing the different measurements. The variables $A_2[i] - \alpha A_1[i]$ and $B_2[i] - \alpha B_1[i]$ will have zero mean and variance $1+\sigma^2$ in units of shot noise, the term 1 arises from the shot noise of the second measurement. We calculate

$$1+\sigma^2 = \frac{1}{N-1}\left(\sum_i^N (A_2[i] - \alpha A_1[i])^2 + \sum_i^N (B_2[i] - \alpha B_1[i])^2\right), \tag{9.42}$$

where α must be chosen such that the right hand side is minimal. The minimization procedure is equivalent to a linear fit through $(0,0)$ if we plot the second pulse results A_2 and B_2 versus the first pulse results A_1 and B_1. If σ^2 is below the level of the coherent spin state κ^2 (symbolized by the atomic part above the dashed line in Fig. 9.2) we have created an entangled state. In Sec. 10.4 we discuss experiments connected to this method. In Sec. 10.1 we discuss other experiments where we for technical reasons did not have the ability to utilize the above method but we were able to estimate the variance of $A_2 - A_1$ and $B_2 - B_1$, i.e. we were forced to put alpha to unity. In this case we have

$$1+\sigma^2 \leq \frac{1}{N-1}\left(\sum_i^N (A_2[i] - A_1[i])^2 + \sum_i^N (B_2[i] - B_1[i])^2\right), \tag{9.43}$$

i.e. our estimation of the entangled state variance is not optimal but put an upper bound on σ^2 which is sufficient for entanglement demonstration. Note, our pure state model predicts $\alpha = \kappa^2/(1+\kappa^2)$. The simple method with $\alpha = 1$ should work best for a large atomic to shot ratio, $\kappa^2 \gg 1$.

9.6 Entanglement Generation and Losses

Let us discuss the role of losses for the generation of entanglement. Consider Fig. 9.3 where we place two spin samples 1 and 2 next to each other and shine

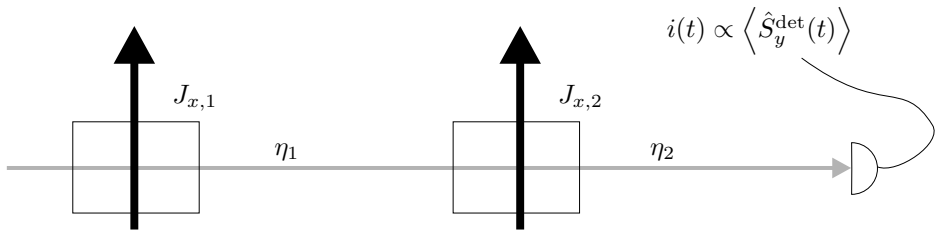

Figure 9.3: Light is propagating through two cells with macroscopic spins J_{x1} and J_{x2} oriented along the x-axis. We parametrize the loss between the two cells by η_1 and the losses after the second cell by η_2 (also including the detector efficiency). The detector measures the $\hat{S}_y$-component of light.

a pulse of light through them as usual. We assume losses to be present between samples 1 and 2 modeled by the transmission efficiency η_1 and between sample 2 and the detector modeled by η_2. In this case the Stokes operators of light will transform according to Eqs. (A.15) and (A.16). If the light before sample 1 is described by $S_x^{\rm in} \equiv S_x$, $\hat{S}_y^{\rm in}$, and $\hat{S}_z^{\rm in}$, we may show that

$$S_x^{\rm det} = \eta_1\eta_2 S_x, \tag{9.44}$$

$$\hat{S}_y^{\rm det} = \eta_1\eta_2\hat{S}_y^{\rm in} + a\eta_1\eta_2 S_x\left(\hat{J}_{z1}(t) + \hat{J}_{z2}(t)\right) + \eta_2\sqrt{\frac{\eta_1(1-\eta_1)S_x}{2}}\hat{V}_{y1} + \sqrt{\frac{\eta_1\eta_2(1-\eta_2)S_x}{2}}\hat{V}_{y2} \tag{9.45}$$

for the light reaching the detectors. The strong S_x-component is attenuated by the overall efficiency $\eta_1\eta_2$. The $\hat{S}_y$ component consists of the attenuated input field $\hat{S}_y^{\rm in}$, a readout of $\hat{J}_{y1} + \hat{J}_{y2}$ with some attenuation, and finally some added vacuum noise described by operators $\hat{V}_{y1}$ and $\hat{V}_{y2}$ (see Sec. A.4). Even in the case of losses between samples 1 and 2 ($\eta_1 < 1$) we readout $\hat{J}_{z1}$ and $\hat{J}_{z2}$ with equal weight. Atoms will see the back action from the $\hat{S}_z$-components which at sample 1 and 2 amount to

$$\hat{S}_z^{\rm cell\ 1} = \hat{S}_z^{\rm in}, \tag{9.46}$$

$$\hat{S}_z^{\rm cell\ 2} = \eta_1\hat{S}_z^{\rm in} + \sqrt{\frac{\eta_1(1-\eta_1)S_x}{2}}\hat{V}_{z1}. \tag{9.47}$$

Since these two are different, there will not be a perfect back action cancellation in the case of opposite spins ($J_{x1} = -J_{x2} = J_x$). The evolution of spins can be found by time integration of Eqs. like (4.4-4.7) which is straightforward but cumbersome. We will not carry out the calculations here but just state the results.

- If we prepare two coherent spin states with x-components J_{x1} and J_{x2} like in Fig. 9.3 and if we perform measurements like those described in connection to Eq. (9.39) we do not expect the measured noise to depend linearly

on the spin magnitude, a quadratic component is added. This quadratic contribution arises from the non-perfect cancellation of back action noise.

- The optimal balancing of spins which reduces the quadratic contribution most is having $J_{x1} = -J_{x2}$. This is independent on η_1.

- The shot noise measured on the detectors depend only on the number of photons received by the detector.

- In the case of balanced spins $J_{x1} = -J_{x2} = J_x$ the measured noise (in units of shot noise) follows Eq. (9.48) below. Here we define PN/SN as the projection noise (PN) to shot noise (SN) ratio. This increases linearly with J_x. The result PN/SN $= \kappa^2 = a^2 S_x T J_x$ in case of no losses is modified to PN/SN $= \eta_1 \eta_2 \kappa^2$.

$$\text{Measured noise } = 1 + \frac{\text{PN}}{\text{SN}} + \frac{1-\eta_1}{12\eta_1\eta_2}\left(\frac{\text{PN}}{\text{SN}}\right)^2. \tag{9.48}$$

The quadratic term vanishes if $\eta_1 = 1$, then back action cancellation is perfect. The front factor $1/12\eta_1\eta_2$ is valid for a quantum noise limited $\hat{S}_z$-component of light. If there is additional classical noise from e.g. the laser the detected back action is larger.

For entanglement generation, the non-canceled back action noise leads to the fact that we cannot measure $\hat{J}_{y1} + \hat{J}_{y2}$ without disturbing $\hat{J}_{z1} + \hat{J}_{z2}$ to some extent. Since back action noise increases quadratically with J_x this is an increasing problem for increasing PN/SN ratios. At the same time, a large PN/SN ratio is required in order to generate strong entanglement as we saw in the previous sections. Hence, avoiding losses between samples 1 and 2 and a good spin balancing is important for efficient entanglement generation. On the other hand, for weak entanglement with small κ^2 we should not worry too much about the back action cancellation.

9.7 The Atomic Projection Noise Level

In previous sections we discussed the entanglement criterion (9.3) and its calibration by linearity of the spin projection noise level like depicted in Fig. 9.2 and discussed in Sec. 9.5. The linearity of the observed noise is a strong indication of the quantum projection noise. For instance, all technical noise sources from external fields acting on the spin state would contribute to all atoms and lead to extra noise which scales quadratically with the atomic spin J_x. However, having support from theoretical estimations on the ratio of atomic to shot noise κ^2 will always be welcome. This section is devoted to such an estimate.

We wish to utilize the DC-Faraday effect described in Eq. (6.9). If a beam with linear polarization is propagating along the x-direction (along the macroscopic

spin) the direction of polarization will rotate by an amount

$$\theta_{\mathrm{DC}}[\mathrm{rad}] = -\frac{a_1 \gamma \lambda^2 J_x}{16\pi A_{\mathrm{eff}} \Delta}. \tag{9.49}$$

This is Eq. (6.9) multiplied by the effective transverse area A_{eff} of the vapour cell in the numerator and denominator and we exploit the fact that $\rho A_{\mathrm{eff}} L \langle \hat{j}_x \rangle = J_x$. From Sec. 9.4 we know that in the rotating frame we expect atomic to shot noise ratio

$$\kappa^2 = a^2 S_x T J_x = 2 a S_x T \frac{a J_x}{2} = 2 a S_x T \theta_{\mathrm{DC}}[\mathrm{rad}]. \tag{9.50}$$

In the last step above we assumed that the $a = \gamma \lambda^2 a_1 / 8\pi A_{\mathrm{eff}} \Delta$ really is the correct a to insert in the equation for κ^2. The probe beam does not have cross section $A = A_{\mathrm{eff}}$ but somewhat smaller (typically around 50% of that area). An argument in favour of using A_{eff} anyway is the fact that atoms move in and out of the beam leading to an effective smaller interaction strength since atoms are inside the beam on average during time $T \cdot A / A_{\mathrm{eff}}$. If this model is valid we arrive at following estimate for κ^2

$$\kappa^2 = \frac{18.6 \cdot P[\mathrm{mW}] \cdot T[\mathrm{ms}] \cdot a_1(\Delta) \cdot \theta_{\mathrm{DC}}[\mathrm{deg}]}{\Delta_{\mathrm{blue}}[\mathrm{MHz}]}. \tag{9.51}$$

We converted θ_{DC} into degrees instead of radians, P is the power of the probe, T the time duration of the pulse, $\Delta_{\mathrm{blue}} = -\Delta$ the blue detuning, and the parameter a_1 was defined in Eq. (5.16). We connected $S_x = (\text{photon flux})/2 = P/2\hbar\omega$ where $\omega = 2\pi\nu = 2\pi c/\lambda$ is the optical frequency of the laser beam and $\lambda = 852\mathrm{nm}$ is the wave length. We also inserted $L = 3.0\mathrm{cm}$ and $A_{\mathrm{eff}} = 6.0\mathrm{cm}^2$. All parameters on the right hand side are easy to access experimentally and serve as a good estimate for the ratio κ^2. In addition to the above equation we should remember that κ^2 is reduced by losses and detector inefficiencies, see Sec. 9.6.

An alternative estimation method is to perform absorption measurements to find the density of atoms in the vapour cell. This leads to an estimate for J_x which again estimates $\kappa^2 = a^2 S_x T J_x$.

CHAPTER 10

Experimental Generation of Entangled States

In this chapter we demonstrate the generation of entanglement. This is the most important result of this thesis, the experimental work was done in 2001 and we devote Sec. 10.1 to the discussion hereof. The results are published in [I]. The experimental setup of this experiment deviates a little from the discussion of Chap. 4 and we comment this when appropriate. After the 2001 entanglement experiment we decided to rebuild the setup for reasons that we discuss in Sec. 10.2. On top of this we moved our laboratories twice, once internally at the Department of Physics and Astronomy at the University of Aarhus, and then from Aarhus to the Niels Bohr Institute at Copenhagen University.

This new experimental setup has at the time of writing not yet demonstrated entangled states for various reasons but the problems encountered on the way have in some cases been very interesting. We describe some of these problems in Sec. 10.3. In Sec. 10.4 we discuss the present state of the entanglement experiment. We conclude this chapter in Sec. 10.5 with a summary of our results.

10.1 Entanglement Demonstration

Let us now turn to the experimental demonstration of entanglement generation. The experimental setup is shown in Fig. 10.1, this is a little different than the setup mentioned in Chap. 4. Here two cells are situated next to each other, they are not placed in their own magnetic shield as in Fig. 4.5. Also, the timing of laser

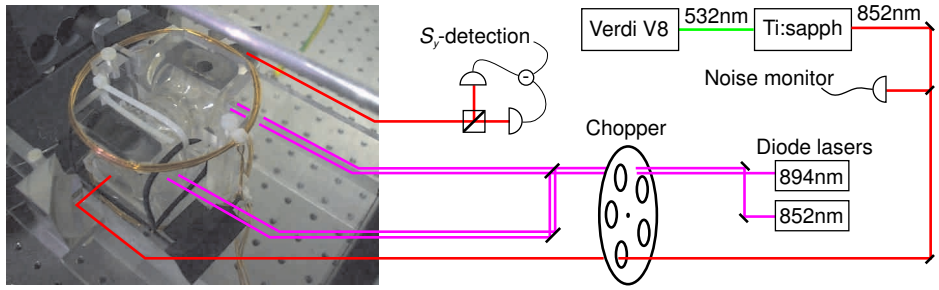

Figure 10.1: Experimental setup for entanglement generation. In this experiment the vapour cells are situated next to each other. The cells can be surrounded by a solenoid and a magnetic shield (not shown here). The laser settings are as described in Sec. 4.1 but the timing is controlled by a chopper. A noise detector monitors the classical noise of the probe laser. After the probe laser from the ti:sapphire laser has passed the atomic samples its $\hat{S}_y$-component is measured. The coil generating the RF-magnetic field for spin state characterization (Chap. 7) is partly visible above the cells.

pulses is controlled by a chopper. The probe laser is detuned by $\Delta = -700$MHz, the duration is $T_{\text{probe}} = 0.45$ms, and the power is $P = 5.0$mW. The optical pump laser is tuned to the $6S_{1/2}, F = 4 \rightarrow 6P_{1/2}, F = 4$ transition and the repump laser is tuned to the $6S_{1/2}, F = 3 \rightarrow 6P_{3/2}, F = 4$ transition as described in Sec. 4.1. The duration of pumping is $T_{\text{pump}} = 0.45$ms. The total experiment cycle is 2ms, it is shown in Fig. 10.2(b). The polarization of the probe laser is 54° with respect to the direction of spin polarization. According to Eq. (6.24) this is the condition for having no Stark shifted Larmor frequencies. From Eq. (6.19) we also know that this setting is vulnerable to excess laser noise. For this reason we use a photo detector for monitoring the classical noise of the probe laser as shown in Fig. 10.1. If the classical noise increases too much we simply wait for it to settle down again before continuing experiments.

The magnitude of the spin components J_{x1} and J_{x2} are measured (on a relative scale) by the magneto-optical resonance method as described in Chap. 7, especially by some of the pulsed methods mentioned in Sec. 7.5. The spin coherence time is also measured by MORS, in absence of lasers we typically find $T_2 = 15 - 30$ms. At the time of this experiment we had not developed the DC-Faraday measurement for direct measurement of J_{x1} and J_{x2}. The absolute value of the spins $J_{x1} = -J_{x2} \equiv J_x$ is estimated by measuring the optical depth α of the atomic sample with a weak, resonant, non-saturating probe beam. The optical depth relates input intensity I_0 to the output intensity I by $I = I_0 \exp(-\alpha)$. The density ρ of atoms can then be found by $\alpha = \rho\sigma L$ where L is the sample length and the relevant cross section σ for our Doppler broadened atoms is estimated by $\sigma = \lambda^2/2\pi \cdot \gamma/\delta\nu_{\text{D}}$. Here γ is the optical line width, $\delta\nu_{\text{D}}$ is the Doppler width, and λ is the optical wave length. With Doppler broadening present, roughly a

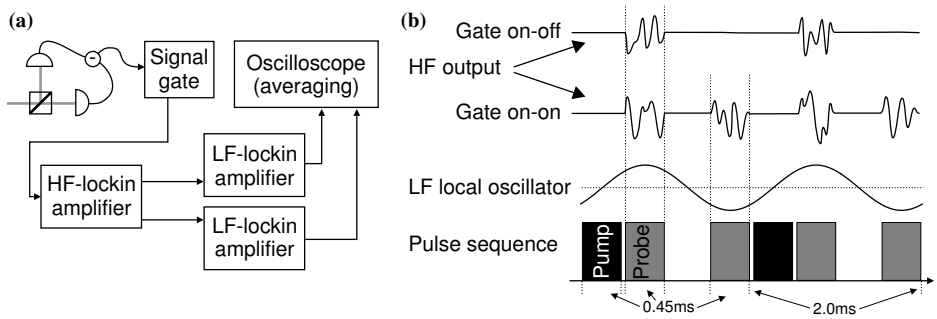

Figure 10.2: **(a)** The signal road from balanced detectors to noise variance estimation. The photo current passes a signal gate which may include or exclude any of the two pulses. The HF lockin amplifier demodulates the signal at the Larmor frequency Ω. The sine and cosine components at Ω from the HF lockin amplifier are fed into two LF lockin amplifiers demodulating the signal at the cycle frequency 500Hz. The outputs are averaged and squared in an oscilloscope. **(b)** At the bottom is shown the laser pulse sequence. The pump and probe lasers both have pulse durations 0.45ms. The total cycle is 2ms. Above this is shown the corresponding local oscillator field for the LF lockin amplifiers. Further above is shown an example of HF lockin output. Mixing these with the LF local oscillator will lead to estimation of A_1 and B_1 for a one pulse experiment and of $A_1 - A_2$ and $B_1 - B_2$ for a two pulse experiment.

fraction $\gamma/\delta\nu_{\mathrm{D}}$ of the atoms are on resonance. This method is a bit crude and hence we should not trust the magnitude in absolute units to better than a factor of 2-3. But on the relative scale we still estimate to have 5% precision.

The spins must be balanced with opposite orientation, $J_{x1} = -J_{x2}$. This is done by simultaneously measuring MORS for the two samples. The MORS should vanish when the spins are balanced if the pumping conditions are similar and if the Larmor frequencies coincide. We estimate this can be done to a precision of 5%. Rough adjustments of spin magnitudes are controlled by the temperature of the vapour cells. Fine tuning is performed by adjusting the power of the repump laser. The two Larmor frequencies are adjusted to coincide by a small extra coil next to one of the cells (a black wire is visible on the left cell in Fig. 10.1). The orientation is also estimated by measuring MORS, for this we increase the magnetic field by roughly a factor of two to better resolve the quadratic Zeeman effect.

When the probe light has passed the two atomic samples its $\hat{S}_y$-component is measured by a set of balanced noise detectors. The differential photo current is then handled as shown in Fig. 10.2(a). First, an electronic gate turns on or off the observation of the two pulses, for CSS noise calibration we only need the first pulse, and for entanglement estimation we need both, see discussions in Sec. 9.5. Then the gated photo current is fed into a high frequency (HF) lockin

amplifier. The local oscillator of this is adjusted to the Larmor frequency of the atomic samples. The two outputs of the HF-lockin amplifier deliver the sine and cosine components of the photo current, or in other words, a signal dependent on $\hat{J}'_{y1} + \hat{J}'_{y2}$ and $\hat{J}'_{z1} + \hat{J}'_{z2}$, respectively, see discussion in Sec. 9.4. These signals are taken to two low frequency (LF) lockin amplifiers the local oscillator of which is a sine wave running at the chopping frequency 500Hz corresponding to the experimental cycle time of 2ms. The demodulation at this frequency ensures that in a two pulse experiment, the value of the two measurements are subtracted from each other. This is also illustrated in Fig. 10.2(b). Now, by setting the lockin amplifier in "r"-mode (delivering the magnitude of the frequency component at 500Hz) we obtain after squaring $\sum_i (A_1[i] - A_2[i])^2$ and $\sum_i (B_1[i] - B_2[i])^2$ in the language of Secs. 9.4 and 9.5. This is exactly what we need for entanglement estimation according to Eq. (9.43). To be complete, for the LF-lockin amplifier to work properly, we need to integrate over a time duration longer than 2ms (otherwise a 500Hz frequency component cannot be singled out). This means that we really average over some pulses (maybe 5-10) before squaring in the above sums. This is perfectly OK for independent measurements.

Now let us concentrate on the noise results. We start out by one pulse measurements and move the Larmor frequency Ω far away from the local oscillator frequency at 325kHz. Then we only measure the noise of light, and we check that the $\hat{S}_y$-measurement is limited by shot noise by observing the linear dependence of the noise on the probe power.

Next, we move the Larmor frequencies of the two atomic samples back to coincide with the local oscillator at 325kHz. The spins are balanced with opposite orientation and with magnitude J_x. The noise properties of the CSS is now measured, the result is shown in Fig. 10.3(a). On the abscissa is the magnitude J_x and on the ordinate we plot the variance of A_1 plus the variance of B_1, and we normalize this to the result for shot noise of light. We see that for low J_x the measured points depend linearly on J_x which is the fingerprint of the atomic spin projection noise according to the discussion around Eq. (9.39) and Fig. 9.2. We make a fit to the linear part of the graph which is now our calibration for the CSS noise level. The non-linear part for higher J_x may arise from non-canceled back action, pile up of technical noise, etc. We do not know in detail the source of this extra noise but this is also irrelevant. The important point is the fact that we reached the linear dependence for our calibration. We note, that the slope of the linear fit is 0.81 when J_x is measured in units of 10^{12}. We compare this to the theoretical value $\kappa^2 = a^2 S_x T J_x$, where $a = \gamma\lambda^2 a_1/8\pi A_{\text{eff}}\Delta$. Inserting the correct detuning and $A_{\text{eff}} \approx 6.0\text{cm}^2$ we obtain $\kappa^2 = 0.83 \cdot J_x[10^{12}]$ which is close to the measured value. But this excludes the effect of losses and we remember that our estimate of J_x in absolute units is quite crude. We only conclude that we find agreement within the right order of magnitude for κ^2.

Next, we turn to the two pulses experiment for demonstrating the entanglement generation. After each pumping pulse we shine two pulses of light through the samples to measure the spin components $\hat{J}'_{y1} + \hat{J}'_{y2}$ and $\hat{J}'_{z1} + \hat{J}'_{z2}$ twice. There is a 0.5ms delay between these two pulses. The resulting noise of the difference

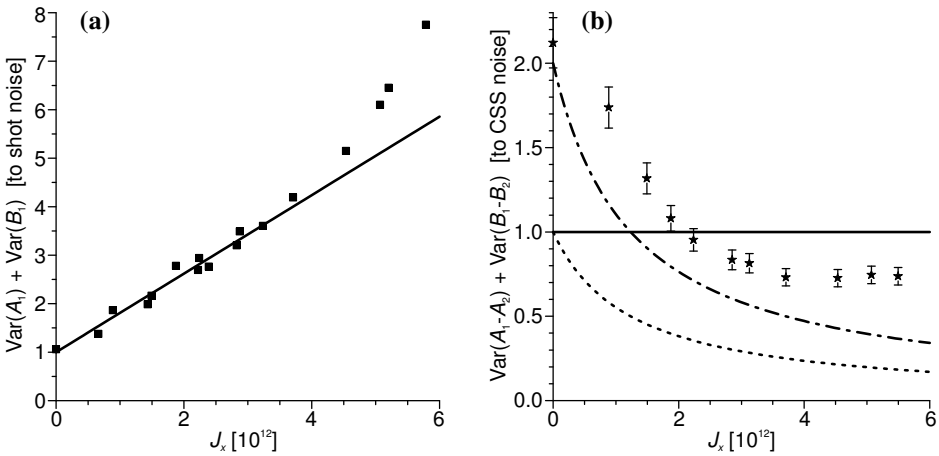

Figure 10.3: **(a)** The measured noise (squares) in a single pulse experiment, the noise variance is normalized to shot noise. On the abscissa we plot J_x, and for $J_x = 0$ we measure the shot noise of light. We see that the noise variance increases linearly with J_x which is the fingerprint of the quantum projection noise of the atomic spins, see the discussion connected to Eq. (9.39) and Fig. 9.2. The straight line is a fit to the linear part of the data points, the slope is 0.81. **(b)** The measured noise (stars) of the difference between two pulses, here normalized to the CSS noise (i.e. divided by the straight line of part (a)). The straight line fit of part (a) has uncertainty in the slope which we recalculate into the error bars in part (b). The data points should fall below horizontal solid line in order to demonstrate entanglement, we see this is indeed the case for the points at higher J_x. The dotted line is the shot noise of a single light pulse, the dash-dotted line is twice the shot noise. The data points cannot fall below twice the shot noise, the reasons for them being higher than this level are decoherence, losses, etc. The lowest data point is $(36 \pm 7)\%$ below unity.

is plotted in Fig. 10.3(b). Here the abscissa is as in part (a) of the figure but the ordinate is now normalized to the CSS noise level, i.e. every data point is divided by the value of the straight line in Fig. 10.3(a). In these units the horizontal solid line is the boundary we have to be below in order to fulfil the entanglement criterion (9.3). This corresponds to $\sigma^2 < \kappa^2$ as we discussed in Sec. 9.5. We see that this is indeed the case for the points at higher J_x and we have proved the generation of entangled states. Since we normalize the data points to the CSS noise level the uncertainty of the slope in Fig. 10.3(a) contributes to the error bars of Fig. 10.3(b). The lowest data point is positioned $(36 \pm 7)\%$ below the CSS noise level.

The dotted line is the shot noise level of light, and the dash-dotted line is twice this level. In our two pulse experiment we can never obtain data points below this level since the noise of $\hat{S}_y^{\text{in}}$ for each pulse is uncorrelated to all other

noise sources. In the ideal case with no decoherence we should on the other hand reach down to this level. The exact reason that we are not at this level is unknown but losses, decoherence, and technical noise will play some role. The crucial point is the fact that we are below the horizontal line and demonstrate the generation of entanglement between the two atomic samples. Since the delay between the two laser pulses is 0.5ms we know that the life time of our entangled state is at least that long.

Some comments are in place for the obtained results. As we discussed above, the fact that the averaging procedure involves several pulses before squaring is OK if the atoms are independent of each other. From the magneto-optical resonance methods we can estimate the refreshing rate Γ_{pump} of the optical pump laser. We know that the transverse spins under influence of pumping decay as $J_y(t) = J_y(0)\exp(-\Gamma_{\text{pump}}t/2)$. We estimate that $\Gamma_{\text{pump}}T_{\text{pump}}/2 \approx 1$ so that we do refresh atoms to a high degree. One may ask whether this level is enough. The straight line observation of Fig. 10.3(a) is a strong indication that we do refresh the spin sample sufficiently, we know that noise piling up in atoms scale quadratically with J_x.

Another issue is the orientation of atoms. We know that for the lower linear part of Fig. 10.3(a) it is better than 95%. This is measured by MORS in a setting where the optical pump power is reduced to resolve the quadratic Zeeman effect (in addition to increasing the magnetic field). We assume that a higher optical pump power will do a better job. A non-perfect orientation compared to the 100% orientated coherent spin state can be regarded as a thermal excitation and we expect this state to be more noise than the CSS. We try to deliberately reduce the orientation and observe the effect on the noise. We do not find any increase in the noise level, however.

10.2 Changing the Experimental Setup

The experiments of the previous section are performed in the old experimental setup. We decide to change the experimental setup for several reasons which we will comment on now.

For the mounting and magnetic shielding of vapour cells we refer to Fig. 10.4 where the old and new setups are shown. In the old setup two vapour cells are placed adjacent to each other inside the same magnetic shielding making laser access very cumbersome. In the new setup the shielding and vapour cells are designed such that laser access is possible from six directions. This setup is suitable for experiments involving three or four vapour cells (we will discuss such experiments in Chap. 11).

On the laser side, in the old setup we use a chopper to control the timing of pulses as we discuss in Sec. 10.1. While being very simple, this setup is not flexible. We wish to vary the time duration of pumping and probing lasers. We would also like to vary the delay between various pulses in order to study decoherence effects. In addition, the new setup with AOMs and EOMs controlling

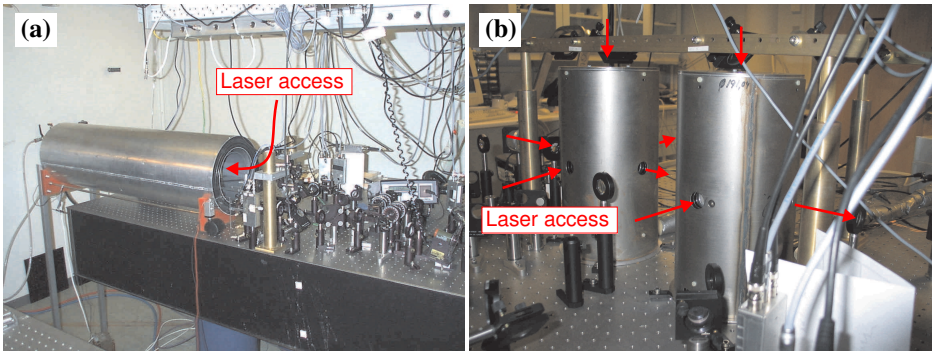

Figure 10.4: **(a)** The old experimental setup. Two vapour cells are placed inside the magnetic shielding cylinder shown. We only have laser access from one end and need to place mirrors inside the cylinder (see picture in Fig. 10.1). **(b)** The new experimental setup. Here each vapour cell is situated in its own magnetic shielding with laser access from six different directions (shown with red arrows). This setup is more suitable for three or four sample experiments.

laser pulses opens up the possibility to shape the temporal profile of the laser pulse.

What regards the data acquisition we would like to implement the weighted entanglement estimation methods of Eq. (9.42) rather than the more simple method of Eq. (9.43). The data acquisition system of the old and new experiments are discussed around Figs. 10.2 and 10.6(a), respectively. The new acquisition methods also enable us to do more detailed statical analysis on our data.

We need to control the temperature of vapour cells. In the old setup an electric heater is placed inside the magnetic shielding. This can in some cases create magnetic fields disturbing the experiments and heating has to be turned on and off during measurements. The new setup utilizes water heating/cooling in an aluminum block as depicted in Fig. 4.5. As we shall see in the next section this aluminum also creates magnetic noise and we are presently working on a non-metallic temperature control using air flow.

Moving from Aarhus to Copenhagen also meant a change in environment. The laboratory magnetic fields in Copenhagen are more noisy than in Aarhus.

10.3 Magnetic Field Noise

For the experiments we need to exclude external fluctuating magnetic fields. If a static magnetic field is added to our bias magnetic field, the Larmor frequency $\Omega = 325$kHz will depend on the external field. For entanglement generation we need to have a stable Larmor frequency for several minutes. In fact, we have

observed stochastic changes of the Larmor frequency at the level of up to 100Hz. The time scale for these changes is of the order of 1 second or slower. These variations correspond to magnetic field changes of 0.3 milligauss at the atoms.

The magnetic noise is much more quiet between roughly 1:30am and 4:30am in the night. This is consistent with the night stand still of the local trains which are running about 1km away from the laboratory at the Niels Bohr Institute. The variations has been discovered to be in the vertical component of the magnetic field which is shielded poorly (only a factor 10-15) by the construction shown in Fig. 4.5(c). The remedy is to rotate the mounts shown in Fig. 4.5 by 90 degrees, the shields have a much higher efficiency perpendicular to the curved surface. So the problem is eliminated but this story tells us in very understandable terms that our measurements are quite sensitive.

Another problem that we have encountered is fluctuating magnetic fields at the Larmor frequency. As discussed in Chap. 7, by introducing a time-varying magnetic field transverse to the x-axis of spin polarization we modulate the transverse components of the spin for atomic spin state characterization. This has proved very useful, but if fluctuating magnetic fields are present beyond our control we encounter problems. In Fig. 4.5(a) we show how our vapour cells are placed on an aluminum block. Below we will see how this aluminum block create random fields disturbing our experiments and we will try to estimate the magnitude of these fields.

With atoms polarized along the x-axis we are sensitive to magnetic field fluctuations along the y- and z-axis. With a magnetic field $\mathbf{B}$ present, the Hamiltonian describing the effect on the entire atomic spin $\mathbf{J}$ reads (to first order) $\hat{H} = g_F \mu_\mathrm{B} \mathbf{B} \cdot \mathbf{J}$, see Eq. (F.4). With B_x being our usual static magnetic field we get Larmor precession and we consider the rotating frame coordinates $\hat{J}'_y$ and $\hat{J}'_z$. In absence of decay mechanisms we can easily show that

$$\begin{aligned} \frac{\partial}{\partial t}\hat{J}'_y(t) &= \frac{g_F \mu_\mathrm{B} J_x}{\hbar}\left(+\cos(\Omega t)B_z(t) - \sin(\Omega t)B_y(t)\right), \\ \frac{\partial}{\partial t}\hat{J}'_z(t) &= \frac{g_F \mu_\mathrm{B} J_x}{\hbar}\left(-\sin(\Omega t)B_z(t) - \cos(\Omega t)B_y(t)\right), \end{aligned} \tag{10.1}$$

where $B_y(t)$ and $B_z(t)$ are the fluctuating magnetic fields which we assume for the moment to be common to all atoms. We wish to integrate the above equations formally and calculate the variance of $\hat{J}'_y(t)$ and $\hat{J}'_z(t)$. To this end we assume that $\langle B_i(t)B_j(t')\rangle = S_B \cdot \delta(t-t')\delta_{ij}$ where $i, j = y, z$ and S_B is a constant describing the spectral noise of the magnetic field. This kind of correlation assumes that the magnetic noise has fast time dynamics compared to our typical spin evolution time. Then we obtain

$$\begin{aligned} \left\langle \hat{J}'^2_y(t)\right\rangle &= \left\langle \hat{J}'^2_y(0)\right\rangle + \left(\frac{g_F \mu_\mathrm{B} J_x}{\hbar}\right)^2 S_B t, \\ \left\langle \hat{J}'^2_z(t)\right\rangle &= \left\langle \hat{J}'^2_z(0)\right\rangle + \left(\frac{g_F \mu_\mathrm{B} J_x}{\hbar}\right)^2 S_B t. \end{aligned} \tag{10.2}$$

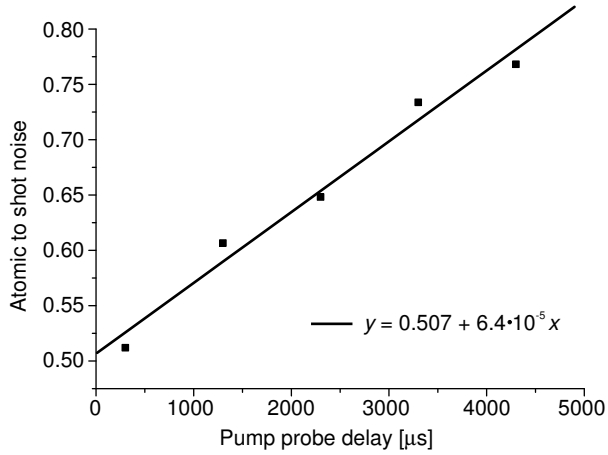

Figure 10.5: The measured noise of a single pulse experiment with a single cell prepared by optical pumping. On the horizontal axis is the delay time between the pump pulse preparing the spin state and the probe pulse measuring the spin. The noise level is believed to be close to the CSS level at $t = 0$, and the linear increase is attributed to the noise generated by random magnetic fields. For this experiment $\theta_{\mathrm{F}} = 13.9°$ and $\Delta = -875$MHz. Removing the aluminum block also removes increase in the noise level.

We see that the variance of $\hat{J}'_y$ and $\hat{J}'_z$ increases linearly with time. In Fig. 10.5 we show the results of an experiment confirming this behavior. For a single spin sample we prepare the coherent spin state as good as we can with optical pumping. Then we wait time t (called the pump-probe delay) before shining a pulse measuring $\hat{J}'_y$ and $\hat{J}'_z$. The measured variance is shown in Fig. 10.5 as a function of t. The units on the vertical axis is the shot noise level of light. We believe that 0.50 is not far from the CSS noise level and we conclude from the data that the slope of the increasing noise is $128\mathrm{s}^{-1}$ in units of the CSS noise. Since the CSS variance of $\hat{J}'_y$ and $\hat{J}'_z$ is $J_x/2$ we get from Eq. (10.2) the theoretical slope

$$\mathrm{Slope} = 2J_x S_B \left(\frac{g_F \mu_{\mathrm{B}}}{\hbar}\right)^2 \tag{10.3}$$

in CSS noise units. To calculate our experimental estimate of S_B we need to find J_x. With $\Delta = -875$MHz and a DC-Faraday measurement of $\theta_{\mathrm{F}} = 13.9°$ we find by Eq. (6.9) that $J_x = 1.5 \cdot 10^{12}$. Then we derive $S_B \approx 9 \cdot 10^{-32}\mathrm{Tesla}^2 s$. The noise in a bandwidth $\delta\omega$ is $S_B \delta\omega$ where $\delta\omega$ is measured in rad/s. Taking the square root and converting to Hz we conclude that our approach estimates magnetic field fluctuations of magnitude $7 \cdot 10^{-15}\mathrm{Tesla}/\sqrt{\mathrm{Hz}}$.

Our assumption that all atoms experience the same magnetic field is probably wrong, and accordingly the real fluctuating field is probably higher than our estimate. In [69] the random magnetic field from a metal filling one half plane

(e.g. $x < 0$ as in our case) is discussed. The origin of these fields is the thermal random currents inside the metal. At a certain point in space (x, y, z) with $x > 0$ their Eq. (10) reads

$$\begin{aligned}\int_{-\infty}^{\infty} d\tau \, \langle B_i(t+\tau) B_j(t) \rangle_T \, e^{i\omega\tau} &= \frac{\mu_0^2 \omega^2 \hbar \epsilon_0 \mathrm{Im}\epsilon(\omega)}{1 - e^{-\hbar\omega/k_\mathrm{B}T}} \frac{t_{ij}}{16\pi x} \\ &\to \frac{3\mu_0^2 \sigma_0 k_\mathrm{B} T}{32\pi x} \delta_{ij} \quad \text{for} \quad i, j = y, z,\end{aligned} \tag{10.4}$$

where $t_{ij} = 3/2$ for $i = j = y, z$. The approximation after the arrow assumes ω to be much slower than the inverse of the electron relaxation time scale τ in order to connect the relative permittivity $\epsilon(\omega)$ to the DC-conductivity σ_0 of aluminum by simple Drude theory $\mathrm{Im}\epsilon(\omega) = \sigma_0/\epsilon_0\omega$. We also assume the typical energy to be less than thermal fluctuations $\hbar\omega \ll k_\mathrm{B}T$. These conditions are easily fulfilled for $\omega \approx 325$kHz. According to the above our approximation $\langle B_i(t) B_j(t') \rangle = S_B \cdot \delta(t - t')\delta_{ij}$ is valid. Inserting relevant values, including $x \approx L = 3.0$cm, we calculate the theoretical estimate of $\sqrt{S_B} = 1.2 \cdot 10^{-12}\mathrm{Tesla}/\sqrt{\mathrm{Hz}}$. We see this number is more than two orders of magnitude higher than our experimental estimate. This is probably an effect of us neglecting spatial correlations. Furthermore, the result for a half plane filled with metal must overestimate the field somewhat. We can probably conclude that the field seen by our atoms is somewhere above $10^{-13}\mathrm{Tesla}/\sqrt{\mathrm{Hz}}$ which still is a small field. We do indeed perform quantum limited measurements of magnetic fields and further study of ultimate sensitivity could be interesting. For our entanglement generation we learn that metal should be avoided close to our atoms.

10.4 Weighted Entanglement Estimation

In this section we describe some aspects of our search for entangled states with our newer experimental setup. We place the atomic vapour cells in mounts as depicted in Fig. 10.4(b) (but rotated by 90 degrees). The separation between the two setups is roughly 30cm. We shine the probe laser as usual to measure the transverse components of the atomic spins, and we may also direct part of the probe laser along the direction of the macroscopic spins in order to measure J_x directly. Then we have the full capability to characterize the spin states by the methods of Chap. 7.

After the probe laser has passed the atomic spins the $\hat{S}_y$-component is measured giving photo current $i(t)$. The following data handling is depicted in Fig. 10.6(a). The HF lockin amplifier gives as outputs $\sin(\Omega t)i(t)$ and $\cos(\Omega t)i(t)$ which are integrated in a home built integrator over the probe pulse duration with results A and B, see Eqs. (9.32) and (9.33). These numbers are stored in a computer and we can process the data afterward. An example of such processing is the analysis discussed in connection to Eq. (9.42) and shown in Fig. 10.6(b). Here we see the result of the second pulse measurement A_2 plotted versus the first

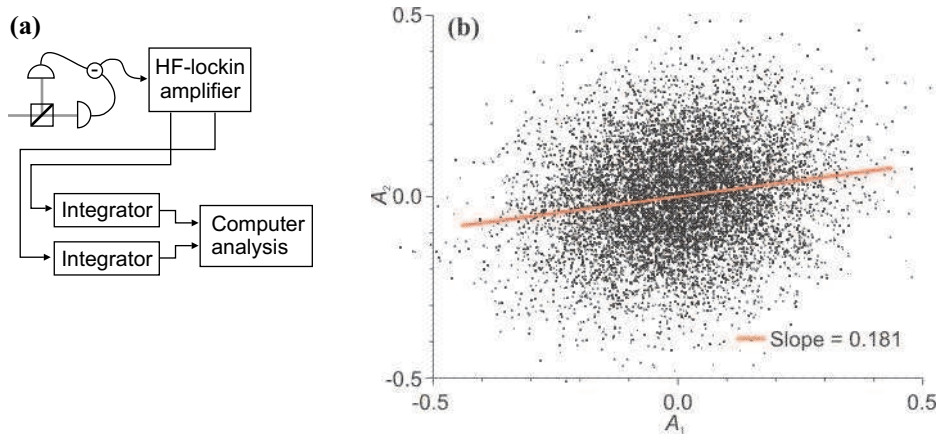

Figure 10.6: **(a)** Schematic view of the signal processing (compare to Fig. 10.2(a)). The differential photo current from the detectors is demodulated in the HF lockin amplifier to give the sine and cosine components at the Larmor frequency Ω as outputs. These are integrated and we obtain two numbers A and B bearing information about the spin state, see Eqs. (9.32) and (9.33). For each probe laser pulse these numbers are stored in a computer and can be used for further analysis. **(b)** An example of correlations between the first and second probe laser pulse giving results A_1 and A_2. We plot A_2 versus A_1 (10.000 points) and perform a linear fit, this is exactly the method described around Eq. (9.42). We see the slope $\alpha = 0.181$ is non-zero, the first pulse result can clearly be used to predict to some extent the second pulse measurement.

pulse result A_1. If atomic noise is much greater than shot noise, and if everything else is ideal, these points should be on a common straight line through $(0, 0)$ with unity slope. In other words, the QND measurement would be perfect and the two measurement results should be identical. But in the case we describe in this section we have atomic noise less than shot noise, the scattering of data points in the Fig. 10.6(b) demonstrates this. We perform a linear fit of the data and get a slope of $\alpha = 0.181$ along the lines of Eq. (9.42). The non-zero slope clearly indicates a correlation between A_1 and A_2 (and a similar plot can be made for B_1 and B_2). The question is, are these correlations strong enough to demonstrate entanglement following the criterion (9.3)?

The answer to this question follows from a thorough analysis as described in Sec. 9.5. First, we must calibrate the noise level of the coherent spin state (CSS). This is done by measuring the variances $\mathrm{Var}(A_1) + \mathrm{Var}(B_1)$ as a function of the magnitude J_x of the oppositely oriented macroscopic spins. This is plotted in Fig. 10.7(a) with black squares. The shot and electronic noise has been subtracted, i.e. we only plot the atomic noise (normalized to shot noise). On the horizontal axis is the DC-Faraday angle θ_{F} which we remember is proportional to J_x. The solid line is a linear fit through $(0, 0)$ of the black points, and it

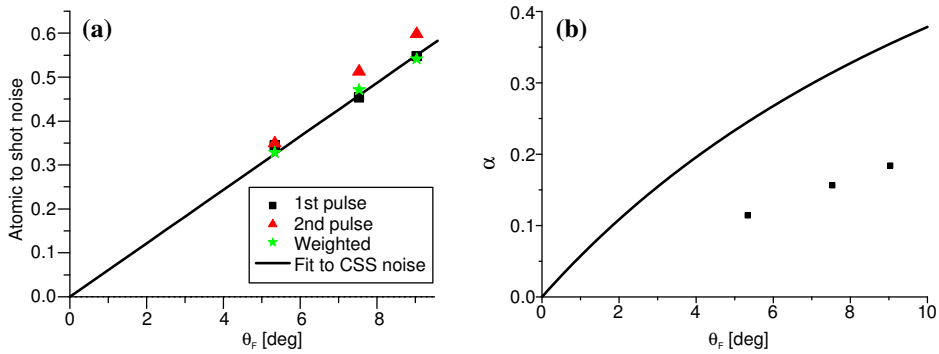

Figure 10.7: Data demonstrating the weighted method of entanglement estimation discussed around Eq. (9.42). **(a)** We vary the magnitude J_x of the macroscopic spin and measure this conveniently by the DC-Faraday rotation angle θ_{F}, see Eq. (6.9). Against this is plotted with black squares the atomic noise variance of the first pulse, with red triangles the second pulse noise, and with green stars the weighted method estimate σ^2 of the state generated by the first pulse. The straight line fit (solid line) is a calibration of the CSS noise level, and with the green stars above this level our data shows no entanglement. The fact that the red triangles are above the black squares indicate decoherence, technical noise pile up, or the like. **(b)** The experimental fitting parameter α (squares) of Eq. (9.42) versus θ_{F} and the theoretical estimate $\alpha = \kappa^2/(1+\kappa^2)$ (solid line) in the ideal case with no losses or decoherence. We see that in some sense we are only effective to the level of 50%.

serves as calibration of the CSS noise level. For the experimental points shown we used laser detuning $\Delta = -875$MHz, probe power $P = 4.0$mW, and probe duration $T_{\mathrm{probe}} = 650\mu$s. The probe laser is polarized along the x-axis parallel to the macroscopic spin direction, we wish to examine the setting where classical laser noise is least likely to play a role according to Eq. (6.19). The setting of the optical pump and repump lasers are as described in Sec. 4.1.

We now use Eq. (9.51) to estimate the slope theoretically. We find the experimental slope to be 48% of the theoretical. If loss of light occurs between the vapour cells and between the cells and detectors the theoretical level should be decreased correspondingly, see Sec. 9.6. But a 52% overall loss is more than expected, a level of 20% would be more acceptable. We conclude either that the simple theoretical estimate of Sec. 9.7 is good only within a factor ≈ 2, or that there effectively may be more losses than we expect.

Now, in the language of Sec. 9.5 the straight line of Fig. 10.7(a) calibrates κ^2 and the weighted method of Eq. (9.42) determines the slope α (see Fig. 10.6(b)) and the variance σ^2 of the possibly entangled state. The value of σ^2 is plotted in Fig. 10.7(a) with green stars and α is plotted in Fig. 10.7(b). Since the green stars are not below the straight line we have no entanglement in the example

shown, i.e. we do not have $\sigma^2 < \kappa^2$.

The reasons for the lack of entanglement is the subject of current investigation and at the time of writing it would be mostly speculation to point at a specific problem. However, we know (without going into details here) that we have not been aware of the full implications of the Stark shifted Larmor frequency discussed around Eq. (6.24). Also, the value of the fitting constant α plotted in Fig. 10.7(b) is roughly 50% of the ideal case theoretical value $\kappa^2/(1+\kappa^2)$, see Eq. (9.38). This indicates that the information provided by the first pulse (A_1, B_1) is only "half as good" as we expect in the ideal case.

Yet another indication that we are further away from ideal measurements that we would like is the fact that the noise variance of the second pulse alone ($\mathrm{Var}(A_2) + \mathrm{Var}(B_2)$ minus shot noise) shown with red triangles in Fig. 10.7(a) is at a higher level than the first pulse variances. This indicates either technical noise pile up, decoherence, or maybe non-canceled back action. Further study is required to understand the decoherence mechanisms behind our data.

But we certainly do conclude that we are not far from observing the entanglement in the new setup. The measurement apparatus works well and supplies us with useful information for understanding the decoherence mechanisms. We also await the possibility to go to higher κ^2 when our hot air heating system is up running (we removed aluminum heating systems for reasons discussed in Sec. 10.3).

10.5 Discussion of the Results

Let us discuss and summarize the results of this chapter. First of all, the experimental results given in Sec. 10.1 demonstrate the generation of entangled states between two macroscopic cesium gas samples. This is the most important result of this thesis. The created states have in the best case a variance fulfilling

$$\mathrm{Var}(\hat{J}_{y1} + \hat{J}_{y2}) + \mathrm{Var}(\hat{J}_{z1} + \hat{J}_{z2}) \leq (64 \pm 7)\% \cdot 2J_x \tag{10.5}$$

which should be compared to the entanglement criterion (9.3). The 64% = (100 - 36)% arise from the fact that the lowest points of Fig. 10.3(b) are 36% below the CSS noise level. This experimental estimate is an upper bound since we here did not take into account the fact that the initial state is the CSS (this is the difference between Eqs. (9.42) and (9.43)).

Our entanglement lives for at least 0.5ms which is a relatively long life time for atomic systems. With our old experimental setup this delay is controlled by a chopper and we do not have much flexibility to test other delays between the first laser pulse creating the entanglement and the second pulse necessary to verify the generation of an entangled state.

We note the fact that the entangled state is created on demand, we perform a measurement with a laser pulse and this inevitably drives the spin samples into the entangled state. The mean values of $\hat{J}_{y1} + \hat{J}_{y2}$ and $\hat{J}_{z1} + \hat{J}_{z2}$ are random, they will be distributed within the CSS variance and can be extracted from

the integrated photo current of the detectors measuring $\hat{S}_y$. This is directly implemented in the newer experiments. The mean values are necessary for future work like teleportation of atomic states (see Chap. 11). To create entangled states with definite mean values, e.g. $\left\langle \hat{J}_{y1} + \hat{J}_{y2} \right\rangle = \left\langle \hat{J}_{z1} + \hat{J}_{z2} \right\rangle = 0$, requires the rotation of the spin state by e.g. a magnetic field. This is still to be implemented.

We have chosen to rebuild the entanglement experiment to make it more suitable for future teleportation protocols, see Chap. 11. This includes the separation of vapour cells to larger distances, design and build up of new cell mounts and magnetic shields, more complicated data acquisition and analysis, and installation of new vapour cells. This process has involved many technical problems and challenges, a few interesting ones are discussed in Sec. 10.3. With the new setup we have reached the CSS noise level for weighted entanglement estimation, see Fig. 10.7(a), or in other words, equality of the criterion (9.3) has been reached and generation of entangled states should not be far away. This setup will also enable us to perform detailed study of the decoherence of entangled states since we will be very flexible in the timing of laser pulses.

CHAPTER 11

Quantum Information Protocols

In this chapter we discuss various protocols for quantum communications purposes, this includes the concept of teleportation which is the transport of an unknown quantum state from one place (which we call Alice's place) to another (which we call Bob's place). According to the no-cloning theorem [2] a quantum state cannot be copied. As a result, in the teleportation process we are not allowed, even in principle, to obtain any information about the initial quantum state to be teleported from Alice to Bob. If we obtain some of this information, the exact same information cannot be sent to Bob. This fact imposes some restrictions on the "handling" of the quantum states and we must follow a certain protocol. A very important resource in such protocols is the use of entangled states, just like the ones we demonstrate in Chap. 10.

A protocol for teleporting the state of a spin-1/2 system was discovered in 1993 [70] and different experiments along these lines have been carried out [26, 27, 29]. Teleportation of continuous variables was proposed in 1994 [71], and the experimental demonstration of continuous variable teleportation for quadratures of the electromagnetic field was demonstrated in [25]. Parts of the contents of the present chapter has been published in [IV].

Experimental studies of teleportation will in practical life have some limitations, therefore it is convenient to define the fidelity $\mathcal{F}$ as a figure of merit for the teleportation protocol

$$\mathcal{F} = \text{Average}\left|\left\langle\psi^{\text{in}}\middle|\,\psi^{\text{out}}\right\rangle\right|^2 \quad \text{or} \quad \mathcal{F} = \text{Average}\,\left\langle\psi^{\text{in}}\middle|\,\hat{\rho}\,\middle|\,\psi^{\text{in}}\right\rangle, \tag{11.1}$$

where the input state is described by the wave function $\left|\psi^{\text{in}}\right\rangle$ and the output state by wave function $|\psi^{\text{out}}\rangle$ or in the case of a mixed state by the density operator

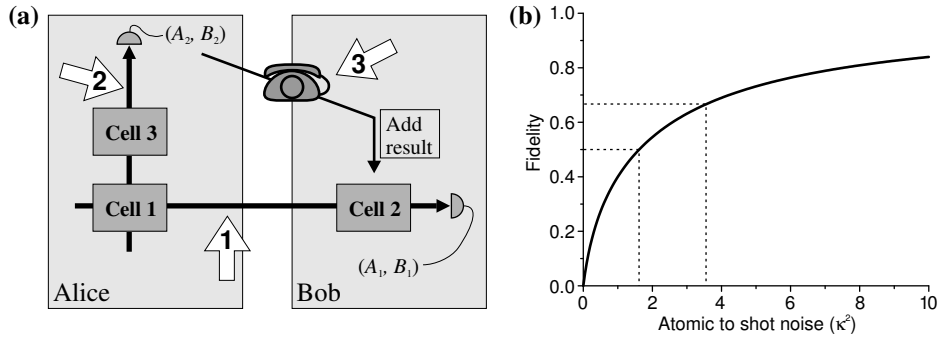

Figure 11.1: **(a)** The teleportation protocol. Alice has two spin samples 1 and 3, the quantum state of sample 3 is unknown and we wish to teleport this to Bob's sample 2. First (marked with an arrow containing the number 1) entangle sample 1 and 2 by a laser pulse. Next measure the joint state of sample 1 and 3 by a similar laser pulse. Last we need by classical communication to transfer numbers A_2 and B_2 from Alice to Bob. This information is required to complete the teleportation. **(b)** The fidelity $\mathcal{F}$ of the teleportation protocol as given by Eq. (11.5). The $\mathcal{F} = 1/2$ and $\mathcal{F} = 2/3$ limit are reached by $\kappa^2 = 1.62$ and $\kappa^2 = 3.56$, respectively.

$\hat{\rho}$. The average is performed over input states. If $\mathcal{F} = 1$, then all input states are teleported perfectly from Alice to Bob. To exceed the limit $\mathcal{F} = 1/2$ for any coherent state we need quantum entanglement, hence this is a boundary between classical and quantum communication [72]. If in addition the limit $\mathcal{F} = 2/3$ is reached we can be sure that the teleported state is the best existing "copy" of the initial state [73].

11.1 Teleportation of an Unknown Spin State

Let us now turn to the protocols for teleportation of spin states. The analysis of continuous variables teleportation for quadratures of light in realistic experimental conditions is given in [74], here some calculation methods for Gaussian continuous variables are also outlined. A proposal for spin state teleportation was given in [62] and in the following we review the basic principle behind.

Consider Fig. 11.1(a) where three vapour cells containing cesium are drawn. Cell 1 and 3 are placed at Alice's site while cell 2 is placed at Bob's site which in principle can be far away. We prepare the atomic spins in these three cells in coherent spin states along the x-axis as usual such that $J_{x1} = J_x$, $J_{x2} = -J_x$, and $J_{x3} = -J_x$. Then two adjacent cells will be polarized along opposite directions. The interesting quantum variables are as always $\hat{J}_y$ and $\hat{J}_z$ (we work in the rotating frame but leave out the primes which will be used for other purposes below) and the aim now is to teleport an unknown state of sample 3 described

by operators $\hat{J}_{y3}$ and $\hat{J}_{z3}$ to sample 2.

The first step is to entangle the spins in sample 1 and 2 by our well known methods from Chaps. 9 and 10. We assume the atomic to shot noise ratio to be very large ($\kappa^2 \gg 1$) such that we essentially perform perfect measurements. Firing a laser pulse through cells 1 and 2 yields results

$$\hat{J}_{y1} + \hat{J}_{y2} = A_1 \quad \text{and} \quad \hat{J}_{z1} + \hat{J}_{z2} = B_1 \tag{11.2}$$

which holds as operator equations for ideal measurements, sample 1 and 2 have changed from independent coherent states into a highly entangled state with $\mathrm{Var}(\hat{J}_{y1} + \hat{J}_{y2}) = \mathrm{Var}(\hat{J}_{z1} + \hat{J}_{z2}) \to 0$.

The next step is to fire a similar laser pulse through sample 1 and 3 to perform an ideal measurement of the spin components. We let primes denote the operators at a time after this second measurement and the primeless operators refer to operators on spin states before the measurement. We have

$$\hat{J}_{y1} + \hat{J}_{y3} = \hat{J}'_{y1} + \hat{J}'_{y3} = A_2 \quad \text{and} \quad \hat{J}_{z1} + \hat{J}_{z3} = \hat{J}'_{z1} + \hat{J}'_{z3} = B_2. \tag{11.3}$$

Note that back action noise is piled up in both spins 1 and 3 such that these individual spins are changed dramatically, i.e. $\hat{J}'_{y1} = \hat{J}_{y1} + \mathrm{BAN}$ and $\hat{J}'_{y3} = \hat{J}_{y3} + \mathrm{BAN}$ and similarly for z-components. Here BAN means back action noise. The sum of primed and unprimed operators are identical, this is the QND nature of the measurement caused by the back action cancellation. We thus measure the properties of the initial state of sample 3 plus the entangled state of sample 1 with sample 2. At the same time $\hat{J}'_{y2} = \hat{J}_{y2}$ and $\hat{J}'_{z2} = \hat{J}_{z2}$, there is no interaction going on at sample 2. Now, the final state of sample 2 can be deduced by

$$\begin{aligned} \hat{J}'_{y2} &= \hat{J}_{y2} = A_1 - \hat{J}_{y1} = \hat{J}_{y3} - (A_2 - A_1), \\ \hat{J}'_{z2} &= \hat{J}_{z2} = B_1 - \hat{J}_{z1} = \hat{J}_{z3} - (B_2 - B_1). \end{aligned} \tag{11.4}$$

Here $\hat{J}_{y3}$ and $\hat{J}_{z3}$ refer to the state of sample 3 before the firing of the second laser pulse. The second equalities hold as a consequence of the initial entanglement between sample 1 and 2, see Eq. (11.2). The third equalities follow from the result of the second QND measurement, see Eq. (11.3). We see that to complete the teleportation we need to add the numbers $A_2 - A_1$ and $B_2 - B_1$ to $\hat{J}'_{y2}$ and $\hat{J}'_{z2}$, respectively, which can be done by suitable magnetic fields. The numbers A_2 and B_2 are completely random and without these Bob has no use of the spin state of sample 2. For Bob to know these numbers we must establish classical communication between Alice and Bob. The initial state of Alice's sample 3 has been destroyed by pile up of back action noise but has also been recreated in Bob's sample 2.

Note, the initial entanglement between samples 1 and 2 could have been prepared while the cells were sitting next to each other. Then one sample could be moved far away, and the rest of the protocol could proceed. This approach of course involves some technical problems (e.g. the magnetic field should be

carried together with the atomic sample). But it underlines the profound nature of teleportation, when the entanglement has been established the rest is local measurements and classical communication.

The above considerations are worked out for ideal measurements. For a finite atomic to shot noise ratio κ^2 the analysis is covered by [62] which again relies on the calculations in [74]. We will just state the result, the fidelity $\mathcal{F}$ is given by[1]

$$\mathcal{F} = 1 \Big/ \left(1 + \frac{1}{1+\kappa^2} + \frac{1}{\kappa^2}\right) . \tag{11.5}$$

We plot this quantity in Fig. 11.1(b). To overcome the threshold $\mathcal{F} = 1/2$ we need $\kappa^2 = 1.62$. With $\kappa^2 = 3.56$ we may break the $\mathcal{F} = 2/3$ limit. We also note that for $\kappa^2 \gg 1$, Eq. (11.5) can be approximated by $\mathcal{F} \approx 1 - 2/\kappa^2$. Hence, to obtain $\mathcal{F} \geq 95\%$ we need $\kappa^2 \geq 40$. We remind ourselves that these calculations are results of a Gaussian wave function modeling which is similar to our pure state considerations for entanglement generation in Sec. 9.3. The only non-ideal factor included in this approach is the fact that atomic to shot noise is finite ($\kappa^2 \neq \infty$). Hence, as experimentalists, given κ^2 we should take the above equation as a theoretical upper limit.

In the experimental demonstration of entanglement generation in Chap. 10 we estimated the variance of the entangled state to be 64% of the CSS noise level, see Eq. (10.5). In this estimation, we neglected the knowledge about the initial CSS which leads us to believe we created a state with variance (relative to the CSS noise level) $1/\kappa^2$ rather than the more correct $1/(1+\kappa^2)$ of Eq. (9.38). If we assume that our estimate corresponds to and effective $1/\kappa^2 = 64\%$ we obtain $\kappa^2 \approx 1.6$, i.e. we now model our operationally obtained entanglement at the real $\kappa^2 \approx 2.8$ (see Fig. (10.3)) by a virtual but perfect experiment working at $\kappa^2 \approx 1.6$. This effective κ^2 is close to the teleportation fidelity of $\mathcal{F} = 1/2$.

The teleportation protocol is a very suitable extension to our experiment, in addition to the magnetic field for adding $A_2 - A_1$ and $B_2 - B_1$ we essentially have two laser beams similar to the one we applied for entanglement generation in Chap. 10. Hence, in principle, the teleportation protocol with three cells is straightforward to implement. However, as experimentalists we need to demonstrate that the teleportation is successful with some fidelity $\mathcal{F}$. For this purpose we would need to perform measurements on sample 2 after the teleportation has been completed. But with our rotating frame this is not straightforward, we cannot measure and characterize a single spin component ($\hat{J}_{y2}$ *or* $\hat{J}_{z2}$) as we remarked in Sec. 4.3. This fact motivated us to consider a four cell protocol which is described in the next section.

11.2 Entanglement Swapping

Let us consider the setup shown in Fig. 11.2(a). At Alice's site we place cells 1 and 3, and at Bob's site we place cells 2 and 4. We create coherent spin states in

[1] In Eq. (3) of [62] we substituted $2\kappa^2 \to \kappa^2$ to account for the rotating frame.

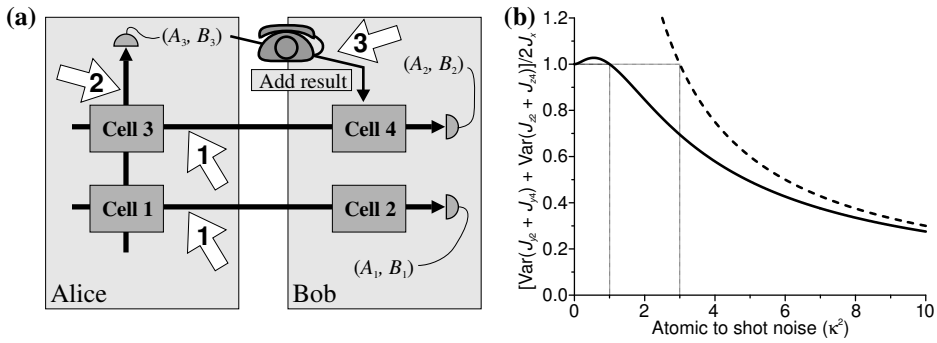

Figure 11.2: **(a)** The four cell entanglement swapping protocol. Alice has two spin samples 1 and 3, and Bob has samples 2 and 4. First we entangle sample 1 with 2 and sample 3 with 4 by two laser pulses. Next measure the joint state of sample 1 and 3 by a similar laser pulse. Last we need by classical communication to transfer numbers A_3 and B_3 from Alice to Bob. If the measurement is ideal, Bob can now use this information to rotate samples 2 and 4 into an entangled state with $\hat{J}_{y2} + \hat{J}_{y4} = 0$ and $\hat{J}_{z2} + \hat{J}_{z4} = 0$. **(b)** Given the atomic to shot noise ratio κ^2 the solid line shows the best obtainable variance of the entangled state by the protocol (calculated numerically). We see that $\kappa^2 > 1$ is required to observe entanglement between samples 2 and 4. The dashed line is the naive guess $3/\kappa^2$ for the variance. At large values of κ^2 the two lines agree.

all four samples oriented such that $J_{x1} = J_{x4} = J_x$ and $J_{x2} = J_{x3} = -J_x$. Then any two adjacent samples have opposite orientation and we may perform QND measurements on any of these pairs. Now we wish to generate entanglement between samples 2 and 4 without direct interaction between these. This is done in the following manner where we assume ideal measurements ($\kappa^2 \gg 1$).

First fire two laser pulses marked with the arrow (1) in Fig. 11.2(a). These perform measurements

$$\begin{aligned} \hat{J}_{y1} + \hat{J}_{y2} = A_1 \quad &\text{and} \quad \hat{J}_{z1} + \hat{J}_{z2} = B_1, \\ \hat{J}_{y3} + \hat{J}_{y4} = A_2 \quad &\text{and} \quad \hat{J}_{z3} + \hat{J}_{z4} = B_2. \end{aligned} \tag{11.6}$$

After this step sample 1 is entangled with sample 2 and sample 3 with sample 4. The next step is to shine a similar laser pulse (shown with arrow (2) in Fig. 11.2(a)) through samples 1 and 3 to measure

$$\hat{J}_{y1} + \hat{J}_{y3} = \hat{J}'_{y1} + \hat{J}'_{y3} = A_3 \quad \text{and} \quad \hat{J}_{z1} + \hat{J}_{z3} = \hat{J}'_{z1} + \hat{J}'_{z3} = B_3. \tag{11.7}$$

In analogy with the previous section we let the primed operators refer to spin states after the measurement on samples 1 and 3, and we remember that the individual samples e.g. $\hat{J}_{1y}$ and $\hat{J}_{y3}$ are destroyd by pile up of back action noise while the sum of the two is conserved. Now let us consider our knowledge about

samples 2 and 4. We have

$$\begin{aligned}\hat{J}'_{y2} + \hat{J}'_{y4} &= \hat{J}_{y2} + \hat{J}_{y4} = (A_1 - \hat{J}_{y1}) + (A_2 - \hat{J}_{y3}) = A_1 - A_2 - A_3, \\ \hat{J}'_{z2} + \hat{J}'_{z4} &= \hat{J}_{z2} + \hat{J}_{z4} = (B_1 - \hat{J}_{z1}) + (B_2 - \hat{J}_{z3}) = B_1 - B_2 - B_3.\end{aligned} \tag{11.8}$$

This measurement does not involve samples 2 and 4 which is the reason for the first equalities to hold above. The second equalities follow from the entanglement (11.6) created by the first laser pulses. The third equalities are valid as a consequence of the second step laser pulse (11.7). The numbers $A_{1,2,3}$ and $B_{1,2,3}$ are completely random, but if Alice sends the values A_3 and B_3 to Bob by classical communication he is able to, as the final step of the protocol, add $-A_1 + A_2 + A_3$ and $-B_1 + B_2 + B_3$ to e.g. $\hat{J}_{y4}$ and $\hat{J}_{z4}$, respectively. We see that we then arrive at $\hat{J}_{y2} + \hat{J}_{y4} = 0$ and $\hat{J}_{z2} + \hat{J}_{z4} = 0$ and a definite entangled state has been created between samples 2 and 4 even though these samples never interact directly. This is known as entanglement swapping.

Note, if we compare Figs. 11.1(a) and 11.2(a) the protocols are very similar. We may consider the four cell protocol as a teleportation experiment where sample 3 is the unknown quantum state to be teleported to sample 2. In Fig. 11.2(a) this state just happens to be an entangled state together with sample 4. After the completion of the protocol it is sample 2 which is entangled with sample 4, an entangled state has been teleported.

Now, the above considerations are valid for perfect measurements, let us discuss what happens in the case of a finite atomic to shot noise ratio κ^2. The protocol works fine in the rotating frame, and to measure e.g. $\hat{J}_{y1} + \hat{J}_{y2}$ we reconsider Eq. (9.33). If we have no prior knowledge about the spin state of samples 1 and 2 and given the results A we could guess

$$\frac{\hat{J}_{y1} + \hat{J}_{y2}}{\sqrt{J_x}} = \frac{2}{\kappa}\left(A - \int_0^T \hat{S}_y^{\text{in}}(t)\sin(\Omega t)dt\right). \tag{11.9}$$

This is just a rewriting of Eq. (9.33). The value of $\hat{J}_{y1} + \hat{J}_{y2}$ is here the number A plus some fluctuating quantity (the integral). If we calculate the variance of the above we get (the number A has variance zero)

$$\frac{\text{Var}\left(\hat{J}_{y1} + \hat{J}_{y2}\right)}{J_x} = \frac{1}{a^2 S_x T J_x} = \frac{1}{\kappa^2}. \tag{11.10}$$

Having three of these kinds of measurements in the protocol leads us to a naive guess for the uncertainty in the final state of $\hat{J}_{y2} + \hat{J}_{y4}$ or $\hat{J}_{z2} + \hat{J}_{z4}$ to be $3/\kappa^2$ in units of J_x. This is plotted in Fig. 11.2(b) as a dashed line. But we do not have to be that naive, in the limit $\kappa^2 \to 0$ this estimate approaches infinity which is wrong. With $\kappa \ll 1$ we hardly touch the spins and we know that we should obtain the coherent spin state limit of unity on the vertical axis of Fig. 11.2(b). We extend the wave function modeling of Sec. 9.3 to the four cell protocol. This is very cumbersome and we get help from numerical methods. The result is

shown as the solid line in the figure, we see that it reaches the correct limits for $\kappa^2 \to 0$ and $\kappa^2 \to \infty$. The interesting part is that with $\kappa^2 > 1$ we are in principle able to detect entanglement between samples 2 and 4. The operational estimate $\kappa^2 \approx 1.6$ of the previous section is well above this limit.

11.3 Quantum Memory for Light

In this section we investigate the possibility to teleport the quantum state of a light pulse onto atomic spins, and later on teleport this state back to light. Reading the introduction in Secs. 2.1 and 2.2 we definitely see that the polarization state of a light pulse and the spin state of atoms are very similar, below we show how the off-resonant interaction can connect the two in a teleportation scheme. To this end we need a source of entanglement between spin states or between beams of light. The contents of this section is close to the ideas of Ref. [75] which discusses similar protocols.

Now, let us assume that we are given a light pulse of duration T in an unknown quantum polarization state. We describe this pulse by $\hat{S}_y^{\rm in}(t)$ and $\hat{S}_z^{\rm in}(t)$ and the relevant quantum variable is the collective property

$$\hat{X}_{\rm L}^{\rm in} = \frac{\int_0^T \hat{S}_y^{\rm in}(t)dt}{\sqrt{S_x T}} \quad \text{and} \quad \hat{P}_{\rm L}^{\rm in} = \frac{\int_0^T \hat{S}_z^{\rm in}(t)dt}{\sqrt{S_x T}}. \tag{11.11}$$

This is similar to Eq. (2.10). As a resource of entanglement we assume to have two ensembles 1 and 2 of spins fulfilling $\hat{J}_{y1} + \hat{J}_{y2} = 0$ and $\hat{J}_{z1} + \hat{J}_{z2} = 0$, i.e. they are perfectly entangled. Like Eq. (2.4) we redefine the spins as

$$\begin{aligned} \hat{X}_{\rm A1} &= \frac{\hat{J}_{y1}}{\sqrt{J_x}} \quad \text{and} \quad \hat{P}_{\rm A1} = \frac{\hat{J}_{z1}}{\sqrt{J_x}}, \\ \hat{X}_{\rm A2} &= \frac{\hat{J}_{y2}}{\sqrt{J_x}} \quad \text{and} \quad \hat{P}_{\rm A2} = -\frac{\hat{J}_{z2}}{\sqrt{J_x}}. \end{aligned} \tag{11.12}$$

Now $\left[\hat{X}, \hat{P}\right] = i$ for both light and the two atomic samples. The entanglement condition (at time $t = 0$ reads) $\hat{X}_{\rm A1}(0) + \hat{X}_{\rm A2}(0) = 0$ and $\hat{P}_{\rm A1}(0) - \hat{P}_{\rm A2}(0) = 0$. In the following we assume no static magnetic field, i.e. we are *not* in the rotating frame. We let the incoming light propagate along the z-axis and let it interact with the spin sample 1. The equations of motion (6.11) and (6.13) will with the above definitions transform into

$$\begin{aligned} \hat{X}_{\rm L}^{\rm out} = \hat{X}_L^{\rm in} + \kappa \hat{P}_{\rm A1}(0) \quad &\text{and} \quad \hat{X}_{\rm A1}(T) = \hat{X}_{\rm A1}(0) + \kappa \hat{P}_{\rm L}^{\rm in}, \\ \hat{X}_{\rm A2}(T) = \hat{X}_{\rm A2}(0) \quad &\text{and} \quad \hat{P}_{\rm A2}(T) = \hat{P}_{\rm A2}(0). \end{aligned} \tag{11.13}$$

Sample 2 is unchanged, there is no interaction going on. If we put $\kappa = 1$ we see that the outgoing $\hat{X}_{\rm L}^{\rm out}$ contains information about the light pulse, $\hat{X}_{\rm L}^{\rm in}$, and the initial atomic state of sample 1, $\hat{P}_{\rm A1}(0)$. We measure this light with outcome A

such that $A = \hat{X}_L^{\rm in} + \hat{P}_{\rm A1}(0)$. The remaining information ($\hat{X}_{\rm A1}(0)$ and $\hat{P}_{\rm L}^{\rm in}$) is stored in the atoms. If we shine a strong light pulse along the y-direction with $\kappa^2 \gg 1$ we may perform a measurement of $\hat{X}_{\rm A1}(T)$ with outcome B, i.e. $B = \hat{X}_{\rm A1}(0) + \hat{P}_{\rm L}^{\rm in}$. We may now consider the state of sample 2,

$$\begin{aligned} \hat{X}_{\rm A2}(T) &= \hat{X}_{\rm A2}(0) = -\hat{X}_{\rm A1}(0) = \hat{P}_{\rm L}^{\rm in} - B, \\ \hat{P}_{\rm A2}(T) &= \hat{P}_{\rm A2}(0) = \hat{P}_{\rm A1}(0) = -\hat{X}_{\rm L}^{\rm in} + A. \end{aligned} \tag{11.14}$$

Now, if we add the numbers B and $-A$ to $\hat{X}_{\rm A2}$ and $\hat{P}_{\rm A2}$, respectively, we have completed the teleportation $\hat{P}_{\rm L}^{\rm in} \to \hat{X}_{\rm A2}$ and $-\hat{X}_{\rm L}^{\rm in} \to \hat{P}_{\rm A2}$.

Now, we could reverse the process, assume we have two entangled beams of light and an unknown atomic quantum spin state. Calculations similar to the above will shown that we also in this case may teleport the spin state to the light pulse. Hence, with both the possibility of writing a quantum state of light onto atoms and reading out this state to another light pulse, we have a protocol for a complete quantum memory. This result should be seen in connection to our discussion in Sec. 8.5.

We demonstrate in Chap. 10 how to generate an entangled state between atomic spins. Also, in our laboratory others have demonstrated entanglement between two beams of light, see [37]. Hence, in principle we have everything at hand to implement a full quantum memory. However, the above protocols do not work in the rotating frame. Experimentally we prefer the rotating frame for several reasons, see Sec. 4.3, and a useful protocol is still to be found.

An alternative to quantum memory is the quantum cloner. An unknown coherent polarization state of light can be optimally cloned onto two oppositely oriented spin states by a single passage of the light through the two atomic samples followed by a measurement [76]. This protocol requires no initial entanglement between the two spin samples.

CHAPTER 12

Summary and Outlook

In this thesis we study the interaction between polarization states of laser light and ground spin states of atomic cesium samples. With strong laser pulses and macroscopic gas samples containing $\approx 10^{12}$ atoms our quantum mechanical description of the collective properties of light and matter becomes very similar to ordinary position $\hat{X}$ and momentum $\hat{P}$ of a single particle. This is also known as continuous variable quantum systems. In this approximation the atoms and light are very similar from a mathematical point of view, and with an off-resonant, dispersive interaction we are able to couple these two different physical systems together.

In the limit of off-resonant coupling we neglect all absorption effects but calculate all dispersive effects of the interaction between laser light and the real hyperfine split ground state of cesium. This leads to an effective Hamiltonian and to light/matter propagation equations. The calculations are then heavily supported by experiments of both classical and quantum nature. During this process we learned that our physical systems of light and atoms really are sensitive to the quantum fluctuations of each other. In particular we followed the quantum fluctuations of a squeezed beam of light into atomic degrees of freedom and back onto light. This study brings optimism for possible future implementations of e.g. quantum memory.

The off-resonant atom/light interaction also allows us to create entangled states between two separate macroscopic atomic gas samples. We exploit the fact that we can perform quantum non-demolition measurements on the joint spin system of two atomic samples. This will, on demand, drive the spin samples into an entangled state. We perform a simple theoretical analysis of this and

we demonstrate the generation of entangled states experimentally. The obtained entanglement corresponds to a noise reduction of $(36 \pm 7)\%$ below the classical limit, and the entangled state lives for at least 0.5ms. Experimental entanglement generation is the most important result of this thesis.

It is feasible to extend our experimental procedures to teleportation protocols with three or more atomic samples. Our operationally obtained entanglement could optimistically lead to teleportation of an unknown quantum state with fidelity close to the limit $\mathcal{F} = 1/2$ which cannot be broken by classical means. A four sample entanglement swapping experiment seems feasible, and our operationally obtained entanglement should be sufficient to observe entanglement created by a swapping protocol. The present work in the laboratory is directed along these lines.

In addition to the important results relevant for future quantum information and communication protocols we learned many aspects of atomic physics for the practical characterization and utilization of atom/light interactions for different purposes. With our efforts on upgrading the experimental setup we also expect to be able to study the dynamical evolution of entangled states.

APPENDIX A

Polarization States of the Light Field

In this appendix we define our notation for Stokes operators, i.e. the operators suitable to describe the polarization state of the light field. We will also discuss vacuum noise and losses for Stokes operators.

A.1 The Quantized Radiation Field

The quantization of the radiation field is well described in many text books and we will here quote results from [77]. The electric field operator can be expressed

$$\mathbf{E} = i \sum_{\lambda} \sqrt{\frac{\hbar \omega_\lambda}{2\varepsilon_0 V}} \left(\hat{a}_\lambda \mathbf{e}_\lambda e^{i\mathbf{k}_\lambda \cdot \mathbf{r}} - \hat{a}_\lambda^\dagger \mathbf{e}_\lambda^* e^{-i\mathbf{k}_\lambda \cdot \mathbf{r}} \right). \tag{A.1}$$

Here λ runs over all modes, i.e. over all directions in k-space and all polarizations. The vector $\mathbf{k}_\lambda$ describes the direction of propagation, the angular frequency is given by $\omega_\lambda = c|\mathbf{k}_\lambda|$, and the complex unit vector $\mathbf{e}_\lambda$ describes the direction of polarization. The vector $\mathbf{e}_\lambda$ is perpendicular to $\mathbf{k}_\lambda$ for all λ, or in other words, it is the *transverse* part of the field which is described above. The creation and annihilation operators $\hat{a}_\lambda$ and $\hat{a}_\lambda^\dagger$ fulfil the commutation relation

$$\left[\hat{a}_\lambda, \hat{a}_{\lambda'}^\dagger \right] = \delta_{\lambda\lambda'}. \tag{A.2}$$

We will make a few simplifications to (A.1). We assume that the field is propagating in the positive z-direction and that the transverse extent of the beam is

much larger than an optical wavelength. In this case a one-dimensional theory is sufficient. The transverse cross section will be denoted A and the quantization volume is then $V = A \cdot L$, where we quantize the beam over a spatial distance L along the z-axis. We will also make an overall phase change[1] to get rid of the i in front of $\mathbf{E}$. Now the electric field may be written

$$\mathbf{E} = \sum_{\lambda} \sqrt{\frac{\hbar\omega_\lambda}{2\varepsilon_0 AL}} \left(\hat{a}_\lambda \mathbf{e}_\lambda e^{ik_\lambda z} + \hat{a}_\lambda^\dagger \mathbf{e}_\lambda^* e^{-ik_\lambda z} \right). \tag{A.3}$$

The Hamiltonian describing the radiation field is given by

$$\hat{H}_{\mathrm{R}} = \sum_{\lambda} \hbar\omega_\lambda \left(\hat{a}_\lambda^\dagger \hat{a}_\lambda + \frac{1}{2} \right). \tag{A.4}$$

A.2 Stokes Operators

To introduce the notation of Stokes operators it will suffice to consider only a single longitudinal mode of (A.3) with wave vector k. We explicitly specify the directions of polarization along x, y or $+, -$ by

$$\begin{aligned} \mathbf{E}_k &= \sqrt{\frac{\hbar\omega}{2\varepsilon_0 AL}} \left([\hat{a}_x \mathbf{e}_x + \hat{a}_y \mathbf{e}_y] e^{ikz} + [\hat{a}_x^\dagger \mathbf{e}_x + \hat{a}_y^\dagger \mathbf{e}_y] e^{-ikz} \right) \\ &= \sqrt{\frac{\hbar\omega}{2\varepsilon_0 AL}} \left([\hat{a}_+ \mathbf{e}_{+1} + \hat{a}_- \mathbf{e}_{-1}] e^{ikz} + [\hat{a}_+^\dagger \mathbf{e}_{+1}^* + \hat{a}_-^\dagger \mathbf{e}_{-1}^*] e^{-ikz} \right). \end{aligned} \tag{A.5}$$

In the first line $\mathbf{e}_x$ and $\mathbf{e}_y$ are unit vectors along the x- and y-directions with corresponding creation and annihilation operators $\hat{a}_x$, $\hat{a}_y$, $\hat{a}_x^\dagger$, and $\hat{a}_y^\dagger$. In the second line the unit vectors $\mathbf{e}_{\pm 1}$ are defined by

$$\mathbf{e}_{+1} = -\frac{\mathbf{e}_x + i\mathbf{e}_y}{\sqrt{2}} \quad \text{and} \quad \mathbf{e}_{-1} = \frac{\mathbf{e}_x - i\mathbf{e}_y}{\sqrt{2}}. \tag{A.6}$$

This particular definition ensures that $\hat{a}_+$ is the annihilation operator of a σ_+-polarized photon and so on. This choice of linear and circular unit vectors fixes the relation between linear and circular creation and annihilation operators,

$$\hat{a}_+ = -\frac{\hat{a}_x - i\hat{a}_y}{\sqrt{2}} \quad \text{and} \quad \hat{a}_- = \frac{\hat{a}_x + i\hat{a}_y}{\sqrt{2}}. \tag{A.7}$$

Now, the Stokes operators are defined by

$$\hat{S}_x = \frac{1}{2} \left(\hat{a}_x^\dagger \hat{a}_x - \hat{a}_y^\dagger \hat{a}_y \right) = -\frac{1}{2} \left(\hat{a}_+^\dagger \hat{a}_- + \hat{a}_-^\dagger \hat{a}_+ \right), \tag{A.8}$$

$$\hat{S}_y = \frac{1}{2} \left(\hat{a}_x^\dagger \hat{a}_y + \hat{a}_y^\dagger \hat{a}_x \right) = -\frac{1}{2i} \left(\hat{a}_+^\dagger \hat{a}_- - \hat{a}_-^\dagger \hat{a}_+ \right), \tag{A.9}$$

$$\hat{S}_z = \frac{1}{2i} \left(\hat{a}_x^\dagger \hat{a}_y - \hat{a}_y^\dagger \hat{a}_x \right) = \frac{1}{2} \left(\hat{a}_+^\dagger \hat{a}_+ - \hat{a}_-^\dagger \hat{a}_- \right), \tag{A.10}$$

[1] This is just a convention. This particular way of defining the fields is common in the quantum optics literature.

where we have the operators in both the x, y and the $+, -$ basis. $\hat{S}_x$ is the number of photons polarized along $\mathbf{e}_x$ minus the number of photons polarized along $\mathbf{e}_y$, $\hat{S}_y$ is the number of photons polarized along $\mathbf{e}_{+45} = (\mathbf{e}_x + \mathbf{e}_y)/\sqrt{2}$ minus the number of photons polarized along $\mathbf{e}_{-45} = (\mathbf{e}_x - \mathbf{e}_y)/\sqrt{2}$, and finally, $\hat{S}_z$ counts the photon difference between σ_+ and σ_- polarization. In the circular basis we may find it useful to express

$$\begin{aligned} \hat{S}_+ &= \hat{S}_x + i\hat{S}_y = -\hat{a}_+^\dagger \hat{a}_-, \\ \hat{S}_- &= \hat{S}_x - i\hat{S}_y = -\hat{a}_-^\dagger \hat{a}_+. \end{aligned} \tag{A.11}$$

We may also define the total photon number $\hat{\phi}$ by

$$\hat{\phi} = \hat{a}_x^\dagger \hat{a}_x + \hat{a}_y^\dagger \hat{a}_y = \hat{a}_+^\dagger \hat{a}_+ + \hat{a}_-^\dagger \hat{a}_-. \tag{A.12}$$

The Stokes operators defined as above satisfy the usual angular momentum commutation relations

$$\left[\hat{S}_j, \hat{S}_k\right] = i\epsilon_{jkl}\hat{S}_l \quad \text{and} \quad \left[\hat{S}_z, S\pm\right] = \pm\hat{S}_\pm \tag{A.13}$$

which can be derived from the commutation relations for for the field operators (A.2). All Stokes operators commute with $\hat{\phi}$.

A.3 Strong, Linearly Polarized Light

In our experiments we often use a linearly polarized beam of light with strong intensity. If the light is polarized along the e.g. x-axis we may treat operators $\hat{a}_x$ and $\hat{a}_x^\dagger$ as numbers, we make an overall phase choice such that $\hat{a}_x \to A_x$ and $\hat{a}_x^\dagger \to A_x$ with A_x real. Then we write

$$\begin{aligned} \hat{S}_x &\approx S_x = \frac{A_x^2}{2}, \\ \hat{S}_y &\approx \frac{A_x}{2}\left(\hat{a}_y + \hat{a}_y^\dagger\right), \\ \hat{S}_z &\approx \frac{A_x}{2i}\left(\hat{a}_y - \hat{a}_y^\dagger\right). \end{aligned} \tag{A.14}$$

We see that the quantum properties of the Stokes operators of light in this approximation solely are governed by the light in the y-polarized mode.

A.4 Stokes Operators and Losses

We finalize this appendix by calculating how the Stokes operators transform when the light is subject to losses of magnitude $1-\eta$, i.e. the fraction η of the photons survive. We continue to assume the approximation of a strong, x-polarized beam.

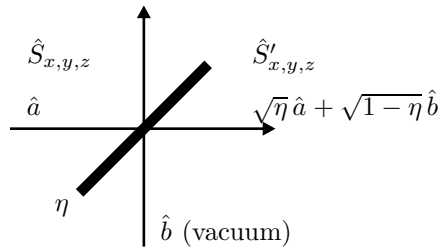

Figure A.1: Losses are modeled by a beam splitter with reflection η. This attenuates the input field $\hat{a}$ and admixes the vacuum component $\hat{b}$ to the output field.

As shown in figure A.1, we model the losses by a beam splitter with transmission η which mixes a vacuum field $\hat{b}$, $\hat{b}^\dagger$ with the incoming field $\hat{a}$, $\hat{a}^\dagger$. We denote the incoming Stokes operators $\hat{S}_{x,y,z}$, and the outgoing operators $\hat{S}'_{x,y,z}$. We shall also assume that all Stokes operators are normalized to photons per second (along the lines of App. C). A calculation shows that

$$\begin{aligned} S'_x &= \eta S_x, \\ \hat{S}'_y(t) &= \eta \hat{S}_y(t) + \sqrt{\frac{\eta(1-\eta)S_x}{2}} \cdot \hat{V}_y(t), \\ \hat{S}'_z(t) &= \eta \hat{S}_z(t) + \sqrt{\frac{\eta(1-\eta)S_x}{2}} \cdot \hat{V}_z(t). \end{aligned} \tag{A.15}$$

We have introduced the vacuum operators $\hat{V}_y(t) = \hat{b}(t) + \hat{b}^\dagger(t)$ and $\hat{V}_z(t) = -i(\hat{b}(t) - \hat{b}^\dagger(t))$ which fulfil

$$\begin{aligned} \left\langle \hat{V}_y(t)\hat{V}_y(t') \right\rangle &= \left\langle \hat{V}_y(t)\hat{V}_y(t') \right\rangle = \delta(t-t'), \\ \left\langle \hat{V}_y(t)\hat{V}_z(t') \right\rangle &= -\left\langle \hat{V}_z(t)\hat{V}_y(t') \right\rangle = i\delta(t-t'). \end{aligned} \tag{A.16}$$

We see from (A.15) that all the Stokes operators are attenuated by a factor η and that the quantum variables $\hat{S}_y$ and $\hat{S}_z$ in addition are mixed with an extra noise source which must be there to preserve commutation relations.

APPENDIX B

Spins and Density Operators

Throughout this thesis we will find it useful to express spin operators in terms of density operators. We will be specifically motivated for describing the spin state of a collection of atoms in a hyperfine multiplet of the ground state of cesium. In this appendix we consider a spin operator $\mathbf{j}$ within a multiplet such that $\mathbf{j}^2 = F(F+1)$ with $\hbar = 1$. For cesium we have for the ground state $F = 3$ or $F = 4$. The connection between spin and density operators is very useful for the derivation of the Hamiltonian (5.18) since we found density operators convenient in the derivation process and spin operators more intuitive in the final Hamiltonian. Also, as we discuss in Sec. 4.3, atoms are oriented along a magnetic field leading to Larmor precession. Expressing density operators in the energy eigen basis (along the x-axis) will reveal the importance of different frequency components.

B.1 Quantization Along the z-axis

Describing the $(2F+1)$-dimensional sub space of a hyperfine multiplet requires first of all a choice of quantization axis. In the following we will take this as the z-axis. In the eigen basis of $\hat{\jmath}_z$ we know from any elementary book on quantum mechanics that

$$\hat{\jmath}_z \left|m\right\rangle = m \left|m\right\rangle \quad \text{and} \quad \hat{\jmath}_\pm \left|m\right\rangle = \sqrt{F(F+1) - m(m \pm 1)} \left|m\right\rangle ,$$

where $\hat{j}_\pm = \hat{j}_x \pm i\hat{j}_y$. In the language of density operators $\hat{\sigma}_{jk} = |j\rangle\langle k|$ we then get

$$\hat{j}_x = \frac{1}{2}\sum_m \sqrt{F(F+1) - m(m+1)}(\hat{\sigma}_{m+1,m} + \hat{\sigma}_{m,m+1}), \tag{B.1}$$

$$\hat{j}_y = \frac{1}{2i}\sum_m \sqrt{F(F+1) - m(m+1)}(\hat{\sigma}_{m+1,m} - \hat{\sigma}_{m,m+1}), \tag{B.2}$$

$$\hat{j}_z = \sum_m m\hat{\sigma}_{m,m}, \tag{B.3}$$

$$\hat{j}_+ = \sum_m \sqrt{F(F+1) - m(m+1)}\hat{\sigma}_{m+1,m}, \tag{B.4}$$

$$\hat{j}_- = \sum_m \sqrt{F(F+1) - m(m+1)}\hat{\sigma}_{m,m+1}. \tag{B.5}$$

By combining the above we can continue to find higher order moments of the spin in terms of density operators, e.g.

$$\hat{j}_z^2 = \sum_m m^2\hat{\sigma}_{m,m}, \tag{B.6}$$

$$\hat{j}_+^2 = \sum_m \sqrt{(F-m)(F+m)(F+1+m)(F+1-m)}\hat{\sigma}_{m+1,m-1}, \tag{B.7}$$

$$\hat{j}_-^2 = \sum_m \sqrt{(F-m)(F+m)(F+1+m)(F+1-m)}\hat{\sigma}_{m-1,m+1}. \tag{B.8}$$

B.2 Quantization Along the x-axis

We will also consider spin operators expressed as a function of density operators when quantized along the x-axis. The main motivation for this is the fact that we experimentally orient the atomic spins along the x-direction such that $\langle\hat{j}_x\rangle \approx F$ (or the opposite direction with $-F$). If $F = 4$ for instance we may in this case assume that the only important density matrix operators are (when quantized along the direction of orientation) $\hat{\sigma}_{44}$, $\hat{\sigma}_{34}$, $\hat{\sigma}_{43}$, and $\hat{\sigma}_{33}$ since all the rest will be much smaller. Furthermore, in this basis and in the presence of a magnetic field, the diagonal elements will be constant, the first off-diagonal elements will rotate with Larmor frequency Ω, the second off-diagonal elements at 2Ω, an so on.

The easiest way to express spin operators in the rotated basis along x is to make a cyclic permutation of x, y, z-indices of the spin operators and then refer

to known results of Sec. B.1. In this way we obtain for the spin components

$$\hat{\jmath}_x = \sum_m m\hat{\sigma}_{m,m}, \tag{B.9}$$

$$\hat{\jmath}_y = \frac{1}{2}\sum_m \sqrt{F(F+1)-m(m+1)}(\hat{\sigma}_{m+1,m}+\hat{\sigma}_{m,m+1}), \tag{B.10}$$

$$\hat{\jmath}_z = \frac{1}{2i}\sum_m \sqrt{F(F+1)-m(m+1)}(\hat{\sigma}_{m+1,m}-\hat{\sigma}_{m,m+1}), \tag{B.11}$$

and we also list some higher order components like

$$\begin{aligned}\hat{\jmath}_y\hat{\jmath}_z+\hat{\jmath}_z\hat{\jmath}_y &= \frac{1}{2i}\sum_m \sqrt{(F-m)(F+m)(F+1+m)(F+1-m)} \\ &\quad\times(\hat{\sigma}_{m+1,m-1}-\hat{\sigma}_{m-1,m+1}) \approx 0, \end{aligned}\tag{B.12}$$

$$\begin{aligned}\hat{\jmath}_x\hat{\jmath}_y+\hat{\jmath}_y\hat{\jmath}_x &= \frac{1}{2}\sum_m \sqrt{F(F+1)-m(m+1)}(2m+1)(\hat{\sigma}_{m+1,m}+\hat{\sigma}_{m,m+1}) \\ &\approx \sigma^{j_x}(2F-1)\hat{\jmath}_y, \end{aligned}\tag{B.13}$$

$$\begin{aligned}\hat{\jmath}_x\hat{\jmath}_z+\hat{\jmath}_z\hat{\jmath}_x &= \frac{1}{2i}\sum_m \sqrt{F(F+1)-m(m+1)}(2m+1)(\hat{\sigma}_{m+1,m}-\hat{\sigma}_{m,m+1}) \\ &\approx \sigma^{j_x}(2F-1)\hat{\jmath}_z, \end{aligned}\tag{B.14}$$

where σ^{j_x} is the sign of j_x. The last terms above are approximations valid for $|\langle\hat{\jmath}_x\rangle| \approx F$. The approximations of Eqs. (B.13) and (B.14) can be derived by comparison to Eqs. (B.10) and (B.11) and maintaining only the most important terms.

Under the same approximation we have $\hat{\jmath}_x^2 \approx F^2$ and $\hat{\jmath}_y^2 \approx \hat{\jmath}_z^2 \approx F/2$ which is seen from the relation $\mathbf{j}^2 = F(F+1)$. Hence we can also state that

$$\left(\hat{\jmath}_x^2-\hat{\jmath}_y^2\right) \approx \left(\hat{\jmath}_x^2-\hat{\jmath}_z^2\right) \approx F\left(F-\frac{1}{2}\right). \tag{B.15}$$

B.3 Commutators

When deriving equations of motion for spins we need to calculate commutators between different spin operators. In this section we state the results for the most important ones used in this thesis. Starting out from the well known

$$[\hat{\jmath}_x, \hat{\jmath}_y] = i\hat{\jmath}_z, \tag{B.16}$$

and with the cyclic permutations thereof, we derive

$$\left[\hat{\jmath}_x, \hat{\jmath}_-^2\right] = +(\hat{\jmath}_x\hat{\jmath}_z+\hat{\jmath}_z\hat{\jmath}_x) - i(\hat{\jmath}_y\hat{\jmath}_z+\hat{\jmath}_z\hat{\jmath}_y), \tag{B.17a}$$

$$\left[\hat{\jmath}_x, \hat{\jmath}_+^2\right] = -(\hat{\jmath}_x\hat{\jmath}_z+\hat{\jmath}_z\hat{\jmath}_x) - i(\hat{\jmath}_y\hat{\jmath}_z+\hat{\jmath}_z\hat{\jmath}_y), \tag{B.17b}$$

$$\left[\hat{\jmath}_x, \hat{\jmath}_z^2\right] = -i(\hat{\jmath}_y\hat{\jmath}_z+\hat{\jmath}_z\hat{\jmath}_y), \tag{B.17c}$$

$$\left[\hat{\jmath}_y, \hat{\jmath}_-^2\right] = -i(\hat{\jmath}_x\hat{\jmath}_z + \hat{\jmath}_z\hat{\jmath}_x) - (\hat{\jmath}_y\hat{\jmath}_z + \hat{\jmath}_z\hat{\jmath}_y), \tag{B.18a}$$

$$\left[\hat{\jmath}_y, \hat{\jmath}_+^2\right] = -i(\hat{\jmath}_x\hat{\jmath}_z + \hat{\jmath}_z\hat{\jmath}_x) + (\hat{\jmath}_y\hat{\jmath}_z + \hat{\jmath}_z\hat{\jmath}_y), \tag{B.18b}$$

$$\left[\hat{\jmath}_y, \hat{\jmath}_z^2\right] = +i(\hat{\jmath}_x\hat{\jmath}_z + \hat{\jmath}_z\hat{\jmath}_x), \tag{B.18c}$$

$$\left[\hat{\jmath}_z, \hat{\jmath}_-^2\right] = -2\hat{\jmath}_-^2, \tag{B.19a}$$

$$\left[\hat{\jmath}_z, \hat{\jmath}_+^2\right] = +2\hat{\jmath}_+^2, \tag{B.19b}$$

$$\left[\hat{\jmath}_z, \hat{\jmath}_z^2\right] = 0. \tag{B.19c}$$

APPENDIX C

Continuous Description of Light and Matter

We will in this section briefly summarize some important aspects of light/matter interactions. This includes a continuum description of the quantized radiation field and spatially continuous description of matter. The results in this appendix are well known to many people (especially theorists) and we may ask, why then use space to derive the results again? The reason is that (for an experimentalist) it is difficult to quickly dig up all the results from the literature. Furthermore, some of these results are so simple that nobody cared to write about it in a text book! The results in this appendix should help giving an overview to some of the theory needed in this thesis. The derivations are heavily inspired by [77, 78, 79].

C.1 Continuous Description of the Electromagnetic Field

We start out from the quantized electric field (A.3) in one dimension. For pedagogic reasons we only care about one polarization mode, e.g. the x-polarization of the electric field. Then we may write

$$E = \sum_{\lambda} \sqrt{\frac{\hbar\omega_\lambda}{2\varepsilon_0 AL}} \left(\hat{a}e^{ik_\lambda z} + \hat{a}^\dagger e^{-ik_\lambda z}\right). \tag{C.1}$$

In this equation the electric field is quantized along a line of length L. Imposing periodic boundary conditions implies a discrete resolution in k-space with resolution $\Delta k = 2\pi/L$. The resolution is going toward zero for $L \to \infty$ and this is the transition we want to make in the following. We need to make the change

$$\sum \Delta k \to \int dk.$$

To do so, we *define* the operator

$$\hat{a}(k) = \frac{\hat{a}_\lambda}{\sqrt{\Delta k}} \quad \text{with } k \approx k_\lambda. \tag{C.2}$$

In this way Eq. (C.1) becomes

$$\begin{aligned} E &= \sum_\lambda \sqrt{\Delta k}\sqrt{\frac{\hbar\omega_\lambda}{2\epsilon_0 L \cdot A}}\left(\hat{a}(k_\lambda)e^{ik_\lambda z} + \hat{a}^\dagger(k_\lambda)e^{-ik_\lambda z}\right) \\ &= \sum_\lambda \Delta k\sqrt{\frac{\hbar\omega_\lambda}{4\pi\epsilon_0 A}}\left(\hat{a}(k_\lambda)e^{ik_\lambda z} + \hat{a}^\dagger(k_\lambda)e^{-ik_\lambda z}\right) \\ &\to \int dk\sqrt{\frac{\hbar\omega}{4\pi\epsilon_0 A}}\left(\hat{a}(k)e^{ikz} + \hat{a}^\dagger(k)e^{-ikz}\right), \qquad (\omega = kc). \end{aligned} \tag{C.3}$$

The operators $\hat{a}(k)$ and $\hat{a}^\dagger(k)$ are now continuous as a function of k and they have units of square root meters. We will now derive the appropriate commutation relation. Consider the sum

$$1 = \sum_{\lambda'}\left[\hat{a}_\lambda, \hat{a}^\dagger_{\lambda'}\right] = \sum_{\lambda'}\Delta k\left[\frac{\hat{a}_\lambda}{\sqrt{\Delta k}}, \frac{\hat{a}^\dagger_{\lambda'}}{\Delta k}\right] \to \int dk'\left[\hat{a}(k), \hat{a}^\dagger(k')\right].$$

These relations hold true whenever the sum of λ' includes λ, or equivalently, for all ranges of integration over k' including k. We conclude

$$\left[\hat{a}(k), \hat{a}^\dagger(k')\right] = \delta(k - k'). \tag{C.4}$$

In the continuous description the free field Hamiltonian (A.4) will turn into

$$\hat{H}_\mathrm{R} = \int dk\, \hbar ck\left(\hat{a}^\dagger(k)\hat{a}(k) + \frac{1}{2}\right). \tag{C.5}$$

We see that $\hat{a}^\dagger(k)\hat{a}(k)dk$ should be interpreted as number of photons which have wave vector in the range $[k, k + dk]$.

C.2 Spatial Description of the Electric field

Up until now the electromagnetic field has been described in reciprocal space, i.e. in k-space. This is the natural way to deal with Maxwell's equations. It is

possible though to give a description in z-space by defining the Fourier transforms

$$\hat{a}(z,t) = \frac{1}{\sqrt{2\pi}} \int_{-\infty}^{\infty} \hat{a}(k,t) e^{ikz} dk \quad \text{and} \quad \hat{a}^\dagger(z,t) = \frac{1}{\sqrt{2\pi}} \int_{-\infty}^{\infty} \hat{a}^\dagger(k,t) e^{-ikz} dk. \tag{C.6}$$

Note, we now explicitly choose to work in the Heisenberg picture and we remind ourselves of the time-dependence by making the operators a function of t. Also, the last line of (C.3) assumes positive k-values. Making the Fourier transform above from $-\infty$ to ∞ is thus strictly not correct since it incorporates wave vectors traveling in the negative z-direction. However, if we make the rotating wave approximation in some band around a carrier frequency the error is negligible. Our particular way of defining the Fourier transform leads to the following commutation relation for the spatial operators

$$\left[\hat{a}(z,t), \hat{a}^\dagger(z',t)\right] = \delta(z - z'). \tag{C.7}$$

The dimension of $\hat{a}(z,t)$ and $\hat{a}^\dagger(z,t)$ is $1/\sqrt{\text{length}}$ and the physical interpretation is that $\hat{a}^\dagger(z,t)\hat{a}(z,t)dz$ is the number of photons in the space between z and $z+dz$.

The time-dependence of $\hat{a}(z,t)$ follows Heisenberg's equation of motion. We decompose the full Hamiltonian into three parts $\hat{H} = \hat{H}_{\mathrm{R}} + \hat{H}_{\mathrm{atoms}} + \hat{H}_{\mathrm{int}}$ where $\hat{H}_{\mathrm{R}}$ describes the pure radiation field, $\hat{H}_{\mathrm{atoms}}$ describes the matter independent of light fields, and $\hat{H}_{\mathrm{int}}$ is the interaction Hamiltonian. Since the light field commutes with $\hat{H}_{\mathrm{atoms}}$ we get

$$\frac{\partial}{\partial t}\hat{a}(z,t) = \frac{1}{\sqrt{2\pi}} \int \frac{\partial}{\partial t}\hat{a}(k,t) e^{ikz} dk = \frac{1}{\sqrt{2\pi}} \int \frac{1}{i\hbar} \left[\hat{a}(k,t), \hat{H}_{\mathrm{R}} + \hat{H}_{\mathrm{int}}\right] e^{ikz} dk.$$

Calculating the commutator with the pure radiation part $\hat{H}_{\mathrm{R}}$ leads to

$$\left[\hat{a}(k,t), \hat{H}_{\mathrm{R}}\right] = \int dk' \, \hbar c k' \left[\hat{a}(k,t), \hat{a}^\dagger(k',t)\right] \hat{a}(k',t) = \hbar c k \, \hat{a}(k,t),$$

where (C.4) has been used in the last step. Since

$$\frac{1}{\sqrt{2\pi}} \int ik\hat{a}(k,t) e^{ikz} dk = \frac{\partial \hat{a}(z,t)}{\partial z},$$

the above equations reduce to

$$\left(\frac{\partial}{\partial t} + c\frac{\partial}{\partial z}\right) \hat{a}(z,t) = \frac{1}{i\hbar} \left[\hat{a}(z,t), \hat{H}_{\mathrm{int}}\right]. \tag{C.8}$$

We have now derived a convenient way to describe how the light field is affected by atoms through the interaction $\hat{H}_{\mathrm{int}}$. Now, if we restrict the radiation field to a narrow band we get a strong motivation for the Fourier transformation of the electric field into z-space. In this case in Eq. (C.3) we have $\omega \approx \omega_0$ where ω_0 is the carrier frequency of e.g. a laser beam. Then

$$\begin{aligned} E &= \int dk \sqrt{\frac{\hbar\omega_0}{4\pi\epsilon_0 A}} \left(\hat{a}(k,t) e^{ikz} + \hat{a}^\dagger(k,t) e^{-ikz}\right) \\ &= \sqrt{\frac{\hbar\omega_0}{2\epsilon_0 A}} \left(\hat{a}(z,t) + \hat{a}^\dagger(z,t)\right). \end{aligned} \tag{C.9}$$

We see that $\hat{a}(z,t)$ can directly be interpreted as the amplitude of the electric field at position z at time t. A final remark in this section is that in free space the time and space dependence is trivial, we may here exclude the z-dependence altogether since $\hat{a}(z,t) = \hat{a}(0, t - z/c)$. If we (relative to some point in space of our choice) make the definition

$$\hat{a}(t) = \sqrt{c} \cdot \hat{a}(z,t), \tag{C.10}$$

and the same for $\hat{a}^\dagger(t)$, we get operators that are normalized such that $\hat{a}^\dagger(t)\hat{a}(t)$ is the flux of photons at time t which is convenient for the description of a laser beam incident on a detector for instance. For light in the vacuum state we have

$$\left[\hat{a}(t), \hat{a}^\dagger(t')\right] = \delta(t - t'). \tag{C.11}$$

C.3 Continuous Matter Operators

When describing the interaction of light with matter it is convenient to express both the electric field and the atoms as a function of the space coordinate z. To illustrate this we assume that we have a collection of two-level atoms coupled to the light by a dipole transition. The generalization to more atomic levels is obvious. We will denote the ground and excited state of the atom by $|g\rangle$ and $|e\rangle$, respectively.

Making the dipole approximation, the Hamiltonian describing the interaction is [77]

$$\hat{H}_{\text{int}} = -\sum_j \mathbf{d}_j \cdot \mathbf{E}(\mathbf{R}_j), \tag{C.12}$$

where $\mathbf{d}_j = -e\mathbf{r}_j$ is the dipole operator for the j'th atom and $\mathbf{R}_j$ is the location of the j'th atom. If we still consider light linearly polarized along x and make the rotating wave approximation, the interaction Hamiltonian is

$$\hat{H}_{\text{int}} = \sqrt{\frac{\hbar\omega_0}{2\epsilon_0 A}} \sum_j \left(d^* \hat{\sigma}_{eg}^{(j)} \hat{a}(z_j,t) + d\hat{\sigma}_{ge}^{(j)} \hat{a}^\dagger(z_j,t) \right). \tag{C.13}$$

We sum over atoms, z_j is the position of the j'th atom, and we have introduced the (dimensionless) density operator $\hat{\sigma}_{ge} = |g\rangle\langle e|$. The dipole moment is defined by $d = e\langle g|\, x\, |e\rangle$. The above Hamiltonian is well known from text books (see e.g. [80]), for the j'th atom the operator $\hat{\sigma}_{eg}^{(j)}$ may change the atomic state from $|g\rangle$ to $|e\rangle$ while the operator $\hat{a}(z_j,t)$ annihilates a photon at position z_j. The strength of this process is governed by the dipole moment d^*.

Instead of assigning a number j to every atom it is convenient to use the position z as the index. If ρ is the density of atoms we may define $\hat{\sigma}_{ge}(z,t)$ such that

$$\hat{\sigma}_{ge}(z,t) = \frac{1}{\rho A dz} \sum_{z_j \in [z, z+dz]} \hat{\sigma}_{ge}^{(j)}(t), \tag{C.14}$$

where A is the transverse extent of the atoms. Note that since $\rho A dz$ is the number of atoms in the slice $[z, z+dz]$ the operator $\hat{\sigma}_{ge}(z,t)$ is the (dimensionless) density operator for an atom picked out from this slice. With this definition, Eq. (C.13) can be written

$$\hat{H}_{\text{int}} = \sqrt{\frac{\hbar\omega_0}{2\epsilon_0 A}} \int_0^L \left(d^* \hat{\sigma}_{eg}(z,t)\hat{a}(z,t) + d\hat{\sigma}_{ge}(z,t)\hat{a}^\dagger(z,t) \right) \rho A dz, \tag{C.15}$$

where the integral runs over the sample length L. We have now obtained a convenient way to describe the interaction Hamiltonian for light coupled to a collection of two-level atoms. For instance, propagation equations through the sample are easily found by combining (C.7), (C.8) and (C.15),

$$\left(\frac{\partial}{\partial t} + c\frac{\partial}{\partial z} \right) \hat{a}(z,t) = -ig\rho A \hat{\sigma}_{ge}(z,t), \tag{C.16}$$

where $g = \sqrt{\omega_0/2\epsilon_0\hbar A}d$. Together with the Heisenberg equation of motion for $\hat{\sigma}_{ge}(z,t)$ we have the coupled quantum Maxwell-Bloch equations describing light/matter interactions. To find the time evolution of the density operator $\hat{\sigma}_{ge}(z,t)$ we must calculate commutators of density operators. From Eq. (C.14) we can in general show that

$$[\hat{\sigma}_{\mu\nu}(z,t), \hat{\sigma}_{\mu'\nu'}(z',t)] = \frac{1}{\rho A} \left(\hat{\sigma}_{\mu\nu'}(z,t)\delta_{\nu\mu'} - \hat{\sigma}_{\mu'\nu}(z,t)\delta_{\nu'\mu} \right) \delta(z-z'). \tag{C.17}$$

A final remark in this section is the extension of the above into the spin language. If we consider density operators among ground state levels in a hyperfine multiplet as in App. B we can express for instance the $\hat{\jmath}_z$ operator as a function of z, i.e.

$$\hat{\jmath}_z(z,t) = \sum_m m\hat{\sigma}_{m,m}(z,t). \tag{generalized B.3}$$

This can be done with all spin operators. We still have dimensionless operators with usual expectation values (i.e. $\langle \hat{\jmath}_z(z,t) \rangle$ is in the range $-F$ to F). The commutation relation will be modified in the following way

$$[\hat{\jmath}_x(z,t), \hat{\jmath}_y(z',t)] = i\hat{\jmath}_z(z,t) \cdot \frac{1}{\rho A}\delta(z-z'), \tag{C.18}$$

that is the commutation relations from Sec. B.3 all hold but with the addition of the z-dependence and the factor $\delta(z-z')/\rho A$.

APPENDIX D

Dipole Matrix Elements

In this thesis we need to calculate the strength of different optical transitions between the ground state $6S_{1/2}$ and the excited state $6P_{3/2}$ multiplets in cesium. This is to a great extent a problem of tensor algebra and some of the following equations can be found in e.g. [81].

D.1 Calculating Matrix Elements

The energy levels of a cesium atom are well described by the total angular momentum $\mathbf{F} = \mathbf{J} + \mathbf{I}$ where $\mathbf{J}$ is the total electronic angular momentum and $\mathbf{I}$ is the nuclear spin. However, the dipole interaction of an optical transition only interacts with the electronic degrees of freedom and we end up with the problem of calculating matrix elements of the kind $\langle \alpha J I F m_F | \, r_q \, | \alpha' J' I F' m'_F \rangle$ where r_q is a spherical tensor component acting on the J-part of the matrix element, $I = 7/2$ is the nuclear spin, $J = 1/2$ is the ground state electron angular momentum and $J' = 3/2$ is the excited state electronic angular momentum. This situation is well known and the result is

$$\begin{aligned} &\langle \alpha J I F m_F \, | r_{-q} | \, \alpha' J' I F' m'_F \rangle = \\ &\quad (-1)^{F' + m'_F - m_F} \, \langle F m_F 1 q | F' m'_F \rangle \sqrt{2F+1} \begin{Bmatrix} F & F' & 1 \\ J' & J & I \end{Bmatrix} \langle \alpha' J' \, \| r \| \, \alpha J \rangle \, , \end{aligned} \tag{D.1}$$

where $q = 0, \pm 1$ is the tensor component index, $\langle F m_F 1 q | F' m'_F \rangle$ is a Clebsch-Gordan coefficient, the curly brackets is a $6j$-symbol, and $\langle \alpha' J' \, \| r \| \, \alpha J \rangle$ is the reduced matrix element.

We wish to calculate the latter in terms of the inverse life time of the $6P_{3/2}$ levels. The easiest is to consider the upper $F' = 5$, $m'_F = 5$ state which can only decay by spontaneous emission to the lower $F = 4$, $m_F = 4$ state. We will first calculate the probability of emitting a photon along the direction $\mathbf{k}$ with polarization $\mathbf{e}^{(j)}$, where we parametrize $\mathbf{k}$ and $\mathbf{e}^{(j)}$, $j = 1, 2$ by

$$\mathbf{k} = \begin{pmatrix} k\sin\theta\cos\phi \\ k\sin\theta\sin\phi \\ k\cos\theta \end{pmatrix}, \quad \mathbf{e}^{(1)} = \begin{pmatrix} \sin\phi \\ -\cos\phi \\ 0 \end{pmatrix}, \quad \mathbf{e}^{(2)} = \begin{pmatrix} -\cos\theta\cos\phi \\ -\cos\theta\sin\phi \\ \sin\theta \end{pmatrix}. \tag{D.2}$$

Note that these three vectors are mutually orthogonal and real. To go on we need the interaction Hamiltonian between the radiation field and the atom. This is

$$\hat{H}_{\text{int}} = e\mathbf{r} \cdot \sum_{\lambda,j} \sqrt{\frac{\hbar\omega_\lambda}{2\epsilon_0 V}} \mathbf{e}_\lambda^{(j)} \left(\hat{a}_{\lambda j} e^{i\mathbf{k}_\lambda \cdot \mathbf{r}} + \hat{a}^\dagger_{\lambda j} e^{-i\mathbf{k}_\lambda \cdot \mathbf{r}} \right) \tag{D.3}$$

which is simply minus the scalar product of the quantized radiation field (A.1) and the dipole operator $\mathbf{d} = -e\mathbf{r}$ of one atom. The two polarizations are indexed by j and λ is running over all directions in space.

With the initial state $|i\rangle = |\alpha' J' I F' m'_F\rangle |n_{\mathbf{k}j} = 0\rangle$ characterizing the upper state with $J' = 3/2$, $F' = 5$, $m'_F = 5$, and no photons in the mode propagating along $\mathbf{k}$ with polarization along $\mathbf{e}^{(j)}$, and the final state $|f\rangle = |\alpha J I F m_F\rangle |n_{\mathbf{k}j} = 1\rangle$ where $J = 1/2$, $F = 4$, $m_F = 4$, and one photon is present in the mode $\mathbf{k}j$, the transition matrix element is given by (in the dipole approximation)

$$\begin{aligned} \left\langle f \left| \hat{H}_{\text{int}} \right| i \right\rangle &= e\sqrt{\frac{\hbar\omega_\lambda}{2\epsilon_0 V}} \left\langle \alpha J I F m_F \left| \mathbf{e}^{(j)} \cdot \mathbf{r} \right| \alpha' J' I F' m'_F \right\rangle \\ &= -e\sqrt{\frac{\hbar\omega_\lambda}{2\epsilon_0 V}} \langle \alpha J I 44 | r_{-1} | \alpha' J' I 55 \rangle (\mathbf{e}^{(j)} \cdot \mathbf{e}_{+1}). \end{aligned} \tag{D.4}$$

In the last equality we use the fact that only the r_{-1} component will contribute to the $\Delta m_F = +1$-transition and that we can write $\mathbf{r} = -\mathbf{e}_{+1} r_{-1} + \mathbf{e}_0 r_0 - \mathbf{e}_{-1} r_{+1}$. Now, the transition rate Γ is found by Fermi's golden rule

$$\Gamma = \frac{2\pi}{\hbar} \left| \left\langle f \left| \hat{H}_{\text{int}} \right| i \right\rangle \right|^2 \rho(E). \tag{D.5}$$

The density $\rho(E)$ of final photonic states is

$$\rho(E) = \frac{V \cdot E^2 \cdot d\Omega}{(2\pi\hbar c)^3} = \frac{V \cdot \omega^2 \cdot d\Omega}{(2\pi c)^3 \hbar}. \tag{D.6}$$

Thus we find the rate into the solid angle $d\Omega$ along $\mathbf{k}$ with polarization $\mathbf{e}^{(j)}$

$$\begin{aligned} \Gamma(\Omega) &= \frac{2\pi}{\hbar} \left(\frac{\hbar\omega e^2}{2\epsilon_0 V} \left| \mathbf{e}^{(j)} \cdot \mathbf{e}_{+1} \right|^2 |\langle \alpha J I 44 | r_{-1} | \alpha' J' I 55 \rangle|^2 \right) \frac{V\omega^2 d\Omega}{(2\pi c)^3 \hbar} \\ &= \frac{\omega^3 e^2}{32\pi^2 \hbar c^3 \epsilon_0} \left| \mathbf{e}^{(j)} \cdot \mathbf{e}_{+1} \right|^2 |\langle \alpha' J' \| r \| \alpha J \rangle|^2 \, d\Omega, \end{aligned} \tag{D.7}$$

where we in the last step used Eq. (D.1) with appropriate values for F, m_F, F', m'_F, J. and J' (the Clebsch-Gordan coefficient is unity while the $6j$-symbol is $1/6$). Now, the total decay rate is found by summing over $j = 1, 2$ and integrating Ω over 4π. By using the definitions (D.2) and (A.6) we find

$$\mathbf{e}^{(1)} \cdot \mathbf{e}_{+1} = \frac{i}{\sqrt{2}} e^{i\phi} \quad \text{and} \quad \mathbf{e}^{(2)} \cdot \mathbf{e}_{+1} = \frac{\cos\theta}{\sqrt{2}} e^{i\phi}, \tag{D.8}$$

and we deduce

$$\begin{gathered} \left|\mathbf{e}^{(1)} \cdot \mathbf{e}_{+1}\right|^2 + \left|\mathbf{e}^{(2)} \cdot \mathbf{e}_{+1}\right|^2 = \frac{1+\cos^2\theta}{2} \quad \Rightarrow \\ \int_{4\pi} \left(\left|\mathbf{e}^{(1)} \cdot \mathbf{e}_{+1}\right|^2 + \left|\mathbf{e}^{(2)} \cdot \mathbf{e}_{+1}\right|^2 \right) d\Omega = \frac{8\pi}{3}. \end{gathered} \tag{D.9}$$

With this result at hand we have the total decay rate

$$\gamma = \frac{e^2}{4\pi\epsilon_0 \hbar c} \frac{\omega^3}{3c^2} \left|\langle \alpha' J' \| r \| \alpha J \rangle\right|^2, \tag{D.10}$$

and isolating the reduced matrix element we get

$$\left|\left\langle 6P_{3/2} \| r \| 6S_{1/2} \right\rangle\right|^2 = \frac{3c^2\gamma}{\alpha\omega^3}. \tag{D.11}$$

Here $\gamma = 2\pi \cdot 5.21\text{MHz}$ is the FWHM line width of the $6P_{3/2}$ states in cesium measured in radians per second, and ω is the angular frequency of the 852nm D2-line. c is the speed of light and α is the fine structure constant. All matrix elements can now be deduced in absolute units from (D.1) and (D.11).

D.2 Dipole Coupling Constants

In Sec. 5.2 we specifically need to calculate numbers like $(g^{\pm}_{F,m;F',m'})^2$ and $(g^{+}_{F,m;F',m'}) \cdot (g^{-}_{F,m;F',m'})$, where $g^{\pm}_{F,m;F',m'}$ is defined in the discussion around Eq. (5.5). The calculation is straightforward from the above results and from the Clebsch-Gordan coefficients and $6j$-symbols of Tab. D.1. We get for the squared coupling constants

$$(g^{\pm}_{F,m;F',m\pm1})^2 = \frac{c\gamma}{4A} \frac{\lambda^2}{2\pi} \frac{1}{3360} \begin{cases} 240m^2 \mp 1200m + 1440 & F=3, F'=2 \\ -315m^2 \mp 315m + 3780 & F=3, F'=3 \\ 75m^2 \pm 675m + 1500 & F=3, F'=4 \\ 35m^2 \mp 245m + 420 & F=4, F'=3 \\ -147m^2 \mp 147m + 2940 & F=4, F'=4 \\ 112m^2 \pm 1232m + 3360 & F=4, F'=5 \end{cases}. \tag{D.12}$$

For the cross terms we get for $F = 3$

$$(g^{+}_{F,m-1;F',m}) \cdot (g^{-}_{F,m+1;F',m}) = \frac{c\gamma}{4A}\frac{\lambda^2}{2\pi}\sqrt{(3+m)(4+m)(3-m)(4-m)} \times \frac{1}{3360}\begin{cases} 240 & F=3, F'=2 \\ -315 & F=3, F'=3 \\ 75 & F=3, F'=4 \end{cases}, \tag{D.13}$$

and for $F = 4$ we have

$$(g^{+}_{F,m-1;F',m}) \cdot (g^{-}_{F,m+1;F',m}) = \frac{c\gamma}{4A}\frac{\lambda^2}{2\pi}\sqrt{(4+m)(5+m)(4-m)(5-m)} \times \frac{1}{3360}\begin{cases} 35 & F=4, F'=3 \\ -147 & F=4, F'=4 \\ 112 & F=4, F'=5 \end{cases}. \tag{D.14}$$

It is worth mentioning a few sum rules. We easily find

$$\sum_{F'}(g^{\pm}_{F,m;F',m\pm1})^2 = \frac{c\gamma}{4A}\frac{\lambda^2}{2\pi}\frac{8\mp m}{4} \quad \text{for } F=3, \tag{D.15}$$

$$\sum_{F'}(g^{\pm}_{F,m;F',m\pm1})^2 = \frac{c\gamma}{4A}\frac{\lambda^2}{2\pi}\frac{8\pm m}{4} \quad \text{for } F=4, \tag{D.16}$$

$$\sum_{F'}(g^{+}_{F,m-1;F',m}) \cdot (g^{-}_{F,m+1;F',m}) = 0 \quad \text{for } F=3 \text{ and } F=4. \tag{D.17}$$

$\langle F, m, 1, 1 \vert F', m+1 \rangle$				
	F'=2	F'=3	F'=4	F'=5
F=3	$\frac{\sqrt{(2-m)(3-m)}}{\sqrt{42}}$	$-\frac{\sqrt{(3-m)(4+m)}}{\sqrt{24}}$	$\frac{\sqrt{(4+m)(5+m)}}{\sqrt{56}}$	0
F=4	0	$\frac{\sqrt{(3-m)(4-m)}}{\sqrt{72}}$	$-\frac{\sqrt{(4-m)(5+m)}}{\sqrt{40}}$	$\frac{\sqrt{(5+m)(6+m)}}{\sqrt{90}}$

$\langle F, m, 1, 0 \vert F', m \rangle$				
	F'=2	F'=3	F'=4	F'=5
F=3	$-\frac{\sqrt{(3-m)(3+m)}}{\sqrt{21}}$	$\frac{m}{\sqrt{12}}$	$\frac{\sqrt{(4-m)(4+m)}}{\sqrt{28}}$	0
F=4	0	$-\frac{\sqrt{(4-m)(4+m)}}{\sqrt{36}}$	$\frac{m}{\sqrt{20}}$	$\frac{\sqrt{(5-m)(5+m)}}{\sqrt{45}}$

$\langle F, m, 1, -1 \vert F', m-1 \rangle$				
	F'=2	F'=3	F'=4	F'=5
F=3	$\frac{\sqrt{(2+m)(3+m)}}{\sqrt{42}}$	$\frac{\sqrt{(4-m)(3+m)}}{\sqrt{24}}$	$\frac{\sqrt{(4-m)(5-m)}}{\sqrt{56}}$	0
F=4	0	$\frac{\sqrt{(3+m)(4+m)}}{\sqrt{72}}$	$\frac{\sqrt{(5-m)(4+m)}}{\sqrt{40}}$	$\frac{\sqrt{(5-m)(6-m)}}{\sqrt{90}}$

$\begin{Bmatrix} F & F' & 1 \\ 3/2 & 1/2 & 7/2 \end{Bmatrix}$				
	F'=2	F'=3	F'=4	F'=5
F=3	$-\sqrt{1/28}$	$\sqrt{3/112}$	$-\sqrt{5/336}$	0
F=4	0	1/12	$-\sqrt{7/432}$	1/6

Table D.1: Relevant Clebsch-Gordan coefficients and $6j$-symbols for the $6S_{1/2} \rightarrow 6P_{3/2}$ transition in cesium.

APPENDIX E

Photo Detection Theory

In this appendix we briefly summarize the most important aspects of photo detection theory and we tailor the theory to be directly applicable to our needs in this thesis. Photo detection is well covered in the literature, see e.g. [82, 83]. Our experiments are made with balanced detection setup as shown in Fig. E.1. This is practically a homodyne measurement which has been described in [84] and results of the sections below follow directly from the approach used in this reference.

E.1 Stokes Vector Detection

Let us assume that the detectors depicted in Fig. E.1 are infinitely fast and that they deliver a current pulse $e\delta(t-t_0)$ if a photon is incident on the detector at time t_0, where e is the unit electrical charge released by the photon. If the detector quantum efficiency is denoted η_d we have

$$\begin{aligned} \langle i_1(t)\rangle = e\eta_\mathrm{d}\left\langle \hat{a}^\dagger_{+45^\circ}(t)\hat{a}_{+45^\circ}(t)\right\rangle \quad \text{and} \quad \langle i_2(t)\rangle = e\eta_\mathrm{d}\left\langle \hat{a}^\dagger_{-45^\circ}(t)\hat{a}_{-45^\circ}(t)\right\rangle \\ \Rightarrow \langle i(t)\rangle_{S_y} = \langle i_1(t)-i_2(t)\rangle = 2e\eta_\mathrm{d}\left\langle \hat{S}_y(t)\right\rangle . \end{aligned} \tag{E.1}$$

The S_y index reminds us of the detector setup as shown in Fig. E.1. The spectrum $\Phi(\omega)$ of the photo current $i(t)$ is defined by

$$\Phi(\omega) = \int_{-\infty}^{\infty} \langle i(t)i(t+\tau)\rangle\, e^{i\omega\tau} d\tau, \tag{E.2}$$

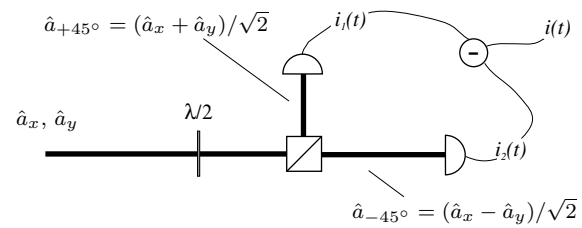

Figure E.1: Detector system for measuring the $\hat{S}_y$-component of light. The incident light described by the field operators $\hat{a}_x$ and $\hat{a}_y$ is rotated by a $\lambda/2$-plate and split on a polarizing beam splitter. The two photo diodes will measure the $\pm 45^\circ$-components of the incident field and the differential photo current $i(t) = i_1(t) - i_2(t)$ is sensitive to $\hat{S}_y(t)$.

and to calculate this spectrum we need the correlation function

$$\langle i(t)i(t+\tau)\rangle_{S_y} = e^2\eta_\mathrm{d}\left\langle\hat{\phi}(t)\right\rangle\delta(\tau) + 4e^2\eta_\mathrm{d}^2\left\langle:\hat{S}_y(t)\hat{S}_y(t+\tau):\right\rangle, \tag{E.3}$$

where the colons denote normal and time ordering of field operators, i.e. the Stokes operators $\hat{S}_y(t)$ and $\hat{S}_y(t+\tau)$ should be written in terms of field operators $\hat{a}_{\pm 45^\circ}$, $\hat{a}^\dagger_{\pm 45^\circ}$ or $\hat{a}_{x,y}$, $\hat{a}^\dagger_{x,y}$ and all daggers should be moved to the left, and time must increase toward the center. Here $\hat{\phi(t)}$ is the total photon flux hitting the two detectors. The first term of (E.3) describes the possibility to count the same electron twice when asking about the current. It only contributes at $\tau = 0$ for an infinitely fast detector and is known as shot noise of the light. The second term is responsible for correlations between photo electrons arising from other reasons, i.e. $\hat{S}_y$ at different times may be correlated if the light beam in the past passed through some medium that affected the light. The correlation function reads in the x, y-basis for $\tau > 0$

$$\begin{aligned}\langle i(t)i(t+\tau)\rangle_{S_y} &= e^2\eta_\mathrm{d}\left\langle\hat{a}_x^\dagger(t)\hat{a}_x(t) + \hat{a}_y^\dagger(t)\hat{a}_y(t)\right\rangle\delta(\tau)\\ &\quad + e^2\eta_\mathrm{d}^2\left\{\left\langle\hat{a}_x^\dagger(t)\hat{a}_x^\dagger(t+\tau)\hat{a}_y(t+\tau)\hat{a}_y(t)\right\rangle\right.\\ &\qquad + \left\langle\hat{a}_y^\dagger(t)\hat{a}_y^\dagger(t+\tau)\hat{a}_x(t+\tau)\hat{a}_x(t)\right\rangle\\ &\qquad + \left\langle\hat{a}_x^\dagger(t)\hat{a}_y^\dagger(t+\tau)\hat{a}_x(t+\tau)\hat{a}_y(t)\right\rangle\\ &\qquad \left.+ \left\langle\hat{a}_y^\dagger(t)\hat{a}_x^\dagger(t+\tau)\hat{a}_y(t+\tau)\hat{a}_x(t)\right\rangle\right\},\end{aligned} \tag{E.4}$$

and for $\tau < 0$ we just interchange t and $t+\tau$ above. This expression is unapproximated but quite annoying to use since we from the light/matter interaction equations get expressions for e.g. $\hat{S}_y$ and not for the normal and time ordered field operators directly. But if we make the approximation of a strong linearly polarized beam of light along the x-axis (see App. A.3) we have

$$\hat{\phi}(t) = A_x^2, \quad \hat{a}_y(t) = \frac{1}{A_x}\left(\hat{S}_y(t) + i\hat{S}_z(t)\right), \quad \hat{a}_y^\dagger(t) = \frac{1}{A_x}\left(\hat{S}_y(t) - i\hat{S}_z(t)\right), \tag{E.5}$$

and inserting this into (E.4) we get for $\tau > 0$

$$\begin{aligned}\langle i(t)i(t+\tau)\rangle_{S_y} &\approx 2e^2\eta_{\mathrm{d}}S_x\delta(\tau)\\ &+ 4e^2\eta_{\mathrm{d}}^2\left(\frac{\left\langle\hat{S}_y(t)\hat{S}_y(t+\tau)\right\rangle+\left\langle\hat{S}_y(t+\tau)\hat{S}_y(t)\right\rangle}{2}-\frac{\left\langle\left[\hat{S}_y(t+\tau),\hat{S}_z(t)\right]\right\rangle}{2i}\right),\end{aligned} \tag{E.6}$$

and for $\tau < 0$ we interchange t and $t+\tau$ which obviously only has an effect on the last term. We could as well have chosen to measure the $\hat{S}_z$ component of light which would be implemented by replacing the $\lambda/2$-plate in Fig. E.1 with a (suitably adjusted) $\lambda/4$-plate. Going through all the above results once again would then yield (for $\tau > 0$)

$$\langle i(t)\rangle_{S_z} = 2e\eta_{\mathrm{d}}\left\langle\hat{S}_z(t)\right\rangle, \tag{E.7}$$

$$\begin{aligned}\langle i(t)i(t+\tau)\rangle_{S_z} &\approx 2e^2\eta_{\mathrm{d}}S_x\delta(\tau)\\ &+ 4e^2\eta_{\mathrm{d}}^2\left(\frac{\left\langle\hat{S}_z(t)\hat{S}_z(t+\tau)\right\rangle+\left\langle\hat{S}_z(t+\tau)\hat{S}_z(t)\right\rangle}{2}-\frac{\left\langle\left[\hat{S}_y(t),\hat{S}_z(t+\tau)\right]\right\rangle}{2i}\right).\end{aligned}$$

Equations (E.6) and (E.7) may be a little cumbersome but they have the advantage that they are expressed directly in terms of Stokes operators $\hat{S}_y$ and $\hat{S}_z$.

E.2 Our Experimental Case and Detection

We will go on with the above equations and show that in our experimental conditions they can be simplified. First of all, if the light is in the coherent state with $\left\langle\hat{S}_y(t)\right\rangle = \left\langle\hat{S}_z(t)\right\rangle = 0$, the y-polarized component of light is in the vacuum state. In this case (C.11) holds and we can easily show that $\left\langle\hat{a}_y(t)\hat{a}_y^\dagger(t')\right\rangle = \delta(t-t')$ while $\langle\hat{a}_y(t)\hat{a}_y(t')\rangle = \left\langle\hat{a}_y^\dagger(t)\hat{a}_y^\dagger(t')\right\rangle = \left\langle\hat{a}_y^\dagger(t)\hat{a}_y(t')\right\rangle = 0$. Under the approximation of strong linearly polarized light along the x-axis we calculate further $\left\langle\hat{S}_y(t)\hat{S}_y(t')\right\rangle = \left\langle\hat{S}_z(t)\hat{S}_z(t')\right\rangle = S_x/2\cdot\delta(t-t')$ and $\left\langle\left[\hat{S}_y(t),\hat{S}_z(t')\right]\right\rangle = iS_x\cdot\delta(t-t')$. In this case we have for perfect detector efficiency $\eta_{\mathrm{d}} = 1$

$$\langle i(t)i(t+\tau)\rangle_{S_y} = \langle i(t)i(t+\tau)\rangle_{S_z} = 2e^2S_x\delta(\tau), \tag{E.8}$$

and we stress that this is only valid for a light in the coherent state incident on a detector with 100% efficiency. We may assume that the light emitted from our lasers are in the coherent state so the above considerations are valid for light *before* an atomic sample, not after. The delta function $\delta(\tau)$ ensures that the spectrum (E.2) is white, i.e. independent on frequency ω.

Now, we may also produce squeezed light experimentally, and the characterization and detection of this is a long story [83, 85, 60]. We make a simplified description assuming that the bandwidth of squeezing is infinite, i.e. the spectrum (E.2) measured with squeezed light incident on a detector is independent on frequency. This is a valid approximation under the circumstances of this thesis since the bandwidth of squeezing is much larger than the dynamical bandwidth of atoms interacting with the light. A result of this assumption is that $\langle i(t)i(t+\tau)\rangle_{S_y,S_z}$ must be proportional to $\delta(\tau)$ and this is then also required for the right hand side of Eqs. (E.6) and (E.7). For the commutator we then only have the choice $\left\langle\left[\hat{S}_y(t),\hat{S}_z(t')\right]\right\rangle = iS_x\delta(t-t')$.

Now, we know that we experimentally would measure $\langle i(t)i(t+\tau)\rangle_{S_y} = \epsilon_y \cdot 2e^2 S_x\delta(\tau)$ and $\langle i(t)i(t+\tau)\rangle_{S_z} = \epsilon_z \cdot 2e^2 S_x\delta(\tau)$ where ϵ_y and ϵ_z characterize the noise of a $\hat{S}_y$ or $\hat{S}_z$ measurement relative to the case of coherent state light (E.8). Putting all the above together we conclude that

$$\left\langle\left[\hat{S}_y^{\text{in}}(t),\hat{S}_z^{\text{in}}(t')\right]\right\rangle = iS_x\delta(t-t'), \tag{E.9}$$

$$\left\langle\hat{S}_y^{\text{in}}(t)\hat{S}_y^{\text{in}}(t')\right\rangle = \epsilon_y\cdot\frac{S_x}{2}\delta(t-t'), \tag{E.10}$$

$$\left\langle\hat{S}_z^{\text{in}}(t)\hat{S}_z^{\text{in}}(t')\right\rangle = \epsilon_z\cdot\frac{S_x}{2}\delta(t-t'), \tag{E.11}$$

which is valid for all input fields before atomic samples encountered in this thesis, squeezed or not. The squeezing parameters must fulfil $\epsilon_y\cdot\epsilon_z \geq 1$. If $\epsilon_y < 1$ and $\epsilon_z > 1$ we have squeezing in $\hat{S}_y$ and anti-squeezing in $\hat{S}_z$, and vice versa.

The physical interpretation of the delta correlations of the above equations is that polarization properties of photons measured at time t and of photons measured an infinitely small time step later are completely independent of each other. This is obvious for the $\hat{a}_y$ mode in the vacuum state ($\epsilon_y = \epsilon_z = 1$). For the squeezed states photons must be correlated to each other, but the above just states that correlated photons arrive in pairs at exactly the same time (i.e. for squeezing in $\hat{S}_y$ with $\epsilon_y < 1$ two photons may be correlated such that they will click in two different detectors of Fig. E.1 giving no contribution in the differential photo current $i(t)$).

The situation is completely different if the light has passed an atomic sample with slow time dynamics, then $\hat{S}_y(t)$ and $\hat{S}_z(t+\tau)$ may posses information about non-commuting observables of the atomic sample and (E.9) would not hold. However, for a very specific case (which is encountered in our experiments) of $\hat{S}_y$, $\hat{S}_z$ transforming like

$$\begin{aligned}\hat{S}_y^{\text{out}}(t) &= \hat{S}_y^{\text{in}}(t) + \int dt'\,\mathcal{L}(\hat{S}_z^{\text{in}}(t'),\ldots),\\ \hat{S}_z^{\text{out}}(t) &= \hat{S}_z^{\text{in}}(t),\end{aligned} \tag{E.12}$$

where $\mathcal{L}$ can be a function of many variables including atomic variables and $\hat{S}_z^{\text{in}}$ but excluding $\hat{S}_y^{\text{in}}$ we easily find $\left\langle\left[\hat{S}_y^{\text{out}}(t),\hat{S}_z^{\text{out}}(t')\right]\right\rangle = \left\langle\left[\hat{S}_y^{\text{in}}(t),\hat{S}_z^{\text{in}}(t')\right]\right\rangle =$

$iS_x\delta(t-t')$ and we end up with

$$\begin{aligned}\langle i(t)i(t+\tau)\rangle_{S_y} &= 2e^2\left(\left\langle \hat{S}_y^{\mathtt{out}}(t)\hat{S}_y^{\mathtt{out}}(t+\tau)\right\rangle + \left\langle \hat{S}_y^{\mathtt{out}}(t+\tau)\hat{S}_y^{\mathtt{out}}(t)\right\rangle\right),\\ \langle i(t)i(t+\tau)\rangle_{S_z} &= 2e^2\left(\left\langle \hat{S}_z^{\mathtt{out}}(t)\hat{S}_z^{\mathtt{out}}(t+\tau)\right\rangle + \left\langle \hat{S}_z^{\mathtt{out}}(t+\tau)\hat{S}_z^{\mathtt{out}}(t)\right\rangle\right),\end{aligned} \tag{E.13}$$

which is valid for 100% effective detectors and for the very special case of (E.12). To include less than unity efficiency detection is straightforward if needed. We also note that including $\eta_{\mathrm{d}} < 1$ in the description above or including it as a loss along the lines of App. A.4 makes no difference. We see that all the trouble caused by the normal and time ordering in photo detection theory in some cases can be boiled down to a simple expression involving only Stokes operators.

We conclude this appendix with a useful result for the spectrum (E.2) of a measurement of $\hat{S}_y^{\mathrm{out}}$ (or similarly $\hat{S}_z^{\mathrm{out}}$). This is close to what is known in the literature as the Wiener-Khintchine theorem [86]. If the Fourier transformed Stokes operator $\hat{S}_y^{\mathrm{out}}(\omega) = 1/\sqrt{2\pi}\int \hat{S}_y^{\mathrm{out}}(t)e^{i\omega t}dt$ has a correlation function on the form

$$\left\langle \hat{S}_y^{\mathrm{out}}(\omega)\hat{S}_y^{\mathrm{out}}(-\omega')\right\rangle = f(\omega)\delta(\omega-\omega'), \tag{E.14}$$

then the spectrum (E.2) of the photo current $i(t)$ can be found by Fourier transforming (E.13) and we get

$$\Phi(\omega) = \frac{2e^2}{\sqrt{2\pi}}\left[f(\omega)+f(-\omega)\right]. \tag{E.15}$$

The front factor is irrelevant but the fact that there are two terms with opposite signs on ω is a result of the normal ordering of light operators. This result is used in Chap. 8.

APPENDIX F

The Quadratic Zeeman Effect

The quadratic Zeeman effect is well understood [87], we will outline the important results in this appendix. An alkaline atom in an external magnetic field $\mathbf{B}$ is described by the Hamiltonian

$$\hat{H} = ha\mathbf{I}\cdot\mathbf{J} - \frac{\mu_J}{J}\mathbf{J}\cdot\mathbf{B} - \frac{\mu_I}{I}\mathbf{I}\cdot\mathbf{B}, \tag{F.1}$$

where $\mathbf{J}$ describes the angular momentum of the outermost electron, $\mathbf{I}$ is the nuclear spin, a describes the strength of the magnetic dipole interaction between the electronic and nuclear spin, and h is Planck's constant. The magnetic moment of the electron (for an s-electron with $L = 0$) is $\mu_J = -1.0011596521869(41)\mu_B$. The value for the nuclear moment in cesium is $\mu_I = 2.582025(4)\mu_N$. Thus, the last term in (F.1) always gives a minor correction compared to the second term, but the relative strength between the first and second terms depends on the magnetic field $\mathbf{B}$.

The exact solution for the energy E to the above Hamiltonian is

$$E_{F,m} = -\frac{h\nu_{\text{hfs}}}{2(2I+1)} - \frac{\mu_I}{I}Bm \pm \frac{h\nu_{\text{hfs}}}{2}\sqrt{1 + \frac{4m}{2I+1}x + x^2}, \tag{F.2}$$

where $\pm$ is used for $F = I \pm 1/2$, m is the magnetic quantum number (quantized along the direction of the magnetic field), $B = |\mathbf{B}|$, and the hyperfine splitting ν_{hfs} relates to a by $h\nu_{\text{hfs}} = \frac{ha}{2}(2I+1)$. The parameter x describes the relative strength between the Zeeman effect and the hyperfine splitting:

$$x = \frac{(-\mu_J/J + \mu_I/I)B}{h\nu_{\text{hfs}}}. \tag{F.3}$$

For weak fields m describes the projection of the total angular momentum $\mathbf{F} = \mathbf{I}+\mathbf{J}$ (the total angular momentum is denoted $\mathbf{J}$ in the rest of this thesis, with the obvious possibility of confusion!). We see from (F.2) that for small field strengths or very strong fields, the energy depends linearly on B. In the intermediate region the situation is quite non-linear. All our experiments are performed in the weak field regime with $x \approx 3 \cdot 10^{-4}$. Here a linear approximation is very good, but it is important to calculate also the second order contribution.

We calculate the separation of adjacent sub-levels starting out by expanding (F.2) to first order in the magnetic field strength B (leaving out the constant shift independent of B). With the standard convention

$$E^{(1)}_{F,m} = g_F \mu_B B m, \tag{F.4}$$

we get for cesium with nuclear spin $I = 7/2$

$$\begin{aligned} g_F &= \frac{1}{\mu_B}\left(-\frac{\mu_I}{I} \pm \frac{-\mu_J/J + \mu_I/I}{2I+1}\right) \\ &= \begin{cases} 0.250390 & \text{for } F = 4 \\ -0.251194 & \text{for } F = 3 \end{cases}. \end{aligned} \tag{F.5}$$

These two numbers differ in magnitude by approximately 0.3%. Thus we have a slightly higher separation between levels for the case of $F = 3$ than for $F = 4$. To calculate the quadratic Zeeman shift, it will suffice to do the approximation $\mu_I = 0$. In this case we may write the first order expansion of (F.2) as $h\nu_\mathrm{L} \equiv E_{m+1} - E_m \approx \frac{-\mu_J/J}{2I+1} \cdot B$, and we then easily derive to second order

$$\frac{E_{m+1} - E_m}{h} = \nu_L \left(1 - \frac{\nu_\mathrm{L}}{\nu_\mathrm{hfs}}(2m+1)\right). \tag{F.6}$$

This equation describes the transition frequency between the m'th and the $(m+1)$'th level. As is described in Sec. 7.1 we perform spectroscopy on transitions with $\Delta m = \pm 1$, see Fig. 7.2(b). The separation ν_QZ caused by the quadratic Zeeman effect between two *lines* will thus be

$$\nu_\mathrm{QZ} = \frac{2\nu_\mathrm{L}^2}{\nu_\mathrm{hfs}}. \tag{F.7}$$

Most of our experiments have ν_L in the vicinity of 325kHz corresponding to a magnetic field of a little less than 1 Gauss. With the cesium hyperfine splitting being $\nu_\mathrm{hfs} = 9.1926$GHz we get a quadratic Zeeman splitting of 23Hz.

APPENDIX G

Spin Decay and Langevin Forces

In this appendix we derive the correlation function for the Langevin noise terms $\hat{\mathcal{F}}_y$ and $\hat{\mathcal{F}}_z$ used in Chap. 8. These Langevin forces are necessary in presence of the decay terms of Eqs. (8.3) and (8.4). We may take these two equations and leave out the terms from the coherent evolution of Heisenberg equations, i.e.

$$\frac{\partial}{\partial t}\hat{J}_y^{\text{out}}(t) = -\Gamma \hat{J}_y(t) + \hat{\mathcal{F}}_y(t), \tag{G.1}$$

$$\frac{\partial}{\partial t}\hat{J}_z^{\text{out}}(t) = -\Gamma \hat{J}_z(t) + \hat{\mathcal{F}}_z(t). \tag{G.2}$$

We assume the reservoir to have no memory, i.e. the correlation functions can be written $\left\langle \hat{\mathcal{F}}_i(t)\hat{\mathcal{F}}_j(t')\right\rangle = k_{ij}\delta(t-t')$. Integrating suitable combinations of the above equations over a small time step Δt will lead to the different k_{ij}'s. Starting with k_{yz} we get to first order

$$\begin{aligned}
i\left\langle \hat{J}_x\right\rangle &= i\left\langle \hat{J}_x(t+\Delta t)\right\rangle = \left\langle \left[\hat{J}_y(t+\Delta t), \hat{J}_z(t+\Delta t)\right]\right\rangle \\
&= (1-2\Gamma\cdot\Delta t)\left\langle \left[\hat{J}_y(t), \hat{J}_z(t)\right]\right\rangle + \int_t^{t+\Delta t}\int_t^{t+\Delta t}\left\langle \left[\hat{\mathcal{F}}_y(t'), \hat{\mathcal{F}}_z(t'')\right]\right\rangle dt'dt'' \\
&= i(1-2\Gamma\cdot\Delta t)\left\langle \hat{J}_x\right\rangle + (k_{yz}-k_{zy})\Delta t \\
&\Rightarrow \qquad (k_{yz}-k_{zy}) = 2i\Gamma\left\langle \hat{J}_x\right\rangle,
\end{aligned} \tag{G.3}$$

where we have assumed the macroscopic mean value of $\hat{J}_x$ to be independent on time for a well oriented sample. Note, that the quantity $(k_{yz} - k_{zy})$ changes sign if the macroscopic spin reverses direction. We could also have calculated the anti-commutator above,

$$\left\langle \left[\hat{J}_y(t+\Delta t), \hat{J}_z(t+\Delta t)\right]_+ \right\rangle = (1 - 2\Gamma \cdot \Delta t) \left\langle \left[\hat{J}_y(t), \hat{J}_z(t)\right]_+ \right\rangle + (k_{yz} + k_{zy})\Delta t. \tag{G.4}$$

But since $\hat{J}_y\hat{J}_z + \hat{J}_z\hat{J}_y = (\hat{J}_+^2 - \hat{J}_-^2)/2i$ and the expectation value of $\hat{J}_+^2$ or $\hat{J}_-^2$ is zero for a completely polarized sample we have $k_{yz} + k_{zy} = 0$ to a high precision. We proceed with k_{zz},

$$\begin{aligned} \left\langle \hat{J}_z^2(t+\Delta t) \right\rangle &= (1 - 2\Gamma \cdot \Delta t) \left\langle \hat{J}_z^2(t) \right\rangle + \int_t^{t+\Delta t} \int_t^{t+\Delta t} \left\langle \hat{\mathcal{F}}_y(t')\hat{\mathcal{F}}_z(t'') \right\rangle dt' dt'' \\ &= (1 - 2\Gamma \cdot \Delta t) \left\langle \hat{J}_z^2 \right\rangle + k_{zz}\Delta t \\ \Rightarrow \qquad & k_{yy} = k_{zz} = 2\Gamma \left\langle \hat{J}_z^2 \right\rangle = \Gamma J_x, \end{aligned} \tag{G.5}$$

where we again assume time independence of the variance of $\hat{J}_z$ (it is given by its steady state value which in our case means the coherent spin state since Γ is governed by optical pumping to this state. The last equality reflects that. We also stated the same result for k_{yy} which is derived in a similar fashion. We conclude this appendix by repeating the results,

$$\begin{aligned} \left\langle \hat{\mathcal{F}}_y(t)\hat{\mathcal{F}}_y(t') \right\rangle &= \left\langle \hat{\mathcal{F}}_z(t)\hat{\mathcal{F}}_z(t') \right\rangle = \Gamma \cdot |J_x| \cdot \delta(t - t'), \\ \left\langle \hat{\mathcal{F}}_y(t)\hat{\mathcal{F}}_z(t') \right\rangle &= -\left\langle \hat{\mathcal{F}}_z(t)\hat{\mathcal{F}}_y(t') \right\rangle = i\Gamma \cdot J_x \cdot \delta(t - t'), \end{aligned} \tag{G.6}$$

where J_x is the mean value of the macroscopic spin $\hat{J}_x$ counted positive along the x-axis.

Bibliography

[1] J. M. Radcliffe, J. Phys. A **4**, 313 (1971).

[2] W. K. Wootters and W. H. Zurek, Nature **299**, 802 (1982).

[3] N. Gisin, G. Ribordy, W. Tittel, and H. Zbinden, Rev. Mod. Phys. **74**, 145 (2002).

[4] M. Hillery, Phys. Rev. A **61**, 022309 (2000).

[5] T. C. Ralph, Phys. Rev. A **61**, 010303 (2000).

[6] N. J. Cerf, M. Levy, and G. V. Assche, Phys. Rev. A **63**, 052311 (2001).

[7] C. Silberhorn, T. C. Ralph, N. Lütkenhaus, and G. Leuchs, Phys. Rev. Lett. **89**, 167901 (2002).

[8] F. Grosshans and P. Grangier, Phys. Rev. Lett. **88**, 057902 (2002).

[9] F. Grosshans *et al.*, Nature **421**, 238 (2003).

[10] L. K. Grover, Phys. Rev. Lett. **79**, 325 (1997).

[11] P. W. Shor, in *Proceedings of the 35th Annual Symposium on the Foundations of Computer Science* (IEEE Computer Society Press, Los Alamitos, California, 1994), p. 124.

[12] D. P. DiVincenzo, Phys. Rev. A **51**, 1015 (1995).

[13] J. I. Cirac and P. Zoller, Phys. Rev. Lett. **74**, 4091 (1995).

[14] C. Monroe *et al.*, Phys. Rev. Lett. **75**, 4714 (1995).

[15] F. Schmidt-Kaler *et al.*, Nature **422**, 408 (2003).

[16] L. M. K. Vandersypen *et al.*, Nature **414**, 883 (2001).

[17] C. H. Bennett and D. P. DiVincenzo, Nature **404**, 247 (2000).

[18] S. Lloyd and S. L. Braunstein, Phys. Rev. Lett. **82**, 1784 (1999).

[19] S. L. Braunstein, Phys. Rev. Lett. **80**, 4084 (1998).

[20] S. Lloyd and J. J. E. Slotine, Phys. Rev. Lett. **80**, 4088 (1998).

[21] T. C. Ralph, W. J. Munro, and G. J. Milburn, Quantum Computation with Coherent States, Linear Interactions and Superposed Resources, quant-ph/0110115.

[22] S. Massar and E. S. Polzik, Phys. Rev. Lett. **91**, 060401 (2003).

[23] M. Brune *et al.*, Phys. Rev. Lett. **77**, 4887 (1996).

[24] C. Monroe, D. M. Meekhof, B. E. King, and D. J. Wineland, Science **272**, 1131 (1996).

[25] A. Furusawa *et al.*, Science **282**, 706 (1998).

[26] D. Bouwmeester *et al.*, Nature **390**, 575 (1997).

[27] D. Boschi *et al.*, Phys. Rev. Lett. **80**, 1121 (1998).

[28] N. Lütkenhaus, J. Calsamiglia, and K. A. Suominen, Phys. Rev. A **59**, 3295 (1999).

[29] Y. H. Kim, S. P. Kulik, and Y. Shih, Phys. Rev. Lett. **86**, 1370 (2001).

[30] M. Fleischhauer and M. D. Lukin, Phys. Rev. Lett. **84**, 5094 (2000).

[31] D. F. Phillips *et al.*, Phys. Rev. Lett. **86**, 783 (2001).

[32] C. Liu, Z. Dutton, C. H. Behroozi, and L. V. Hau, Nature **409**, 490 (2001).

[33] A. V. Turukhin *et al.*, Phys. Rev. Lett. **88**, 023602 (2002).

[34] Y. H. Shih and C. O. Alley, Phys. Rev. Lett. **61**, 2921 (1988).

[35] Z. Y. Ou, S. F. Pereira, H. J. Kimble, and K. C. Peng, Phys. Rev. Lett. **68**, 3663 (1992).

[36] P. G. Kwiat *et al.*, Phys. Rev. Lett. **75**, 4337 (1995).

[37] C. Schori, J. L. Sørensen, and E. S. Polzik, Phys. Rev. A **66**, 033802 (2002).

[38] J. S. Bell, Physics **1**, 195 (1965).

[39] A. Aspect, J. Dalibard, and G. Roger, Phys. Rev. Lett. **49**, 1804 (1982).

[40] E. Hagley *et al.*, Phys. Rev. Lett. **79**, 1 (1997).

[41] C. A. Sackett *et al.*, Nature **404**, 256 (2000).

[42] D. J. Wineland *et al.*, Phys. Rev. A **46**, R6797 (1992).

[43] G. Santarelli *et al.*, Phys. Rev. Lett. **82**, 4619 (1999).

[44] J. Hald, J. L. Sørensen, C. Schori, and E. S. Polzik, Phys. Rev. Lett. **83**, 1319 (1999).

[45] A. Kuzmich, L. Mandel, and N. P. Bigelow, Phys. Rev. Lett. **85**, 1594 (2000).

[46] H. J. Briegel *et al.*, Lect. Notes Comput. Sc. **1509**, 373 (1999).

[47] S. Haroche, M. Brune, and J. M. Raimond, Phil. Trans. Roy. Soc. A **355**, 2367 (1997).

[48] G. C. Bjorklund, M. D. Levenson, W. Lenth, and C. Ortiz, Appl. Phys. B **32**, 145 (1983).

[49] O. Schmidt, K. M. Knaak, R. Wynands, and D. Meschede, Appl. Phys. B **59**, 167 (1994).

[50] M. A. Bouchiat and J. Brossel, Phys. Rev. **147**, 41 (1966).

[51] E. B. Alexandrov *et al.*, Laser Phys. **6**, 244 (1996).

[52] E. B. Alexandrov *et al.*, Phys. Rev. A **66**, 042903 (2002).

[53] P. W. Milonni and J. H. Eberly, *Lasers* (John Wiley & Sons, New York, 1988).

[54] D. Kleppner, N. F. Ramsey, and H. M. Goldenberg, Phys. Rev. **126**, 603 (1962).

[55] H. J. Metcalf and P. van der Straten, *Laser Cooling and Trapping* (Springer, New York, 1999).

[56] W. Happer, Rev. Mod. Phys. **44**, 169 (1972).

[57] D. Tupa and L. W. Anderson, Phys. Rev. A **36**, 2142 (1987).

[58] A. Kuzmich, N. P. Bigelow, and L. Mandel, Europhys. Lett. **42**, 481 (1998).

[59] Y. Takahashi *et al.*, Phys. Rev. A **60**, 4974 (1999).

[60] E. S. Polzik, J. L. Sørensen, and J. Hald, Appl. Phys. B **66**, 759 (1998).

[61] A. Einstein, B. Podolsky, and N. Rosen, Phys. Rev. **47**, 777 (1935).

[62] L. Duan, J. I. Cirac, P. Zoller, and E. S. Polzik, Phys. Rev. Lett. **85**, 5643 (2000).

[63] L. Duan, G. Giedke, J. I. Cirac, and P. Zoller, Phys. Rev. Lett. **84**, 2722 (2000).

[64] R. Simon, Phys. Rev. Lett. **84**, 2726 (2000).

[65] M. G. Raymer, A. C. Funk, B. C. Sanders, and H. de Guise, Phys. Rev. A **67**, 052104 (2003).

[66] F. Hong-yi and J. R. Klauder, Phys. Rev. A **49**, 704 (1994).

[67] I. Bouchoule and K. Mølmer, Phys. Rev. A **66**, 043811 (2002).

[68] A. DiLisi and K. Mølmer, Phys. Rev. A **66**, 052303 (2002).

[69] C. Henkel and M. Wilkens, Europhys. Lett. **47**, 414 (1999).

[70] C. H. Bennett *et al.*, Phys. Rev. Lett. **70**, 1895 (1993).

[71] L. Vaidman, Phys. Rev. A **49**, 1473 (1994).

[72] S. L. Braunstein, C. A. Fuchs, H. J. Kimble, and P. van Loock, Phys. Rev. A **64**, 022321 (2001).

[73] F. Grosshans and P. Grangier, phys. Rev. A **64**, 010301 (2001).

[74] S. L. Braunstein and H. J. Kimble, Phys. Rev. A **80**, 869 (1998).

[75] A. Kuzmich and E. S. Polzik, Phys. Rev. Lett. **85**, 5639 (2000).

[76] J. Fiurasek, Private communication.

[77] C. Cohen-Tannoudji, J. Dupont-Roc, and G. Grynberg, *Introduction to Quantum Electrodynamics* (John Wiley & Sons, Inc., New York, 1989).

[78] K. J. Blow, R. Loudon, S. J. D. Phoenix, and T. J. Shepherd, Phys. Rev. A **42**, 4102 (1990).

[79] M. Fleishhauer and T. Ricter, Phys. Rev. A **51**, 2430 (1995).

[80] C. Cohen-Tannoudji, J. Dupont-Roc, and G. Grynberg, *Atom-Photon Interactions* (John Wiley & Sons, Inc., New York, 1992).

[81] A. R. Edmonds, *Angular momentum in quantum mechanics* (Princeton University Press, Princeton, 1974).

[82] C. W. Gardiner and P. Zoller, *Quantum Noise*, 2nd ed. (Springer, Heidelberg, Germany, 2000).

[83] Z. Y. Ou, C. K. Hong, and L. Mandel, J. Opt. Soc. Am. B **4**, 1574 (1987).

[84] B. Huttner and Y. Ben-Aryeh, Phys. Rev. A **40**, 2479 (1989).

[85] S. F. Pereira, X. Min, H. J. Kimble, and J. L. Hall, Phys. Rev. A **38**, 4931 (1988).

[86] P. Meystre and M. Sargent III, *Elements of Quantum Optics* (Springer-Verlag, Berlin, 1991).

[87] N. F. Ramsey, *Molecular Beams* (Oxford University Press, Amen House, London EC4, 1956).

Erratum

In the following we list errors in the thesis *Entanglement and Quantum Interactions with Macroscopic Gas Samples* by Brian Julsgaard, University of Aarhus, October 2003. This erratum has been updated August 28th, 2005.

1 Interaction Hamiltonian

There is a mistake of a factor of two in the derived effective Hamiltonian Eq. (5.18). This error arises from a mistake in the adiabatic elimination procedure of Sec. 5.2. I am grateful to Klemens Hammerer for finding the error. Below we will explain it in detail.

1.1 A Spin-1/2 Toy Model

It is unnecessary going through the calculations of Sec. 5.2 with the full level structure and propagating optical fields. We shall consider a single spin-1/2 atom as depicted in Fig. 1 interacting with only two light modes, $\hat{a}_+$ and $\hat{a}_-$. The interaction Hamiltonian for this system is (in the frame rotating with the laser field)

$$\hat{H}_{\text{int}} = \hbar\Delta(\hat{\sigma}_{33} + \hat{\sigma}_{44}) + \hbar g(\tilde{a}_+^\dagger \tilde{\sigma}_{14} + \tilde{\sigma}_{41}\tilde{a}_+ + \tilde{a}_-^\dagger \tilde{\sigma}_{23} + \tilde{\sigma}_{32}\tilde{a}_-), \tag{1}$$

where g is a real parameter describing the interaction strength and the atomic operators $\tilde{\sigma}_{ij}$ and light operators $\tilde{a}_\pm$ have already been written in the slowly

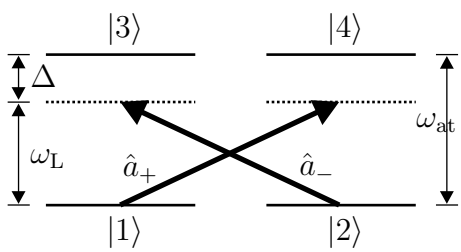

Figure 1: The level structure of a simple spin-1/2 model with optical frequencies and detunings included. The propagation direction of the light mode coincides with the quantization axis of the atomic states and we decompose the light into the two polarization modes $\hat{a}_+$ and $\hat{a}_-$.

varying form (see Eq. (5.9)). From this Hamiltonian we may derive the equations of motion. For the ground state operators we find

$$\begin{aligned}
\frac{\partial \hat{\sigma}_{11}}{\partial t} &= \frac{1}{i\hbar}\left[\hat{\sigma}_{11}, \hat{H}_{\text{int}}\right] = -ig(\tilde{a}_+^\dagger \tilde{\sigma}_{14} - \tilde{\sigma}_{41}\tilde{a}_+), \\
\frac{\partial \hat{\sigma}_{22}}{\partial t} &= -ig(\tilde{a}_-^\dagger \tilde{\sigma}_{23} - \tilde{\sigma}_{32}\tilde{a}_-), \\
\frac{\partial \hat{\sigma}_{12}}{\partial t} &= -ig(\tilde{a}_-^\dagger \tilde{\sigma}_{13} - \tilde{\sigma}_{42}\tilde{a}_+).
\end{aligned} \tag{2}$$

To proceed we need approximate results for the atomic operators on the right hand side of these equations. For $\tilde{\sigma}_{14}$ we find

$$\frac{\partial \tilde{\sigma}_{14}}{\partial t} = -i\Delta\tilde{\sigma}_{14} - ig\tilde{a}_+(\hat{\sigma}_{11} - \hat{\sigma}_{44}) \quad \Rightarrow \quad \tilde{\sigma}_{14} \approx -\frac{g}{\Delta}\tilde{a}_+\hat{\sigma}_{11}, \tag{3}$$

where the adiabatic elimination is carried out by setting the time derivative equal to zero. We also neglect the excited state population $\hat{\sigma}_{44}$. For $\tilde{\sigma}_{13}$ we have

$$\frac{\partial \tilde{\sigma}_{13}}{\partial t} = -i\Delta\tilde{\sigma}_{13} - ig(\tilde{a}_-\tilde{\sigma}_{12} - \tilde{a}_+\tilde{\sigma}_{43}) \quad \Rightarrow \quad \tilde{\sigma}_{13} \approx -\frac{g}{\Delta}\tilde{a}_-\tilde{\sigma}_{12}, \tag{4}$$

where the excited state coherence $\tilde{\sigma}_{43}$ was neglected. In similar manners we find

$$\tilde{\sigma}_{23} \approx -\frac{g}{\Delta}\tilde{a}_-\hat{\sigma}_{22} \quad \text{and} \quad \tilde{\sigma}_{24} \approx -\frac{g}{\Delta}\tilde{a}_+\hat{\sigma}_{21}. \tag{5}$$

Now we insert the approximations (3)-(5) into the equations of motion (2) and obtain

$$\begin{aligned}
\frac{\partial \hat{\sigma}_{11}}{\partial t} &= \frac{\partial \hat{\sigma}_{22}}{\partial t} = 0, \\
\frac{\partial \hat{\sigma}_{12}}{\partial t} &= \frac{ig^2}{\Delta}(\tilde{a}_-^\dagger\tilde{a}_- - \tilde{a}_+^\dagger\tilde{a}_+)\tilde{\sigma}_{12}.
\end{aligned} \tag{6}$$

These equations are reproduced by the effective ground state Hamiltonian

$$\hat{H}_{\text{eff}} = -\frac{\hbar g^2}{\Delta}\left(\hat{\sigma}_{11}\tilde{a}_+^\dagger\tilde{a}_+ + \hat{\sigma}_{22}\tilde{a}_-^\dagger\tilde{a}_-\right). \tag{7}$$

If we instead (as was done in Sec. 5.2) insert the approximations (3)-(5) directly into the un-approximated Hamiltonian (1) we obtain an effective Hamiltonian twice as big which is wrong since the correct Eq. (6) would then not be reproduced.

1.2 Implications on the Experimental Results

The erroneous factor of two discussed above is of course inherited to many equations in the thesis chapters following the derivation of the interaction Hamiltonian. In Eq. (6.15) the correct interaction parameter is

$$a = -\frac{\gamma}{8A\Delta}\frac{\lambda^2}{2\pi}a_1, \tag{6.15}$$

and whenever we encounter an expression proportional to a (or a_1, a_2) we must reduce the result by a factor of two. It is not convenient to list all the cases here but one important equation is the estimation of the atomic to shot noise ratio κ^2 in the entanglement generation experiment. We find

$$\kappa^2 = \frac{9.3 \cdot P[\mathrm{mW}] \cdot T[\mathrm{ms}] \cdot a_1(\Delta) \cdot \theta_{\mathrm{DC}}[\mathrm{deg}]}{\Delta_{\mathrm{blue}}[\mathrm{MHz}]}. \tag{9.51}$$

On page 106 (and in different papers published after the Ph.D. thesis, the error was found in the summer of 2005) we actually discuss a discrepancy of a factor of approximately two in the observed atomic to shot noise ratio. With the error found there is now a much better agreement between theory and experiment.

2 Simple Errors

There is a mistake in Eq. (5.19). For $F = 3$ the sign of a_1 has to be reversed such that we have

$$a_1 = \frac{1}{56}\left(\frac{45}{1+\Delta_{24}/\Delta} - \frac{21}{1+\Delta_{23}/\Delta} - 80\right) \to -1 \tag{8}$$

Updates

Below we list publications which are a result of work performed after the Ph.D. thesis. Hence, this should not be considered as a part of the thesis but as a supplement. I hope it will be useful to the reader.

- D. V. Kupriyanov, O. S. Mishina, I. M. Sokolov, B. Julsgaard, and E. S. Polzik, Phys. Rev. A **71**, 032348 (2005). This publication treats the higher order effects as discussed in Chap. 6. It also coveres the noise properties of the higher order terms. Available at `quant-ph/0411083`.

- B. Julsgaard, J. Sherson, J. I. Cirac, J. Fiurasek, and E. S. Polzik, *Quantum Memory for Light*, Nature **432**, 482 (2004). Also available at `quant-ph/0410072`. This publication describes an experiment carried out with a setup quite similar to the entanglement experiments in the thesis.

- J. Sherson, B. Julsgaard, and E. S. Polzik, *Distant Entanglement of Macroscopic Gas Samples* in *Decoherence, Entanglement and Information Protection in Complex Quantum Systems*, eds. W. M. Akulin, A. Sarfati, G. Kurizki, and S. Pellegrin (Springer, Dordrecht, 2005). Also available at `quant-ph/0408146`. This publication describes very well the new entanglement procedure as discussed in Sec. 10.4.